

Portland State University

PDXScholar

Dissertations and Theses

Dissertations and Theses

8-17-2021

Mechanistic Investigation of Neuropeptide S-nitrosylation by Nitric Oxide Moieties: A Kinetic and Thermodynamic Approach

Vusumuzi Leroy Sibanda
Portland State University

Follow this and additional works at: https://pdxscholar.library.pdx.edu/open_access_etds

 Part of the [Chemistry Commons](#)

Let us know how access to this document benefits you.

Recommended Citation

Sibanda, Vusumuzi Leroy, "Mechanistic Investigation of Neuropeptide S-nitrosylation by Nitric Oxide Moieties: A Kinetic and Thermodynamic Approach" (2021). *Dissertations and Theses*. Paper 5837. <https://doi.org/10.15760/etd.7708>

This Dissertation is brought to you for free and open access. It has been accepted for inclusion in Dissertations and Theses by an authorized administrator of PDXScholar. Please contact us if we can make this document more accessible: pdxscholar@pdx.edu.

Mechanistic Investigation of Neuropeptide S-nitrosylation by Nitric Oxide Moieties:
A Kinetic and Thermodynamic Approach

by

Vusumuzi Leroy Sibanda

A dissertation submitted in partial fulfillment of the
requirements for the degree of

Doctor of Philosophy
in
Chemistry

Dissertation Committee:
Robert M. Strongin, Chair
Mark Woods
Shankar Ranavare
Anna-Louise Reysenbach

Portland State University
2021

© 2021 Vusumuzi Leroy Sibanda

ABSTRACT

This dissertation focuses on providing quantitative insights regarding kinetic, thermodynamic and mechanistic parameters of neuropeptide S-nitrosylation by nitrous acid (HNO_2), peroxyxynitrite (ONOO^-) and S-nitroso-N-acetyl-D,L-penicillamine (SNAP) to produce S-nitrosothiols (SNOs). Peptide thiol stability and the formation of SNOs from neuropeptides; arginine vasopressin (AVP), somatostatin-14 (SST-14) and urotensin II (U-II) was studied. Investigations into the effects of temperature, copper chelators and pH on peptide thiol autoxidation show that AVP, SST-14 and U-II thiols have half-lives of 30, 44 and 28.2 mins respectively at physiologically relevant temperature and pH in the absence of metal chelators. Target peptide thiols were shown to have half-lives sufficient for subsequent S-nitrosylation reactions. The stability of peptide thiol in physiologically relevant conditions suggests novel peptide thiol-mediated chemical signaling mechanisms. We report the formation of S-nitrosothiols: AVP(SNO), SST-14(SNO) and U-II(SNO) through HNO_2/NO^+ mediated S-nitrosylations. Reported bimolecular rate constants suggest that HNO_2 and NO^+ would be the predominant nitrosating agents at low pH. Kinetic and EPR analysis implicated copper redox cycling mechanism as catalysts for SNO formation and decomposition. The release of NO during SNO decomposition suggests a potential role for SNOs as efficient NO carrier and donors. Peroxyxynitrite reactions with peptide thiols showed a complex dependence of acid concentrations with lower bimolecular rates at physiological pH. We present peptide thiols as good candidates for further studies as a peroxyxynitrite detoxifying compounds. Highly negative activation entropies are reported for SNAP transnitrosation reactions with rate-limiting steps that are

characterized by a relatively ordered associative transition state. These activation parameters suggest low energy barriers for transnitrosylation under physiological conditions and support growing evidence that transnitrosylation may be a viable posttranslational mechanism for NO transport *in vivo*. This dissertation proposes kinetic reaction schemes, thermodynamics and mechanisms related to neuropeptide SNO formation. Researchers can use these insights in the development of potential therapeutics that target endogenous SNOs, and/or utilize synthetic SNOs to stimulate or inhibit NO signaling. Kinetic models presented in this work can be used to infer the NO release profiles of potential NO-donor based drugs by enhancing our understanding of the underlying pharmacokinetics.

DEDICATION

I dedicate this dissertation to the three most important women in my life; my wife Andrea Sibanda, mother Celesani Sibanda and sister Zandile Sibanda. Special mention also goes to my brother Advocate Lewis Sibanda; I am proud of you buddy. This is for all of you!

ACKNOWLEDGMENTS

I would like to give thanks to my dissertation committee members; Dr Robert Strongin, Dr Mark Woods, Dr Shankar Rananavare and Dr Anna-Louise Reysenbach. Thank you for your mentorship during my PhD journey. To Drs Strongin and Rananavare, words cannot express the impact you have had on my life, thank you! Many thanks also go to Dr Simoyi for the opportunity to join PSU and the guidance to grow as a well-rounded scientist. Last but certainly not least, I thank the Sigma Xi Columbia-Willamette board for allowing me to serve as a board member and for the funding to attend various conferences that emanated in numerous student awards. You believed in me even when I didn't believe in myself and for that I am eternally grateful.

TABLE OF CONTENTS

ABSTRACT	i
DEDICATION	iii
ACKNOWLEDGMENTS	iv
LIST OF TABLES	x
LIST OF FIGURES	xii
LIST OF SCHEMES	xvi
LIST OF ABBREVIATIONS	xvii
CHAPTER 1: INTRODUCTION	1
1.1 Nitric oxide: synthesis, signaling and toxicity.....	1
1.1.1 Nitric oxide synthesis and isoforms.....	1
1.1.2 NO diffusion, reactivity and signaling.....	12
1.2 Peroxynitrite chemistry in health and disease.....	14
1.3 Thiol biochemistry and S-nitrosylation.....	17
1.4 Overarching goals and aims of this study.....	20
CHAPTER 2: INSTRUMENTATION, MATERIALS AND METHODS	22
2.1 Introduction.....	22
2.2 Instrumentation.....	22
2.2.1 UV/Vis Spectrophotometry.....	22

2.2.2 Stopped-Flow Spectrophotometry.....	23
2.2.3 Chromatography and mass spectrometry.....	23
2.2.4 Electron Paramagnetic Resonance (EPR) Spectroscopy.....	24
2.3 Materials.....	25
2.4 Experimental Methods.....	26
2.4.1 Peptide thiol formation, isolation, and identification.....	26
2.4.2 Peptide thiol stability.....	27
CHAPTER 3: KINETICS AND MECHANISMS OF ARGININE VASOPRESSIN S-NITROSYLATION BY NITRIC OXIDE	29
3.1 Introduction.....	29
3.2 Results and Discussion.....	31
3.2.1 AVP Dithiol Formation and Stability.....	31
3.2.2 Nitrous acid mediated S-nitrosylation Product Identification.....	33
3.2.2.1 Effect of AVP(SH) variation.....	35
3.2.2.2. Effect of nitrite variation.....	39
3.2.2.3 Effect of acid variation.....	40
3.2.2.4 Effect of Cu ²⁺ variation.....	40
3.2.2.5 Nitrous acid kinetic reaction scheme.....	43
3.2.2.6 Temperature dependence and thermodynamic analysis.....	45
3.2.2.7 EPR analysis.....	49
3.2.3 Peroxynitrite mediated AVP(SH) S-nitrosylation.....	50

3.2.3.1 Effect of AVP (SH) variation on ONOO ⁻ depletion and AVP(SNO) formation.....	52
3.2.3.2 Effect of acid variation on ONOOH mediated S-nitrosylation.....	52
3.2.3.3 Effect of peroxyxynitrite variation and EPR analysis.....	53
3.2.3.4 Temperature dependence and thermodynamic parameters.....	59
3.2.4 SNAP mediated transnitrosation.....	64
3.2.4.1 Effect of AVP(SH) and SNAP variation.....	64
3.2.4.2 SNAP temperature dependence and thermodynamic parameters....	68
3.3 Conclusion.....	71
CHAPTER 4: KINETICS AND ENERGETICS OF S-NITROSO-SOMATOSTATIN FORMATION	73
4.1 Introduction.....	73
4.2 Results and Discussion.....	74
4.2.1 SST-14 dithiol formation and stability.....	74
4.2.2 Nitrous acid mediated S-nitrosylation.....	76
4.2.2.1 Effect of SST-14(SH) variation.....	76
4.2.2.2 Effect of nitrite variation.....	79
4.2.2.3 Effect of acid variation.....	80
4.2.2.4 NO ⁺ S-nitrosylation temperature dependence and thermodynamic parameters.....	82
4.2.3 Peroxyxynitrite mediated SST-14 S-nitrosylation.....	84

4.2.3.1 Effect of SST-14 variation.....	84
4.2.3.2 Effect of acid variation on ONOO ⁻ mediated SST-14(SNO) formation.....	86
4.2.3.3 Peroxynitrite variation and EPR analysis.....	88
4.2.3.4 Peroxynitrite mediated S-nitrosylation reaction scheme.....	89
4.2.3.5 Temperature dependence and thermodynamic parameters.....	91
4.2.4 SNAP mediated SST-14(SH) S-nitrosylation.....	98
4.2.4.1 Effect of SST-14 and SNAP variation.....	98
4.2.4.2 SST-14(SH) transnitrosation thermodynamic parameters.....	101
4.3 Conclusion.....	104
CHAPTER 5: KINETICS AND THERMODYNAMICS OF THE REVERSIBLE BINDING OF NITRIC OXIDE TO UROTENSIN-II	105
5.1 Introduction.....	105
5.2 Results and Discussions.....	107
5.2.1 U-II thiol Formation and Stability.....	107
5.2.2 Reaction kinetics and thermodynamics.....	111
5.2.2.1 Nitrous acid mediated U-II(SH) S-nitrosylation.....	111
5.2.2.2 Effect of nitrite variation.....	111
5.2.2.3 Effect of acid on U-II(SNO) formation.....	111
5.2.2.4 Effect of U-II(SH) variation.....	115

5.2.2.5 Thermodynamic parameters for NO ⁺ mediated U-II(SNO) formation.....	115
5.2.3 Peroxynitrite-mediated U-II(SH) S-nitrosylation.....	118
5.2.3.1 Effect of U-II(SH) variation.....	118
5.2.3.2 Effect of acid variation on ONOOH depletion and U-II(SNO) formation.....	120
5.2.3.4 Peroxynitrite variation and EPR analysis.....	122
5.2.3.5 Thermodynamic parameters for ONOO ⁻ /ONOOH mediated U-II(SNO) formation.....	122
5.3 Conclusion.....	129
 CHAPTER 6: SUMMARY, CONCLUSIONS AND FUTURE PERSPECTIVES	
6.1 Summary.....	130
6.2 Conclusions and Future Perspectives.....	135
REFERENCES.....	137

LIST OF TABLES

Table 1.1 NOS Isoforms.....	5
Table 3.1: The effects of temperature, pH and metal chelators on time required for AVP disulfide reformation.....	33
Table 3.2: Observed rate constants for NO ⁺ mediated AVP thiol S-nitrosylation reactions.....	49
Table 3.3: Thermodynamic parameters for NO ⁺ mediated AVP thiol S-nitrosylation reactions.....	49
Table 3.4: ONOOH mediated AVP thiol S-nitrosylation k _{on} and k _{off} values.....	60
Table 3.5: ONOOH mediated AVP thiol S-nitrosylation thermodynamic parameters.....	60
Table 3.6. Observed rate constants for ONOO ⁻ mediated AVP thiol S-nitrosylation reactions.....	61
Table 3.7. Thermodynamic parameters for ONOO ⁻ mediated AVP thiol S-nitrosylation reactions.....	61
Table 3.8: Observed rate constants for SNAP mediated AVP thiol S-nitrosylation reactions.....	70
Table 3.9: Thermodynamic parameters for SNAP mediated AVP thiol S-nitrosylation.....	70
Table 4.1. Effects of temperature, pH and copper chelators on time for SST-14 disulfide reformation.....	76
Table 4.2. NO ⁺ mediated SST-14 thiol S-nitrosylation k _{on} and k _{off} values.....	82
Table 4.3: NO ⁺ mediated SST-14 thiol S-nitrosylation thermodynamic parameters.....	84
Table 4.4: ONOOH mediated SST-14 S-nitrosylation observed rate constants; k _{on} and k _{off}	92
Table 4.5: ONOOH mediated SST-14 S-nitrosylation thermodynamic parameters.....	93
Table 4.6: ONOO ⁻ mediated SST-14 S-nitrosylation observed rate constants; k _{on} and k _{off}	96
Table 4.7: ONOO ⁻ mediated SST-14 S-nitrosylation thermodynamic parameters.....	96
Table 4.8: SST-14(SH) SNAP mediated S-nitrosylation observed k _{on} and k _{off} rate constants.....	102

Table 4.9: SST-14(SH) SNAP mediated S-nitrosylation thermodynamic parameters.....	102
Table 5.1. The effects of temperature, pH, and copper chelators on required for U-II(S-S) reformation.....	110
Table 5.2. NO ⁺ mediated U-II S-nitrosylation observed rate constants: k _{on} and k _{off}	116
Table 5.3: NO ⁺ mediated U-II(SH) S-nitrosylation thermodynamic parameters.....	116
Table 5.4: Observed rate constants for ONOOH mediated U-II(SH) thiol S-nitrosylation reactions.....	126
Table 5.5: Thermodynamic parameters for ONOOH mediated U-II(SH) thiol S-nitrosylation reactions.....	126
Table 5.6: Observed rate constants for ONOO ⁻ mediated U-II(SH) thiol S-nitrosylation reactions.....	128
Table 5.7: Thermodynamic parameters for ONOO ⁻ mediated U-II(SH) thiol S-nitrosylation reactions.....	128
Table 6.1: HNO ₂ /NO ⁺ mediated S-nitrosylations bimolecular rate constants (M ⁻¹ s ⁻¹)	131
Table 6.2: Bimolecular rate constants (M ⁻¹ s ⁻¹) for ONOO ⁻ /ONOOH mediated S-nitrosylations.....	133

LIST OF FIGURES

Figure 1.1: NO signaling is linked to NMDA-R activation in the inferior colliculus (IC).....	4
Figure 1.2: iNOS regulates the expression of various immune cells and responses.....	7
Figure 1.3: (A) eNOS can be activation through various calcium dependent/independent pathways. (B) NO is also produced through cytochrome P450 reductase mediated NO ₃ reduction.....	10
Figure 1.4: Processes leading to peroxynitrite production and eNOS uncoupling in endothelial cells.....	11
Figure 1.5: Kinetic model for nitric oxide synthase catalysis.....	12
Figure 1.6: (a) Direct and Indirect effects of NO, (b) The interplay between nitric oxide, super oxide, peroxynitrite and nitrogen dioxide.....	14
Figure 1.7: Main redox modifications of cysteine residues.....	18
Figure 3.1: HPLC-UV-MS analysis of AVP disulfide reduction.....	32
Figure 3.2: Spectra scan of; (a) [HNO ₂ ⁻] = 3.5 mM, (b) [NO ₂ ⁻] = 4 mM, (c) [AVP] = 1 mM, [NO ₂ ⁻] = 10 mM and [H ⁺] = 50 mM, (d) [AVP(S-S)] = 0.17 mM and (e) AVP(SH) = 0.17mM.....	36
Figure 3.3: HPLC-UV-MS analysis of the reaction between 5 mM AVP thiol and 20 mM nitrous acid.....	37
Figure 3.4: (A) Effect of [AVP(SH)] variation on AVP(SNO) formation at 25 °C	38
Figure 3.5: (A) Effect of [NO ₂ ⁻] variation on AVP(SNO) formation at 25 °C.....	39
Figure 3.6: (A) Effect of [H ⁺] variation on AVP(SNO) formation at 25 °C.....	41
Figure 3.7: (A) Effect of [Cu ²⁺] variation on AVP(SNO) production at 25 °C.....	42
Figure 3.8: (A) Observed rate constants for the S-nitrosylation of AVP(SH) by varied NO ⁺ concentrations.....	48
Figure 3.9: EPR spectra of NO radical generation during AVP(SNO) decomposition.....	51
Figure 3.9: Spectra scan of; (a) [AVP(SH)] = 150 μM, (b) [ONOO ⁻] = 300 μM, (c) AVP(SNO) formation from reaction mixture with; [AVP(SH)] = 1.5 mM, [ONOO ⁻] = 1.5 mM in PBS at pH 7.4.	50

Figure 3.10: Effect of varying AVP(SH) concentrations on ONOO ⁻ depletion in PBS at pH 7.4.....	54
Figure 3.11: (A) Effect of varying H ⁺ concentrations on ONOO ⁻ mediated AVP(SNO) formation.....	55
Figure 3.12: (A) Effect of varying H ⁺ concentrations on ONOO ⁻ depletion.....	55
Figure 3.13: Effect of varying ONOO ⁻ concentrations on AVP(SNO) formation in PBS at pH 7.4.....	56
Figure 3.14: EPR spectra of DMPO radical adducts in ONOO ⁻ mediated AVP(SNO) formation.....	58
Figure 3.15: Observed rate constants for the S-nitrosylation of AVP(SH) by varied ONOOH concentrations.....	62
Figure 3.16: Observed rate constants for the S-nitrosylation of AVP(SH) by varied ONOO ⁻ concentrations.....	63
Figure 3.17: Effect of varying AVP(SH) concentrations on SNAP mediated AVP(SNO) formation.....	65
Figure 3.18: Effect of varying AVP(SH) concentrations on SNAP depletion in PBS at 590 nm and pH 7.4.....	66
Figure 3.19: Varying SNAP concentrations and AVP(SNO) formation in PBS at pH 7.4.....	66
Figure 3.20: Varying SNAP concentrations and SNAP depletion at 590 nm in pH 7.4 PBS.....	67
Figure 3.21: k _{obs} values for AVP(SNO) formation obtained by varying temperature and SNAP concentrations.....	69
Figure 4.1: HPLC-UV analysis of SST-14 disulfide reduction.....	75
Figure 4.2: ESI-MS analysis of HPLC chromatograms.....	77
Figure 4.3: 1st-order dependence SST-14(SNO) formation in SST-14(SH) concentrations.....	78
Figure 4.4: Effect of varying [NO ₂ ⁻] concentrations on SST-14(SNO) formation at 25 °C.....	79

Figure 4.5: Effect of $[H^+]$ variation SST-14(SNO) formation at 25 °C.....	81
Figure 4.6: Observed rate constants for SST-14(SH) S-nitrosylation by HNO_2 concentrations.....	83
Figure 4.8: Effect of varying SST-14(SH) concentrations on $ONOO^-$ depletion in pH 7.4 PBS at 302 nm.....	85
Figure 4.9: Effect of varying H^+ concentrations on $ONOO^-$ mediated S-nitrosylations in PBS at pH 7.4.....	87
Figure 4.10: (A) Effect of $[H^+]$ variation on SST-14 depletion of $ONOO^-$	87
Figure 4.11: Effect of $[ONOO^-]$ variation on SST-14(SNO) formation in PBS at pH 7.4.....	88
Figure 4.12: EPR spectra of DMPO adducts in on $ONOO^-$ mediated SST-14(SNO) formation.....	89
Figure 4.13: K_{obs} values for the S-nitrosylation of SST-14(SH) by varied $ONOOH$ concentrations.....	95
Figure 4.14: Observed rate constants for the S-nitrosylation of SST-14(SH) by $ONOO^-$	97
Figure 4.15: Effect of $[SST-14(SH)]$ variation on reaction with SNAP in PBS at pH 7.4.....	98
Figure 4.16: (A) Effect of $[SST-14(SH)]$ variation on SNAP depletion at 590 nm in PBS at pH 7.4.....	99
Figure 4.17: Depletion of varied SNAP concentrations at 590 nm in PBS at pH 7.4.....	100
Figure 4.18: Effect of $[SNAP]$ variation on SST-14(SNO) formation in PBS at pH 7.4.....	101
Figure 4.19: Temperature dependence plot of k_{obs} vs $[SNAP]$ for the reaction with SST-14(SH).....	103
Figure 5.1: U-II isopeptides sequences conserved in vertebrates.....	105
Figure 5.2: HPLC-UV analysis of U-II(S-S) reduction.....	108
Figure 5.3: ESI-MS analysis of HPLC chromatograms in Fig 5.2.....	109
Figure 5.4: Spectra scan of; (a) $[HNO_2^-] = 16$ mM, (b) $[NO_2^-] = 27$ mM, (c) $[U-II] = 1$ mM, $[NO_2^-] = 5$ mM and $[H^+] = 5$ mM, (d) $[U-II(S-S)] = 77$ μ M and (e)	112

U-II(SH) = 32 μ M.....	113
Figure 5.5: (A) Effect of $[\text{NO}_2^-]$ variation on U-II(SNO) formation.....	113
Figure 5.6: Effect of $[\text{H}^+]$ variation on U-II(SNO) formation.....	114
Figure 5.7: The reaction between U-II(SH) and HNO_2 exhibits 1 st -order kinetics in U-II(SH).....	115
Figure 5.8: (A) Observed rate constants for the S-nitrosylation of U-II(SH) by varied HNO_2 concentrations.....	117
Figure 5.10: Effect of varying U-II(SH) concentration on U-II(SNO) formation in pH 7.4 PBS.....	119
Figure 5.11: Effect of varying U-II(SH) concentration on ONOO^- depletion in pH 7.4 PBS.....	120
Figure 5.12: (A) Effect of varying H^+ concentration on ONOO^- depletion.....	121
Figure 5.13: (A) Effect of varying H^+ concentration on ONOO^- mediated U-II(SNO) formation.....	121
Figure 5.14: Effect of $[\text{ONOO}^-]$ variation on U-II(SNO) formation in phosphate buffer pH 7.4.....	123
Figure 5.15: EPR spectra of OH radical adducts produced during ONOO^- mediated U-II(SNO) formation.....	124
Figure 5.16: (A) Observed rate constants for the S-nitrosylation of U-II(SH) by varied ONOOH concentrations.....	125
Figure 5.17: (A) Observed rate constants for the S-nitrosylation of U-II(SH) by varied ONOO^- concentrations.....	127

LIST OF SCHEMES

Scheme 1.1: NO biological production.....	2
Scheme 1.2: Acid catalyzed peroxyxynitrite decomposition.....	15
Scheme 3.1: O ₂ and NO ₂ ⁻ production during ONOO ⁻ decomposition.....	57
Scheme 6.1: Proposed reactions of peptide thiols with HNO ₂	131
Scheme 6.2: Proposed scheme for Cu ⁺ catalyzed SNO decomposition.....	132
Scheme 6.3: Proposed mechanism for reactions involving peptide thiol transnitrosation by SNAP.....	134

LIST OF ABBREVIATIONS

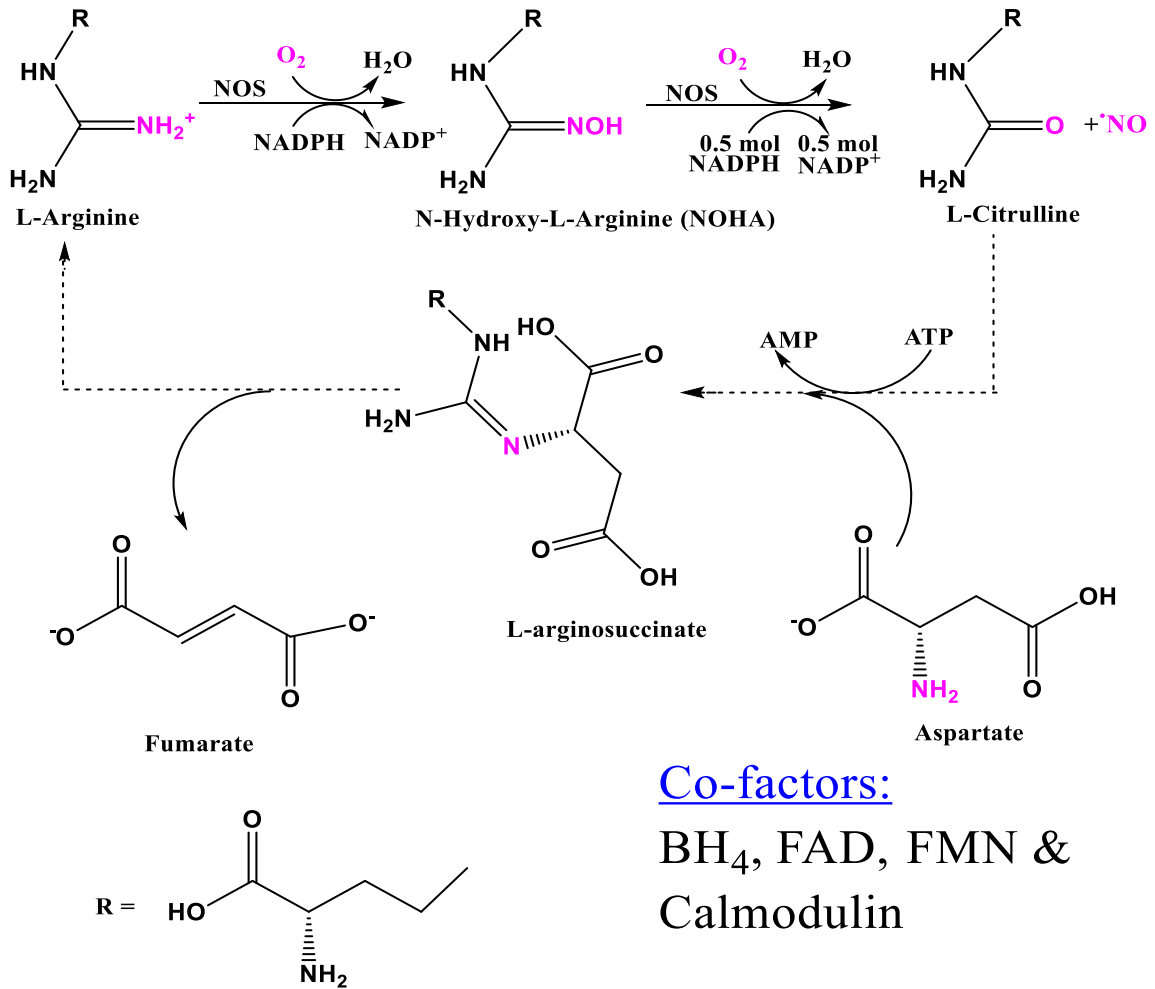
CNS	Central nervous system
NOS	Nitric oxide synthase
sGC	Soluble guanylyl cyclase
cGMP	Cyclic guanosine monophosphate
AVP	Arginine vasopressin
SST-14	Somatostatin-14
U-II	Urotensin-II
AVP(SNO)	S-nitroso-arginine vasopressin
SST-14(SNO)	S-nitroso-somatostatin-14
U-II(SNO)	S-nitroso-urotensin-II
SNAP	<i>S</i> -Nitroso- <i>N</i> -acetyl-DL-penicillamine
RSH	Thiol
RSNO	S-nitrosothiol

CHAPTER 1: INTRODUCTION

1.1 Nitric Oxide: synthesis, signaling and toxicity.

1.1.1 Nitric oxide synthesis and isoforms. Nitric oxide (NO), is a signaling molecule that receives a lot of attention due to its role in pathologies like hypertension, stroke, and neurodegenerative diseases¹. More than 90,000 research articles on NO biochemistry have been published since its discovery as the endothelium-derived relaxing factor (EDRF) more than a 25 years ago². The three isozymes of nitric oxide synthase (NOS) are endothelial (eNOS), inducible (iNOS), neuronal (nNOS) NOS. Each of these isozymes forms antiparallel homodimers³, with monomers that contain two primary domains; (i) a N-terminal oxygenase region that consists of individual complements of heme and tetrahydrobiopterin (BH₄) that bind to L-arginine, (ii) and a C-terminal reductase region that consists of binding sites for flavin adenine dinucleotide (FAD), flavin mononucleotide (FMN) and nicotinamide adenine dinucleotide phosphate (NADPH). These primary domains are linked to another domain that binds to calmodulin (CaM). CaM (an acidic Ca²⁺ binding protein) has been implicated in physiological processes like cell defense, neurotransmission, cell proliferation and apoptosis⁴. An essential process in the production of NO from L-arginine, involves inter-subunit electron transfer between the reductase and oxygenase domains which is facilitated by binding to CaM⁵. The oxygenase domain then catalyzes the transformation of L-arginine to L-citrulline whilst also producing NO in two steps: (1) production of N-hydroxy-L-arginine (NOHA) as an intermediate, and (2) formation of L-citrulline through NOHA oxidation (Scheme 1.1)⁶⁻⁹. Regardless differences in isozyme Ca²⁺ dependence, electron transfer in all NOS homodimers is initiated by the

binding of CaM to the central linker region and ensues *in trans* from NADPH through the FAD/FMN subunit and finally to a heme iron subunit^{5, 10}.



Scheme 1.1: NO biological production (Reprinted with permission from Safia Habib)¹¹

The NOS isoforms have unique expression patterns and enzymatic activity (Table 1.1)¹²⁻¹⁴. Various studies exploring NO signaling in the hippocampus, cerebellum, and cortex, generally agree that NO is essential for long-term potentiation, which is the most researched neuronal analogous of learning *in vitro*¹⁵⁻¹⁸. The isoform nNOS is exceptionally equipped to produce NO in a way that promotes synaptic plasticity¹⁹⁻²⁰. NO is known to

enhance the synaptic effectualness of active neighboring neuronal axonal arbors, while also weakening inactive axonal arbors. The central nervous system's (CNS) capacity to regulate local circuit neurons is closely related to its role as a principal source of NOS²⁰⁻²³.

nNOS is anchored to the cytoskeleton in postsynaptic boutons underneath the glutamate N-methyl-D-aspartate receptor (NMDA-R), through an amino terminus that is not present in the other NOS isozymes²⁴. NMDA-R is linked to cognitive learning and other modes of excitotoxic neurodegeneration²⁵. NMDA-R is activated when neurons are firing frequently (few milliseconds) and partially depolarized resulting in localized increases in NO production. Several studies have shown that Ca²⁺ entering through the NMDA-R activates nNOS with subsequent NO production, which then activates soluble guanylyl cyclase (sGC) and increases cyclic guanosine monophosphate (cGMP) levels²⁶⁻²⁷. This functional coupling of NMDA-R, nNOS, and sGC led researchers to propose that they must be located near each other and at glutamatergic synapses. Further studies revealed that nNOS actually binds to a scaffolding protein now known as postsynaptic density protein 95 (PSD95), which anchors NMDA-R at the postsynaptic membrane²⁸⁻³¹. Olthof *et al.*,³² were the first to publish images of a multiprotein complex in the inferior colliculus (IC; a sensory structure that constitutively produces high levels of nNOS) with all four proteins (nNOS, NMDA-R, sSG and PSD95,) ³³⁻³⁵. The multiprotein complex was found to be in apposition to vesicular glutamate transporters (VGluTs); VGluT1 and VGluT2 (Fig 1.1). Glutamate binding to the α -amino-3-hydroxy-5-methyl-4-isoxazolepropionic acid (AMPA) receptor is proposed to activate NMDA-R, which allows Ca²⁺ ions to enter the cell leading to NO synthesis through nNOS activation.

Such evidence of previously undescribed nNOS puncta in a domain originally thought to

be void of nNOS, emphasizes our limited understanding of the expression of NOSs and should lead to studies of NO signaling in other unreported tissues.

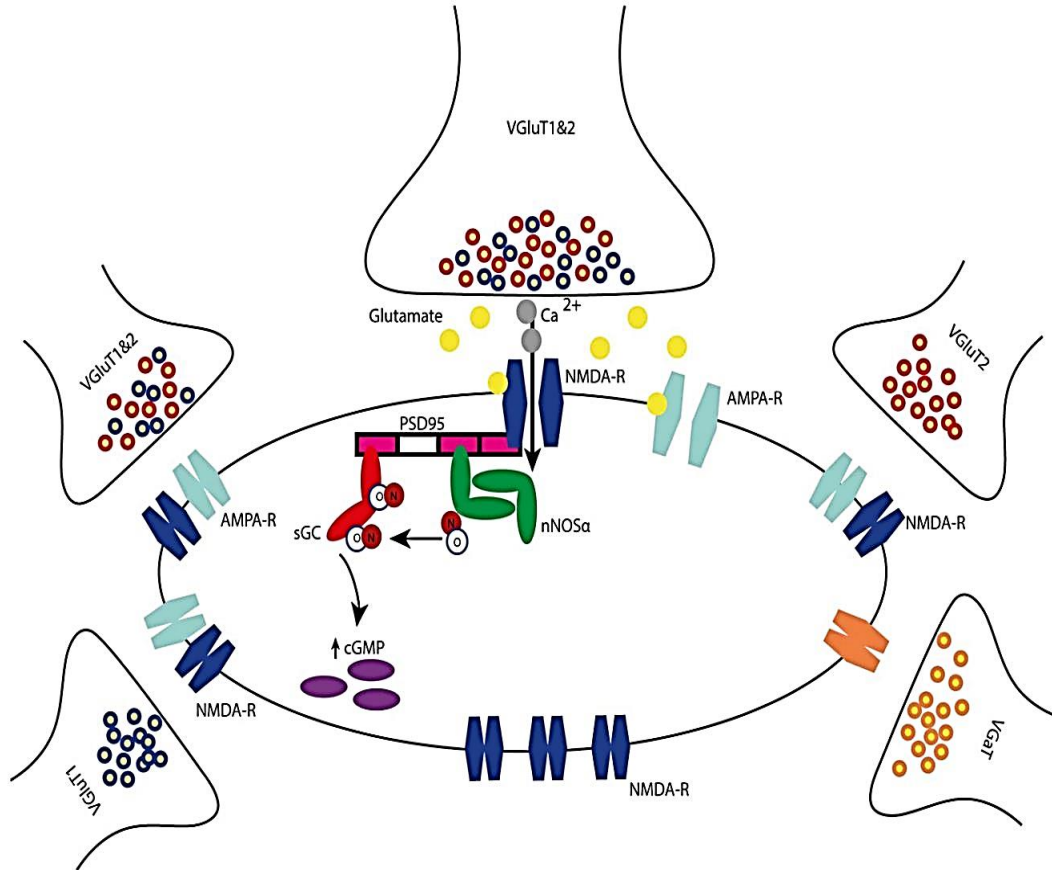


Figure 1.1: NO signaling is linked to NMDA-R activation in the inferior colliculus (IC) (Reprinted with permission from Bas M.J Olthof).

Dysregulation of nNOS expression is linked to CNS disorders such as Parkinson’s disease (PD), amyotrophic lateral sclerosis (ALS) and borderline personality disorder (BPD)³⁶⁻³⁸. Disease pathologies like chronic renal failure, heart failure, and diabetes mellitus³⁹ are also associated with nNOS dysregulation, therefore the key to novel therapeutic strategies might be dependent on further elucidation of nNOS signaling mechanisms.

Table 1.1: NOS Isoforms⁴⁰

	Location	Function	Cytosolic/ membrane- associated	Activity
Neuronal NOS (nNOS)	Central and peripheral neurons	Cell-to-cell communication	Cytosolic	Produces low concentrations of NO over long periods
Inducible NOS (iNOS)	Immune cells and glial cells	Mediate cell death in response to pathogens	Cytosolic	Produces high concentrations of NO over short periods
Endothelial NOS (eNOS)	Endothelial tissue of blood vessels	Vasodilation and relaxation of muscles and soft tissue	Membrane- associated	Produces low concentrations of NO over long periods

Of the three known isoforms of NO, iNOS over expression in disease states is believed to be the most detrimental due to iNOS's ability to produce excess NO. In macrophages, iNOS produces bolus amounts of NO that directly causes DNA strand breaks in parasitic microorganisms and tumor cells. NO also binds to protein-bound iron which inhibits numerous iron-sulfur cluster-dependent enzymes⁴¹⁻⁴². The life span of induced macrophages is largely dependent on NO; because in order to be cytotoxic to other cells, macrophages have to be more resistant to NO than their target cells⁴³. Studies have shown that most macrophages are resistant to endogenously generated NO but are hypersensitive to exogenous NO⁴⁴. Therefore, unique pathways must exist through which exogenous NO induces apoptosis in otherwise resistance cells. Exploiting such a mechanism, could allow for targeted apoptosis as a way of eliminating cancerous cell growth. However, the biochemical basis of these unique NO signaling pathways are not known yet, which is a further testament to the complexities of NO signaling mechanisms.

The effects of iNOS function are widespread and further complicated by the fact that iNOS is expressed by both immune and non-immune cells^{36, 45}. Much attention has been focused on iNOS expression by T cells with an emphasis on exploring how iNOS regulates immune cell activity by nitrating crucial molecules associated with signaling pathways⁴⁶⁻⁴⁸. T-cell expression of iNOS is known to downregulate Th17 differentiation with no effect on Th1 or Th2 cells (Fig 1.2A), this is consistent with reports that also implicate NO donors; S-nitrosoglutathione (GSNO) and diethylenetriamine NONOate (NOC-18) in inhibiting Th17 cell differentiation⁴⁹⁻⁵⁰. Incidence of inflammatory bowel disease (IBD), is also linked to iNOS mediated modification of the transcription factor IRF5 which inhibits classical pathway-activated macrophages (M1) polarization, without any significant effect on alternatively activated macrophages (M2) polarization (Fig 1.2B)⁵¹⁻⁵³. Innate immune responses are dependent on iNOS expression profiles which modulate M1 gene expression and de-differentiation.

Effector dendritic cells promote pathogen clearance by secreting cytokines which activate an adaptive immune response⁵⁴. Upregulation of iNOS expression inhibits effector dendritic cells differentiation (Fig 1.2C), thereby suppressing the expression of receptors involved in detecting pathogen-associated molecular patterns (PAMPs)⁵⁵⁻⁵⁶. Research aimed at understanding regulatory mechanisms associated with DC-intrinsic iNOS expression could facilitate the development of powerful medicinal strategies for immune and inflammatory disorders.

In tumorigenesis, iNOS expression is upregulated thus producing more NO which is then used by myeloid-derived suppressor cells (MDSCs) to initiate antitumor immune responses (Fig 1.2D) and promotes antimicrobial activity by stimulating the expression of tumor

necrosis factor producing DCs (Fig 1.2E) ⁵⁷.

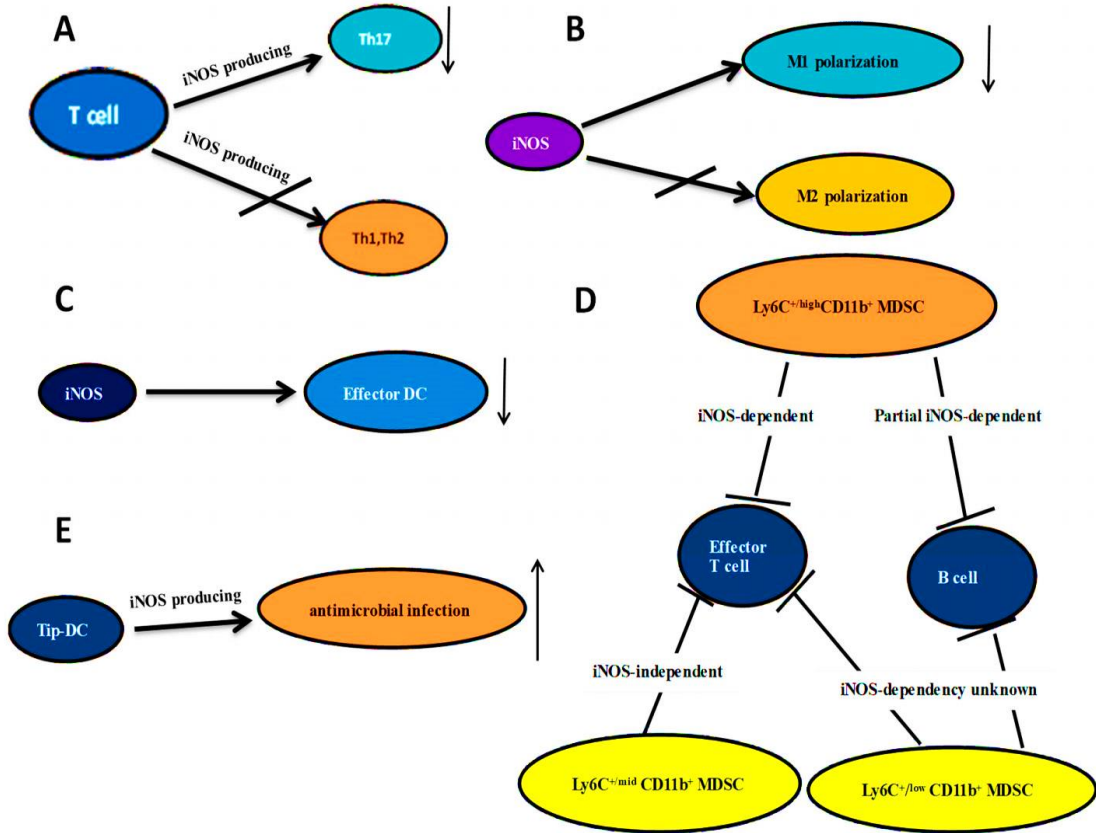


Figure 1.2: iNOS regulates the expression of various immune cells and responses. Arrows ↓: decreasing expression; ↑: increasing expression. Graphic from Xue *et al.*, 2018 ⁵⁸.

It is still unknown if iNOS is expressed by all immune effector cells, therefore the extent to which NO regulates immune response is unclear. Future studies should aim to elucidate iNOS-derived NO regulatory mechanisms as this shed more light on the role of NO in autoimmune and inflammatory disorders.

Endothelial cells constitutively express eNOS in cardiac myocytes, renal tubular epithelial cells and platelets⁵⁹⁻⁶⁰. eNOS mediated NO release modulates endothelium-dependent hyperpolarizations (EDH), which control vascular tone and the release of numerous

vasoactive molecules⁶¹⁻⁶⁶. Agonists like histamine interact with receptors on endothelial cell membranes to stimulate increased production of intracellular calcium (Ca^{2+}). The Ca^{2+} activates the calmodulin-binding motif of eNOS to release NO by binding to calmodulin (CaM). eNOS activation can be through calcium-dependent or independent pathways (Fig1.3a). Fluid shear stress and phosphorylation are known to regulate eNOS mRNA and eNOS protein expression in the absence of Ca^{2+} ⁶⁷⁻⁶⁹. Phosphorylation based modulation of eNOS activity is site-specific as phosphorylation on distinct sites Thr495 and Ser635/Ser1177 result in inhibition and activation respectively⁷⁰⁻⁷¹. Bradykinin also stimulates eNOS to release NO through phosphorylation and dephosphorylation processes on sites Ser1177 and Thr495 respectively⁷². Whilst shear stress has been reported to promote eNOS phosphorylation on site Ser1179 in a protein kinase A-dependent manner⁷³⁻⁷⁴. NADPH-cytochrome P450 reductase (CPR) reduces NO_3^- to NO in endothelial cells, which is considered an essential mechanism in replenishing NO levels during eNOS dysfunction as typically seen in patients with cardiovascular risk factors (Fig 1.3b)⁷⁵⁻⁷⁶. Various factors ranging from oxidative stress to eNOS uncoupling have been implicated in eNOS dysfunction. Oxidative stress alters eNOS function from releasing NO to generating superoxide anions. Reactions between NO and the superoxide anion form peroxynitrite (ONOO^-) which is an extremely potent oxidant that alters the functions of numerous intracellular molecules⁷⁷.

eNOS uncoupling can be due to ONOO^- mediated BH_4 oxidation in a cycle that leads to further uncoupling of eNOS from BH_4 and production of more superoxide anion (Fig 1.4)⁷⁸⁻⁷⁹. Depletion of L-arginine, S-glutathionylation and the build-up of autogenous methylarginines can also result in eNOS uncoupling⁸⁰⁻⁸¹.

Despite extensive studies⁸²⁻⁸⁴, electron transfer processes between NOSs and holoenzyme CaM are poorly understood. Kinetic studies on holo CaM binding rates to nNOS and iNOS peptides using surface plasmon resonance (SPR) reported bimolecular rate constants of $1.58 \times 10^5 \text{ M}^{-1}\text{s}^{-1}$ and $3 \times 10^4 \text{ M}^{-1}\text{s}^{-1}$, respectively⁸⁵. These rates implied a slow rate-limiting holo CaM binding process, which is contrary to heme binding rates in NOS catalysis making it plausible that immobilizing NOS peptides on the SPR matrix could have curtailed binding rates⁸⁶⁻⁸⁷. Almost two decades later, Gang Wu *et al.*, determined CaM to NOS binding rates using fluorescence stopped flow to be ~4 orders of magnitude greater than those evaluated on a SPR matrix⁸⁸. McMurry *et al.*, employed interferometry-based biosensors to measure association (k_{on}) and dissociation (k_{off}) rates for CaM binding to endothelial and neuronal NOS⁸⁸. Their data suggests rates CaM binding rates that are essentially diffusion limited within ~3 orders of magnitude of Smoluchowski diffusion coefficients as defined by the Einstein–Smoluchowski diffusion equation. Phosphorylation of CaM-binding sites greatly decreases CaM/NOS binding rates and as a general rule; changes in Ca^{2+} concentrations modulate CaM/NOS affinities.

NOS isozymes are excellent heme-binding ligands that produce NO which binds to the heme before its released into the physiological milieu⁸⁹. Therefore, an essential aspect of deciphering NOS activity must include the determination of five pivotal kinetic parameters that regulate NO production and release from NOS. As illustrated in scheme 1.1, two sequential steps constitute NOS mediated NO production with rate constants k_{cat1} and k_{cat2} respectively (Fig 1.5). A ferric heme–NO complex is formed which can either undergo reduction or dissociation with rate constants k_r and k_d respectively.

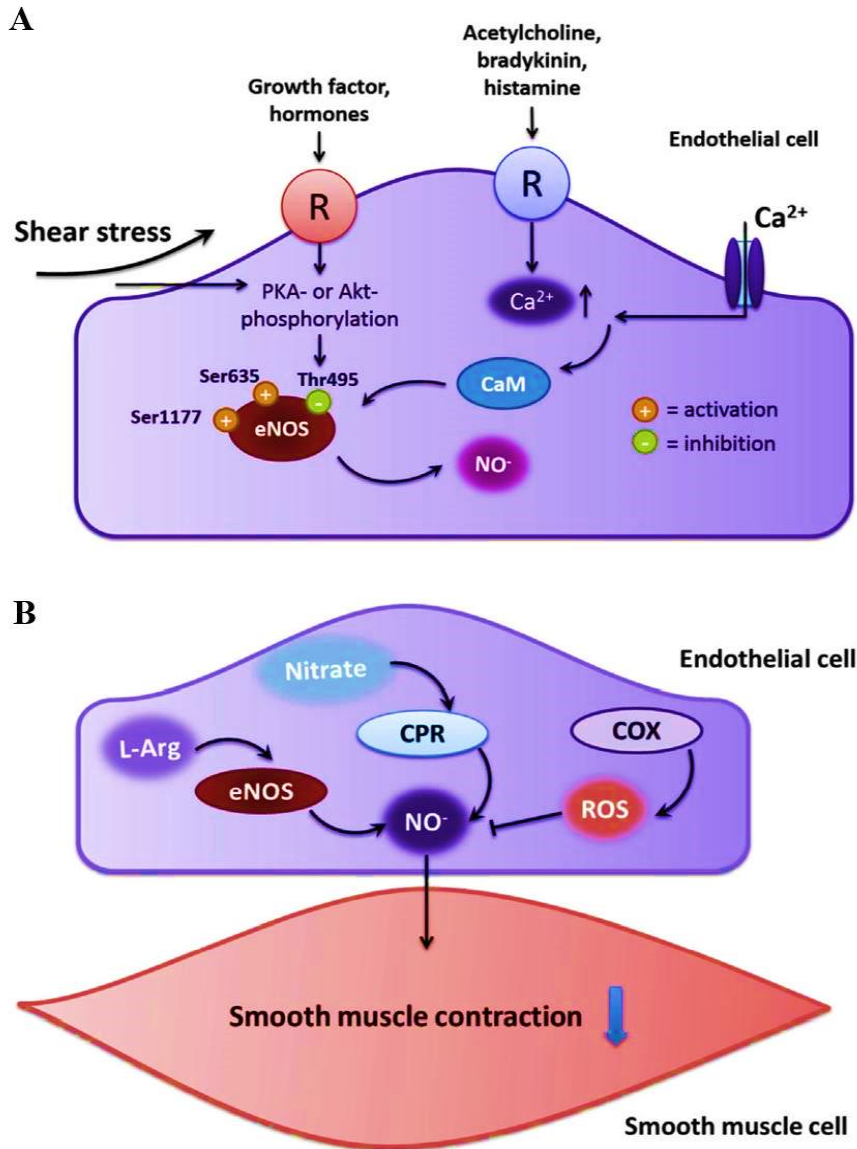


Figure 1.3: (A) eNOS can be activation through various calcium dependent/independent pathways. (B) NO is also produced through cytochrome P450 reductase mediated NO_3^- reduction. Graphic from Zhao *et al.*, 2015⁹⁰.

Reduction of ferric heme- NO forms a ferrous complex that can reform the ferric NOS isoenzyme through a reaction with O_2 with a rate constant; k_{ox} . Ray *et al.*, determined temperature dependencies of these rate constants using single-turnover kinetic

measurements, computer simulations and stopped-flow spectroscopy⁹¹.

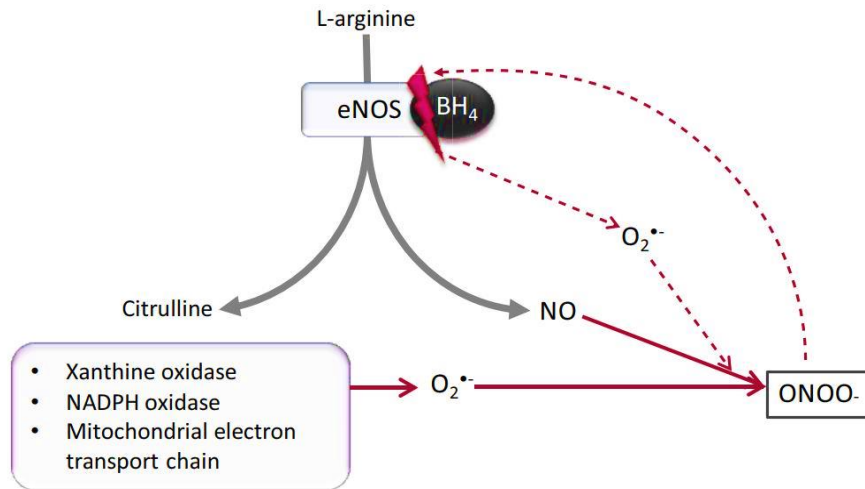


Figure 1.4: Processes leading to peroxynitrite production and eNOS uncoupling in endothelial cells. Grey arrows indicate physiological processes, whilst red arrows depict pathological processes. Graphic from Leiper *et al.*, 2007⁷⁸.

The study proposes a global kinetic model aimed at providing a detailed understanding of how steady-state NO generation is affected by factors like O₂ concentration, temperature-dependence of catalytic activity and NOS specific activity (Fig 1.5). The model depicts reduction of NOS isoenzyme with ferric heme (k_r) followed by binding of O₂ to the ferrous heme to form of a Fe^{II}O₂ species. Two sequential steps with rate constants; k_{cat1} and k_{cat2} , converts the Fe^{II}O₂ species to products in L-arginine and N(omega)-hydroxy-l-arginine oxidation reactions that ultimately form a Fe^{III}NO complex. The Fe^{III}NO complex can either undergo productive (k_d) or futile cycles (k_{ox}) that either release or destroy NO respectively. Thermodynamic parameters were then evaluated from these observed rate constants allowing for the accurate modelling of nNOS regulation under physiologically relevant conditions. Such integrated experimental approaches that use multiple analytic techniques (resonance raman, stopped flow and electroparamagnetic resonance) are

essential in deciphering mechanisms that govern NOS regulation.

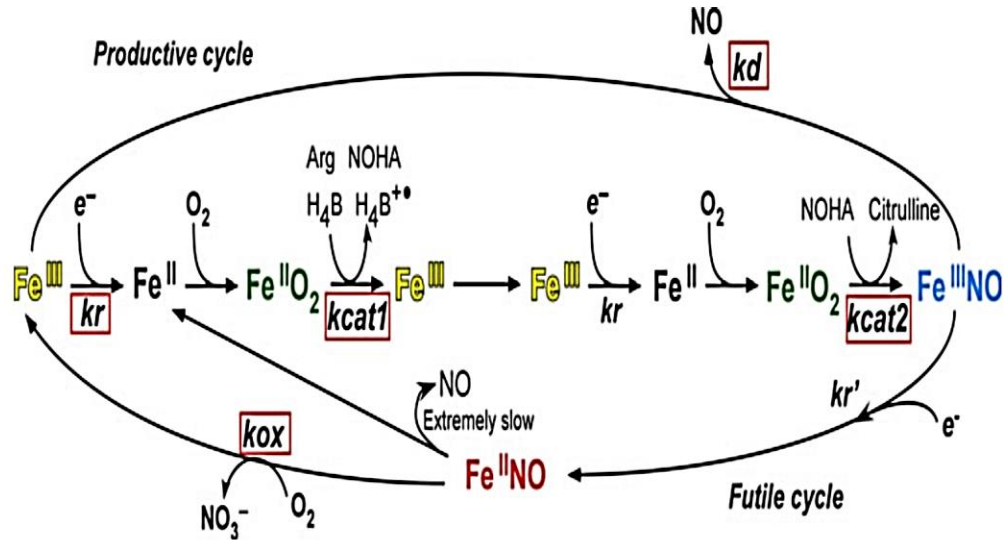


Figure 1.5: Kinetic model for nitric oxide synthase catalysis. Graphic from Ray *et al.*, 2007⁹¹.

1.1.2. NO diffusion, reactivity and signaling. Intracellular NO diffuses out of cells and binds to heme-containing proteins, thereby modulating biological function. Under physiological concentrations of oxygen, the NO radical is fairly unstable and rapidly diffuses into the blood stream⁹². Nitric oxide's ability to strongly bind heme is linked to cyclic guanosine monophosphate (cGMP) activation through interactions with heme in soluble guanylate cyclase (sGC). NO concentrations in the nanomolar range are required to activate sGC. Once cGMP is activated, a down-stream cascade of reactions activates cGMP-dependent kinases which in turn regulate Ca²⁺ levels in various tissues. Kinetic modeling and steady-state approximation techniques, have implicated NO binding to heme in cytochrome-c oxidase as the major process responsible for decreasing mitochondrial respiration rates⁹³. Despite having the ability to detect subtle deviations in molecular shape,

receptors in tissues are deceived by NO's unique properties (one unpaired electron and two atoms), which is the main reason why NO is implicated as a signaling molecule in various physiological and pathophysiological signal transduction pathways⁹⁴. The effects of NO are localized and concentration dependent, as concentrations greater than one micromolar result in reactive nitrogen oxygen species (RNOS) that are deleterious effects (Fig 1.6a). Therefore, to mitigate the effects of excess NO build-up and prolonged sGC activation; NO is removed by oxyhemoglobin⁹⁵⁻⁹⁶. The heme: protoporphyrin IX in hemoglobin has a great affinity for NO, with some reports stating that deoxyhemoglobin has a 10⁴-fold greater affinity for NO than O₂⁹⁷⁻⁹⁸. *In vitro* experiments show a steep diffusion gradient between red blood cells (RBC) and intracellular NO, as RBC's effectively remove NO from cells and prevent reentry⁹⁹⁻¹⁰¹. The half-life of NO in conjunction with its ability to diffuse across various cell membranes makes NO a major signal transduction messenger molecule that modulates a plethora of physiological processes¹⁰².

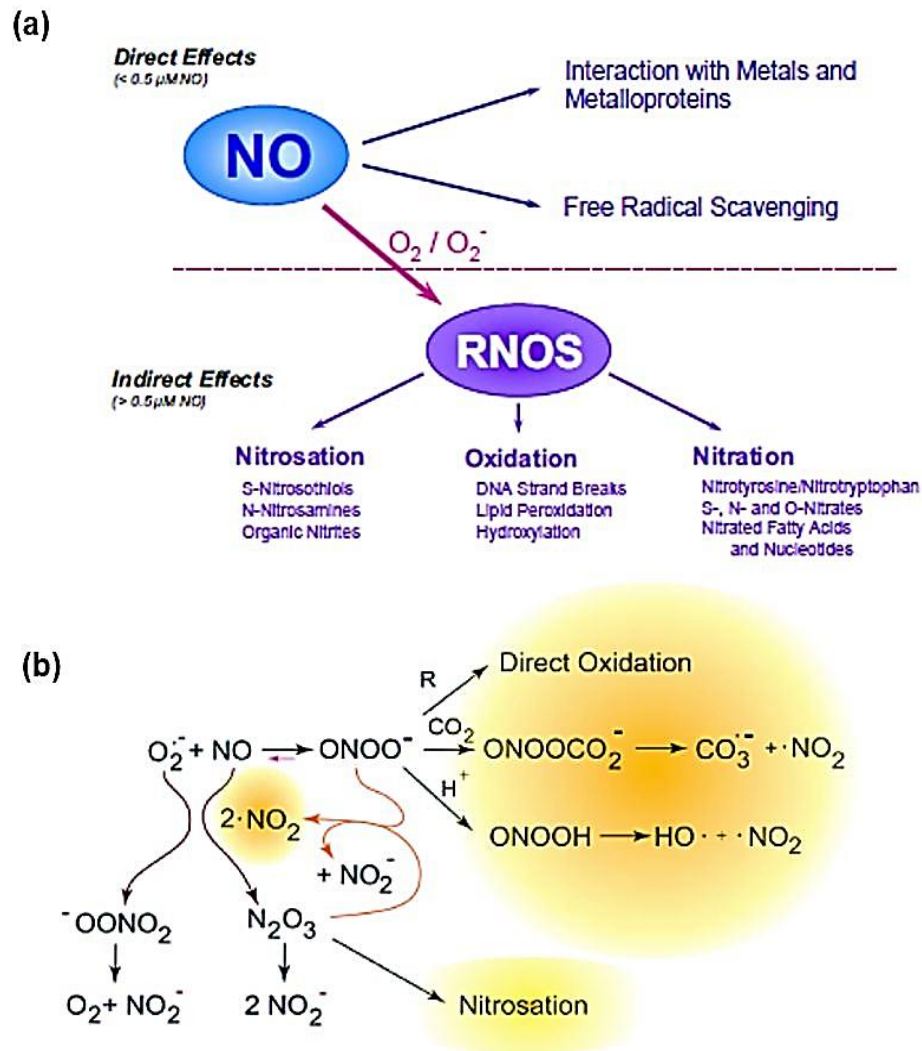
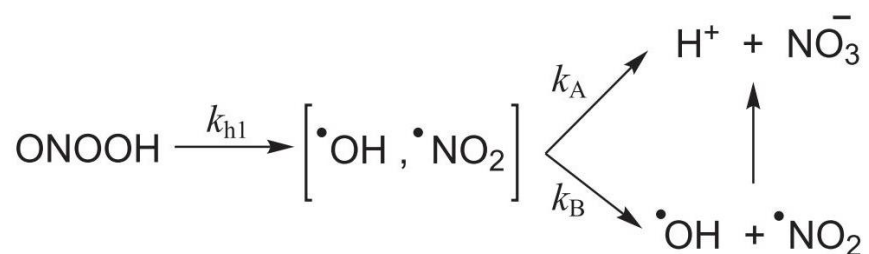


Figure 1.6: (a) Direct and Indirect effects of NO, (b) The interplay between nitric oxide, superoxide, peroxynitrite and nitrogen dioxide. Graphic is adapted from Pacher *et al.*, 2007⁷⁷.

1.2 Peroxynitrite chemistry in health and disease. NO cytotoxicity is largely due to oxidation products like peroxynitrite (ONOO^-), which are more stable and therefore promote various nitration and oxidation processes (Fig 1.6b). As mentioned earlier, most of NO's cytoprotective effects are at low NO concentrations and this is mainly because NO cannot out-compete superoxide dismutase (SOD) for superoxide at low concentrations¹⁰³.

In excess NO concentrations, it reacts with superoxide to yield ONOO⁻, essentially positioning NO as the sole biological molecule that can out-compete SOD, with a bimolecular rate (6.7 x 10⁹ M⁻¹s⁻¹) that is diffusion-limited¹⁰⁴. The pK_a of ONOO⁻ and peroxyntrous acid (ONOOH) is 6.8, thus under physiologically relevant conditions both ONOO⁻ and ONOOH coexist¹⁰⁵. Coexistence of these species further complicate peroxyntrite reactivity studies because ONOO⁻ and ONOOH react differently. Peroxyntrous acid is highly unstable in aqueous media, with a half-life of 0.6s at physiologically relevant temperature and pH¹⁰⁶. Beckman *et al.*, reported •OH and •NO₂ radical production during ONOOH decomposition and implicated these radicals in processes that result in endothelial injury (scheme 1.2)¹⁰⁷. Peroxyntrite concentrations in the nanomolar range are also linked to various disease phenotypes including atherosclerosis, cancer, inflammation, and sepsis^{77, 108-109}.



Scheme 1.2: Acid catalyzed peroxyntrite decomposition.

Peroxyntrous acid readily diffuses across cell membranes and decomposes to produce the aforementioned secondary radicals resulting in undesired protein oxidation and nitration reactions. Radi *et al.*, using stopped-flow spectrophotometry were the first to report bimolecular rate constants of ONOO⁻ reactions with thiols that were faster than ONOO⁻ homolysis¹¹⁰. Earlier kinetic studies had suggested that direct reactions between ONOO⁻

and proteins were only possible with fast-reacting thiols in the presence of metal cofactors¹¹¹. Surprisingly, their data showed rate constants of hydrogen peroxide reactions with thiols which were ~3 orders of magnitude smaller than ONOO⁻/ thiol reactions. Elucidation of these kinetic aspects of ONOO⁻ mediated oxidations of biomolecules provided essential insights about peroxynitrite's quantitative relevance in biological systems. A major area of contention between researchers in free radical biology involves the determination of precise "quantities" of radicals generated in tissues and how to adequately account for these when conducting *in vitro* experiments. To account for this, kinetic studies aim to make a clear distinction between formation rates and steady-state concentrations¹¹²⁻¹¹⁴. Indirect measurements of ONOO⁻ formation rates in activated macrophages are estimated to be in the micromolar range¹¹⁵⁻¹¹⁶. A comparison between kinetic estimates and biological experimental data supports the conclusion that estimated ONOO⁻ formation rates agree with reported ONOO⁻ cellular flux rates¹⁰⁸. Alvarez *et al.*, conducted exhaustive experiments aimed at determining macrophage intracellular ONOO⁻ concentrations that are required for effective pathogen clearance¹¹⁷⁻¹¹⁹. Due to variations in how different cell types generate and consume ONOO⁻, moderate estimates of ONOO⁻ steady-state concentrations *in vivo* are in the nanomolar range¹²⁰. Another essential ONOO⁻ detoxification pathway; is the nucleophilic addition of ONOO⁻ to CO₂ to yield ONOOCO₂⁻, which decomposes to form nitrogen dioxide and carbonate radicals (Fig 1.6b)¹²¹⁻¹²⁴. Kinetic and mechanistic studies are especially well suited for probing ONOO⁻ properties and reaction conditions that modulate peroxynitrite specificity. Implementing such a holistic approach would provide further insights into the fundamentals of ONOO⁻ mediated reactions and assist in the development of therapeutic tools aimed at attenuating

peroxynitrite's cytotoxic effects.

1.3 Thiol biochemistry and S-nitrosylation. Thiols are highly nucleophilic organosulfur compounds that play fundamental roles in protecting cells from oxidative stress and nitrosative injury¹²⁵⁻¹²⁷. Cysteine is a unique canonical amino acid which is a major component of protein structure through the formation of cystine disulfide bridges¹²⁸. Cysteine residues also facilitate metal ion coordination and maintain redox homeostasis within cells¹²⁹. Cysteine residues are known to form mixed disulfides and are readily oxidized by ROS to sulfenic acid in a reaction called S-sulfenylation (Fig 1.7). Subsequent two electron oxidation reactions can result in sulfinylation and sulfonylation respectively with the latter being irreversible¹³⁰. Palmitate (an ester of palmitic acid) forms covalent thioester bonds with cysteine in a post-translational modification called palmitoylation¹³¹. Since cysteines have pivotal structural and regulatory functions, posttranslational modifications are often linked to protein dysregulation and various acquired and hereditary disorders¹³². Therefore, unraveling molecular mechanisms associated with the post-translational modification of key amino acids (like cysteine residues) is of paramount importance in enhancing our understanding of protein function and dysregulation.

Of particular interest in this dissertation is S-nitrosylation/S-nitrosation; the covalent bonding of NO to cysteine form S-nitrosothiols (RSNOs). Some examples of naturally occurring RSNOs are S-nitrosoglutathione (GSNO) and S-nitrosocysteine (CySNO)¹³³⁻¹³⁴. It is now widely accepted that S-nitrosylation is a significant post-translational modification that regulates cellular signal transduction mechanisms of various types of proteins¹³⁵⁻¹³⁷.

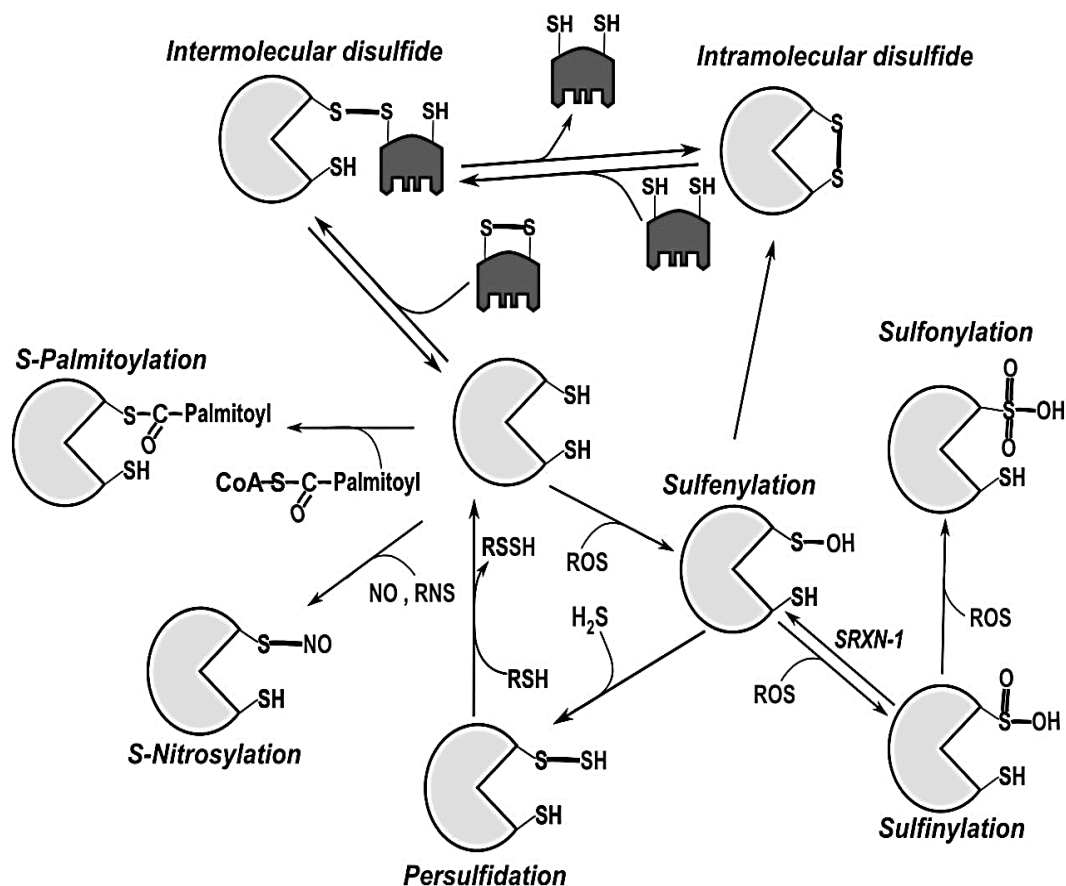


Figure 1.7: Main redox modifications of cysteine residues. Graphic from Fra *et al.* . . , 2017 ¹³⁸

S-nitrosylation chemical reactivity is independent of substrate-enzyme recognition but solely relies on interactions between the nitrosylating agent and peptide/protein thiols ¹³⁹⁻¹⁴⁰.

Three main factors that are essential in regulating S-nitrosylation specificity include (i) peptide/protein residue reactivity, (ii) local concentrations of peptide/protein thiols and the S-nitrosylating agent and finally (iii) stability of the S-NO bond.

(i) Peptide/protein residue reactivity. Studies have shown that not all peptide/protein thiols are S-nitrosylated, however elucidating the structural motifs that make some thiols more

susceptible to S-nitrosylation than others is still a hot area of research¹⁴¹⁻¹⁴². Generally, formation of RSNOs is favored in more ionizable cysteines, where the nucleophilic thiolate ions are stabilized by redox reactions with adjacent residues¹⁴³⁻¹⁴⁴. Cysteine residue pKa determines thiol reactivity as amino acid conformation changes in response to cellular conditions.

(ii) Local concentrations of peptide/protein thiols and the S-nitrosylating agent. S-nitrosylation relies on the formation of RNS (HNO_2 , NO_2^- , ONOO^- , NO^+), since NO itself is not the main S-nitrosylating agent¹⁴⁵⁻¹⁴⁷. Chemical reactivity is largely dependent the concentrations of both the peptide/protein thiols and S-nitrosylating agent, with are functions of kinetic and thermodynamic parameters. Therefore, one cannot overstate the importance of co-localization of NO and target thiols in subcellular compartments, as a pivotal factor in identifying S-nitrosylable proteins¹⁴⁸⁻¹⁵¹.

(iii) Stability of the S-NO bond. Cleavage of the labile S-NO bond in S-nitrosothiols occurs primarily through heterolytic or homolytic bond cleavage, whilst enzymatic cleavage have been reported for some low molecular weight S-nitrosothiols at high Michaelis constant values¹⁴⁸. S-NO bond cleavage is accelerated by some transition metals like copper¹⁵².

Transnitrosation (NO exchange between thiols) is another mechanism for S-NO bond cleavage. Kinetic studies of transnitrosation reactions between low mass thiols and NO donors, report a fast reaction at physiological pH¹⁵³. The relative ease of transnitrosation under physiologically relevant conditions, suggests a role for peptide thiols as NO reservoirs that are relatively stable on a time scale that allows peptide S-nitrosothiols to modulate physiological processes. Denitrosylation is believed to be an essential signal

transduction mechanism, however not much work has been done in this area¹⁵⁴⁻¹⁵⁵. Despite growing evidence that implicates protein/peptide S-nitrosothiols as biologically significant NO signaling molecules, kinetic and thermodynamic parameters of peptide S-nitrosothiols formation and denitrosylation are yet to be fully explored.

1.4 Overarching goals and aims of this study. S-nitrosylation of peptide and/or protein residues produces S-nitrosothiols (SNOs) that are associated with modulating the functions of various peptides. Co-localization of neuropeptide oxytocin (OT) with neuronal nitric oxide synthase (nNOS) (which produces NO facilitating synaptic plasticity) in the hypothalamo-neurohypophyseal network, has been linked to OT S-nitrosylation *in vivo*. Additionally, both the reduction and S-nitrosylation of OT disulfide is believed to illicit a decentralized, temporal, and site-specific alteration of OT hormonal sensory activity as OT-(SNOs) could alter signaling pathways through chemical modification of OT receptors. S-nitrosylation and de-nitrosylation are believed to have roles as predominant effector mechanisms implicated in disrupting cellular redox homeostasis, thus resulting in various pathophysiological conditions. Our limited understanding of S-nitrosylation/de-nitrosylation mechanisms has hampered the development of therapeutic strategies for remedying aberrations in protein conformation and protein-protein interactions as a result of this reversible post-translational modification.

The overarching goal of this project is to decipher the kinetics, thermodynamics and mechanisms of neuropeptide SNO formation, which would fill missing gaps in contemporary research. We aim to develop a protocol and kinetic models that will be used to elucidate the energetics and mechanisms of neuropeptide SNO formation. This work

will focus on providing a quantitative understanding of SNO formation from three neuropeptides namely; arginine vasopressin (AVP), somatostatin-14 (SST-14) and urotensin II (U-II).

Peptide thiols are known to have unique autoxidation rates which largely depend on amino acid sequence, peptide structure and cellular redox conditions. We hypothesize that target peptide thiols have half-lives sufficient for subsequent S-nitrosylation reactions under physiologically relevant conditions. To test this hypothesis, we will evaluate the effects of temperature, copper chelators and pH on peptide thiol autoxidation to ascertain the formation and stability of target peptide thiols under physiologically relevant conditions.

The second hypothesis is that S-nitrosylation of target peptide thiols by NO moieties is both kinetically and thermodynamically favorable under physiological conditions and peptide SNOs are efficient carriers of NO. This study will determine the kinetics and thermodynamic parameters for target peptide S-nitrosylation by nitrous acid, peroxyxynitrite and SNA using Stopped-flow spectrophotometry. The determination of rate constants at different temperatures allows for the calculation of enthalpy, entropy, Gibbs free energy and activation energies for S-nitrosylation reactions.

Our final hypothesis is that peptide S-nitrosylation produces radicals and SNOs that may modify peptide function by altering peptide-receptor interactions and signaling pathways. Identification of radical/non-radical pathways elucidates molecular mechanisms that will enhance our understanding of S-nitrosylation/de-nitrosylation mechanisms which would aid in the development of therapeutics. This study will use electroparamagnetic resonance (EPR) to investigate radical formation and structure-activity relationships infer novel peptide SNO.

CHAPTER 2: INSTRUMENTATION, MATERIALS AND METHODS

2.1 INTRODUCTION

Elucidation of kinetic parameters and mechanisms involved in complex biological reactions requires the identification of rate limiting steps, intermediates, and reaction products. Evaluations of the effects of variations in concentration, rate dependence, temperature and pH are essential. Specialized instrumentation and analytical techniques are required when reaction time scales are rapid, and the half-lives of intermediates and products are short lived. Specialized equipment, methods and techniques described in this chapter include UV/Vis spectrophotometry, electron paramagnetic resonance, high performance liquid chromatography (HPLC), stopped-flow spectrophotometry and mass spectrometry.

2.2 INSTRUMENTATION

2.2.1 UV/Vis Spectrophotometry

A Perkin Elmer Lambda 25 spectrophotometer with halogen and deuterium lamps (190 to 1100 nm) was used to monitor reaction progress for slower reactions (>120s timescale). The Perkin-Elmer UV WinLab software was used for data capture, archiving and analysis. Constant parameters during data capture include a cuvette path length of 1 cm and a temperature of 25 °C. Temperature variation experiments were carried out by coupling a NESLAB RTE101 thermostated water bath recirculatory to the Perkin Elmer Lambda 25 spectrophotometer.

2.2.2 Stopped-flow Spectrophotometry.

Stopped-flow spectrophotometers are especially well-suited for monitoring rapid reactions with reaction solutions in the flow cell having a dead time of approximately 0.3 ms. Rapid reactions with a timescale of less than 120 s were monitored with a Hi-Tech Scientific SF61-DX2 double mixing stopped-flow spectrophotometer. The double mixing feature of the stopped-flow spectrophotometer allows for the mixing of reactants in reservoirs A and B facilitating the *in-situ* production of an unstable reactive intermediate like nitrous acid or peroxyxynitrite. After a short time delay, reactants from reservoirs C and/or D are introduced to the solution containing the reactive intermediate until a steady-state flow is attained. The final solution with a millisecond dead time is funneled through to a flow cell by a stopping syringe where the flow is stopped allowing for the measurement of cell optics. Employing appropriate techniques, reaction kinetics can be determined thus providing a method for the expeditious mixing of reactants coupled with immediate analytical signal generation.

2.2.3 Chromatography and mass spectrometry

A Phenomenex Synergi Fusion-RP (4 μm) HPLC column connected to an HP Agilent Series II 1090 HPLC was used for chromatographic separations. Solvents acetonitrile and water in 0.1 % formic acid were used to prepare mobile phases A and B, comprising of 10 % and 90 % acetonitrile respectively. A gradient elution of 0–30 % for mobile phase B at flow rates between 0.5 mL min⁻¹ was employed for all peptide sample analysis. A diode-array detector at wavelengths 280 nm and 545 nm was used for monitoring peptide and S-nitrosothiol signals respectively. A Micromass Q-TOF II LC/MS/MS Hybrid Quadrupole

TOF mass spectrometer in positive-ion mode was used for product identification in peptide disulfide reduction experiments. Mass spectrometry samples were rendered in 50:50 water and acetonitrile solution then subsequently injected through capillary tubing at flow rates ranging from 1 – 1000 $\mu\text{L min}^{-1}$. A high voltage of 3200 V was applied directly to a stainless-steel capillary emitter contained in the ionization source. Nebulizing nitrogen gas at the tip of the capillary emitter creates an electric field that promotes solvent evaporation forming charged droplets. The nitrogen gas (kept 150 °C and injected at flow rate of 1 $\mu\text{L min}^{-1}$) also aids in directing the spray of droplets through the cone (35 V) towards the mass analyzer. Collision-cell, TOF voltages and source block temperatures were maintained at 10 V, 9.1 kV and 80 °C respectively.

2.2.4 Electron Paramagnetic Resonance (EPR) Spectroscopy.

A Bruker EMX EPR Spectrometer was used for the detection of short-lived hydroxyl and nitric oxide radicals using 5,5-dimethyl-1-pyrroline N-oxide (DMPO) and nitroethane spin-traps respectively. Planck's law states that absorption of electromagnetic radiation results in different energy states occurring, with the energy difference (the Zeeman effect) being equal to the product of Planck's constant (h) and microwave frequency (ν). The microwave energy (ΔE) is also equal to the product of the Bohr magneton (β), the spectroscopic splitting constant; g-factor (g) and the magnetic field (H). Our X-band EPR held the frequency of radiation constant at 9.78 gigahertz (GHz), while varying the magnetic field used to acquire absorption spectrum. When radical species (with one unpaired electron) are placed in a magnetic field, absorption of electromagnetic radiation occurs when the electron transitions to a higher energy state. The two spin states have

different energies that would increase linearly with an increase in the magnitude of the applied magnetic field.

The amount of EPR active adduct formed is directly proportional to the intensity of the signal detected by the EPR. Spectra band width, line shape and hyperfine splitting are essential parameters that are used to identify various radical species. All EPR measurements were carried out at standard room temperature and pressure. The following EPR setup used in this study was adapted from Morakinyo, (2010), “microwave power, 19.91 mW; modulation amplitude, 1.41 G; receiver gain, 448; time constant, 10.24 ms; sweep width, 100 G and frequency, 9.78 GHz”¹⁵⁶.

2.3 MATERIALS

Three neuropeptides; Arginine vasopressin (AVP: Cys-Tyr-Phe-Gln-Asn-Cys-Pro-Arg-Gly), Somatostatin-14 (SST-14: Ala-Gly-Cys-Lys-Asn-Phe-Phe-Trp-Lys-Thr-Phe-Thr-Ser-Cys) and Urotensin-II (U-II: Glu-Thr-Pro-Asp-Cys-Phe-Trp-Lys-Try-Cys-Val) were purchased from Sigma Aldrich. Peptides were used without further purification at a purity of approximately 95%. Peptides were chosen on the basis of known physiological functions and the presence of chromophores whose reaction progression can be followed using spectroscopic and stopped-flow techniques. These analytical chemicals were purchased from Sigma Aldrich: formic acid, tris(2-carboxyethyl) phosphine (TCEP) gel, sodium nitrite (99.5%), phosphate buffered saline (PBS) tablets, a mMonium formate, hydrogen peroxide solution (30% w/w), DMPO (5,5- dimethyl-1-pyrroline-N-oxide), sodium hydroxide, ethanol (>99%), perchloric acid (70-72 %), acetonitrile (ACN), neocuproine

hydrochloride, manganese dioxide and sodium perchlorate. Nitrous acid (HNO_2) [nitrosating agent 1], was formed in situ by reacting sodium nitrite and perchloric acid. A quenched flow reactor comprising of a syringe pump, 30 mL disposable syringes and two tygon tubing connectors was used to synthesize peroxyxynitrite (ONOO^-) [nitrosating agent 2]. Solutions of 0.7 M HClO_4 and 0.6 M NaNO_2 reacted through the first T junction tubing connector to produce nitrous acid (HNO_2) which was then pumped into a flask containing 0.7 M H_2O_2 resulting in the formation of the yellowish colored peroxyxynitrous acid (ONOOH). The reaction was then quenched by introducing a 1.5 M NaOH solution through the second T junction tubing connector at a flow rate of 17 mL min^{-1} . Granular manganese dioxide was used to remove excess H_2O_2 from the ONOO^- solution, and standardization at 302 nm ($\epsilon_{320} = 1670 \text{ M}^{-1} \text{ cm}^{-1}$) was carried out using spectrophotometric and iodometric techniques. Fresh peroxyxynitrite was prepared daily. SNAP (*S*-Nitroso-*N*-acetyl-DL-penicillamine) [nitrosating agent 3], was purchased from Sigma Aldrich as a powder with $\geq 97\%$ purity.

2.4 EXPERIMENTAL METHODS

2.4.1 Peptide thiol formation, isolation, and identification. To establish conditions needed for complete disulfide reduction, a spin column was filled with an 8 mM suspension of TCEP-gel in distilled water followed by centrifugation at 4000 rpm. Distilled water was collected in Eppendorf tube and discarded. A 200 μL aliquot of a 2 mg mL^{-1} peptide disulfide solution in water was incubated with the gel for 15 to 120 mins with continuous agitation by vortexing at the lowest intensity. Agitation prevented the gel from settling to

the bottom of the column, which would result in incomplete disulfide reduction. Peptide dithiols were collected in the Eppendorf tube by spinning the column at 4000 rpm for 90 °C at 4 °C and 10-fold diluted aliquot was analyzed by HPLC to confirm complete disulfide reduction. TCEP was either washed, re-suspended in water and stored at 4 °C or discarded. All peptide dithiol samples are frozen at -80 °C until use.

2.4.2 Peptide thiol stability. Using HPLC the stability of peptide thiols was evaluated by monitoring the rate of disulfide reformation over time. The effects of temperature, pH, and the presence of trace copper impurity on peptide disulfide reformation were examined. A stock of 1 mM peptide dithiol in water was prepared and aliquots of this sample were further diluted to 250 μM in the appropriate buffer. Samples were removed at different time points and diluted to 25 μM before being injected into the HPLC column. The temperature dependence of disulfide reformation was examined by incubating samples of peptide dithiols at 21, 37 and 50 °C. Peptide thiol stability was also compared in water (pH 3.0) and in 30 mM PBS buffer at pH 7.4. Copper catalysis of disulfide reformation was evaluated using two copper-specific chelators: neocuproine (Cu^+) and DTPA (Cu^{2+}). The thiol and disulfide peaks in the various HPLC chromatograms were integrated to obtain calculated peak areas. The percent disulfide reformation was determined from the thiol peak areas divided by the sum of the thiol and disulfide peak areas multiplied by 100. Since peptide disulfides can reform very quickly under specific conditions and also because the injection into the HPLC might be delayed, two measures were taken in order to limit peptide disulfide reformation between aliquoting and analysis. Firstly, experiments run in 30 mM PBS at pH 7.4, contained 100 - 200 μM neocuproine and DTPA, since the redox

properties of the copper are known to favor disulfide formation between thiols. Secondly, all samples were kept in a refrigerated (4 °C) HPLC tray before injection.

CHAPTER 3: KINETICS AND MECHANISMS OF ARGININE VASOPRESSIN

S-NITROSYLATION BY NITRIC OXIDE

3.1 INTRODUCTION

Vasopressin is an oligopeptide produced in the hypothalamus and it comprises of only nine amino acid residues. It is essential for osmoregulation, homeostasis and has also been implicated in cognition and memory¹⁵⁷. The human analog contains arginine and is thus called arginine vasopressin (AVP). AVP is produced by both magnocellular [located in the supraoptic (SON) and paraventricular nucleus (PVN)] and parvocellular hypothalamic neurons. Numerous signals from perimetric organs prompt neurosecretory endings that are positioned on distal axons of the pituitary gland to discharge AVP which then readily enters the bloodstream because pituitary gland capillaries are devoid of a blood–brain barrier¹⁵⁸. The three established receptors of AVP are: V1aR (V1a), V3 (V1b) and V2 (AVPR2). V1aR receptors are expressed in vascular smooth muscle cells, adrenal medulla, brain, liver and kidney^{56, 159}. V1aR and AVPR2 receptors are known to mediate the effects of AVP secretion on arterial blood pressure through a phospholipase C-mediated pathway and have also been linked to AVP-mediated stress responses in rats and in humans¹⁶⁰⁻¹⁶¹. V3 receptors are located in the anterior pituitary and mediate the release of the adrenocorticotrophic hormone (ACTH) which is stimulated by increases in AVP expression also through the phospholipase C and adenylate cyclase-mediated pathways¹⁶². Long-acting AVP analogs like triglycyl lysine vasopressin (Terlipressin) with a higher affinity for V1aR and AVPR2 receptors are undergoing clinical studies for the treatment of tachycardia with shock¹⁶³. Histochemical studies have detected the presence of NOS in

SON and PVN nuclei located in the posterior pituitary gland, this colocalization of NOS and AVP has also been linked to regulatory mechanisms that suggest an interplay between AVP secretion and NOS activity¹⁶⁴⁻¹⁶⁵. *In vitro* and *in vivo* studies with AVP and NO donors, show a correlation between the inhibition of NO synthesis and increased AVP secretion¹⁶⁶⁻¹⁶⁷. Despite mounting evidence of NO as a neuromodulator of AVP activity, it is surprising that no kinetic, thermodynamic or mechanistic studies of biochemical reactions between AVP and NO have been reported to date. It is therefore plausible that AVP thiols might be targets of NO post-translational modification through S-nitrosylation resulting in a steady state equilibrium with AVP S-nitrosothiols^{135, 168-169}. AVP S-nitrosylation has the potential to alter S-nitrosothiol blood levels resulting in the dysregulation of physiological and pathological processes which could culminate into various pathophysiological disease states¹⁷⁰⁻¹⁷⁴. Peptide-peptide transnitrosylation reactions have emerged as a distinctive mechanism by which NO can be transferred to peptide thiols within the same vicinity as peptide S-nitrosothiol. Over 3000 peptides/proteins are S-nitrosylated in tissues with various outcomes including active-site specific and allosteric cysteine thiols modifications which have been implicated in human disease¹⁷⁵⁻¹⁷⁷. The rates of trans-nitrosation and the decomposition of S-nitrosothiols are essential in elucidating nitrosylating/denitrosylating mechanisms and evaluating whether peptide S-nitrosothiols are effective NO transporters.

This chapter gives a detailed kinetic, thermodynamics and mechanistic study of NO mediated S-nitrosylation of AVP. Rate constants, energetics and AVP structural modifications associated with S-nitrosylation reactions are investigated with the aim of providing links to alterations in peptide function.

3.2 RESULTS AND DISCUSSION

3.2.1 AVP dithiol formation and stability. A method for isolating pure AVP thiol (AVP(SH)) was established using LC-MS, to probe whether vasopressin thiols are kinetically stable under physiological conditions to allow for S-nitrosylation to occur. Since certain amino acids (tryptophan and tyrosine and cysteine) are known to have absorptivity in the UV at 280 nm, we used the absorptivity characteristics of cystine and tyrosine residues in AVP disulfide to elute the peptide using an HPLC-UV chromatogram. AVP disulfide reduction was achieved by incubating of 60 μ M AVP disulfide dissolved in distilled water with 2.5 M gel-bound TCEP (40-fold excess) for 30 min in a spin column followed by centrifugation. TCEP was chosen due to its stability over a relatively broad pH range (1.5–8) ¹⁷⁸⁻¹⁸⁰. AVP disulfide and thiol forms were separated using HPLC-UV (Fig 3.1A and B). Mass spectrometric (MS) analysis confirmed peak 1 (Fig 3.1A) as AVP disulfide with singly protonated (M+H)⁺ ions at m/z 1084.44 and the doubly protonated (M+2H)²⁺ ions at m/z 542.72 (Fig 3.1C). Peak 2 (Fig 3.1B) was identified as singly protonated (M+H)⁺ AVP (m/z 1086.46) and the doubly protonated (M+2H)²⁺ AVP dithiol at m/z 543.73 (Fig 3.1D). The effects of pH, copper chelators and temperature on the rate of AVP thiol autoxidation was investigated in phosphate-saline buffer (PBS). Since trace amounts of copper are known to accelerate disulfide reformation, we used Cu²⁺ and Cu⁺ metal chelators; diethylenetriaminepentaacetic acid (DTPA) and neocuproine respectively, to investigate the effects of metal ions on thiol autoxidation¹⁸¹.

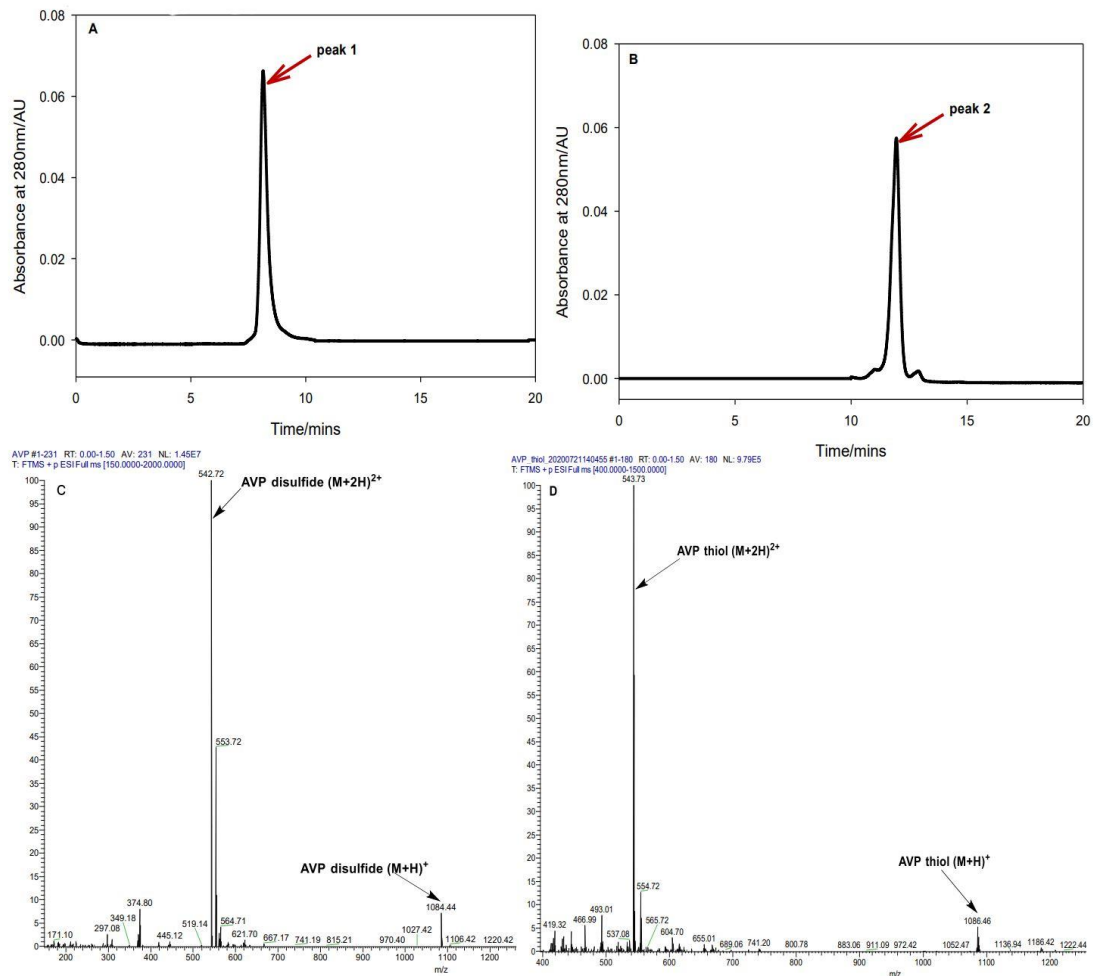


Figure 3.1: HPLC-UV-MS analysis of AVP disulfide reduction. (A) An HPLC chromatogram of 60 μM AVP disulfide was run as a standard and eluted in peak 1 at 8.1 mins. (B) 60 μM AVP disulfide in pH 3 water was incubated for 30 minutes in 2.5 M TCEP (40-fold excess), the product was eluted in peak 2 at 11.9 mins. (C). ESI mass spectra confirmed peak 1 as AVP disulfide. (D) ESI mass spectra shows peak 2 as AVP dithiol.

AVP thiol stability was investigated by monitoring the rate of disulfide reformation using HPLC chromatograms at varying temperatures and pH, the effect of metal chelators. The rate of disulfide reformation was evaluated using Eq 3.1.

$$\% \text{ Peptide} = \frac{\text{Peptide disulfide peak area}}{\text{Peptide disulfide peak area} + \text{peptide dithiol peak area}} \times 100 \text{ Eq 3.1}$$

The time course for > 95% AVP disulfide reformation is summarized in Table 3.1, which shows that reducing temperature decelerates the rate of thiol autoxidation. Lowering pH from 7.4 to 3.0 reduced the rate of disulfide reformation by a factor of 6 when compared to the effect of chelators. These data agrees with previous studies showing that dithiol–disulfide exchange reactions are disfavored under low pH conditions¹⁸². Copper chelators have an inhibitory effect on disulfide reformation, as solutions at pH 7.4 containing chelators had > 20-fold inhibition of disulfide reformation. AVP thiol was shown to have a half-life of 29.5 min at physiological temperature and pH.

Table 3.1: The effects of temperature, pH and metal chelators on time required for AVP disulfide reformation.

Temperature °C	Time for disulfide reformation (>95%)		
	water pH 3.0	30 mM PBS, pH 7.4	30 mM PBS, pH 7.4 + chelators
25°C	135 h	65 min	22.2 h
37°C	54.4 h	29.5 min	8.6 h
50°C	22.4 h		

3.2.2 Nitrous acid mediated S-nitrosylation and product identification. Researchers have identified cysteines proximal to acid, alkaline and aromatic residues in protein consensus motifs as being the most susceptible to S-nitrosylation¹⁸³. The reactivity of NO signaling molecules like other RSNOs, HNO₂ and other NO⁺ to these consensus motifs is another important factor that determines whether protein thiols are S-nitrosylated. Transnitrosylation reactions between peptide RSNOs and peptide thiols are further complicated by variable cysteine residue pKa, changes in peptide conformations and cellular redox environments^{141, 184-185 186}. The protonation of NO₂⁻ to HNO₂ is favored in

acidic conditions that are found in lysosomes, protein membrane microdomains and mitochondria intermembrane spaces ¹⁸⁷. In these acidic solutions, HNO₂ exists predominantly as HONO which can be further protonated to form the nitrosonium ion (NO⁺) as depicted by Eq 3.2.



High acidity coupled with reduced water activity favor the formation of NO⁺. S-nitrosylation of AVP by HNO₂ was studied by generating HNO₂ in situ through the reaction between NaNO₂ and HClO₄. A typical UV spectrum of reactants was obtained, which shows HNO₂ (Fig 3.2a) and NaNO₂ (Fig 3.2b) both having a significant absorbance at 355 nm, with absorptivity coefficient of 22.9 M⁻¹cm⁻¹. The vasopressin S-nitrosothiol [AVP-(SNO)] absorbs at both 335 nm and 545 nm (Fig 3.2c), with molar absorptivity coefficients (ε) of 922 M⁻¹cm⁻¹ and 16 M⁻¹cm⁻¹ respectively. With this data, which was in good agreement with other ε₅₄₅ values reported for RSNOs ¹⁸⁸⁻¹⁹⁰, we determined that each AVP-(SNO) group's molar absorptivity coefficient at 545 nm would be 16 M⁻¹ cm⁻¹. We followed AVP-(SNO) production at 545 nm as that region was devoid of any interference. At 280 nm peptides with tryptophan (Trp), cysteine and tyrosine (Tyr) amino acid residues exhibit significant absorptivities¹⁹¹.

Since the absorption of these amino acids at 280 nm is additive, the extinction coefficient of the whole peptide can be determined. Figure 3.2d shows 0.17 mM AVP disulfide [AVP(S-S)] with a molar absorptivity coefficient, ε₂₈₀=1615 M⁻¹cm⁻¹. The total AVP(S-S) ε₂₈₀ was a result of individual contributions of 125 M⁻¹cm⁻¹ and 1490 M⁻¹cm⁻¹ from

cystine and tyrosine residues respectively¹⁹². In Figure 3.2e; 0.17 mM AVP dithiol [AVP(S-H)] had $\epsilon_{280}=1490 \text{ M}^{-1}\text{cm}^{-1}$ which only accounts for the molar absorptivity from the tyrosine residue. HPLC-UV-MS was employed for monitoring AVP S-nitrosylation reactions, and two distinct products were identified. HPLC-UV chromatograms (Fig 3.3A) show the reaction between nitrous acid and AVP dithiol where $[\text{HNO}_2]_0 \gg [\text{AVP(SH)}]_0$, such that AVP(SH) was the limiting reagent. Two species were identified as shown by peak 1 eluted at 13.5 mins and peak 2 eluted at 15 mins. Mass spectrometry (Fig 3.3B) identified peak 1 as doubly protonated $(\text{M}+2\text{H})^{2+}$ (m/z 558.76) singly S-nitrosylated AVP [AVP(SNO)]. Whilst peak 2 was identified as doubly protonated $(\text{M}+2\text{H})^{2+}$ (m/z 572.72) doubly S-nitrosylated AVP [AVP(SNO)₂]. Even though our product contains a mixture of both AVP(SNO) and AVP(SNO)₂, the latter had the highest relative abundance and was the dominant product under our established reaction conditions.

3.2.2.1 Effect of AVP(SH) variation. Our stopped-flow setup involved mixing AVP(SH), H⁺ and NaClO₄ (for maintaining ionic strength) in feeding stream one, whilst the second feeding stream contained NaNO₂. The injection of H⁺ and NaNO₂ in separate feeding streams allowed for the generation of HNO₂ *in-situ* and obviated the possibility of HNO₂ decomposition before S-nitrosylation could commence. Figure 3.4A, depicts the effects of [AVP(SH)] variation at constant [H⁺] and [NO₂⁻]. Plots of initial rate vs [AVP(SH)] were linear with an intercept kinetically indistinguishable from zero (Fig 3.4B). The reaction shows first order dependence in [AVP(SH)] for a broad range of AVP(SH) concentrations where $[\text{NO}_2^-]_0$ and $[\text{H}^+]_0 > [\text{AVP(SH)}]_0$.

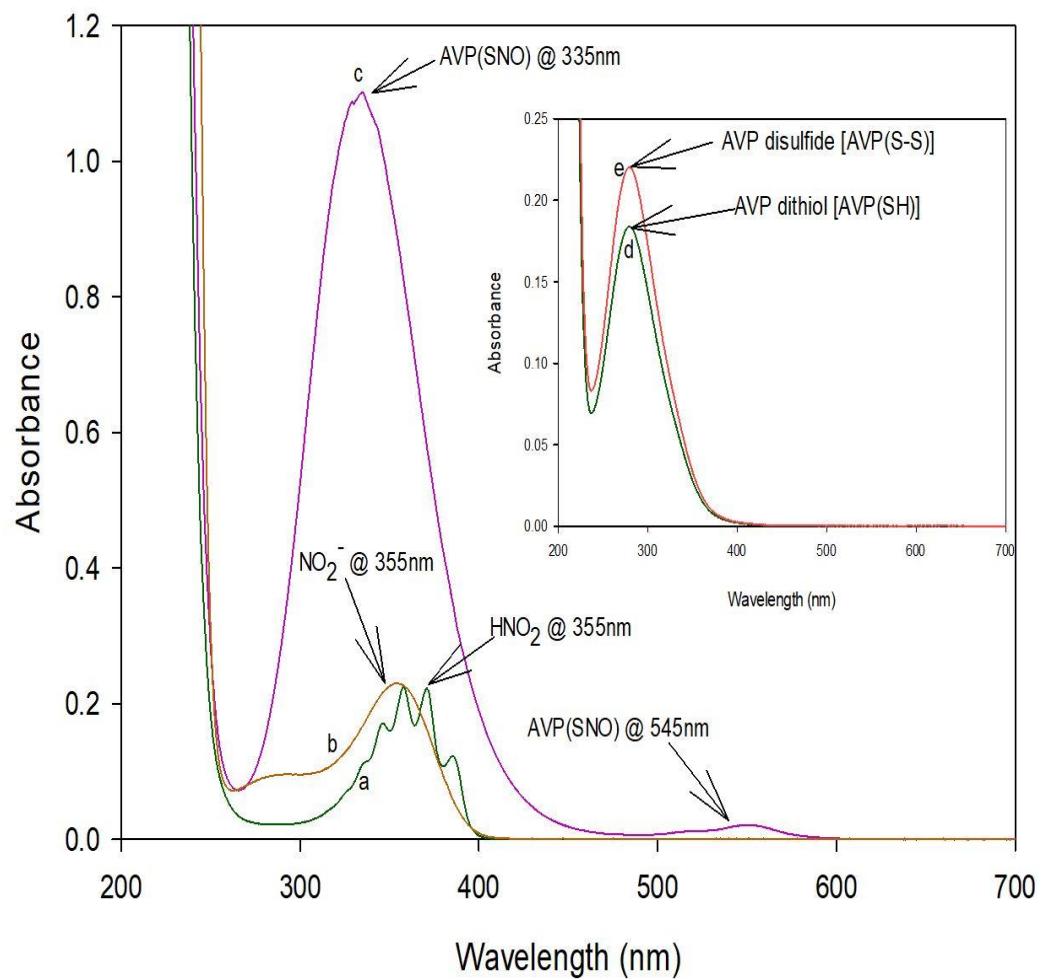


Figure 3.2: Spectra scan of; (a) $[\text{HNO}_2] = 3.5 \text{ mM}$, (b) $[\text{NO}_2^-] = 4 \text{ mM}$, (c) $[\text{AVP}] = 1 \text{ mM}$, $[\text{NO}_2^-] = 10 \text{ mM}$ and $[\text{H}^+] = 50 \text{ mM}$, (d) $[\text{AVP(S-S)}] = 0.17 \text{ mM}$ and (e) $[\text{AVP(SH)}] = 0.17 \text{ mM}$

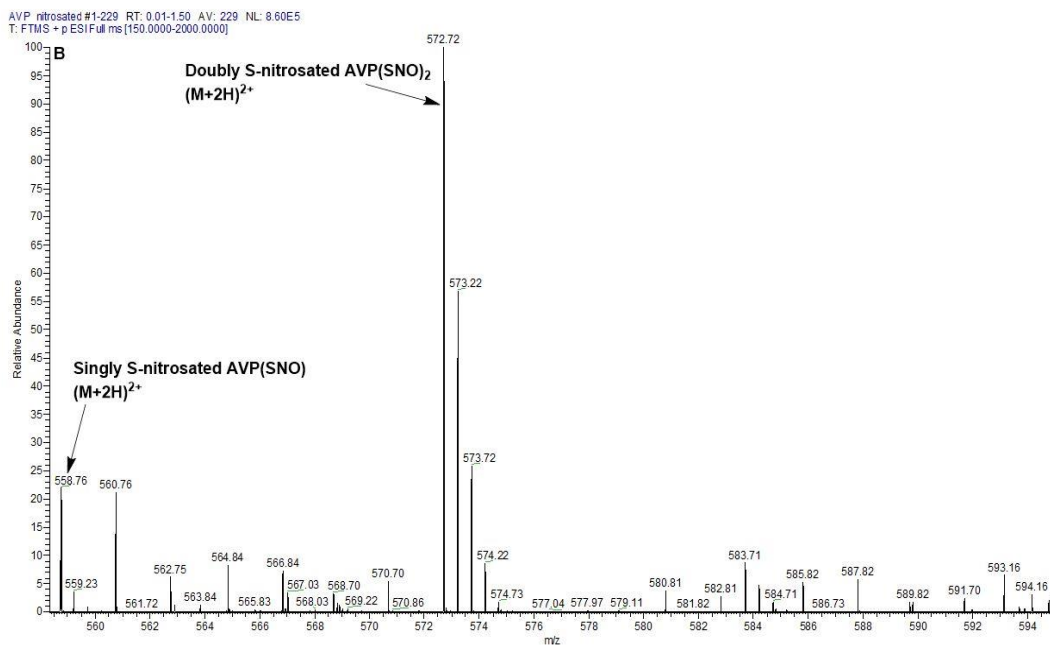
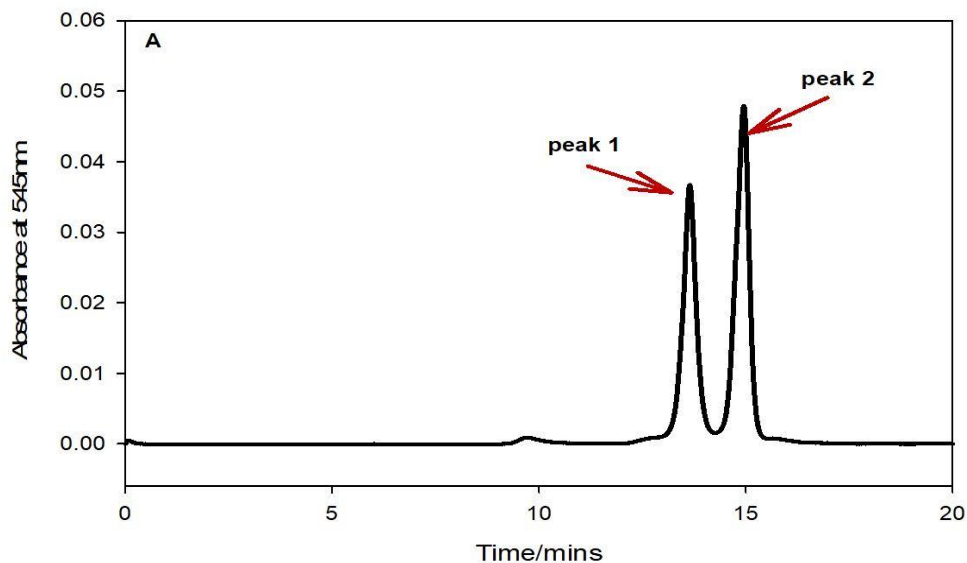


Figure 3.3: HPLC-UV-MS analysis of the reaction between 5 mM AVP thiol and 20 mM nitrous acid. HPLC chromatogram; (A) shows the elution times of two species; peak 1 at 13.5 mins and peak 2 at 15 mins. ESI mass spectra (B), identifies compounds eluted in peak 1 as singly S-nitrosylated AVP(SNO) and peak 2 doubly S-nitrosylated AVP(SNO)₂.

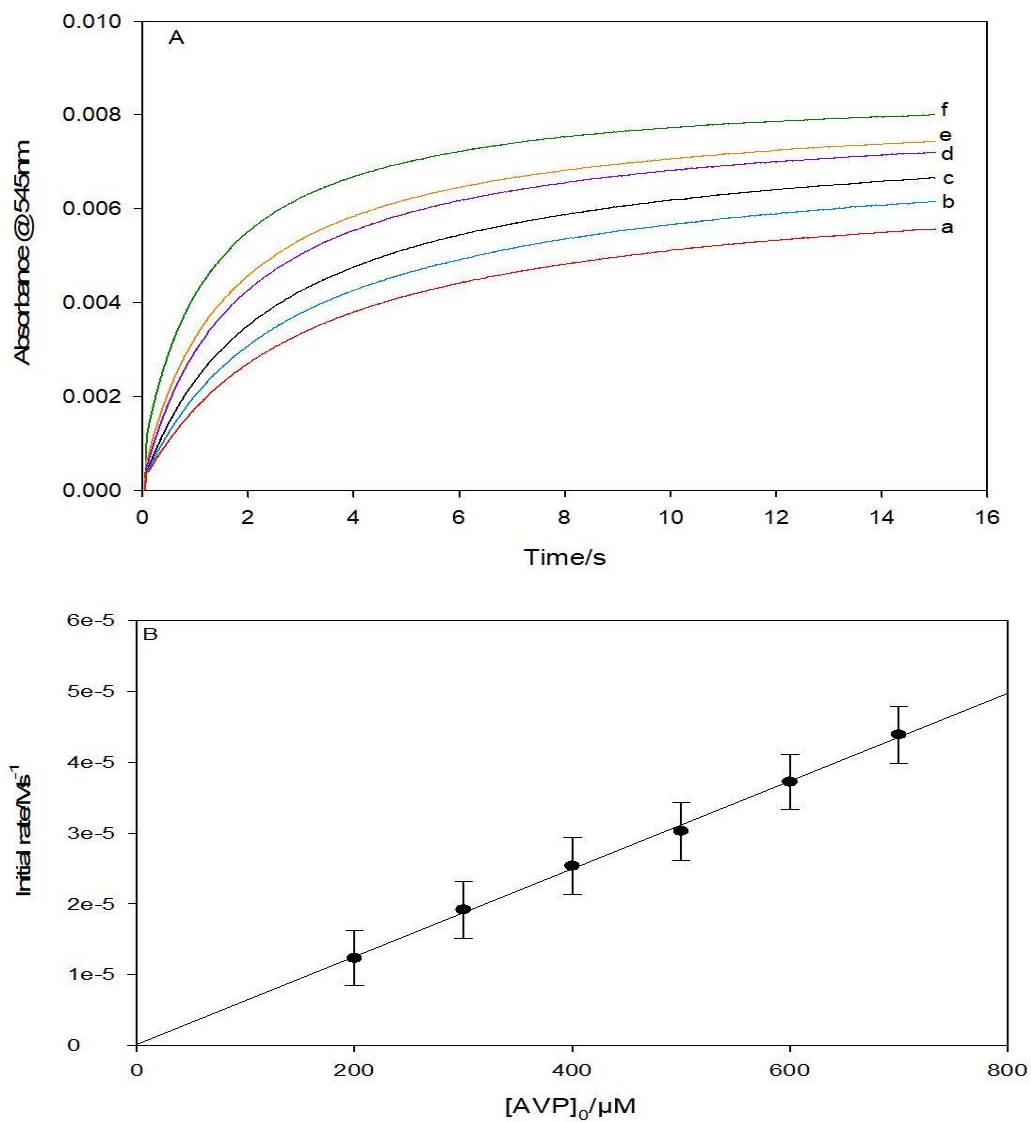


Figure 3.4: (A) Effect of [AVP(SH)] variation on AVP(SNO) formation at 25 °C. Fixed [H⁺] = 1 mM, [EDTA] = 100 μM, [NO₂⁻] = 1 mM. Varied [AVP(SH)] = (a) 200 μM, (b) 300 μM, (c) 400 μM, (d) 500 μM, (e) 600 μM, (f) 700 μM. (B) Initial rate plot shows strong dependence of AVP(SNO) formation on AVP(SH) concentration.

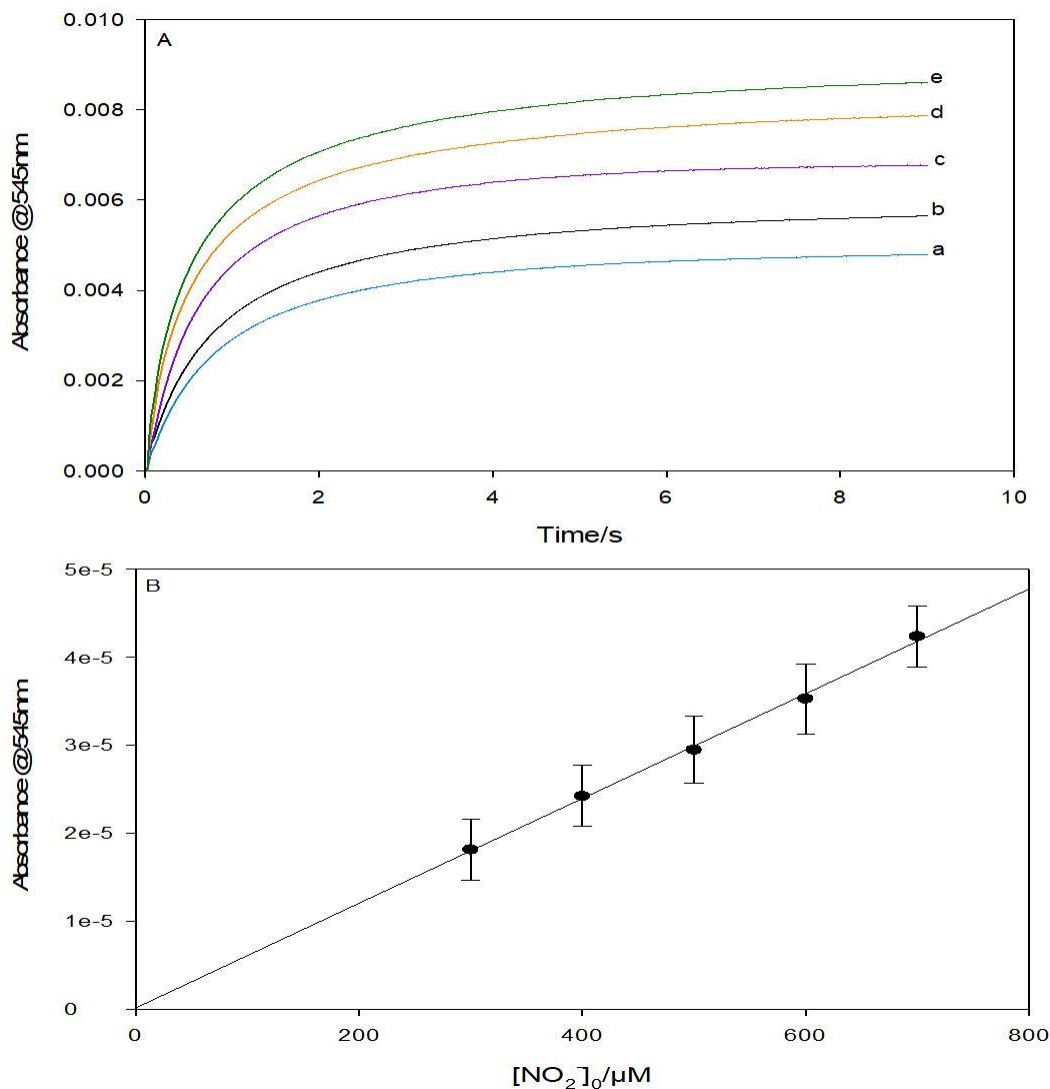


Figure 3.5: (A) Effect of $[\text{NO}_2^-]$ variation on AVP(SNO) formation at 25 °C. Fixed $[\text{H}^+] = 1 \text{ mM}$, $[\text{EDTA}] = 100 \text{ }\mu\text{M}$, $[\text{AVP}] = 1 \text{ mM}$. Varied $[\text{NO}_2^-] =$ (a) 300 μM , (b) 400 μM , (c) 500 μM , (d) 600 μM , (e) 700 μM . (B) Initial rate plot shows strong dependence of AVP(SNO) formation on NO_2^- concentration.

3.2.2.2 Effect of nitrite variation. Nitrite variation gave simple and first order kinetics (Fig 3.5A), when initial nitrite concentrations ($[\text{NO}_2^-]_0$) remained below $[\text{H}^+]_0$, therefore all reactive nitrogen species (RNS) were in the form of protonated HNO_2 . The amount of AVP(SNO) formed increased until $[\text{NO}_2^-]_0$ exceeded $[\text{AVP}(\text{SH})]_0$ resulting in saturation. Plots of initial rate vs $[\text{NO}_2^-]_0$ were also linear with a zero intercept (Fig 3.5B).

3.2.2.3 Effect of acid variation. The effects of H^+ variation were complex and largely dependent on the ratio of $[H^+]_0$: $[NO_2^-]_0$. The rate of AVP(SNO) formation was especially dependent on whether $[H^+]_0$ exceeded $[NO_2^-]_0$. Figure 3.6A, traces (a-c) depict AVP(SNO) formation in low $[H^+]_0$ conditions where $[H^+]_0 < [NO_2^-]_0$, and the rate of AVP(SNO) formation is 1st order with respect to $[H^+]_0$. Interestingly, when $[H^+]_0 \geq [NO_2^-]_0$ as shown in Figure 3.6A, traces (a-c)), still resulted in an increase in the rate of AVP(SNO) formation despite a saturation with regards to $[HNO_2]$ in the reaction solution. A plot of initial rate vs $[H^+]_0$ was linear with a non-zero intercept with points to another nitrosating agent after the amount of HNO_2 saturates (Fig 3.6B).

3.2.2.4 Effect of Cu^{2+} variation. Our data suggest a catalytic role for Cu^{2+} ions in AVP(SNO) formation. Figure 3.7A depicts the effect of Cu^{2+} on reactant concentrations from Figure 3.5A, trace (e) which were run with no added $[H^+]$ and in the absence of metal chelator EDTA. Clearly Cu^{2+} ions are effective catalysts of AVP(SNO) formation even in micromolar concentrations. A rate plot of Cu^{2+} ions' catalyst effect on AVP(SNO) formation (Fig 3.7B) depicts a linear relationship between $[Cu^{2+}]$ and the rate of AVP(SNO) formation with initial rates an order of magnitude higher than acid catalyzed reactions (Fig 3.5B). The non-zero y-intercept represents the nitrosating effect of NO_2^- in the absence of H^+ and Cu^{2+} . Interestingly, a closer comparison of the final absorbance values of Fig 3.5A, trace (e) and the highest absorbance attained by Fig 3.7A, trace (f); 0.008 vs 0.005, points to another reaction mechanism in which Cu^{2+} ions would also catalyze the decomposition of AVP(SNO) thus affecting the maximum amount of AVP(SNO) detected. There are competitive kinetics involved in both AVP(SNO)

formation and depletion due to redox cycling that occurs between Cu^{2+} and Cu^+ ions as shown by R3.1 and R3.2:

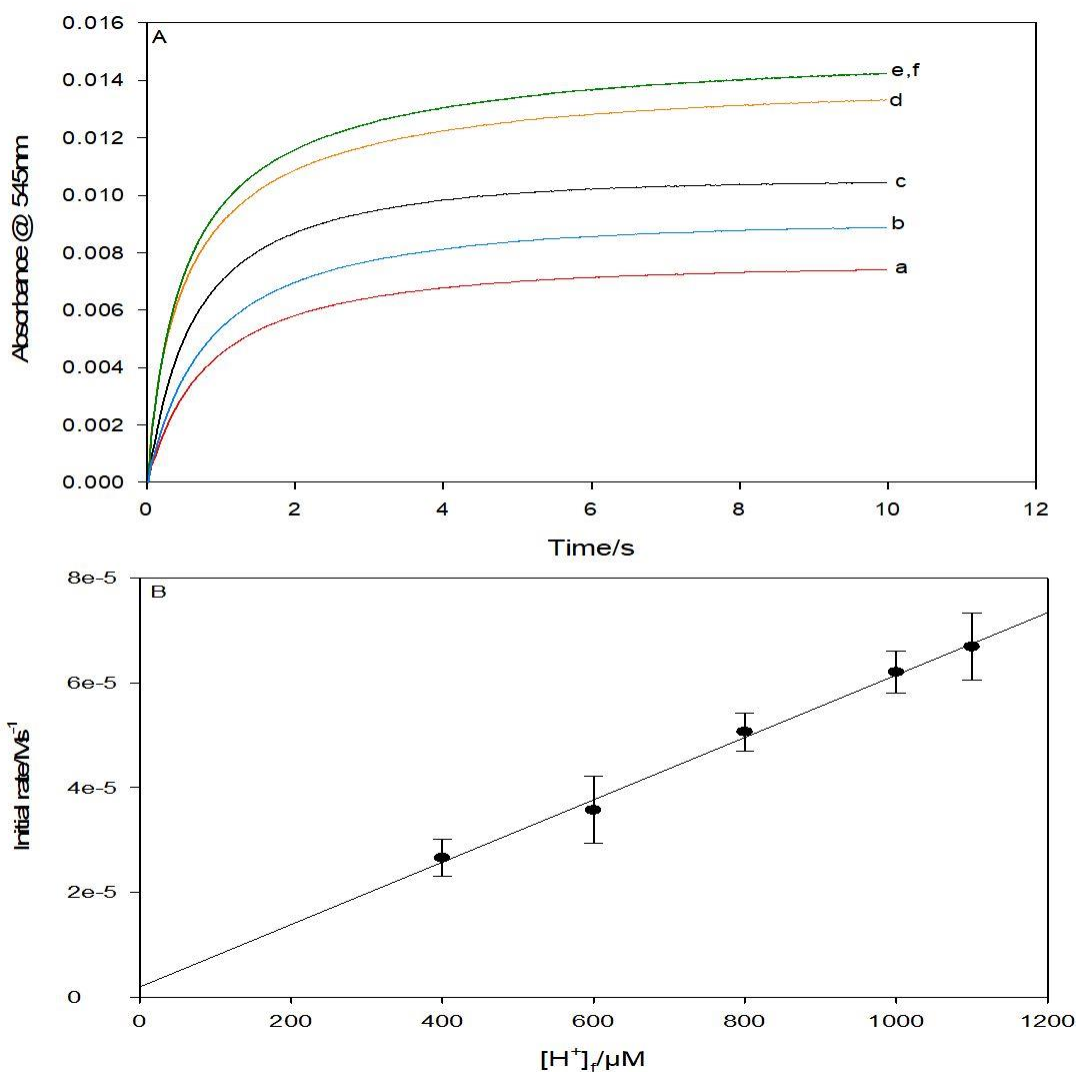
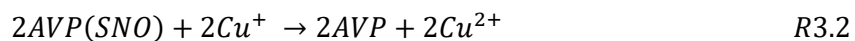
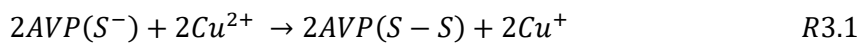


Figure 3.6: (A) Effect of $[\text{H}^+]$ variation on AVP(SNO) formation at 25 °C. Fixed $[\text{NO}_2^-] = 1 \text{ mM}$, $[\text{EDTA}] = 100 \mu\text{M}$, $[\text{AVP}] = 1 \text{ mM}$. Varied $[\text{H}^+] =$ (a) 400 μM , (b) 600 μM , (c) 800 μM , (d) 1 mM, (e) 1.1 mM, (f) 1.2 mM. (B) A plot of initial rates vs $[\text{H}^+]_0$ was linear with a non-zero intercept.

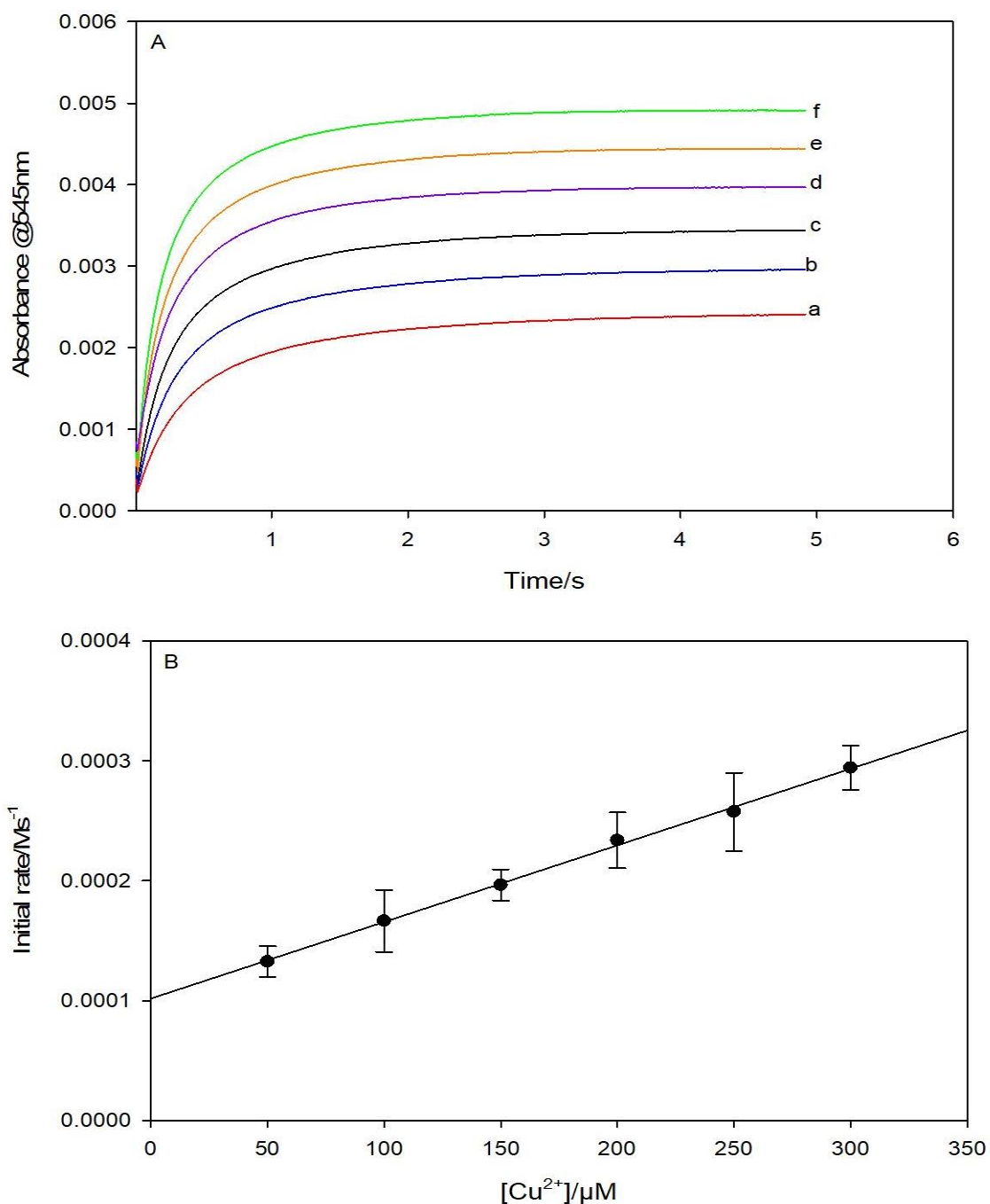
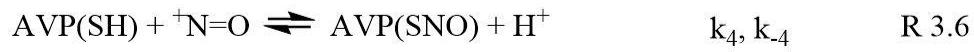
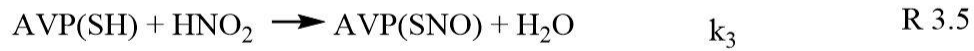


Figure 3.7: (A) Effect of $[\text{Cu}^{2+}]$ variation on AVP(SNO) production at 25 °C. The rate of AVP(SNO) production increases as $[\text{Cu}^{2+}]$ increases. Fixed $[\text{NO}_2^-] = 700\mu\text{M}$, $[\text{AVP}] = 1 \text{ mM}$, $[\text{H}^+] = 0.00 \text{ M}$. Varied $[\text{Cu}^{2+}] =$ (a) 50 μM , (b) 100 μM , (c) 150 μM , (d) 200 μM , (e) 250 μM , (f) 300 μM . (B) A plot of initial rate vs $[\text{Cu}^{2+}]$ was linear with a non-zero intercept.

3.2.2.5 Nitrous acid kinetic reaction scheme. The dynamics of this bimolecular reaction suggests 4 reactions as being essential in HNO₂-mediated S-nitrosylation of AVP thiol. Reaction 3.3, involves protonation of NO₂⁻ to produce HNO₂, this followed nitrosyl cation (NO⁺) production in excess acid (R3.4) and the reactions of both HNO₂ and NO⁺ with AVP(SH).



Based on AVP(SNO) formation the rate of reaction is given by equation 3.3:

$$\frac{d[\text{AVP(SNO)}]}{dt} = k_3[\text{AVP(SH)}][\text{HNO}_2] + k_4[\text{AVP(SH)}][\text{NO}^+] - k_{-4}[\text{AVP(SNO)}][\text{H}^+] \quad \text{Eq 3.3}$$

Before accumulation of AVP(SNO), the terminal term in Eq 3.3 is irrelevant. All reactive nitrogen species ([RNS_T]) in solution adhere to the mass balance equation 3.4:

$$[\text{RNS}_T] = [\text{NO}_2^-] + [\text{HNO}_2] + [\text{AVP(SNO)}] + [\text{NO}^+] \quad \text{Eq 3.4}$$

The sole source of [RNS]_T in the reaction mixture is NO₂⁻. The cation NO⁺ is essentially a reactive intermediate, that is relevant in excess acid. A steady-state approximation is applied on the NO⁺, as this allows us to estimate NO⁺ concentrations (Eq 3.5).

$$[NO^+] = \frac{k_2[HNO_2][H^+]}{k_{-2}+k_4[AVP(SH)]} \quad \text{Eq 3.5}$$

Employing the dissociation constant of HNO₂ and Eq 3.5, we obtained an initial rate law (Eq 3.6) that accounts for the complex effect of H⁺ concentrations.

$$\frac{d[AVP(SNO)]}{dt} = \frac{[AVP(SH)][RNS_T][H^+]}{K_a+[H^+]} \left[k_3 + \frac{k_2k_4[H^+]}{k_{-2}+k_4[AVP(SH)]} \right] \quad \text{Eq 3.6}$$

Kinetic data from Figures 3.4 – 3.6 conforms to the parameters outlined by Eq 3.6. Our initial rate law predicts 1st order kinetics in H⁺ (at low acid), AVP(SH) and NO₂⁻ concentrations without saturation. At low [H⁺]₀ the second term in Eq 3.6 would be negligible, therefore kinetic runs retain first-order kinetics in accordance with first term. When [H⁺]₀ ≥ [NO₂⁻]₀, there is saturation with regards to HNO₂ concentrations. Interestingly, traces (e)-(f) in Fig 3.6A depict a continuous increase in initial rate despite HNO₂ saturation which implicates another nitrosating agent formed in excess [H⁺] according to reaction R3.7.



Considering both nitrosating agents (HNO₂/NO⁺) gives an overall rate of reaction governed by Eq 3.7:

$$\frac{d[AVP(SNO)]}{dt} = \left\{ \frac{[H^+][RNS_T]}{[H^+]+K_a} \right\} [AVP(SH)] [k_3 + k_4K_b[H^+]] \quad \text{Eq 3.7}$$

The bimolecular rate constants for HNO_2/NO^+ mediated S-nitrosylation of AVP(SH) are represented by k_3 and k_4 respectively in Eq 3.7. In subsequent calculations, we used the K_a of HNO_2 ($5.62 \times 10^{-4} \text{ M}^{-1}$) and K_b ($1.2 \times 10^{-8} \text{ M}^{-1} \text{ s}^{-1}$) from reaction R3.7. At high $[\text{H}^+]$, a plot of initial rate/ $[\text{RNS}_T][\text{AVP}(\text{SH})]$ vs. $[\text{H}^+]$ is linear with a slope ($k_4 K_b$) and intercept (k_3) (Fig 3.6 and Eq 3.7). Using Eq 3.7 and kinetic data from Fig 3.6, we determined our k_3 to be $278 \pm 10 \text{ M}^{-1} \text{ s}^{-1}$ and k_4 as $2.24 \times 10^3 \text{ M}^{-1} \text{ s}^{-1}$. These studies show that AVP(SNO) formation is through the direct reaction of HNO_2 with AVP(SH), with NO^+ as the major nitrosating agent in high acidic media.

3.2.2.6 Temperature dependence and thermodynamic analysis. An essential component of kinetic data is that it does not only elucidate reaction dynamics but also provides an in-depth comprehension of thermodynamic parameters. In this study, we employ transient state kinetics to elucidate the dynamics of HNO_2 mediated AVP thiol S-nitrosylation reactions. Transient state kinetics allow for the determination of observed rate constant (k_{obs}) based on an approach that compares reactant concentrations with the time scale required for the reaction to attain a state of equilibrium. Therefore, k_{obs} values are fundamentally distinct from bimolecular rate constants. Pseudo-1st-order kinetics would be obtained for the rate of a reaction (R3.6) approaching equilibrium [equilibrium constant (K) = $k_{\text{on}}/k_{\text{off}}$], if an overwhelming excess of HNO_2/NO^+ was used in AVP S-nitrosylation thus resulting in k_{obs} values that are function of $[\text{NO}^+]$ (Eq 3.8). Linear plots of k_{obs} vs $[\text{NO}^+]$ would allow for the determination of k_{on} and k_{off} from the slope and intercept, respectively.

To mitigate extrapolation errors which are usually prevalent in evaluating slope and intercept values, all reported k_{on} and k_{off} values in this study are obtained from an average of 5 kinetic experiments and standard deviation is used for all uncertainty estimates.

$$k_{obs} = k_{on}[NO^+] + k_{off} \quad \text{Eq 3.8}$$

The natural log of k_{obs} was then plotted against the inverse of temperature in kelvins. The linear fitting function in SigmaPlot 14 and the Arrhenius equation (Eq 3.9) were used to calculate the activation energy (E_a). In Eq 3.9; A is the Arrhenius pre-exponential factor; T is temperature in kelvins and R is the gas constant ($8.314472 \text{ J mol}^{-1} \text{ K}^{-1}$). Eyring plots [$\ln(k/T)$ against $1/T$] were used to evaluate activation enthalpies (ΔH^\ddagger) and entropies (ΔS^\ddagger) according to the Eyring equation (Eq 3.10). Gibbs free energy of activation (ΔG^\ddagger) values were determined at 37°C according to Eq 3.11. In Eq 3.11, h is Planck's constant ($6.626 \times 10^{-34} \text{ J.s}^{-1}$), R and T are temperature (kelvins) and R is the gas constant respectively and k_B is the Boltzmann constant ($1.3806504 \times 10^{-23} \text{ J}^{-1}\text{K}^{-1}$).

$$\ln k_{obs} = \ln A - \frac{E_a}{RT} \quad \text{Eq 3.9}$$

$$\ln \left(\frac{k}{T} \right) = - \frac{\Delta H^\ddagger}{RT} + \frac{\Delta S^\ddagger}{R} + \ln \left(\frac{k_B}{h} \right) \quad \text{Eq 3.10}$$

$$\Delta G^\ddagger = RT \left[\frac{\ln(k_B T)}{h} - \ln k_{obs} \right] \quad \text{Eq 3.11}$$

We ran traces in Fig 3.6 in pseudo-1st-order conditions with at least 10-fold excess of HNO_2 (10-55 mM) in temperatures ranging from $15\text{-}35^\circ \text{C}$ as depicted by Fig 3.8A.

Observed rate constants from these kinetic runs (Table 3.2) show S-nitrosylation rates that increase ~2.7-fold with each 10 °C increment in temperature with stopped-flow spectra that was highly analogous exhibiting characteristics of typical pseudo-1st-order reactions. Eyring plots (Fig 3.8B) and the Eyring equation (Eq 3.10) utilized observed k_{on} and k_{off} values from Table 3.2 to determine the following thermodynamic parameters; for k_{on} as $E_a = 35.7 \text{ kJmol}^{-1}$; $\Delta H^\ddagger_{\text{on}} = 33.3 \pm 2 \text{ kJ mol}^{-1}$ and $\Delta S^\ddagger_{\text{on}} = -1 \pm 0.06 \text{ J mol}^{-1} \text{ K}^{-1}$; and for k_{off} as $E_a = 43.0 \text{ kJmol}^{-1}$; $\Delta H^\ddagger_{\text{off}} = 41.06 \pm 4 \text{ kJ mol}^{-1}$ and $\Delta S^\ddagger_{\text{off}} = 1.5 \pm 0.2 \text{ J mol}^{-1} \text{ K}^{-1}$) (Table 3.3). Activation parameters ΔG^\ddagger and ΔH^\ddagger for HNO_2/NO^+ mediated AVP(SNO) formation suggest an endergonic and endothermic reaction for both k_{on} and k_{off} . The negative ΔS^\ddagger for k_{on} implicates an associative mechanism with an unstable transition state. As expected, the positive ΔS^\ddagger for k_{off} describes a dissociative mechanism as would be the case for AVP(SNO) decomposition. As previously noted, our calculated ΔS^\ddagger and ΔH^\ddagger values are derived kinetic runs where k_{obs} parameters are determined by extrapolation from slope and intercept values. Given that our stopped-flow instrument has a reaction dead time of 2 milliseconds, one could rightfully question whether using other more sensitive methods would produce different ΔH^\ddagger and ΔS^\ddagger values. Laser flash photolysis is a nanosecond (ns) time-resolved spectroscopic technique that is used to probe sample excitation levels with a laser beam¹⁹³. This technique has garnered much interest among biochemists working to explore various protein metastable states and dynamics.

A study comparing semi-independent kinetic data from various laboratories investigating metmyoglobin and NO interactions using both stopped flow and flash photolysis found that ΔH^\ddagger values had statistically insignificant differences that were within a margin of error¹⁹⁴. Extraction of these essential thermodynamic parameters provides an in-depth

understanding of elementary reaction mechanisms involved in nitrosation and denitrosation process.

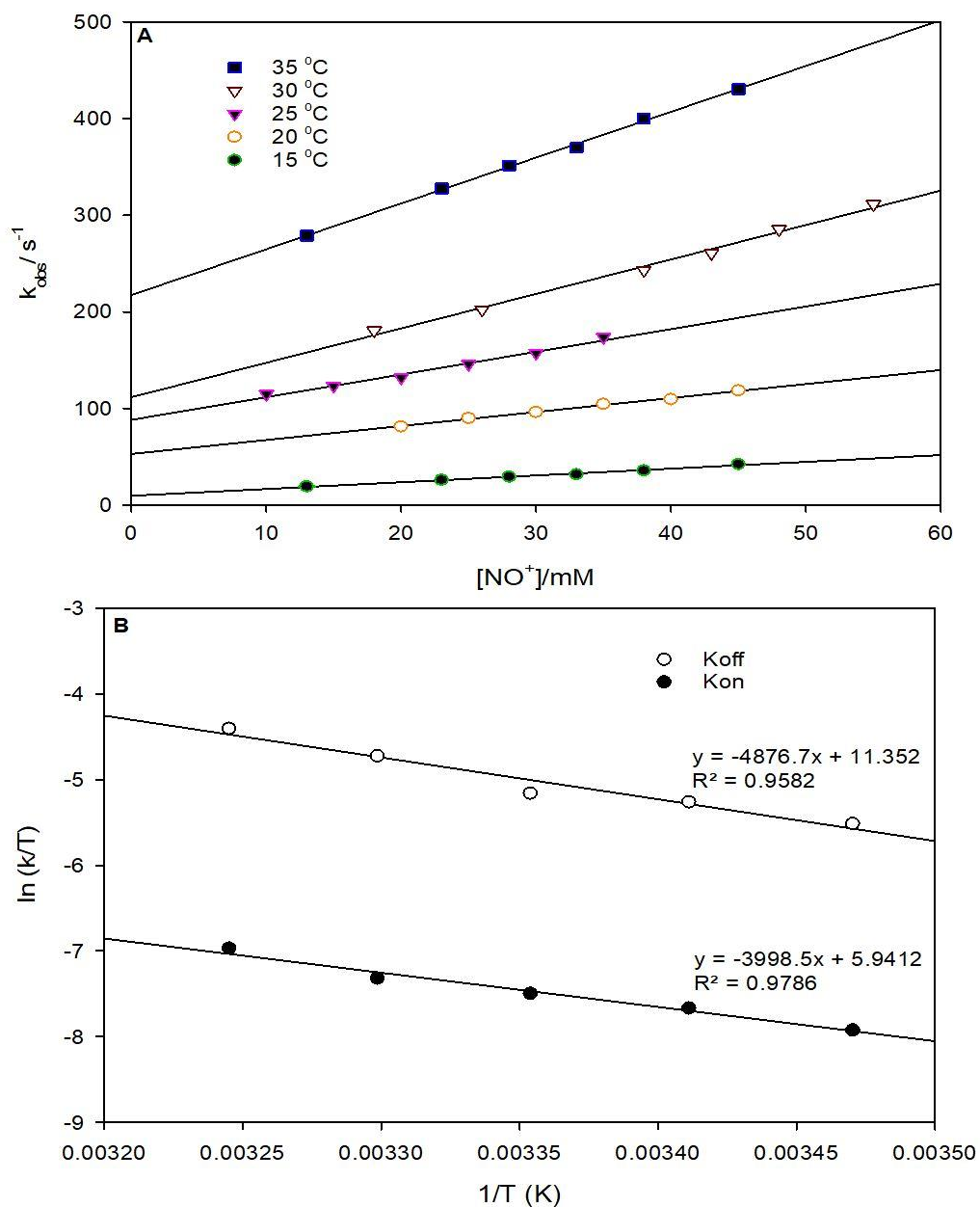


Figure 3.8: (A) Observed rate constants for the S-nitrosylation of AVP(SH) by varied NO^+ concentrations over a broad temperature range of 15-35 °C. Fixed [EDTA] = 100 μ M, [AVP] = 1 mM. Varied $[H^+]$ and $[NO_2^-]$ from 10-55 mM (B) Linear Eyring plots determining activation parameters ΔH^\ddagger and ΔS^\ddagger measured by stopped-flow spectroscopy.

Table 3.2: Observed rate constants for NO⁺ mediated AVP thiol S-nitrosylation reactions.

Temp (°C)	k_{on} (M ⁻¹ s ⁻¹)	k_{off} (s ⁻¹)
15	0.70 ± 0.03	9.61 ± 1.1
20	1.45 ± 0.05	52.98 ± 1.70
25	2.35 ± 0.14	88.17 ± 3.31
30	3.57 ± 0.15	111.71 ± 5.86
35	4.74 ± 0.09	217.54 ± 3

Table 3.3: Thermodynamic parameters for NO⁺ mediated AVP thiol S-nitrosylation reactions.

	E _a ^a	ΔG ^{‡b}	ΔH ^{‡c}	ΔS ^{‡d}
k_{on}				
	35.7	33.6	33.3	-1.0
k_{off}				
	43.0	41.06	40.6	1.5

^{a, b and c} Values are in kJ/mol, whilst ^d values are in J.mol⁻¹K⁻¹. Temperature = 37°C^b

3.2.2.7 EPR analysis. Figure 3.9 shows a series of EPR spectra which depicts the involvement of NO in AVP(SNO) decomposition. Spectra are similar to those reported with nitroethane-NO trap¹⁹⁵. A mixture of a nitroethane trap (forms adduct with NO[•]) and AVP(SH) does not show any signal (Fig 3.9A), whilst spectra taken 20s (Fig 3.9B) and 30s (Fig 3.9C) after NO₂⁻ addition depict an increase in EPR signal with time. The broad signal in Fig 3.9A may be due to some cavity contamination, however spectra B through G appear to ride over this spectral feature. To evaluate the effect of Cu²⁺ on AVP(SNO) decomposition, we ran EPR spectra on Fig 3.7A traces (a)-(c) in the presence of a nitroethane trap (Figs 3.9D-3.9F). We observed an increase in signal with increase in [Cu⁺] in spectra taken 5s after the addition of Cu⁺. Our data confirms copper redox cycling as

depicted by R3.1 and R3.2.

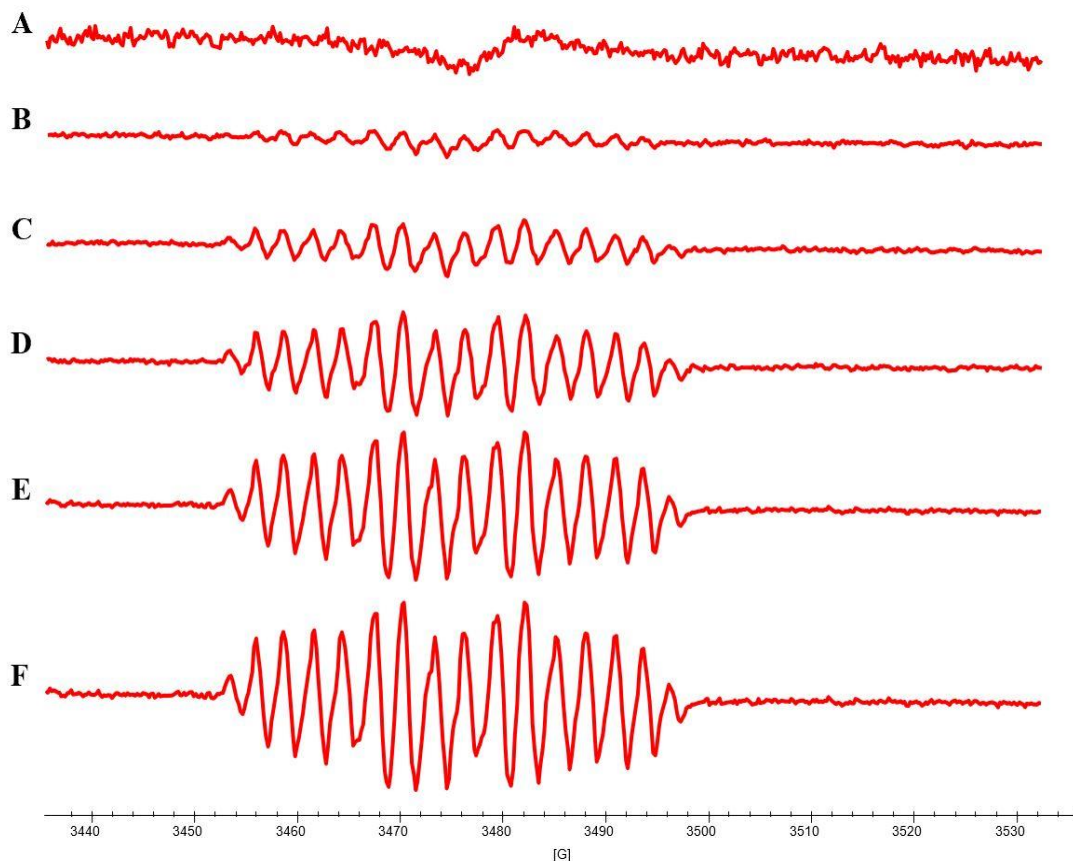


Figure 3.9: EPR spectra of $\text{NO}\cdot$ generation during AVP(SNO) decomposition using 0.5 M nitroethane spin trap. (A) $[\text{nitroethane}] = 0.5\text{M}$, $[\text{AVP(SH)}] = 1\text{ mM}$. (B) $[\text{nitroethane}] = 0.5\text{M}$, $[\text{AVP(SH)}] = 1\text{ mM}$, $[\text{NO}_2^-] = 700\mu\text{M}$ and $[\text{H}^+] = 1\text{ mM}$ after 20s. (C) $[\text{nitroethane}] = 0.5\text{M}$, $[\text{AVP(SH)}] = 1\text{ mM}$, $[\text{NO}_2^-] = 700\mu\text{M}$ and $[\text{H}^+] = 1\text{ mM}$ after 30s. (D-F) Spectra taken after 5s with fixed $[\text{nitroethane}] = 0.5\text{M}$, $[\text{AVP(SH)}] = 1\text{ mM}$, $[\text{NO}_2^-] = 700\mu\text{M}$. Varied $[\text{Cu}^+] =$ (D) $50\mu\text{M}$, (E) $100\mu\text{M}$, (F) $150\mu\text{M}$.

3.2.3 Peroxynitrite mediated AVP(SH) S-nitrosylation. The kinetics of oxidation and S-nitrosylation of AVP(SH) by ONOO^- were monitored by tracking AVP(SNO) formation and ONOO^- depletion at 545 nm and 302 nm ($\epsilon = 1670\text{ M}^{-1}\text{cm}^{-1}$) respectively (Fig 3.9). The reactivity of ONOO^- (pK_a 6.8) is multifaceted, extremely pH-dependent and ONOO^- is highly unstable in acidic media as it spontaneously disintegrates with a half-life less than a second at physiological pH and temperature¹⁹⁶. At pH 1.0, NO_3^- is the main product of

ONOO⁻ decomposition with an absorption peak 302 nm, which complicates ONOO⁻ depletion experiments in highly acidic medium (R3.10)¹⁹⁷. At physiological pH both ONOO⁻ /ONOOH co-exist, with NO₂⁻ and O₂ as major decomposition products (R3.11), as is the case at pH >8.0 (R3.12).

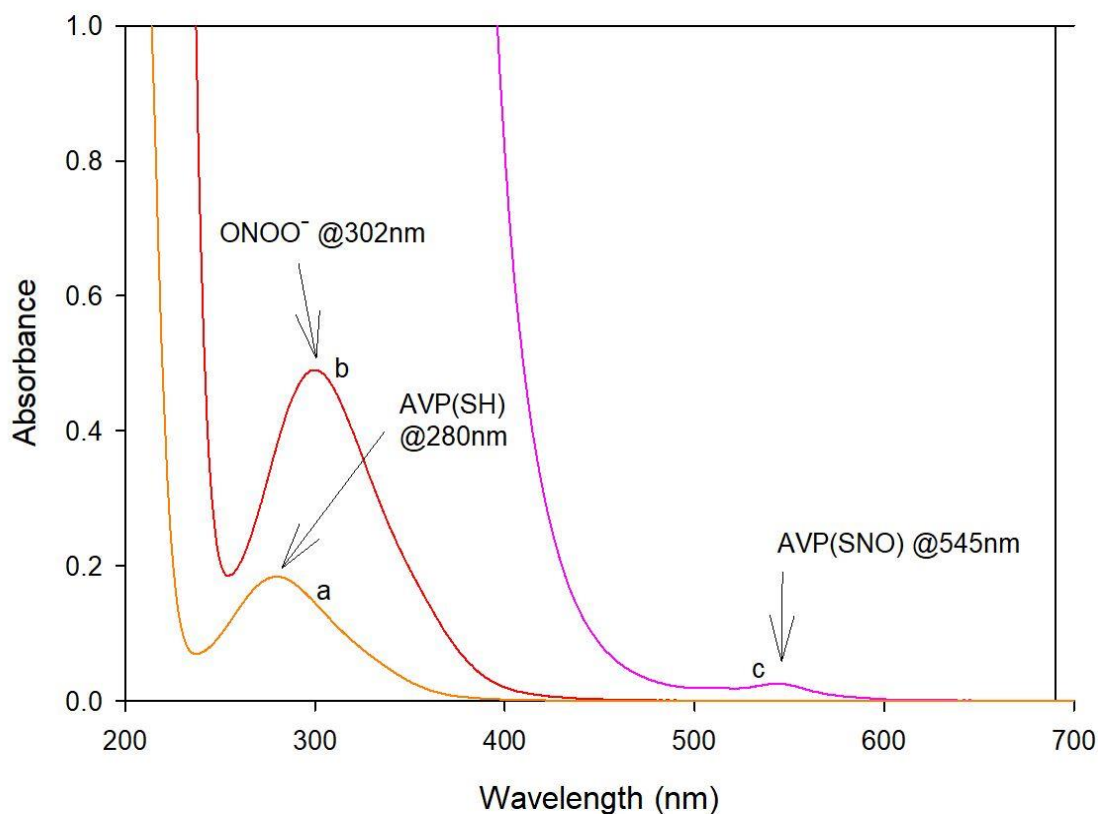
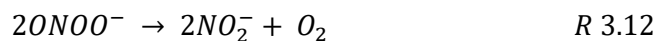
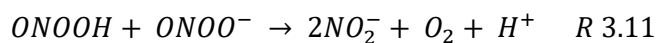


Figure 3.9: Spectra scan of; (a) [AVP(SH)] = 150 μM, (b) [ONOO⁻] = 300 μM, (c) AVP(SNO) formation from reaction mixture with; [AVP(SH)] = 1.5 mM, [ONOO⁻] = 1.5 mM in PBS at pH 7.4.

Subsequent kinetic analysis was conducted at pH 7.4 in 0.1M PBS buffer and also in mildly acidic media.



3.2.3.1 Effect of AVP(SH) variation on ONOO⁻ depletion and AVP(SNO) formation. By varying concentrations of AVP(SH) we probed the role of AVP(SH) in ONOO⁻ depletion while [ONOO⁻] was held constant (Fig 3.10A). All ONOO⁻ oxidations at pH 7.4 show fast autocatalytic decomposition kinetics. Increments in [AVP(SH)] gave higher ONOO⁻ depletion rates and we determined the bimolecular rate constant for the direct S-nitrosylation of AVP(SH) by ONOO⁻ to be $884 \pm 31 \text{ M}^{-1} \text{ s}^{-1}$ from spectra depicted in Figure 3.10B. The non-zero y-intercept ($1 \times 10^{-4} \text{ Ms}^{-1}$) represents the rate of ONOO⁻ decomposition under our reaction conditions in the absence of AVP(SH). For [ONOO⁻]₀: [AVP(SH)]₀ ratios utilized in our kinetic runs, an evaluation of AVP(SNO) formation at pH 7.4 showed 1st-order dependence of AVP(SNO) formation on [AVP(SH)] (Fig 3.1°C and D). The reaction kinetics were also similar when [ONOO⁻] is in overwhelming excess over AVP(SH) concentrations (data not shown).

3.2.3.2 Effect of acid variation on ONOOH mediated S-nitrosylation. Kinetics of AVP(SNO) formation by ONOO⁻ showed a complex dependence on acid concentrations as illustrated by R3.10. The effect of adding acid when $[\text{H}^+] < \text{ONOO}^-$ is shown Figure 3.11. The data shows the catalytic effect of acid on AVP(SNO) formation, as an increase in $[\text{H}^+]$ increases the rate of AVP(SNO) formation until [AVP(SH)] becomes limiting and saturation sets in. Increments in $[\text{H}^+]$ did not reduce the amount of AVP(SNO) formed, this suggests that rates of AVP(SNO) formation do not need to be faster than the rate of ONOO⁻ decomposition due to the formation of ONOOH as the major nitrosating agent. As expected, the rate of ONOO⁻ depletion by AVP(SH) is also highly dependent on acid concentrations. Holding [AVP(SH)] and [ONOO⁻] constant while varying $[\text{H}^+]$ where

[AVP(SH)] < [ONOO⁻] (Fig 3.12A), shows rates of ONOO⁻ depletion by AVP(SH) that are proportional to increases in acid concentration with nonlinear curved rate plots with respect to [H⁺] (Fig 3.12B). Using experimental data from Figures 3.11 and 3.12, we determined the bimolecular rate constant for the direct S-nitrosylation of AVP(SH) by ONOOH to be $1.72 \times 10^4 \text{ M}^{-1}\text{s}^{-1}$ at 25°C.

3.2.3.3 Effect of peroxy nitrite variation and EPR analysis. Variation of ONOO⁻ at pH7.4 to determine its effect on AVP(SNO) formation shows a steady increase in the rate of AVP(SNO) formation with increments in [ONOO⁻] (Fig 3.13A). The reaction is rapid without an induction period. Rate plots depict 1-st order kinetics with regards to [ONOO⁻] (Fig 3.13B). Addition of micromolar Cu²⁺ concentrations in both mildly acidic and pH7.4 ONOO⁻ mediated reactions, reproduced the catalyst effect of Cu²⁺ on AVP(SNO) formation rates as shown in Figure 3.7. As expected, addition of NO₂⁻ on traces in Figure 3.10 resulted in increased AVP(SNO) absorbance values due to the formation of HNO₂. The same but smaller effect was observed when NO₂⁻ was added to traces in Fig 3.13, due to the limited nitrosating power of NO₂⁻ in the absence of acid. It is generally accepted that decomposition of ONOOH/ONOO⁻ yields NO₂⁻ and O₂ under widely varying reaction conditions (Scheme 3.1), and kinetic predictive models have been developed based on the evidence that the decomposition reaction forms NO₂, [•]NO and [•]O₂⁻ and [•]OH radical intermediates¹⁹⁸. For CO₂⁻ catalyzed ONOOH/ONOO⁻ decomposition, formation of nitrogen dioxide and carbonate radicals from the nitrosoperoxycarbonate anion is a feasible unimolecular activation step¹⁹⁹⁻²⁰⁰. A current area of intense research is aimed at determining if rates of ONOOH/ONOO⁻ decomposition agree with the thermodynamics of

O-O bond homolysis to form nitrogen dioxide and hydroxide radicals.

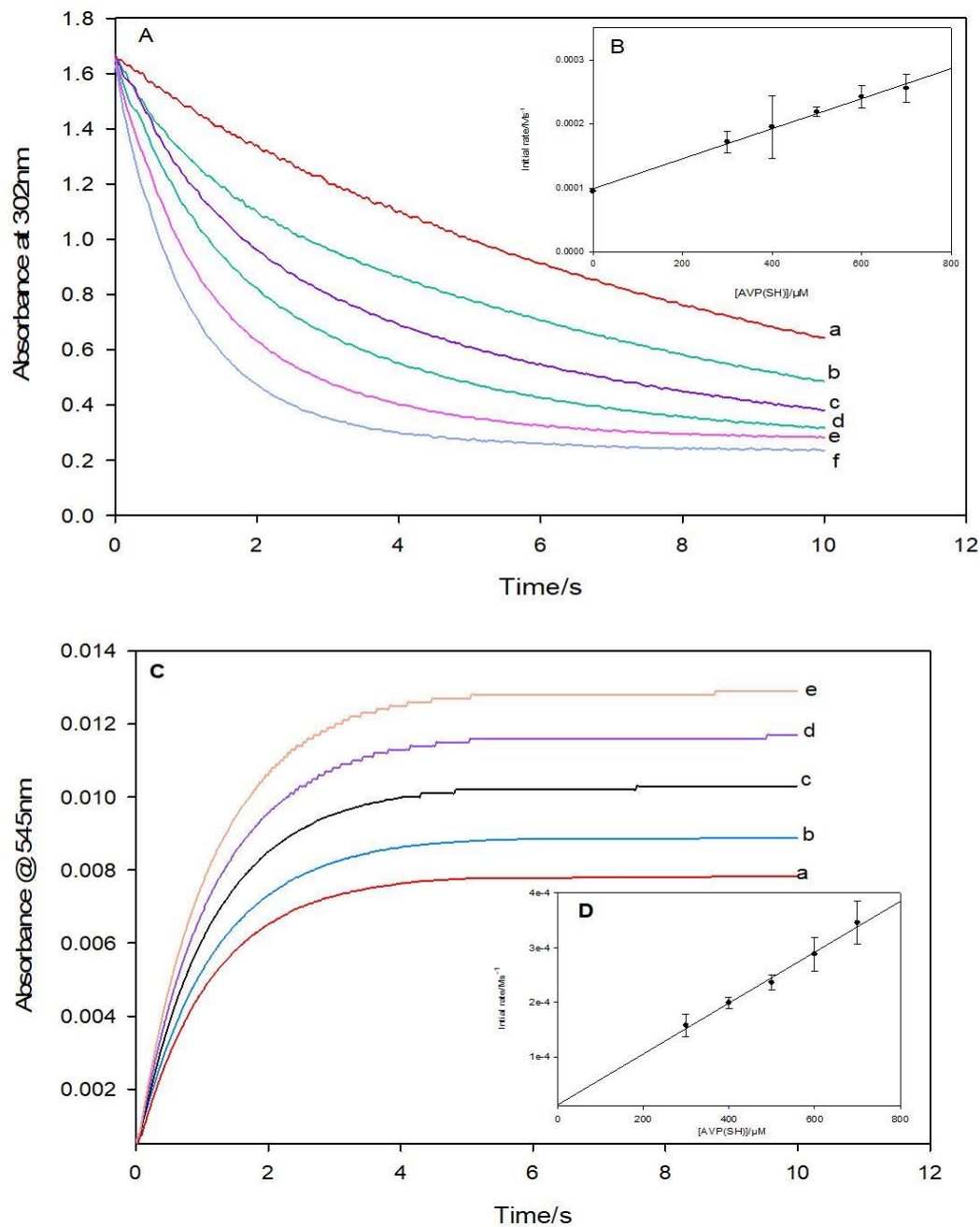


Figure 3.10: Effect of varying AVP(SH) concentrations on ONOO⁻ depletion in PBS at pH 7.4. Fixed [EDTA] = 100 μM, [ONOO⁻] = 1 mM. **(A)** Varied [AVP(SH)] = (a) 300 μM, (b) 400 μM, (c) 500 μM, (d) 600 μM, (e) 700 μM. **(B)** Shows linear relationship between initial rates of ONOO⁻ depletion and AVP(SH) concentrations for traces in (A). Effect of varying AVP(SH) concentrations on AVP(SNO) formation in PBS at pH 7.4. **(C)** Varied [AVP(SH)] = (a) 300 μM, (b) 400 μM, (c) 500 μM, (d) 600 μM, (e) 700 μM. **(D)** Shows linear relationship between initial rates of AVP(SNO) and AVP(SH) concentrations for traces in (C).

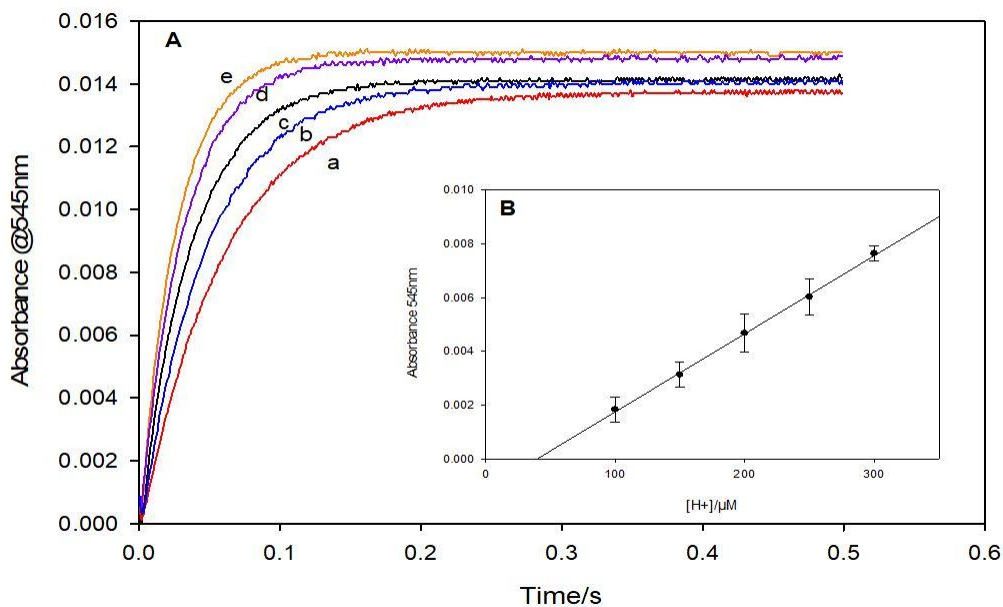


Figure 3.11: (A) Effect of varying H^+ concentrations on $ONOO^-$ mediated AVP(SNO) formation. Fixed $[AVP(SH)] = 1 \text{ mM}$, $[EDTA] = 100 \text{ } \mu\text{M}$, $[ONOO^-] = 1 \text{ mM}$. Varied $[H^+] =$ (a) $100 \text{ } \mu\text{M}$, (b) $150 \text{ } \mu\text{M}$, (c) $200 \text{ } \mu\text{M}$, (d) $250 \text{ } \mu\text{M}$, (e) $300 \text{ } \mu\text{M}$. (B) Linear relationship between initial rates of AVP(SNO) and H^+ concentrations for traces in (A)

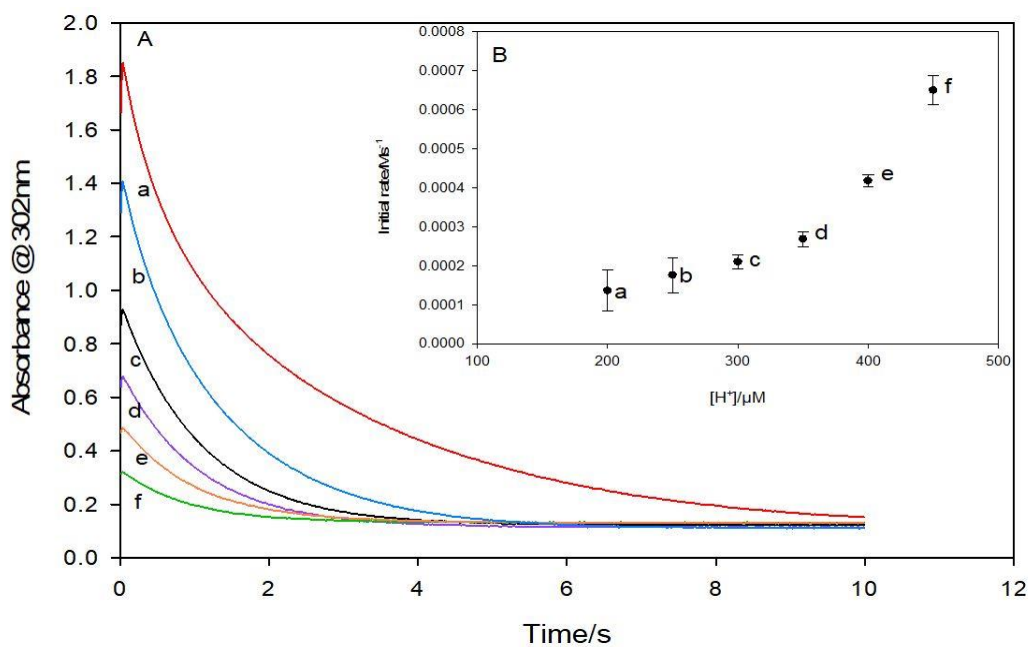


Figure 3.12: (A) Effect of varying H^+ concentrations on $ONOO^-$ depletion. Fixed $[AVP(SH)] = 700 \text{ } \mu\text{M}$, $[EDTA] = 100 \text{ } \mu\text{M}$, $[ONOO^-] = 1 \text{ mM}$. Varied $[H^+] =$ (a) $200 \text{ } \mu\text{M}$, (b) $250 \text{ } \mu\text{M}$, (c) $300 \text{ } \mu\text{M}$, (d) $350 \text{ } \mu\text{M}$, (e) $400 \text{ } \mu\text{M}$, (f) $450 \text{ } \mu\text{M}$. (B) Initial rates plot shows an exponential increase in $ONOO^-$ depletion with increased acid concentrations.

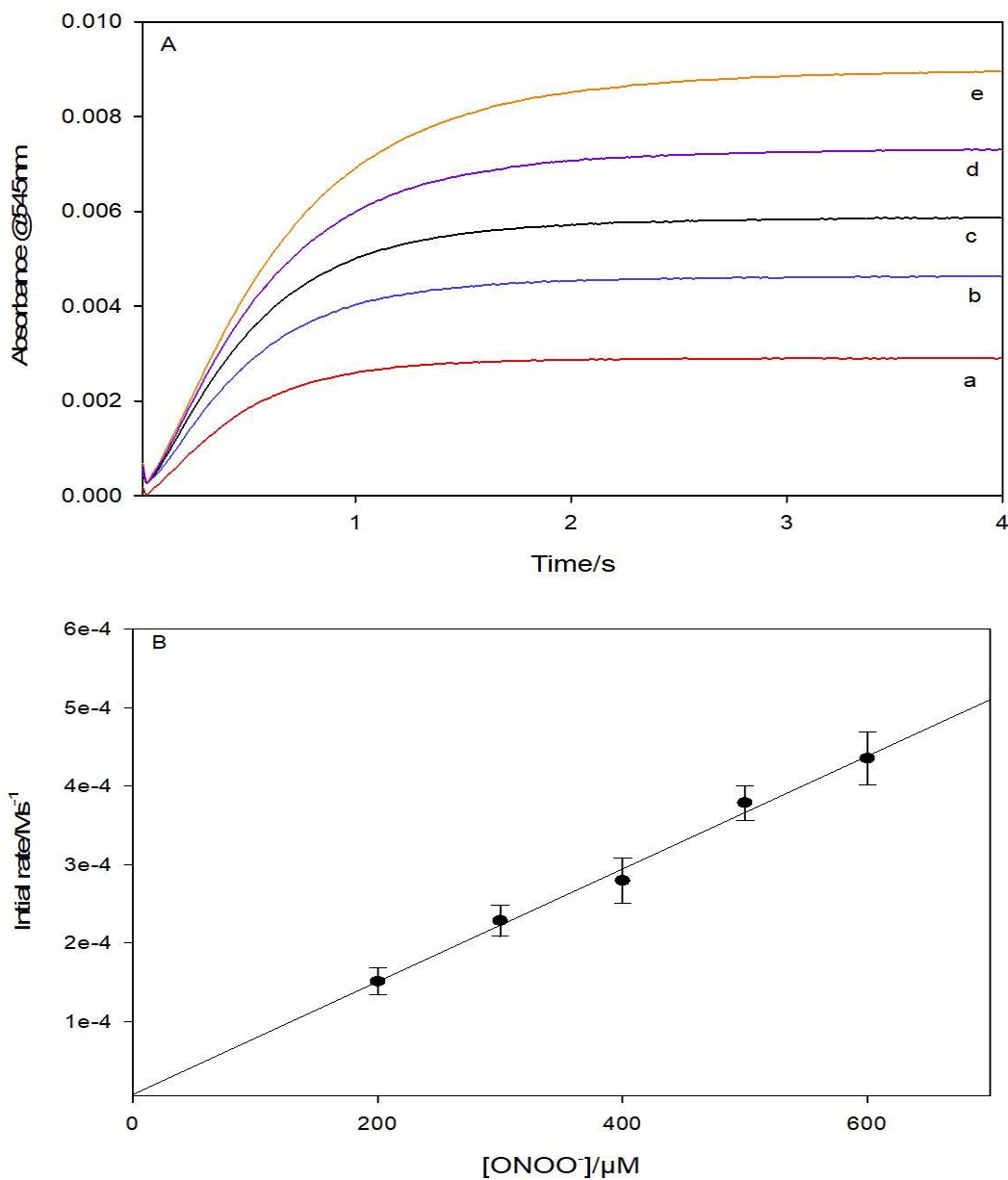
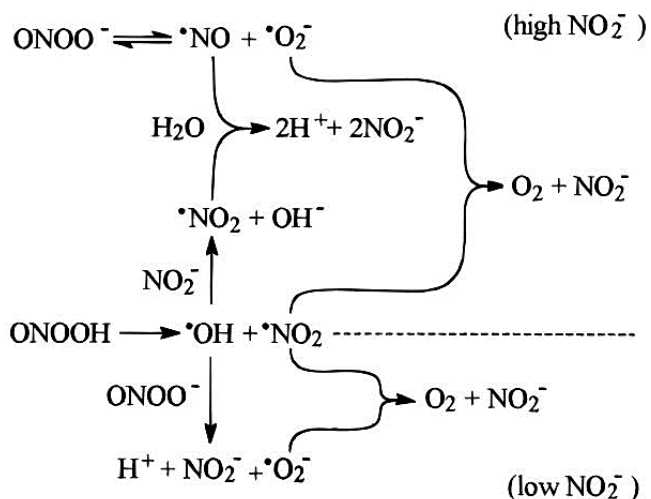


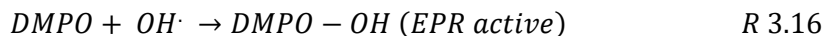
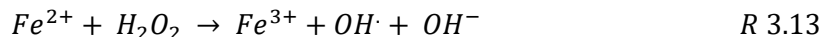
Figure 3.13: Effect of varying ONOO⁻ concentrations on AVP(SNO) formation in PBS at pH 7.4. Fixed [EDTA] = 100 μM, [AVP(SH)] = 1 mM. **(A)** Varied [ONOO⁻] = (a) 200 μM, (b) 300 μM, (c) 400 μM, (d) 500 μM, (e) 600 μM. **(B)** Shows linear relationship between initial rates of AVP(SNO) formation and ONOO⁻ concentrations for traces in (A).

To identify oxidizing intermediates, we conducted EPR analysis at pH7.4 where both ONOOH/ONOO⁻ species are known to exist. EPR spectra obtained in Figure 3.14 shows DMPO (spin trap) radical adduct of ONOOH mediated AVP(SH) S-nitrosylation in mildly

acidic media. The Fenton's reaction (R3.13 - R3.16) which is known to generate $\cdot\text{OH}$, was used as a standard to monitor hydroxyl radical production (Fig 3.14A). This trace shows the 1:2:2:1 quartet spectrum with splitting of $a_{\text{N}} = a_{\text{H}} = 14.9 \text{ G}$ which is characteristic of DMPO-OH radical adduct²⁰¹.



Scheme 3.1: O_2 and NO_2^- production during ONOO^- decomposition



Trace (B) in Fig 3.14 shows a mixture of DMPO and ONOO^- without AVP(SH) with no signal. Addition of increasing amount of AVP(SH) in traces (C)-(E) shows an increase in DMPO-OH radical adduct formation depicted by a stronger signal intensity with a 1:2:2:1 quartet with splitting of $a_{\text{N}} = 15.4 \text{ G}$; $a_{\text{H}} = 16.2 \text{ G}$. Addition of mannitol (a well-known $\cdot\text{OH}$ scavenger), resulted in total signal loss (Fig 3.14F), which is conclusive evidence of

hydroxyl radical production during ONOO⁻ mediated AVP(SNO) formation.

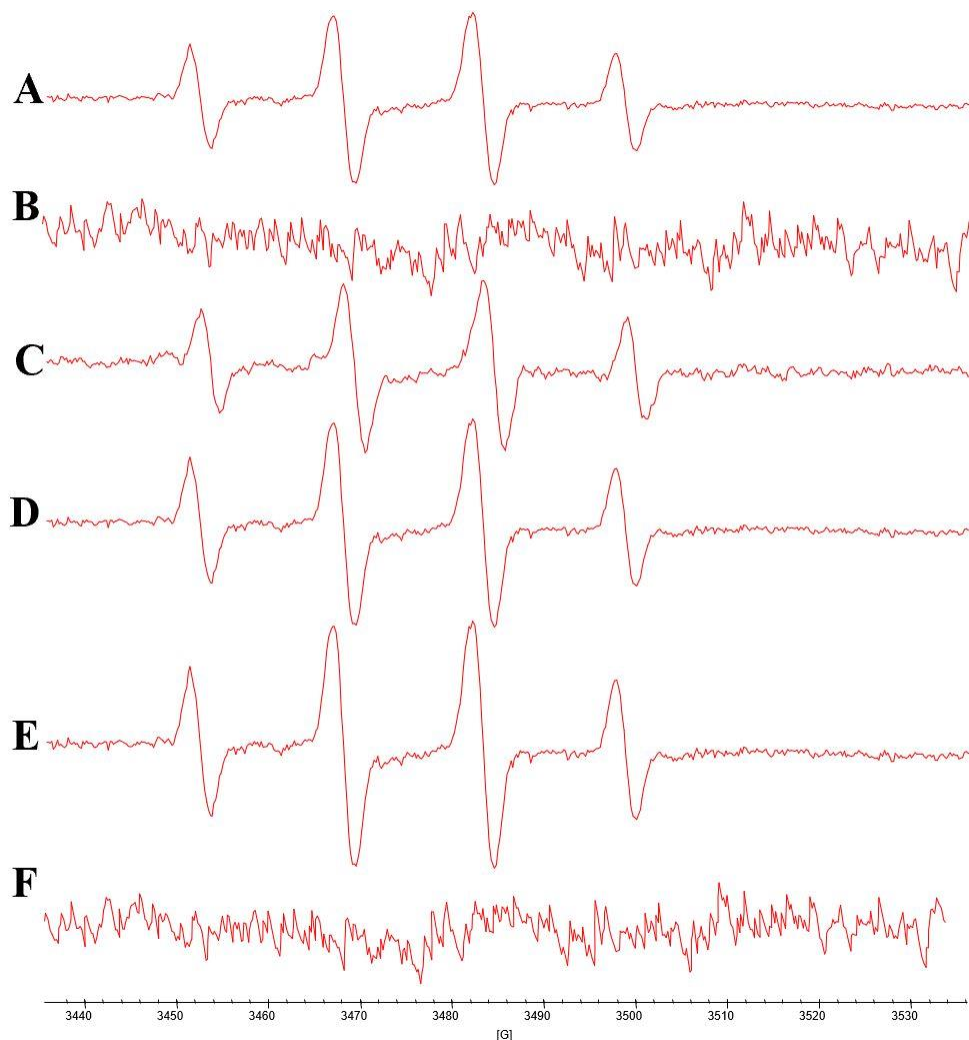


Figure 3.14: EPR spectra of DMPO radical adducts ONOO⁻ mediated AVP(SNO) formation at pH 7.4. Spectra was collected immediately upon mixing reactants at room temperature. **(A)** Fenton's reaction; [H₂O₂] = 0.1M, [FeSO₄] = 0.025M, [DMPO]= 50 mM. Spectra **(B-F)** had fixed [ONOO⁻] = 1 mM and [DMPO]= 50 mM. **(B)** [AVP(SH)] = 0 M, **(C)** [AVP(SH)] = 300 μM, **(D)** [AVP(SH)] = 500 μM, **(E)** [AVP(SH)] = 700 μM. **(F)** [AVP(SH)] = 700 μM and [Mannitol]= 1.5 mM

We also probed the formation of NO[•] by ONOO⁻ reactions with AVP(SH) as an intermediate during AVP(SNO) formation and decomposition using EPR and nitroethane as a spin trap. The EPR spectra was similar to Fig 3.9 and that proves the release of NO radicals upon decomposition of AVP(SNO). Our data is in agreement with earlier

studies²⁰²⁻²⁰³ where injection of ONOO⁻ into buffer solutions containing thiols within the reaction vessel of a chemiluminescence analyzer also resulted in NO[•] production. Onset of NO[•] formation was only detected after the reaction of ONOO⁻ with AVP(SH) was complete (after 10s). Since no NO[•] formation was detected prior to the addition to AVP(SH), our data suggests that ONOO⁻ decomposition itself at pH 7.4 does not produce NO[•] (Scheme 3.1) within the time scale of our experiments. Signal intensity of NO[•] production gradually increased with time for over 2 min until no further change was observed. This suggests that AVP(SNO) slowly decomposes to release NO[•], which would make it a good NO carrier and donor. The reported stabilities of RSNOs varies widely, with primary and secondary RSNOs being commonly reported to be highly unstable, with half-lives of seconds to minutes²⁰⁴.

3.2.3.4 Temperature dependence and thermodynamic parameters. Using methods described in section 3.2.2.5. We ran traces from Figures 3.11 and 3.13 in pseudo-1st-order conditions with at least 10-fold excess (10-55 mM) of ONOOH and ONOO⁻ respectively in temperatures ranging from 15-35 °C. The observed k_{obs} rates for ONOOH mediated S-nitrosylation spectral results were plotted against [ONOOH], with varied [ONOOH] concentrations at each temperature (Fig 3.15A) and derived k_{obs} values from Table 3.4. We observed an approximately 2-fold increase in AVP(SNO) formation with every 10 °C rise in temperature. These k_{obs} rates were 2-orders of magnitude greater than those for HNO₂/NO⁺ mediated nitrosation reactions. The corresponding Eyring plots for k_{on} and k_{off} are shown in Figures 3.15B and 3.15C respectively. The slope and intercept values were used to calculate thermodynamic parameters; for k_{on} as $E_a = 24.9 \text{ kJmol}^{-1}$ (Eq 9); $\Delta H_{\text{on}}^{\ddagger} =$

42.6 kJ mol⁻¹ and $\Delta S^\ddagger_{\text{on}} = -53.7 \text{ J mol}^{-1} \text{ K}^{-1}$; for k_{off} these are $E_a = 34.8 \text{ kJmol}^{-1}$; $\Delta H^\ddagger_{\text{off}} = 33.3 \text{ kJ mol}^{-1}$ and $\Delta S^\ddagger_{\text{off}} = 62.1 \text{ J mol}^{-1} \text{ K}^{-1}$ (Table 3.5).

ONOOH is a more robust nitrosating agent than its conjugate base, as it is kinetically and thermodynamically favorable as evidenced by the larger k_{obs} values and E_a , ΔH^\ddagger and ΔG^\ddagger values. Data from k_{obs} rates for ONOO⁻ mediated S-nitrosylation reactions (Fig 3.16A) and the derived k_{on} and k_{off} values (Table 3.6), shows a slow reaction with k_{obs} rates at least 3-orders of magnitude less than those for ONOOH.

Table 3.4: ONOOH mediated AVP thiol S-nitrosylation k_{on} and k_{off} values.

Temp (°C)	$k_{\text{on}} (\text{M}^{-1}\text{s}^{-1})$	$k_{\text{off}} (\text{s}^{-1})$
15	186 ± 18	10049 ± 561
20	242 ± 27	10661 ± 918
25	340 ± 36	14133 ± 886
30	465 ± 30	17114 ± 1195
35	616 ± 51	26815 ± 1627

Table 3.5: ONOOH mediated AVP thiol S-nitrosylation thermodynamic parameters.

	E_a^a	ΔG^\ddagger^b	ΔH^\ddagger^c	ΔS^\ddagger^d
k_{on}				
	24.9	26.0	42.6	-53.7
k_{off}				
	34.8	16.8	33.3	62.1

^{a, b and c} Values are in kJ/mol, whilst ^d values are in J.mol⁻¹K⁻¹. Temperature = 37°C ^b

With the following thermodynamic parameters; for k_{on} as $E_a = 75.4 \text{ kJmol}^{-1}$; $\Delta H^\ddagger_{\text{on}} = 77.2 \text{ kJ mol}^{-1}$ and $\Delta S^\ddagger_{\text{on}} = -13.8 \text{ J mol}^{-1} \text{ K}^{-1}$; and for k_{off} as $E_a = 44.8 \text{ kJmol}^{-1}$; $\Delta H^\ddagger_{\text{off}} = 42.3 \text{ kJ mol}^{-1}$ and $\Delta S^\ddagger_{\text{off}} = 84.1 \text{ J mol}^{-1} \text{ K}^{-1}$ (Table 3.7). As established earlier, acid catalyzes

AVP(SNO) formation. Therefore, we propose that the nitrosating agent HNO₂, which is produced as a result of ONOOH decomposition in acidic media (Scheme 3.1), adds to the nitrosating power of ONOOH over its conjugate base.

Table 3.6. Observed rate constants for ONOO⁻ mediated AVP thiol S-nitrosylation reactions.

Temp (°C)	k_{on} (M ⁻¹ s ⁻¹)	k_{off} (s ⁻¹)
15	0.0882 ± 0.01	6.7 ± 0.2
20	0.107 ± 0.01	11.04 ± 0.22
25	0.112 ± 0.005	12.8 ± 0.12
30	0.45 ± 0.04	19.5 ± 1.41
35	0.56 ± 0.06	22.9 ± 1.9

Table 3.7. Thermodynamic parameters for ONOO⁻ mediated AVP thiol S-nitrosylation reactions.

	Ea ^a	ΔG ^{‡b}	ΔH ^{‡c}	ΔS ^{‡d}
k_{on}				
	75.4	77.2	72.9	-13.8
k_{off}				
	44.8	67.4	42.3	81.4

^a, ^b and ^c Values are in kJ/mol, whilst ^d values are in J.mol⁻¹K⁻¹. Temperature (T) = 37°C

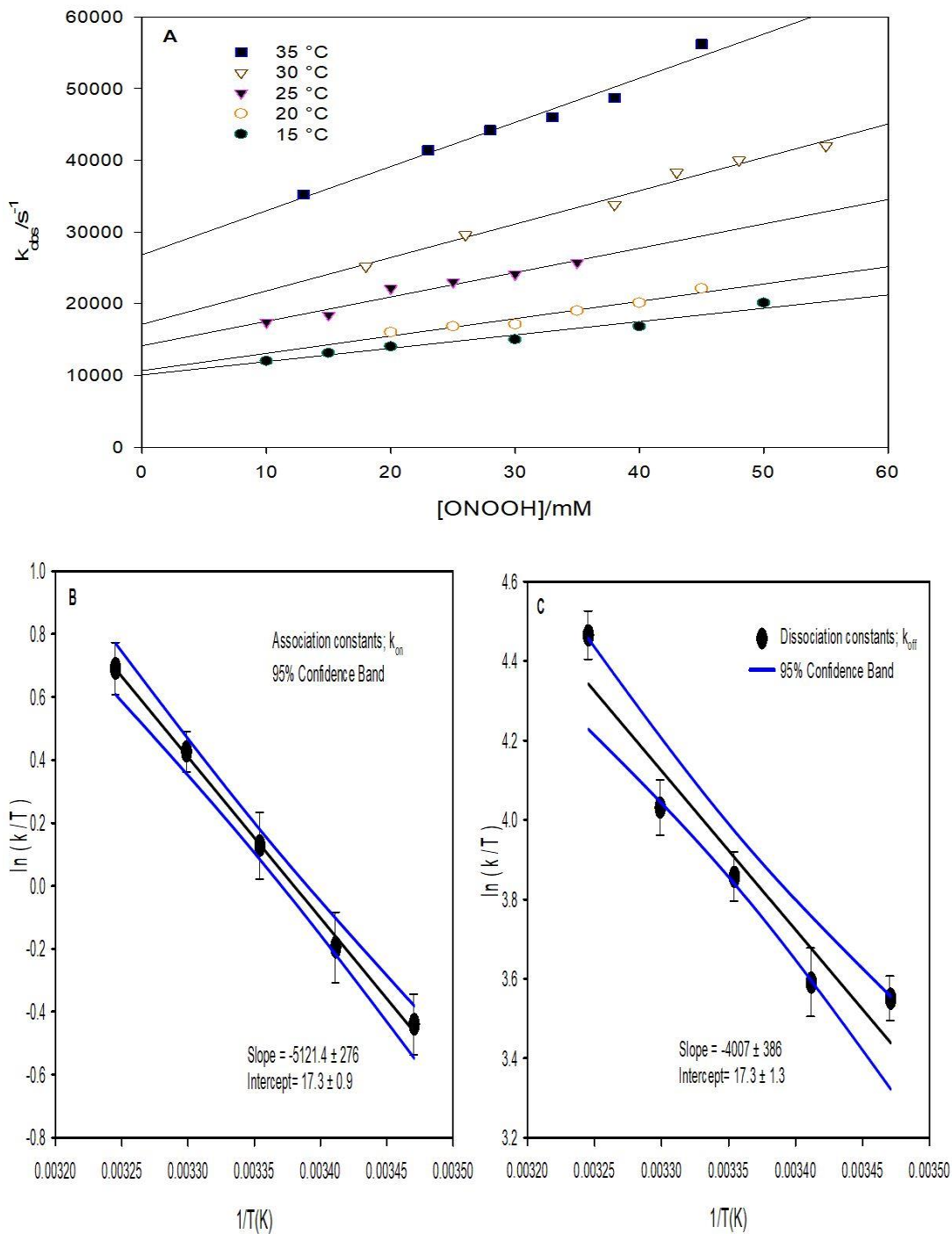


Figure 3.15: (A) Observed rate constants for the S-nitrosylation of AVP(SH) by varied ONOOH concentrations over a broad temperature range of 15-35 °C. Fixed [EDTA] = 100 μ M, [AVP] = 1 mM. Varied [ONOO]: [H⁺] on a 1:1 ratio in the range 10-55 mM. (B) and (C) depict linear Eyring plots from k_{on} and k_{off} values that are stated in Table 3.4 respectively.

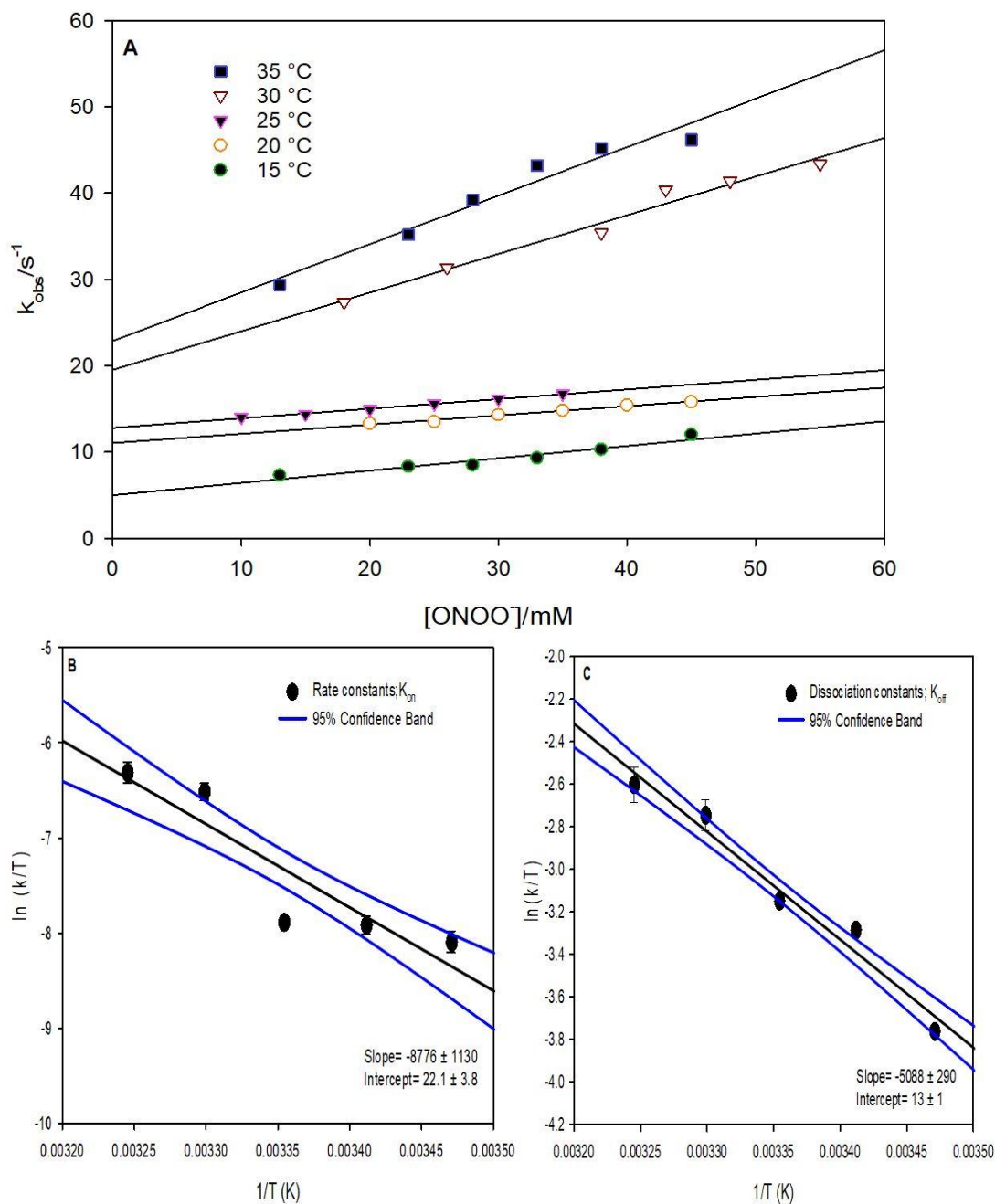


Figure 3.16: (A) Observed rate constants for the S-nitrosylation of AVP(SH) by varied $ONOO^-$ concentrations over a broad temperature range of 15-35 °C in PBS at pH 7.4. Fixed [EDTA] = 100 μM , [AVP] = 1 mM. Varied $[ONOO^-]$ in the range 10-55 mM. (B) and (C) depicts linear Eyring plots from k_{on} and k_{off} values that are stated in Table 7.

3.2.4 SNAP mediated transnitrosation. Transnitrosation is the transfer of NO from an S-nitrosothiol to a thiol thus forming a new S-nitrosothiol species in the process (R3.17). Transnitrosation is prevalent *in vivo* with reported outcomes ranging from altered protein activity to the formation of S-nitrosothiol species that are effective NO carriers²⁰⁵. We investigated AVP(SNO) formation through transnitrosation by SNAP. It's been reported that acid induces high rates of SNAP decomposition²⁰⁶, therefore transnitrosation reactions were conducted only at pH 7.4 in 0.1M phosphate buffer.



3.2.4.1 Effect of AVP(SH) and SNAP variation. The effect of AVP(SH) variation on transnitrosation by SNAP is depicted in Figure 3.17A. Initial rate plots of AVP(SNO) formation (Fig 3.17B) and SNAP decay (Fig 3.18) at 545 and 590 nm respectively, were linear with 1st-order dependence in AVP(SH) concentrations. We also probed the effect of SNAP variation on AVP(SNO) formation (Fig 3.19) and depletion of SNAP (Fig 3.20). As anticipated, transnitrosation rates increased with increments in SNAP concentrations (Fig 3.19A) with linear rate plots depicting 1st-order dependence in SNAP concentrations for AVP(SNO) formation and SNAP depletion (Fig 3.19B and Fig 3.20B) respectively. The zero-intercepts on these rate plots, suggests that there are no other competing reactions with regards to either AVP(SNO) formation or SNAP depletion besides the direct fiduciary transnitrosation reaction.

From kinetic data in Figures 3.17-3.20, we derived Eq 3.12, which depicts the rate of SNAP depletion as a function of [AVP(SH)] and we evaluated the bimolecular rate constant for AVP(SH) S-nitrosylation by SNAP to be $233 \pm 7 \text{ M}^{-1} \text{ s}^{-1}$.

$$\frac{-d[\text{SNAP}]}{dt} = \frac{k_f(K_{\text{AVP}(\text{SH})}[\text{AVP}(\text{SH})]_t)}{(K_{\text{AVP}(\text{SH})} + H^+)} [\text{SNAP}] \quad \text{Eq 3.12}$$

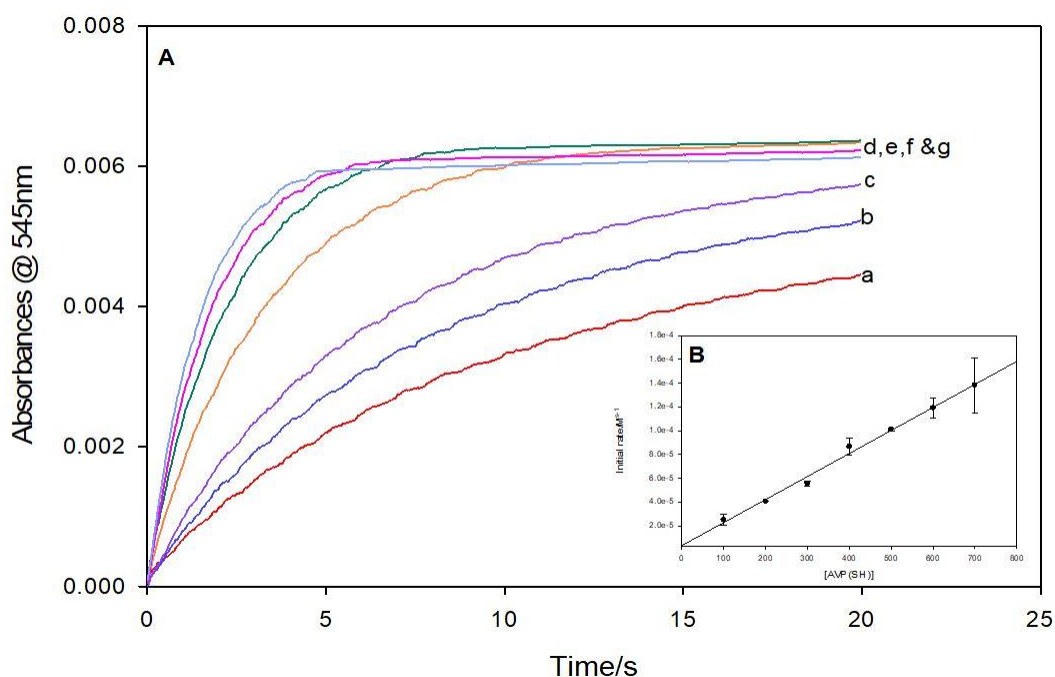


Figure 3.17: (A) Effect of varying AVP(SH) concentrations on SNAP mediated AVP(SNO) formation in PBS at pH 7.4. Fixed [EDTA] = 100 μM , [SNAP] = 1 mM. (A) Varied [AVP(SH)] = (a) 100 μM , (b) 200 μM , (c) 300 μM , (d) 400 μM , (e) 500 μM , (f) 600 μM , (g) 700 μM . (B) Shows linear relationship between initial rates of AVP(SNO) formation and AVP(SH) concentrations for traces in (A).

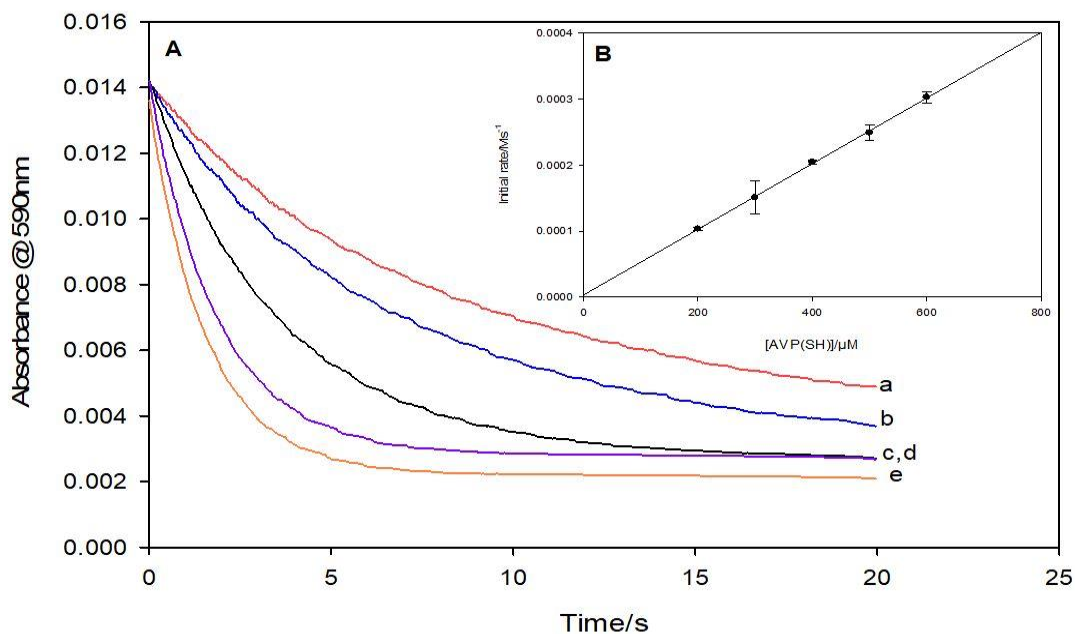


Figure 3.18: (A) Effect of varying AVP(SH) concentrations on SNAP depletion in PBS at 590 nm and pH 7.4. Fixed [EDTA] = 100 μM , [SNAP] = 1 mM. (A) Varied [AVP(SH)] = (a) 200 μM , (c) 300 μM , (d) 400 μM , (e) 500 μM , (f) 600 μM . (B) Shows linear relationship between initial rates of SNAP depletion and AVP(SH) concentrations for traces in (A).

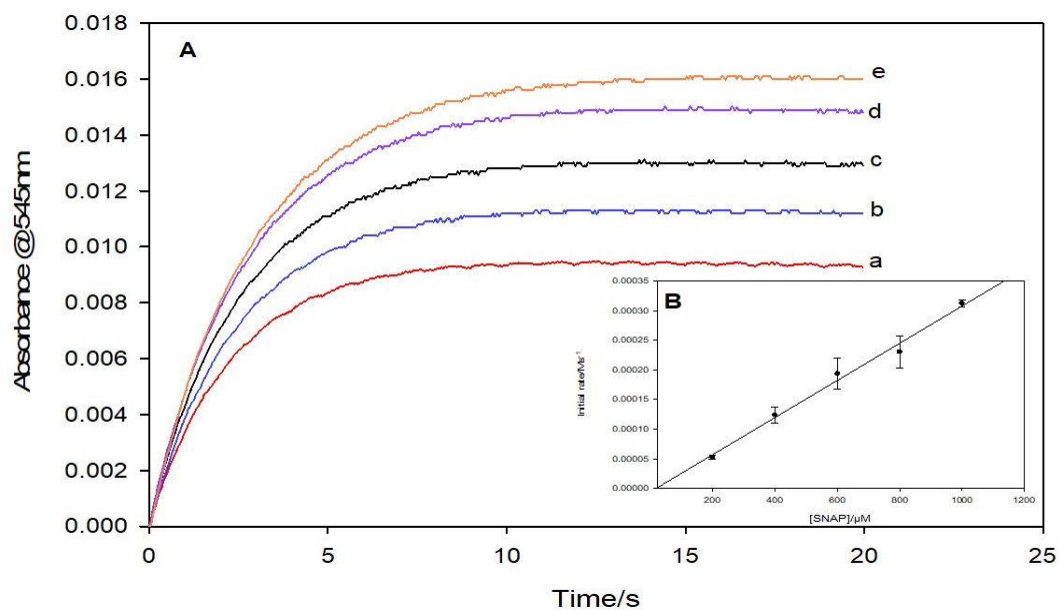


Figure 3.19: (A) Varying SNAP concentrations and AVP(SNO) formation in PBS at pH 7.4. Fixed [EDTA] = 100 μM , [AVP(SH)] = 1 mM. (A) Varied [SNAP] = (a) 200 μM , (b) 400 μM , (dc) 600 μM , (d) 800 μM , (e) 1 mM. (B) Shows linear relationship between initial rates of AVP(SNO) formation and [SNAP] concentrations for traces in (A).

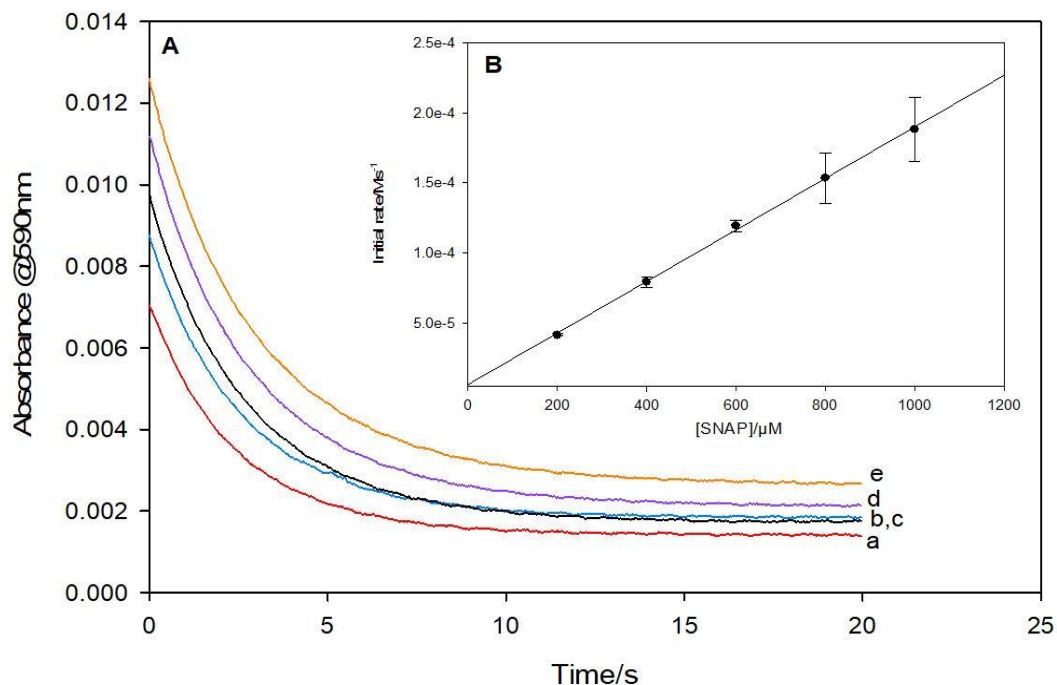
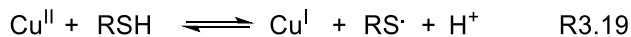
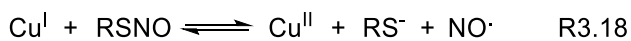
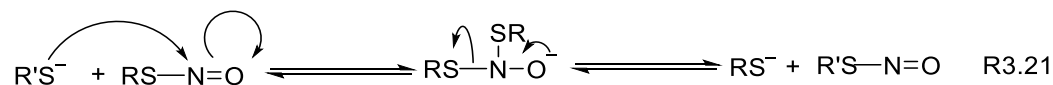


Figure 3.20: (A) Varying SNAP concentrations and SNAP depletion at 590 nm in pH 7.4 PBS. Fixed [EDTA] = 100 μM, [AVP(SH)] = 400 μM. (A) Varied [SNAP] = (a) 600 μM, (c) 700 μM, (d) 800 μM, (e) 900 μM. (B) Rate plot depicts a linear relationship between SNAP depletion initial rates and AVP(SH) concentrations for traces in (A).

The mechanism by which SNAP transfers its NO moiety to other thiols *in vivo* is still disputed. An interaction between copper and thiols in the catalysis of NO transfer has been implicated as a possible mechanism. Studies have shown that RSNO formation by protein thiols in hemoglobin and calbindin requires copper (R3.18 – R3.20)²⁰⁷⁻²⁰⁸, and is inhibited in the presence of copper chelators.



Our results suggest that transfer of NO from RSNO to thiols is a direct process without the formation of free NO as an intermediate²⁰⁹. Nucleophilic attack of the thiolate ion (RS⁻) on the nitrogen atom of RSNO is proposed to be fast and facile under physiological conditions, as well as being insensitive to copper and other transition metal ions (R3.21).



In this mechanism, the thiol pK_a is critical factor. In peptides and proteins, the pK_a values of thiols vary greatly depending on their microenvironment, so some thiols may be more susceptible to transnitrosation than others.

3.2.4.2 SNAP temperature dependence and thermodynamic parameters. Using methods described in section 3.2.2.5 we ran traces from Fig 3.19 in excess SNAP (10-55 mM), the observed k_{obs} rates for SNAP mediated S-nitrosylation were plotted against [SNAP] at each temperature (Fig 3.21A) and the derived k_{obs} values stated in Table 3.8. We observed an approximately 2-fold increase in AVP(SNO) formation with each 10 °C increment in temperature. These k_{obs} rates were 1 and 2-orders of magnitude greater than those for HNO₂/NO⁺ and ONOO⁻ mediated nitrosation reactions respectively. In comparison to ONOOH, they were an order of magnitude lower.

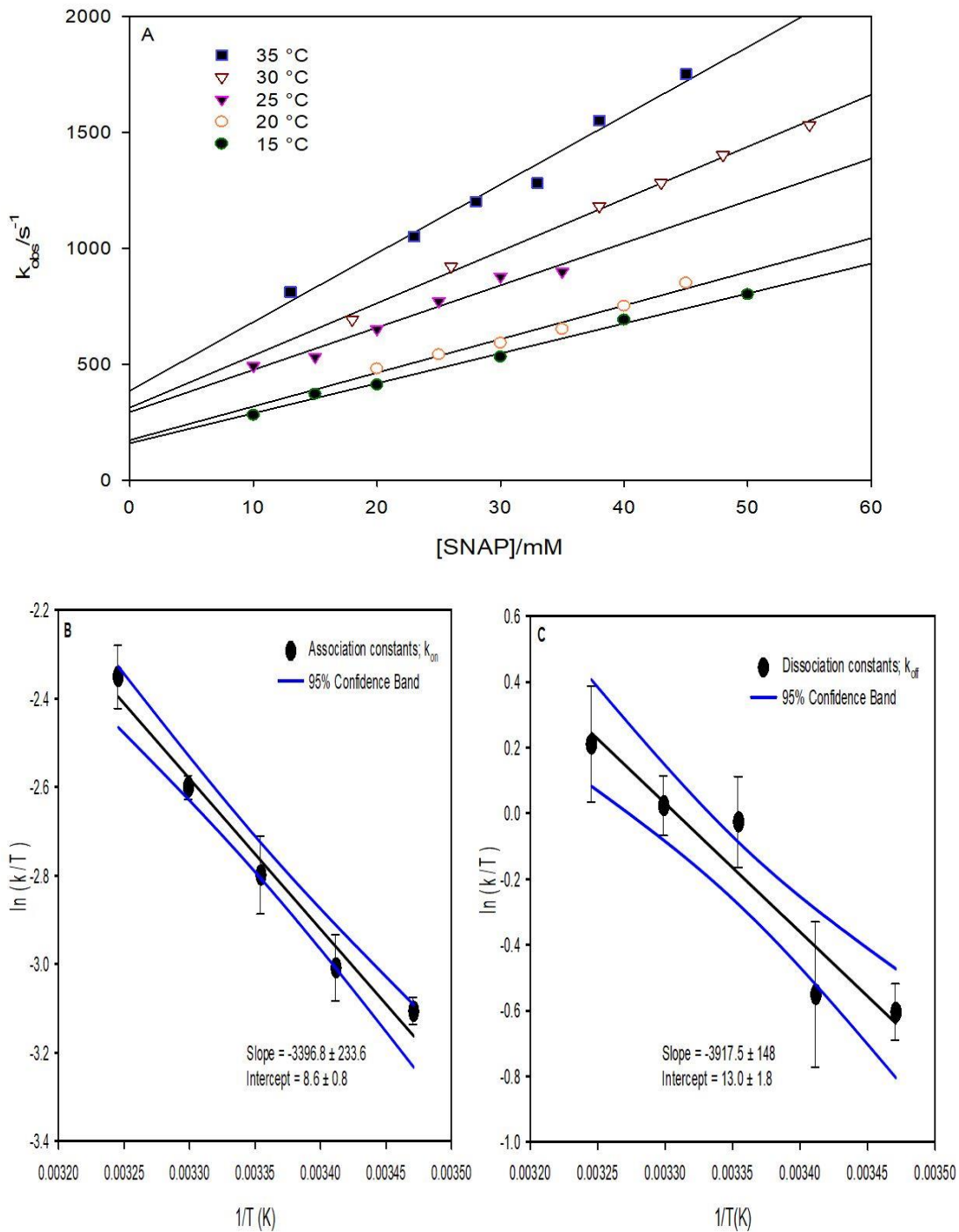


Figure 3.21: (A) k_{obs} values for AVP(SNO) formation obtained by varying temperature and SNAP concentrations in pH 7.4 PBS. Fixed [EDTA] = 100 μ M, [AVP] = 1 mM. Varied [SNAP] in the range 10-55 mM. (B) and (C) depicts linear Eyring plots from k_{on} and k_{off} values that are stated in Table 3.8.

The corresponding Eyring plots for k_{on} and k_{off} are shown in Figures 3.21B and 3.21C respectively. Derived thermodynamic parameters were for k_{on} are $E_a = 30.7 \text{ kJmol}^{-1}$; $\Delta H^\ddagger_{\text{on}} = 28.2 \text{ kJ mol}^{-1}$ and $\Delta S^\ddagger_{\text{on}} = -320 \text{ J mol}^{-1} \text{ K}^{-1}$; for k_{off} are $E_a = 35.1 \text{ kJmol}^{-1}$; $\Delta H^\ddagger_{\text{off}} = 32.6 \text{ kJ mol}^{-1}$ and $\Delta S^\ddagger_{\text{off}} = -288.6 \text{ J mol}^{-1} \text{ K}^{-1}$) (Table 3.9). The highly negative activation entropy suggests a rate-limiting transnitrosylation step comprising of an ordered associative transition state (R3.21). These activation parameters suggest low energy barriers for transnitrosylation under physiological conditions and support growing evidence that transnitrosylation maybe a viable posttranslational mechanism for NO transport *in vivo*²¹⁰.

Table 3.8: Observed rate constants for SNAP mediated AVP thiol S-nitrosylation reactions.

Temp (°C)	$k_{\text{on}} (\text{M}^{-1}\text{s}^{-1})$	$k_{\text{off}} (\text{s}^{-1})$
15	12.9 ± 0.4	157.8 ± 13.5
20	14.5 ± 1.1	171.7 ± 37.3
25	18.2 ± 1.6	292.30 ± 40
30	22.5 ± 0.6	311 ± 28
35	29.4 ± 2.1	384.1 ± 67.1

Table 3.9: thermodynamic parameters for SNAP mediated AVP thiol S-nitrosylation.

	E_a^a	ΔG^\ddagger^b	ΔH^\ddagger^c	ΔS^\ddagger^d
k_{on}				
	30.7	21.5	28.2	-320.0
k_{off}				
	35.1	29.9	32.6	-288.6

a, b and c Values are in kJ/mol, whilst d values are in $\text{J}\cdot\text{mol}^{-1}\text{K}^{-1}$. Temperature = 37°C b

3.3 Conclusion. Our study evaluated the effects of pH, copper chelators and temperature on the rate of AVP thiol autoxidation. We discovered that AVP thiols have half-lives sufficient for subsequent S-nitrosylation reactions to occur. The temporarily reduction of AVP(S-S) to AVP(SH) and the stability of AVP(SH) suggests a likelihood for novel signaling mechanisms. Since thioredoxin (Trx) is known to increase the rate of NADPH regeneration *in vitro* in the presence of the neurohypophysial peptide oxytocin, we propose that Trx and similar proteins may produce AVP(SH) *in vivo* ²¹¹⁻²¹². Even though high cellular concentrations of glutathione would promote AVP(S-S) reformation there are still several mechanisms within cells that could inhibit or slow down AVP(S-S) reformation. The chemical modifications of AVP(S-S) to produce AVP(SH) and AVP(SNO) thus promoting site-specific modulation of AVP functions. S-Nitrosylation of AVP(SH) gave both singly and doubly S-nitrosylated AVP(SNO). Nitrous acid and nitrosonium mediated AVP(SNO) formation were shown to be rapid in acidic media with low and positive activation parameters for ΔG^\ddagger and ΔH^\ddagger for both k_{on} and k_{off} . Thermodynamic data suggests an associative mechanism for k_{on} and a dissociative mechanism for k_{off} as shown by negative and positive ΔS^\ddagger values respectively. Kinetic and EPR analysis implicated copper redox cycling between Cu^{2+} and Cu^+ in catalyzing AVP(SNO) formation and decomposition respectively. Therefore, we propose that AVP(SNO) formation and half-lives *in vivo* would be largely dependent on cellular concentrations of copper ions and possibly other transition metal ions. The reactions of AVP(SH) and ONOO⁻/ONOOH showed a complex dependence of acid concentrations with lower bimolecular rates at physiological pH. Our data suggests that ONOOH is a more robust nitrosating agent than it's conjugate base with higher bimolecular rate constants and lower activation energy. We

propose that ONOO⁻/ONOOH mediated AVP(SNO) formation might be a potential peroxynitrite detoxifying pathway. EPR analysis revealed hydroxyl radical production in thiol reactions with ONOO⁻/ONOOH and NO radical release during AVP(SNO) decomposition. Hydroxyl radical production can lead to oxidative stress and radical induced damage that has been linked to various disease pathologies²¹³. The release of NO during AVP(SNO) decomposition suggests a role as an NO carrier and donor. It is feasible that AVP(SNO) could modify AVP receptors leading to modifications in major signaling pathways. There is already evidence of reversible SNO mediated trans-S-nitrosylation of free cysteines on G protein-coupled receptors, which can alter signaling pathways²¹⁴⁻²¹⁵. Our results show that AVP(SH) trans-S-nitrosylation reactions are both kinetically and thermodynamically favorable with highly negative activation entropies that are typical of associative transition states. These activation parameters suggest low energy barriers for transnitrosylation under physiological conditions and support growing evidence that transnitrosylation maybe a viable post-translational mechanism for NO transport *in vivo*.

CHAPTER 4: KINETICS AND ENERGETICS OF S-NITROSO-SOMATOSTATIN FORMATION

4.1 INTRODUCTION.

Somatostatin (SST) is a neuropeptide that inhibits the release of various hypothalamic hormones and coordinates regulatory activities with inhibitory neurotransmitter gamma-aminobutyric acid (GABA) in the CNS^{216 217}. The SST gene expresses two active forms; somatostatin-14 (SST-14) which has 14 amino-acid residues and somatostatin-28 (SST-28) that comprises of 28 amino-acid residues²¹⁸. Reports of NO production from neuronal NOS and nicotinamide adenine dinucleotide phosphate diaphorase (NADPH-d) which are both co-localized with SST in the CNS suggest the possibility of novel neurochemical signaling mechanisms²¹⁹⁻²²⁰. Stimulation of SST receptors in human retinal pigment epithelial (RPE) cells is linked to elevated NO production which confers restorative effects on damaged blood-retina barriers (BRB)²²¹⁻²²². SST thiol and disulfide exchange rates with other abundant biological thiols like glutathione are rapid and there constant inter and intra-molecular exchange reactions that often involve the formation of mixed disulfides²²³.

Despite growing evidence of SST mediated regulation of NO and numerous reports of SST thiol reactions with other biologically relevant thiols, little is known about NO-mediated SST modifications. This chapter explores kinetic and thermodynamic parameters of SST-14 thiol S-nitrosylation reactions.

4.2 RESULTS AND DISCUSSION

4.2.1 SST-14 dithiol formation and stability. To establish whether the SST-14 thiol has half-lives sufficient for subsequent S-nitrosylation reaction under physiologically relevant conditions, SST-14 disulfide reduction was carried out using methods described in section 3.2.1. The extinction coefficients of SST-14 disulfide and thiol at 280 nm were determined to be $5750 \text{ M}^{-1}\text{cm}^{-1}$ and $5500 \text{ M}^{-1}\text{cm}^{-1}$ respectively (Eq 4.1). Chromatogram (A) was a standard sample of $35 \mu\text{M}$ SST-14 disulfide which was eluted at 1.87 mins (Fig. 4.1). Chromatogram (B) shows the reaction product of incubating $10\mu\text{M}$ SST-14 disulfide for 30 minutes in $400 \mu\text{M}$ TCEP (40-fold excess), the product was eluted at 2.03 mins. Mass spectrometry analysis of chromatogram (A), shows SST-14 disulfide with singly protonated $(\text{M}+\text{H})^+$ ions at m/z 1638.7 and the doubly protonated $(\text{M}+2\text{H})^{2+}$ ions at m/z 820.4 (Fig 4.2A). ESI-MS identified chromatogram (B) as singly protonated $[(\text{M}+\text{H})^+]$ thiol at m/z 1639.7 and the doubly protonated $[(\text{M}+2\text{H})^{2+}]$ thiol at m/z 820.4 (Fig. 4.2B).

$$\epsilon_{280} = (\# \textit{Tryptophan} \times 5500) + (\# \textit{Cysteine} \times 125) \quad \text{Eq 4.1}$$

We then probed SST-14 thiol stability by monitoring the rate of SST-14 disulfide reformation at varying temperatures, pH and in the presence of copper chelators using HPLC chromatograms and equation 3.1.

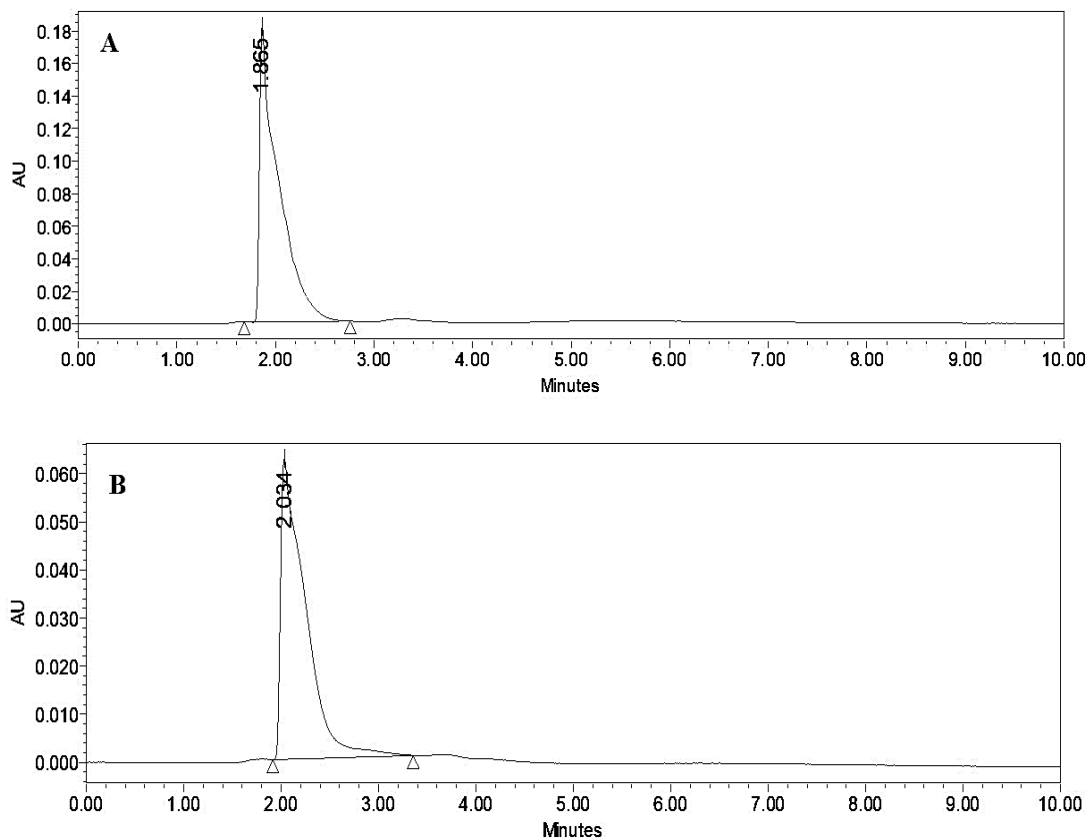


Figure 4.1: HPLC-UV analysis of SST-14 disulfide reduction. (A) A chromatogram of 35 μM SST-14 disulfide was run as a standard, which was eluted at 1.87 mins. (B) 10 μM AVP SST-14 thiol in pH 3 water was incubated for 30 minutes in 400 μM TCEP (40-fold excess), the product was eluted at 2.03 mins.

The time course reformation of SST-14 disulfide is summarized in Table 4.1. Our data suggests that SST-14 thiol autoxidation occurs without a catalyst in acidic media. An increase in temperature from 25-50 $^{\circ}\text{C}$ in acidic media markedly increased the rate of autoxidation by 6-fold. Disulfide reformation rates also increased under mild oxidizing conditions (pH 7.4), indicating the potential participation of the thiolate species in the reaction. As expected, the introduction of copper chelators at pH 7.4 had a large inhibitory effect on disulfide reformation. A comparison between AVP and SST-14 disulfide

reformation rates highlights the difference in reactivities according to the peptide sequence, hydrophobicity and electronic environment which determine access to thiol groups and affects respective reaction rates²²⁴. The half-life of SST-14 thiol at pH 7.4 and 37 °C was determined to be 44 mins under physiological conditions.

Table 4.1. Effects of temperature, pH and copper chelators on time for SST-14 disulfide reformation.

Temperature	Time for disulfide reformation (>95%)		
	Water pH 3.0	30mM PBS, pH 7.4	30mM PBS, pH 7.4 + chelators
25°C	236hrs	104mins	37.7hrs
37°C	87hrs	44mins	14.9hrs
50°C	34.7hrs		

4.2.2 Nitrous acid mediated S-nitrosylation.

4.2.2.1 Effect of SST-14(SH) variation. A 1:1 ratio of $[H^+]_0$: $[NO_2^-]_0$ was used to probe the effects of SST-14(SH) concentrations on SST-14(SNO) rates formation. We observed a linear increase in the rates of SST-14(SNO) formation with gradual increments in SST-14(SH) concentrations (Fig 4.3A) for as long as suboptimal SST-14(SH) concentrations were used. Rate plots in Figure 4.3B depicts 1st-order dependence of SST-14(SNO) formation on [SST-14(SH)].

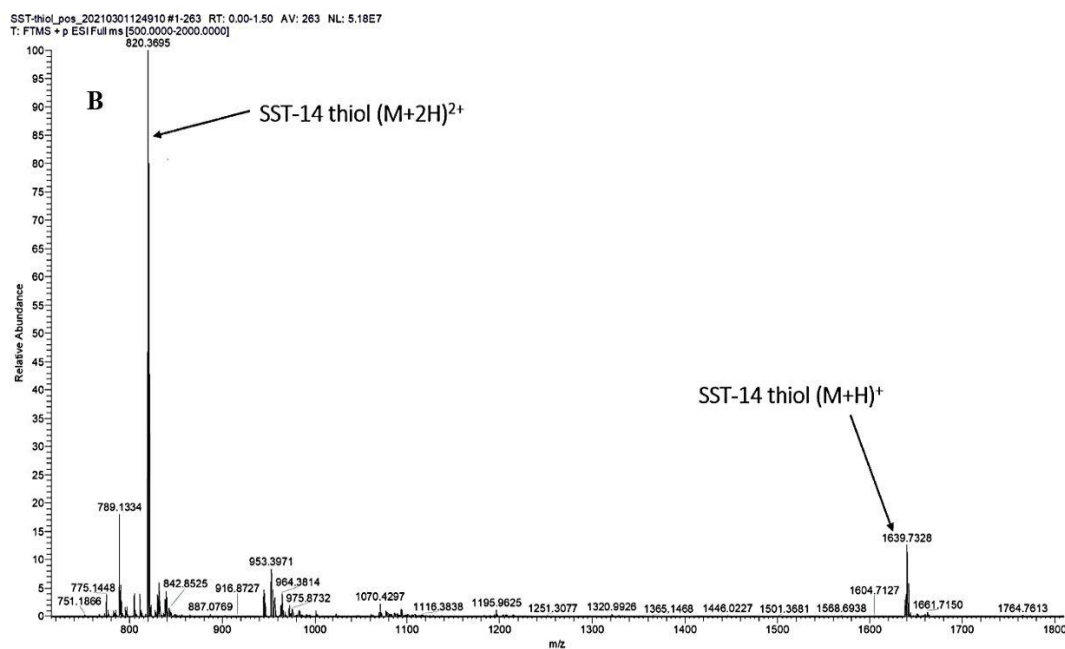
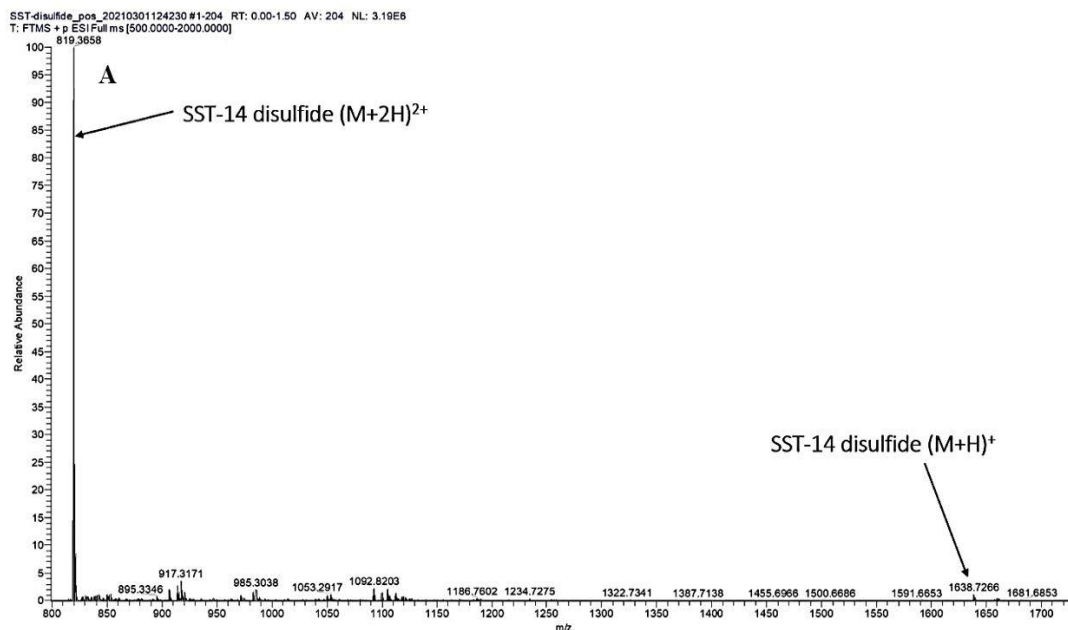


Figure 4.2: ESI-MS analysis of HPLC chromatograms Fig 29. (A) ESI mass spectra confirmed chromatogram A as SST-14 disulfide. (B) ESI mass spectra confirms chromatogram B as SST-14 thiol.

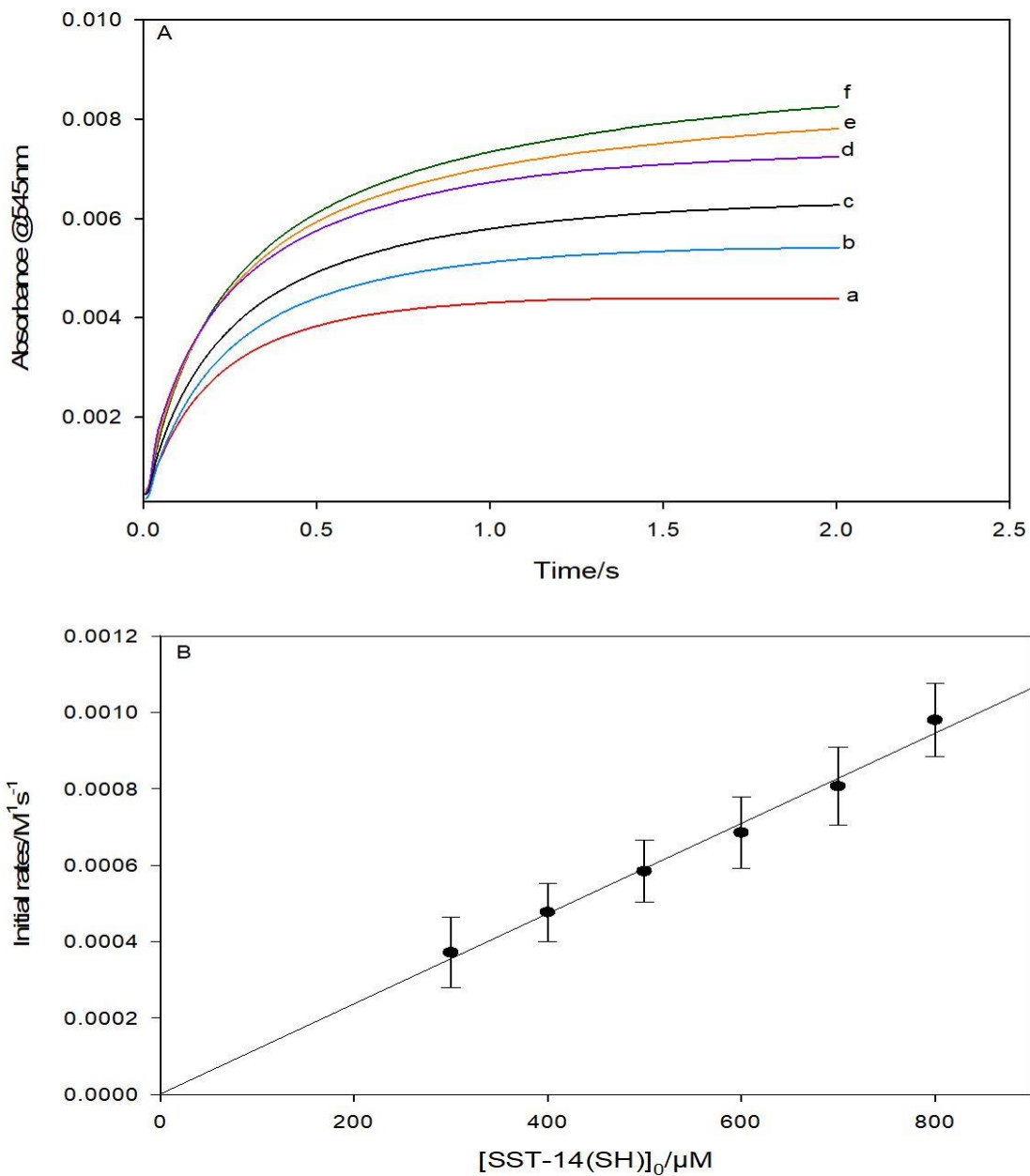


Figure 4.3: 1st-order dependence SST-14(SNO) formation in SST-14(SH) concentrations. (A) Effect of varying SST-14(SH) concentrations on SST-14(SNO) formation at 25 °C. Fixed $[\text{NO}_2^-] = 1 \text{ mM}$, $[\text{EDTA}] = 100 \text{ }\mu\text{M}$, $[\text{H}^+] = 1 \text{ mM}$. Varied $[\text{SST-14(SH)}] = (\text{a}) 300 \text{ }\mu\text{M}$, $(\text{b}) 400 \text{ }\mu\text{M}$, $(\text{c}) 500 \text{ }\mu\text{M}$, $(\text{d}) 600 \text{ }\mu\text{M}$, $(\text{e}) 700 \text{ }\mu\text{M}$, $(\text{f}) 800 \text{ }\mu\text{M}$. (B) Initial rate plots with respect to $[\text{SST-14(SH)}]_0$ concentrations show a linear plot which indicates a strong dependence of SST-14(SNO) formation on SST-14(SH) concentrations. ddd

4.2.2.2 Effect of nitrite variation. Nitrite variation also gave is simple and 1st-order kinetics (Fig 4.4) as long as $[\text{NO}_2^-]_0$ do not exceed $[\text{H}^+]_0$, therefore all RNS where form of protonated HNO_2 .

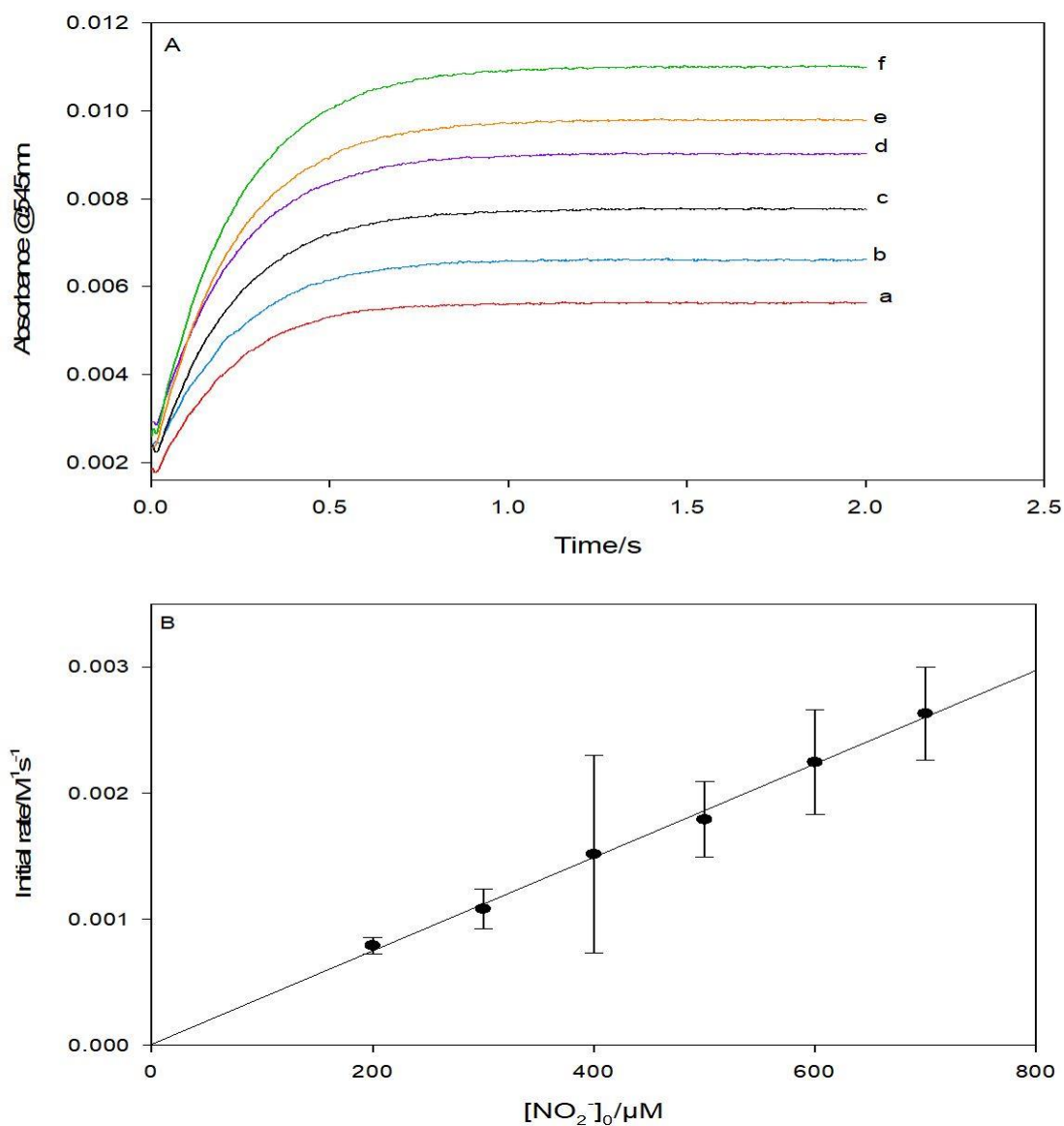


Figure 4.4: (A) Effect of varying $[\text{NO}_2^-]$ concentrations on SST-14(SNO) formation at 25 °C. Fixed $[\text{SST-14(SH)}] = 1 \text{ mM}$, $[\text{EDTA}] = 100 \mu\text{M}$, $[\text{H}^+] = 1 \text{ mM}$. Varied $[\text{NO}_2^-] =$ (a) 200 μM , (b) 300 μM , (c) 400 μM , (d) 500 μM , (e) 600 μM , (f) 700 μM . (B) Rate plot shows 1-st order dependence of SST-14(SNO) formation on $[\text{NO}_2^-]_0$ concentrations.

4.2.2.3 Effect of acid variation. Acid variation is complex (Fig 4.5). The data involves a range of acid concentrations ranging from $[\text{H}^+]_0 < [\text{NO}_2^-]_0$ to $[\text{H}^+]_0 \geq [\text{NO}_2^-]_0$. When $[\text{NO}_2^-]_0 \geq [\text{H}^+]_0$, HNO_2 concentrations are limited which results in slower rates of SST-14(SNO) formation (Fig 4.5A, traces (a)-(d)). Traces (e)-(h) in Fig 4.5 show reaction conditions in which $[\text{H}^+]_0 > [\text{NO}_2^-]_0$ and

Fig 4.5B depicts the complex effect of acid variation as a sigmoidal curve which starts out with a low slope that then increases to an inflection point ($[\text{H}^+]_0 = 1 \text{ mM}$) before leveling off as it approaches maximum rates of SST-14(SNO) formation. Since $[\text{NO}_2^-]_0$ concentrations were constant, then constant $[\text{HNO}_2]_0$ is expected after the inflection point and the effect of $[\text{H}^+]_0$ can be evaluated. The gradual but steady increase in rate of SST-14(SNO) formation can only be attributed to NO^+ as the major nitrosating agent (R3.4), and a rate plot of traces (e)-(h) gives linear plot which suggests first order kinetics in high $[\text{H}^+]$ with a non-zero y-intercept which gives an estimate of the S-nitrosylation effect of HNO_2 without excess H^+ (Fig 4.5C). Using Eq 3.7 (section 3.2.2.4) and Fig 4.5, we determined the bimolecular rate constants for SST-14 S-nitrosylation by HNO_2 and NO^+ to be $390 \pm 56 \text{ M}^{-1}\text{s}^{-1}$ and $8.7 \times 10^4 \text{ M}^{-1}\text{s}^{-1}$.

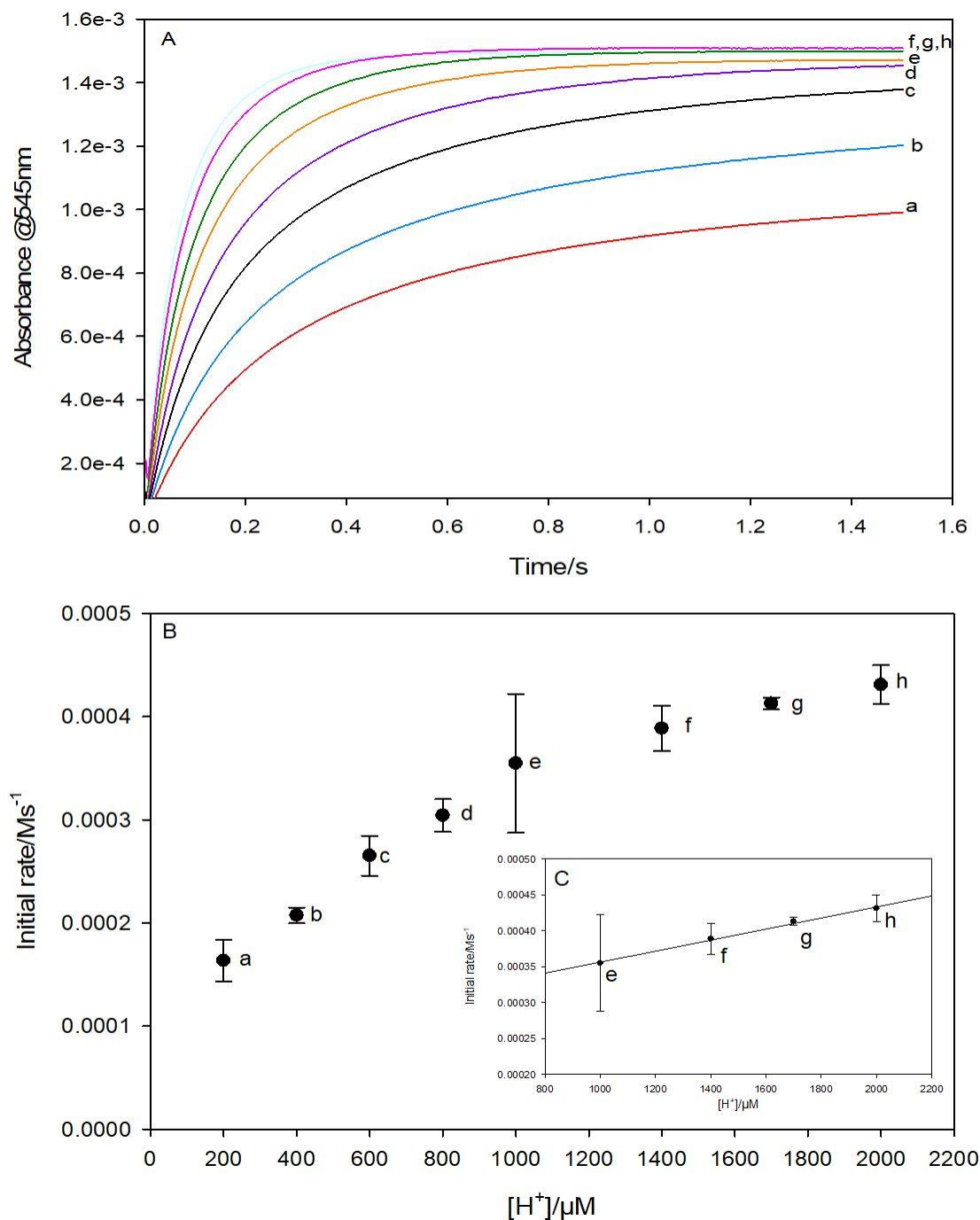


Figure 4.5: (A) Effect of $[H^+]$ variation SST-14(SNO) formation at 25 °C. Fixed $[SST-14(SH)] = 1$ mM, $[EDTA] = 100 \mu M$, $[NO_2^-] = 1$ mM. Varied $[H^+] =$ (a) 200 μM , (b) 400 μM , (c) 600 μM , (d) 800 μM , (e) 1 mM, (f) 1.4 mM, (g) 1.7 mM, (h) 2 mM (B) Rate plots also show 1st-order dependence on H^+ concentrations (C) Effect of $[H^+]$ variation when $[H^+] \geq 1$ mM.

4.2.2.4 NO⁺ S-nitrosylation temperature dependence and thermodynamic parameters.

Using methods described in section 3.2.2.5, traces in Fig 4.5 were ran large excess of HNO₂ (10-55 mM). We observed k_{obs} rates that were an order of magnitude greater in comparison to those reported earlier in this work for HNO₂/NO⁺ mediated AVP(SNO) formation, with an ~1.5-fold increase in SST-14(SNO) formation rates (Table 4.2). The corresponding Eyring plots for k_{on} and k_{off} are shown in Figures 4.6B and 4.6C respectively. The slope and intercept values were used to calculate thermodynamic parameters; for k_{on} and k_{off} (Table 4.3). Interestingly, the Gibbs free energy was identical to that obtained in NO⁺ mediated AVP(SNO) formation. Despite being kinetically more favorable SST-14(SNO) formation, showed slight differences in ΔH^\ddagger and ΔG^\ddagger values with AVP(SNO).

Table 4.2. NO⁺ mediated SST-14 thiol S-nitrosylation k_{on} and k_{off} values

Temp (°C)	k_{on} (M ⁻¹ s ⁻¹)	k_{off} (s ⁻¹)
15	9.2 ± 0.6	98.7 ± 18.9
20	10.6 ± 0.4	108.9 ± 14.1
25	16.1 ± 1.1	181.4 ± 27.6
30	16.8 ± 0.5	207.3 ± 19.3
35	21.7 ± 0.8	298.4 ± 25.9

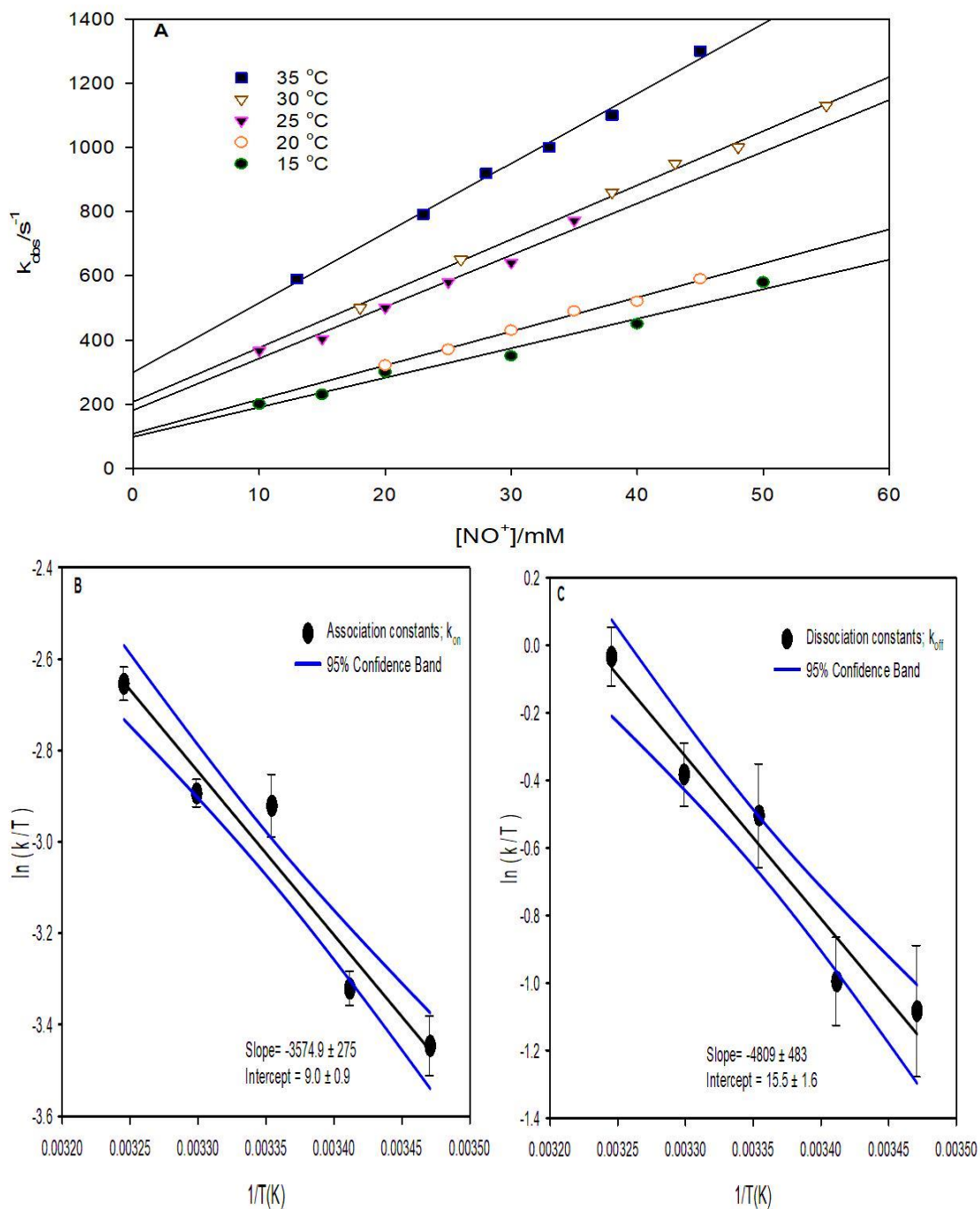


Figure 4.6: (A) Observed rate constants for SST-14(SH) S-nitrosylation by HNO_2 concentrations. Fixed $[EDTA] = 100 \mu M$, $[SST-14(SH)] = 1 mM$. Varied $[HNO_2]$ in the range 10-55 mM. (B) and (C) depicts linear Eyring plots from k_{on} and k_{off} values that are stated in Table 12 respectively.

Table 4.3: NO⁺ mediated SST-14 thiol S-nitrosylation thermodynamic parameters.

	E_a^a	ΔG^{‡b}	ΔH^{‡c}	ΔS^{‡d}
<i>k_{on}</i>	32.2	33.6	29.7	-12.7
<i>k_{off}</i>	42.1	43.0	40.0	9.68

^{a, b and c} Values are in kJ/mol, whilst ^d values are in J.mol⁻¹K⁻¹. Temperature = 37°C ^b

4.2.3 Peroxynitrite mediated SST-14(SH) S-nitrosylation.

4.2.3.1 Effect of SST-14 variation. The rates of ONOO⁻ depletion by SST-14(SH) are fast with reaction completion times of ~15 s (Fig 4.8A). ONOO⁻ depletion rates increase with increasing SST-14(SH) concentrations. The initial rates plot of ONOO⁻ depletion (Fig 4.8B) show 1st-order dependence in SST-14(SH) concentrations, whilst the effect of SST-14(SH) on SST-14(SNO) formation showed a linear dependence without an induction period (Fig 4.8C). Figure 4.8D shows a first-order dependence of SST-14(SNO) formation on SST-14(SH) concentrations. We determined the bimolecular rate constant for the direct S-nitrosylation of SST-14(SH) by ONOO⁻ to be 308 ± 24 M⁻¹s⁻¹ at 25°C.

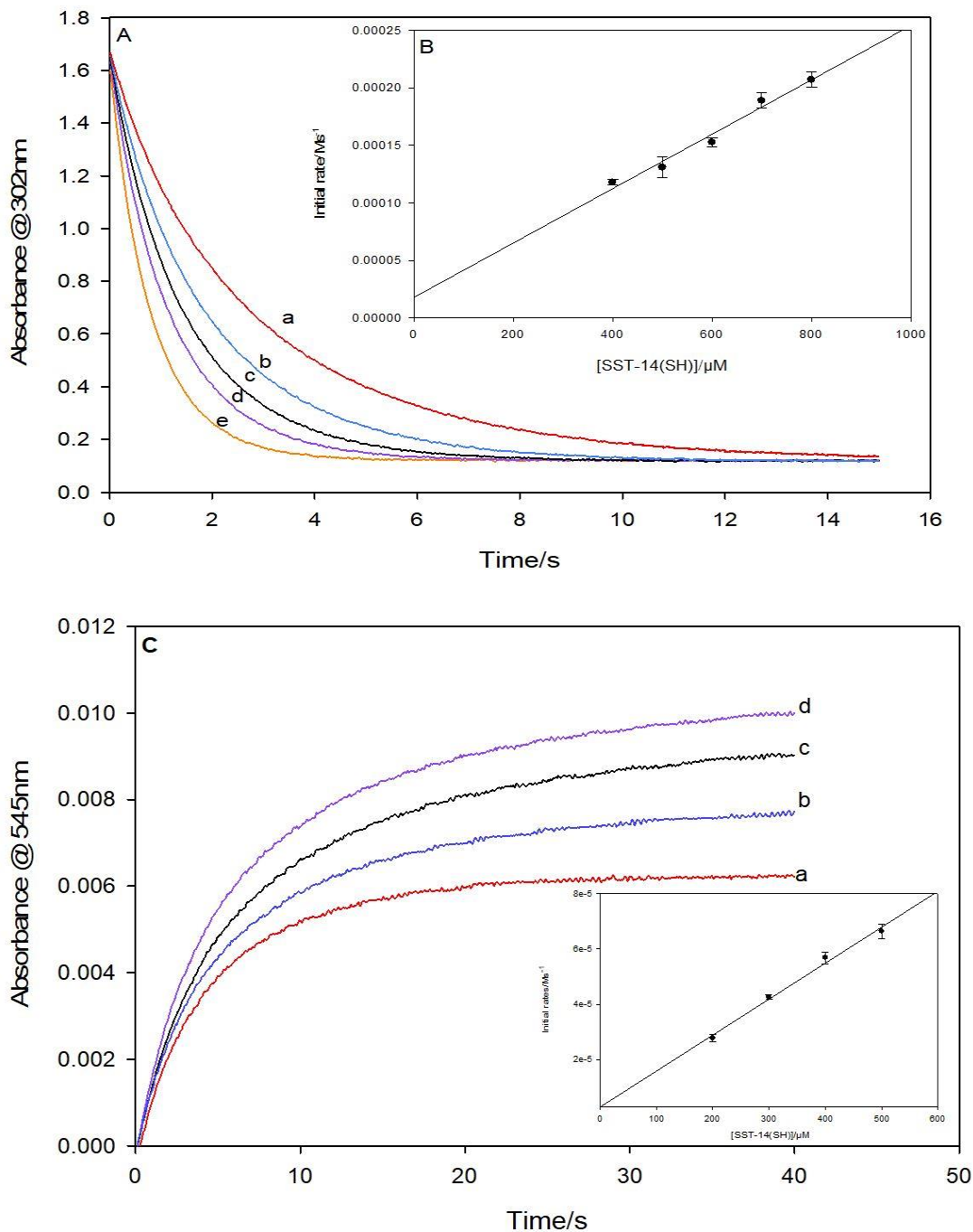


Figure 4.8: Effect of varying SST-14(SH) concentrations on ONOO⁻ depletion in pH 7.4 PBS at 302 nm. Fixed [EDTA] = 100 μM , [ONOO⁻] = 1 mM. **(A)** Varied [SST-14(SH)] = (a) 400 μM , (b) 500 μM , (c) 600 μM , (d) 700 μM , (e) 800 μM . **(B)** Shows linear relationship between initial rates of ONOO⁻ depletion and SST-14(SH) concentrations for traces in (A). **(C)** Varied [SST-14(SH)] = (a) 200 μM , (b) 300 μM , (c) 400 μM , (d) 500 μM . **(D)** Shows linear relationship between initial rates of SST-14(SNO) and SST-14(SH) concentrations for traces in (C).

4.2.3.2 Effect of acid variation on ONOO⁻ mediated SST-14(SNO) formation. Kinetics of SST-14(SNO) formation through ONOOH mediated S-nitrosylation showed a complex dependence on acid. At $[H^+] < [ONOO^-]$, we observed the catalytic effect acid on SST-14(SNO) formation (Fig 4.9A, traces (a)-(c)). However, increasing acid concentrations in excess of ONOO⁻, did not result in further increase in SST-14(SNO) formation and actually catalyzed its decomposition as depicted by a decrease in absorbance (Fig 4.9A, traces (d)-(f)). Rate plots of $[H^+]$ were discontinuous as the first three H^+ concentrations (Fig 4.9B, (a)-(c)) showed reasonable linearity as a function of gradual increases in H^+ concentrations, which supports the conclusion that rates of SST-14(SNO) formation at low H^+ concentrations have a 1st-order dependence on ONOOH concentrations. This linearity was lost at higher acid concentrations (Fig 4.9B, (d)-(f)), therefore we anticipate a simple rate law equations at low H^+ concentrations and a complicated multi-term rate law at high H^+ concentrations. Rates of SST-14 mediated ONOO⁻ depletion were found to be directly proportional to acid concentration (Fig 4.10A), with nonlinear curved rate plots as shown in Fig 4.10B. Using the experimental data from Figures 4.9 and 4.10, we evaluated the bimolecular rate constant for SST-14(SH) S-nitrosylation by ONOOH to be $1.55 \times 10^3 \text{ M}^{-1} \text{ s}^{-1}$ at 25°C.

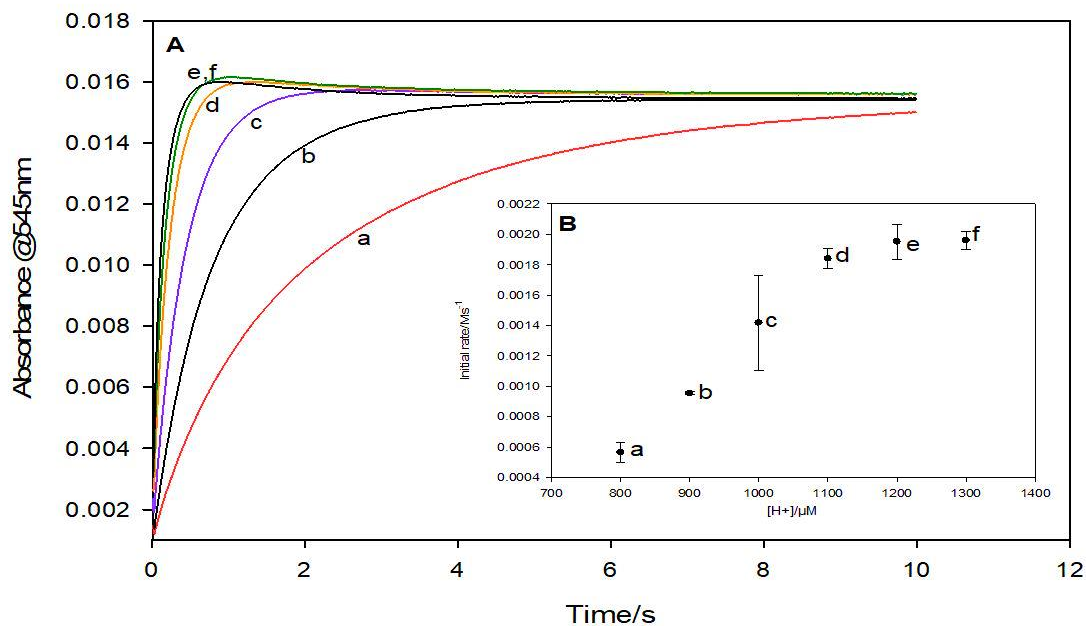


Figure 4.9: (A) Effect of varying H^+ concentrations on $ONOO^-$ mediated S-nitrosylations in PBS at pH 7.4. Fixed $[SST-14(SH)] = 1 \text{ mM}$, $[EDTA] = 100 \text{ }\mu\text{M}$, $[ONOO^-] = 1 \text{ mM}$. Varied $[H^+] =$ (a) $800 \text{ }\mu\text{M}$, (b) $900 \text{ }\mu\text{M}$, (c) 1 mM , (d) 1.1 mM , (e) 1.2 mM , (f) 1.3 mM (B) Initial rate plot shows a direct relationship between acid concentration and SST-14(SNO) formation, with a slowdown in SST-14(SNO) formation in excess acid.

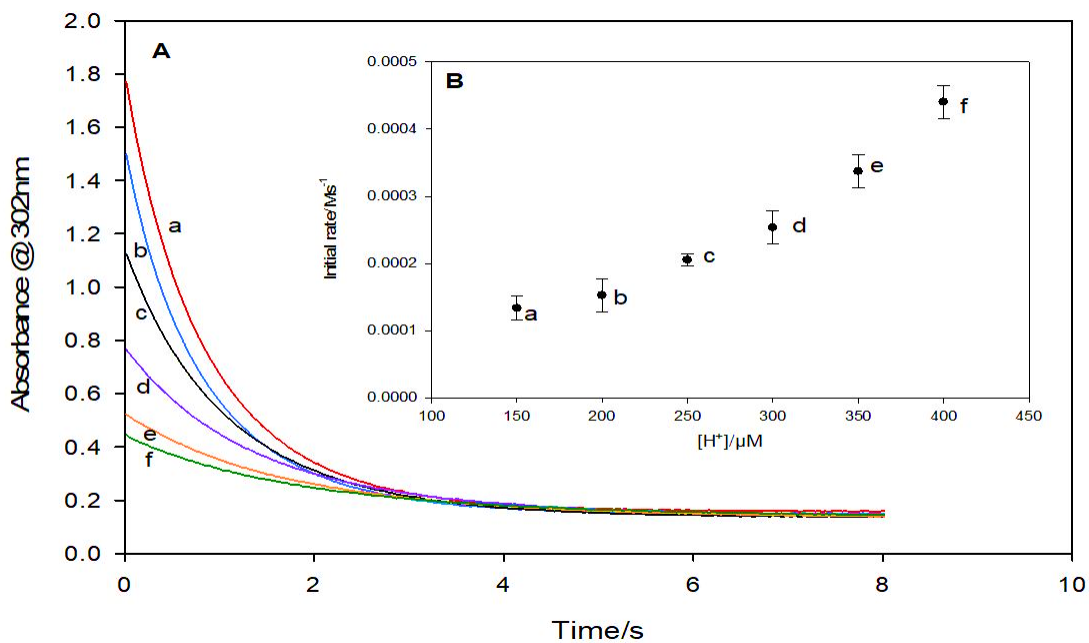


Figure 4.10: (A) Effect of $[H^+]$ variation on SST-14 depletion of $ONOO^-$. Fixed $[SST-14(SH)] = 600 \text{ }\mu\text{M}$, $[EDTA] = 100 \text{ }\mu\text{M}$, $[ONOO^-] = 1 \text{ mM}$. Varied $[H^+] =$ (a) $150 \text{ }\mu\text{M}$, (b) $200 \text{ }\mu\text{M}$, (c) $250 \text{ }\mu\text{M}$, (d) $300 \text{ }\mu\text{M}$, (e) $350 \text{ }\mu\text{M}$, (f) $400 \text{ }\mu\text{M}$. (B) Initial rates plot shows an exponential increase in $ONOO^-$ depletion with increased acid concentrations.

4.2.3.3 Peroxynitrite variation and EPR analysis. The reaction of SST-14(SH) and ONOO^- in pH 7.4 phosphate buffer showed a simple dependence on $[\text{ONOO}^-]$ (Fig 4.11). We observed a linear 1st-order dependence in ONOO^- concentrations.

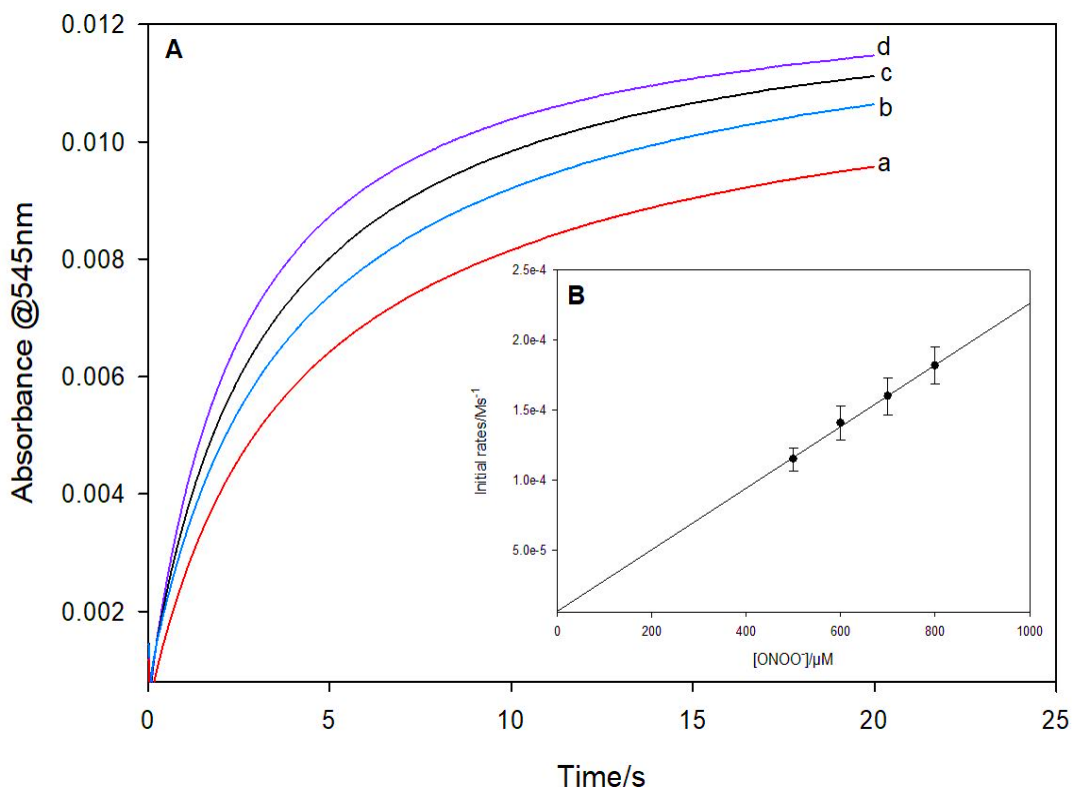


Figure 4.11: Effect of $[\text{ONOO}^-]$ variation on SST-14(SNO) formation in PBS at pH 7.4. Fixed $[\text{EDTA}] = 100 \mu\text{M}$, $[\text{SST-14(SH)}] = 1 \text{ mM}$. (A) Varied $[\text{ONOO}^-] =$ (a) $500 \mu\text{M}$, (b) $600 \mu\text{M}$, (c) $700 \mu\text{M}$, (d) $800 \mu\text{M}$. (B) Shows linear relationship between initial rates of SST-14(SNO) formation and ONOO^- concentrations for traces in (A).

EPR spectra using DMPO (Fig 4.12), showed hydroxyl radical production with an increase in signal intensity as SST-14(SH) concentrations increased. SST-14(SH) by itself in DMPO at pH 7.4 did not generate any EPR signal. EPR spectra using nitroethane of traces in Figure 4.11 taken 60s after mixing the reactants, detected NO radicals upon decomposition of SST-14(SNO). We also observed an increase in NO radicals intensity

with increased ONOO⁻ concentrations.

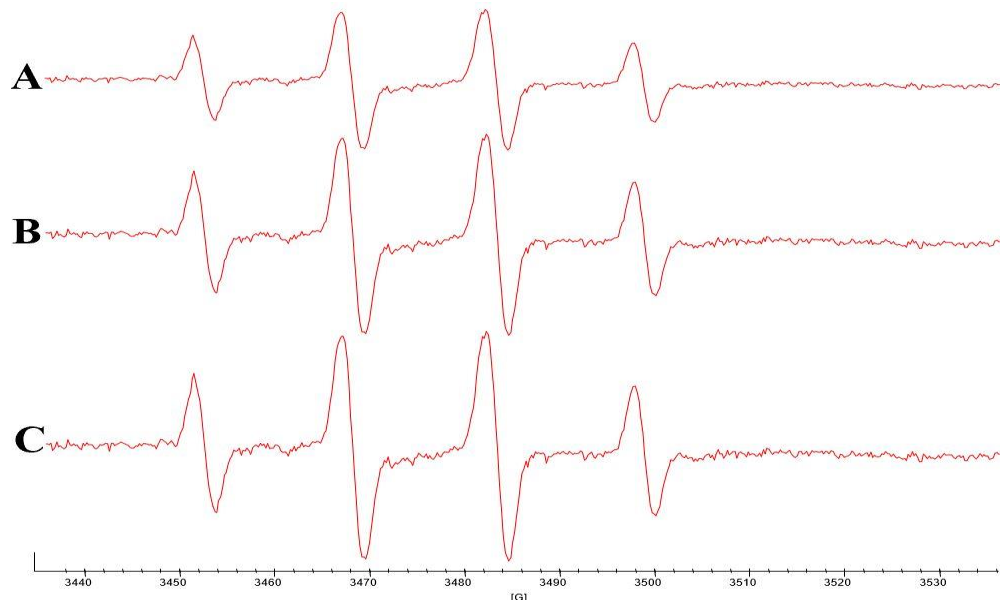
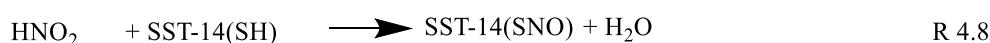
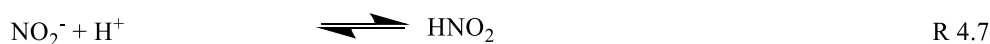
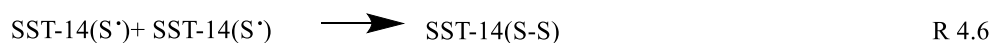
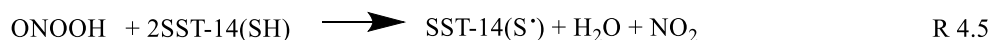
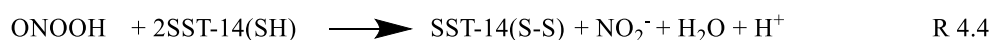
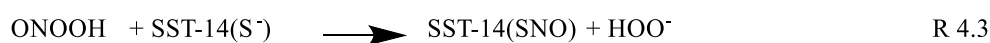
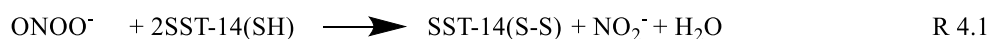


Figure 4.12: EPR spectra of DMPO radical adducts ONOO⁻ mediated SST-14(SNO) formation at pH 7.4. Fixed [ONOO⁻] = 1 mM and [DMPO] = 50 mM. Varied; (A) [SST-14(SH)] = 600 μM, (B) [SST-14(SH)] = 700 μM, and (C) [SST-14(SH)] = 800 μM.

4.2.3.4 Peroxynitrite mediated S-nitrosylation reaction scheme. The reaction dynamics observed in sections 3.2.3 and 4.2.3, implicate eight reactions (R4.1 – R4.8) as being the most relevant in ONOO⁻ mediated S-nitrosylation reactions. At pH ≥ 7, the stoichiometry of thiol S-nitrosylation by ONOO⁻ is shown by R 4.1. Mass spectrometry experiments were unable to detect the highly unstable sulfenic acid intermediate, which would mostly likely be formed as a result of two electron transfers from ONOO⁻ to the peptide sulfhydryl group. We propose this as the pathway for thiol oxidation through sulfenic acid formation and its subsequent reaction with other thiols to form the disulfide (R4.1). Based on its pK_a, we expect that ONOO⁻ is reasonably protonated and that its decomposition would occur according to reaction R4.2. Peroxynitrous acid mediated S-nitrosylation is most likely mediated through thiolate anion nucleophilic attack on peroxynitrous acid, resulting in the

release of the hydrogen peroxide anion which can subsequently be protonated to hydrogen peroxide (H₂O₂) (R4.3). Hydrogen peroxide readily diffuses across the cell membranes and it is postulated that it can be converted, through the Fenton reaction (R3.16) to the more toxic [•]OH radicals in the presence of ferrous ion²²⁵⁻²²⁶. Detection of [•]OH radicals in our EPR experiments at pH 7.4 supports the feasibility of this reaction mechanism. The glutathione thiolate anion is known to react with thiyl radicals to generate disulfide radical anions²²⁷. Analogous reactions occur with other protein Cys residues intramolecularly if protein/peptide structure allows. When the pH is lower than the pKa of the thiol, the ONOOH reaction with a thiol would result in oxidation to the disulfide with the release of NO₂⁻ (R4.4). Thiol oxidation could also occur through a one electron transfer mechanism, resulting in the formation of NO₂ and thiyl radicals which would form the disulfide (R4.5 and R4.6).



Thiyl radical reactions with NO can form S-nitrosocysteine which is regarded as important product of thiol-dependent signaling²²⁸. Kinetic data has shown that disulfides and thiols are not the only reaction products formed from protein/peptide thiyl reactions even in the presence of antioxidants²²⁹. Especially at suboptimal levels of antioxidants or when thiyl radicals are not accessible to antioxidants. The detection of ONOO⁻-induced tyrosine radicals in blood plasma of has prompted researchers to question their involvement in electron transfer with cysteine residues²³⁰. Importantly, there is growing evidence that implicates peptide thiyl radicals in GTPase nucleotide exchange process and other pathways that promote S-nitrosylation²³¹⁻²³³. In acidic media, the nitrite ions formed in reactions R4.1 and R4.4 would be converted to HNO₂ in a fast proton-transfer reaction with an equilibrium determined by nitrous acid's pKa (R4.5). Nitrous acid reacts with the peptide thiol to form RSNO and water (R4.6). Our data suggests that ONOOH S-nitrosylation reactions are analogous to S-nitrosylation mediated by HNO₂, similar reaction dynamics have been observed for alkyl nitrite (RONO) mediated S-nitrosylation reactions which are reported to involve the elimination of hydroxyl ions²³⁴.

4.2.3.5 Temperature dependence and thermodynamic parameters. Pseudo first-order k_{obs} rates for ONOOH and ONOO⁻ S-nitrosylation reactions were obtained from data shown in Figures 4.9 and 4.11, respectively. The observed k_{obs} rates for ONOOH mediated S-nitrosylation spectral results were plotted against [ONOOH], with varied [ONOOH] concentrations at each temperature (Fig 4.13A) and derived k_{obs} values as stated in Table 4.4. These k_{obs} rates were an order of magnitude below values for ONOOH mediated AVP(SNO) formation. Cleavage of the disulfide between residue Cys³ and Cys¹⁴ in SST-

14 has been linked to altered conformational dynamics and aggregation resulting in modifications to its native structure, with the thiol-containing structure having a wide range of conformations and being highly dynamic²³⁵. Essentially, SST-14(SH) has increased conformational dynamics, lower mechanical stability, and increased entropy as compared to the disulfide. Surprisingly, the conformational flexibility of SST-14(SH) due to linearization did not result in increased access to thiol residues and higher S-nitrosylation rates than those for AVP(SH), even though SST-14(SH) autoxidation to the disulfide takes longer (Table 4.1).

Table 4.4: ONOOH mediated SST-14 S-nitrosylation observed rate constants; k_{on} and k_{off} .

Temp (°C)	k_{on} (M ⁻¹ s ⁻¹)	k_{off} (s ⁻¹)
15	11 ± 0.9	307.1 ± 27
20	15 ± 1.6	363 ± 55
25	26 ± 0.8	723 ± 20
30	37.9 ± 1.1	979 ± 43
35	54 ± 3	1137 ± 87

As expected, ONOOH reactions with SST-14(SH) were kinetically and thermodynamically more favorable as evidenced by the larger k_{obs} values (Table 4.4) and lower E_{a} , ΔH^{\ddagger} and ΔG^{\ddagger} values (Table 4.5) than reactions with ONOO⁻.

Table 4.5: ONOOH mediated SST-14 S-nitrosylation thermodynamic parameters.

	Ea^a	ΔG^{‡b}	ΔH^{‡c}	ΔS^{‡d}
<i>k</i>_{on}	45.7	49.3	41.6	-25
<i>k</i>_{off}	44.2	46.1	38	73

a, b and c Values are in kJ/mol, whilst **d** values are in J.mol⁻¹K⁻¹. Temperature = 37°C **b**

Data from *k*_{obs} rates for ONOO⁻ mediated S-nitrosylation reactions (Fig 4.14) and the derived *k*_{on} and *k*_{off} values (Table 4.6), shows a slow reaction. Thiol oxidation through sulfenic acid formation and its subsequent reaction with other thiols to form the disulfide (R4.1) does provide a potential explanation for this. Additionally, the physiological relevance of ONOO⁻-induced S-nitrosylation cannot be fully understood without considering the presence of CO₂, which is a major physiological target for ONOO⁻²³⁶. Studies have shown that ONOO⁻ reactions with thiol can be inhibited by adding bicarbonate (HCO₃⁻; as a source of CO₂) in a concentration-dependent manner²³⁷. Several mechanisms have been proposed that involve the reaction between peroxynitrite and bicarbonate forming various peroxybicarbonate species²³⁸. Given that carbon dioxide concentrations *in vivo* are not high but mainly persist as HCO₃⁻ in biological fluids, one could rightly question whether carbon dioxide and carbonate mediated ONOO⁻ depletion is a major mechanism for ONOO⁻ detoxification *in vivo*²³⁹. Kinetic data suggests that in excess CO₂, ONOO⁻ mediated S-nitrosylation reactions produce two-electron oxidation products with rapid decomposition of nitrosoperoxy carbonate adducts to form nitrogen dioxide and carbonate radicals^{199, 240}. Decomposition of ONOO⁻ in phosphate and bicarbonate buffer

systems was found to be a least 10 times slower in phosphate buffer, confirming bicarbonate's catalytic effect on ONOO⁻ decomposition resulting in NO₃⁻ release and the regeneration of CO₂²⁴¹. While it may be feasible that dissolved CO₂ in our reaction mixture may deplete some of the initial ONOO⁻, we emphasize that it's effect would only be relevant if bolus amounts of CO₂ were present and the rate of ONOO⁻ depletion in phosphate buffer ($1.11 \pm 0.01 \text{ s}^{-1}$)²⁴¹ was rapid enough to out-compete S-nitrosylation reactions.

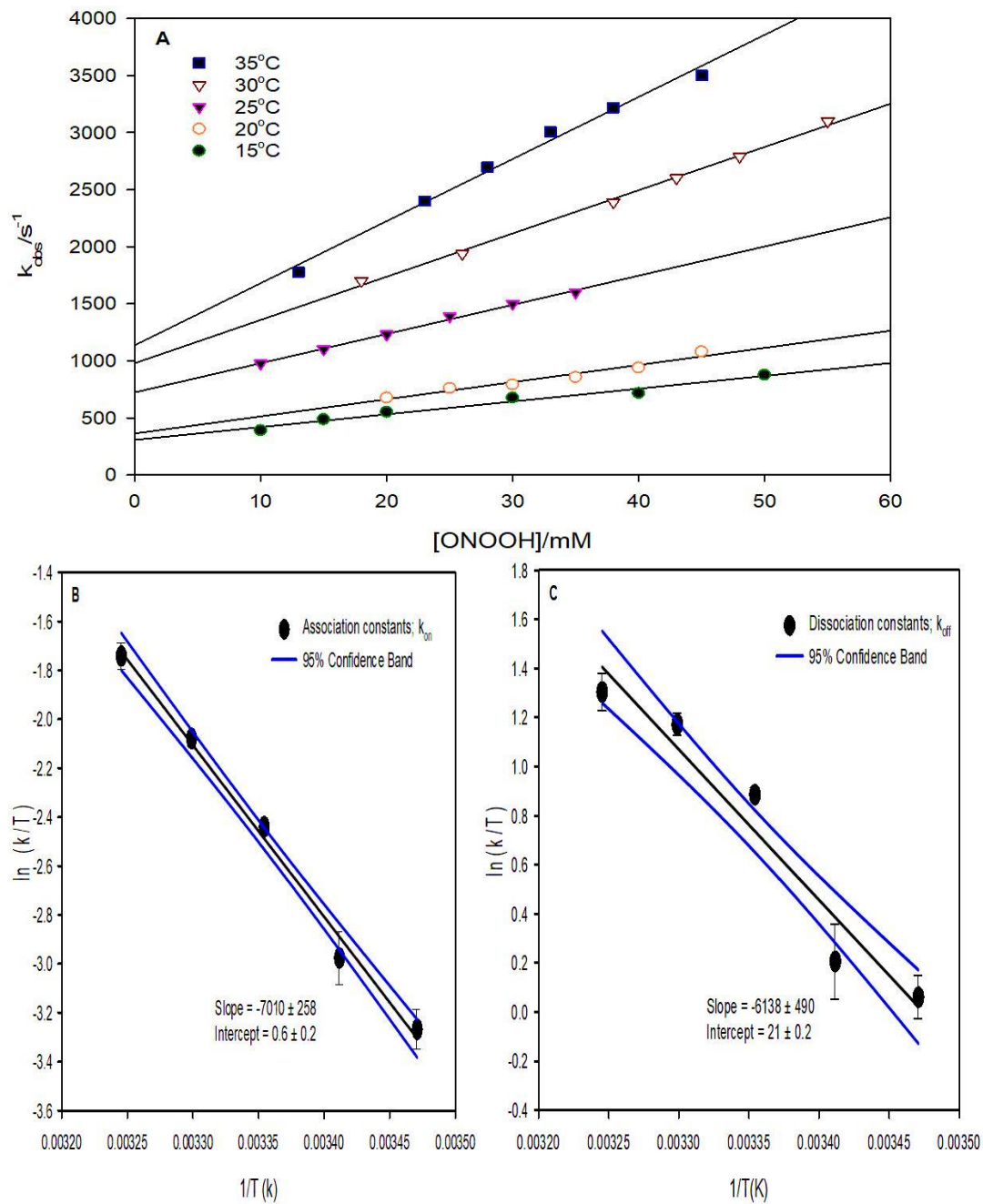


Figure 4.13: (A) K_{obs} values for the S-nitrosylation of SST-14(SH) by varied ONOOH concentrations. Fixed [EDTA] = 100 μ M, [SST-14(SH)] = 1 mM. Varied [ONO^o]: [H⁺] on a 1:1 ratio in the range 10-55 mM (B) and (C) depicts linear Eyring plots from k_{on} and k_{off} values in Table 4.4 respectively.

Table 4.6: ONOO⁻ mediated SST-14 S-nitrosylation observed rate constants; k_{on} and k_{off} .

Temp (°C)	k_{on} (M ⁻¹ s ⁻¹)	k_{off} (s ⁻¹)
15	0.87 ± 0.14	165 ± 4.3
20	1.05 ± 0.06	171 ± 2.1
25	1.14 ± 0.05	220 ± 1.3
30	1.18 ± 0.2	225 ± 7.1
35	1.25 ± 0.07	269 ± 2.2

Table 4.7: ONOO⁻ mediated SST-14 S-nitrosylation thermodynamic parameters.

	E_{a} ^a	$\Delta G^{\ddagger b}$	$\Delta H^{\ddagger c}$	$\Delta S^{\ddagger d}$
k_{on}				
	60.7	65.4	58.3	-22.9
k_{off}				
	53.4	57.6	50.9	21.7

^{a, b and c} Values are in kJ/mol, whilst ^d values are in J.mol⁻¹K⁻¹. Temperature = 37°C ^b

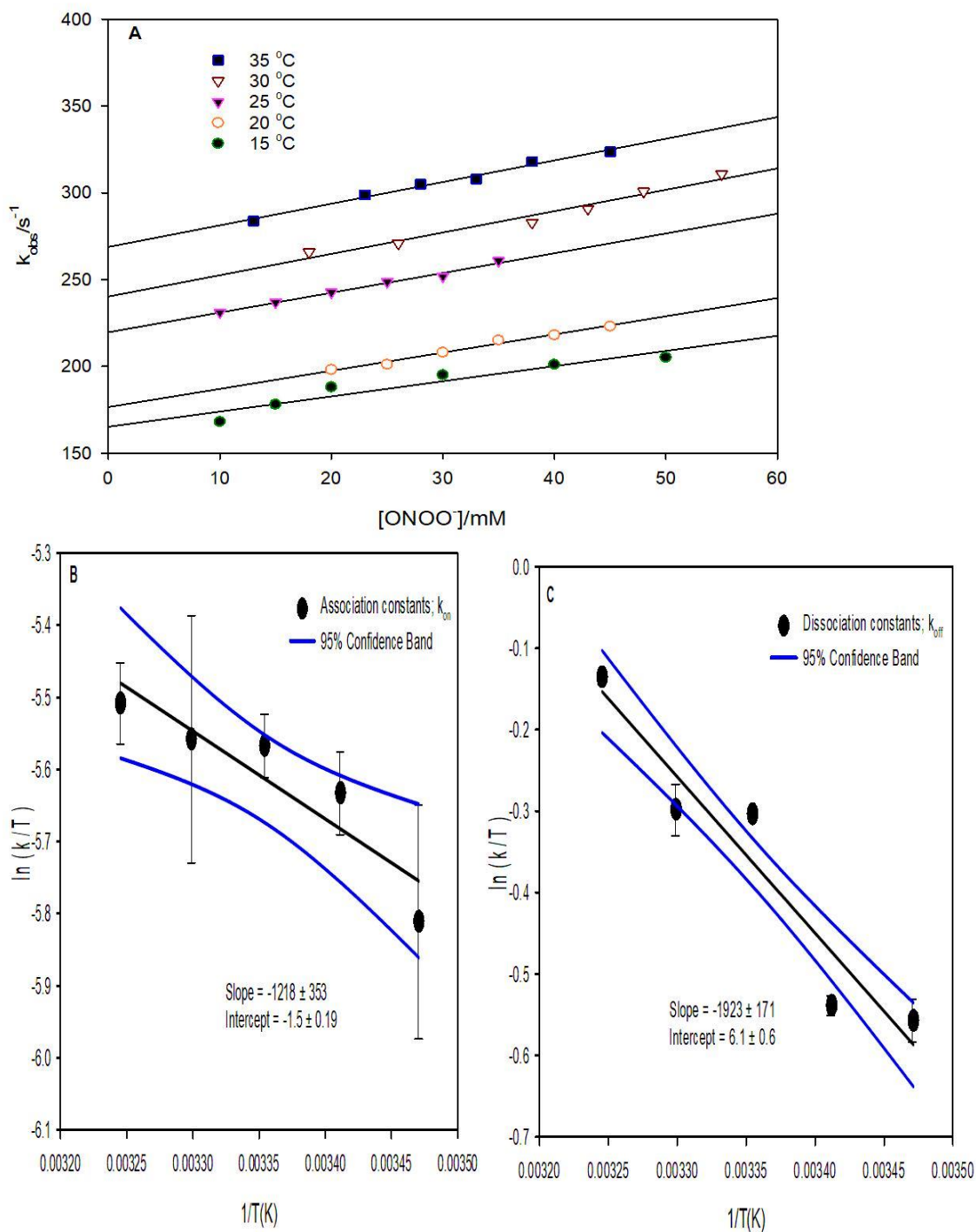


Figure 4.14: (A) Observed rate constants for the S-nitrosylation of SST-14(SH) by ONOO⁻. Fixed [EDTA] = 100 μM, [SST-14(SH)] = 1 mM. Varied [ONOO⁻] in the range 10-55 mM. (B) and (C) depicts linear Eyring plots from k_{on} and k_{off} values stated in Table 4.6.

4.2.4 SNAP mediated SST-14(SH) S-nitrosylation.

4.2.4.1 Effect of SST-14 and SNAP variation. We investigated SST-14(SNO) formation through transnitrosation by SNAP PBS at pH 7.4. The reaction is rapid and complete in less than 10 secs, with a green to red color which are representative of SNAP and SST-14(SNO), respectively (Fig 4.15A). Initial rate plots indicate the first order dependence of SST-14(SNO) formation on SST-14(SH) concentrations (Fig 4.15B). The effect of varying sub-stoichiometric concentrations of SST-14(SH) on SNAP depletion at 590 nm, also gave simple first order kinetics (Fig 4.16A-B), with residual absorbance.

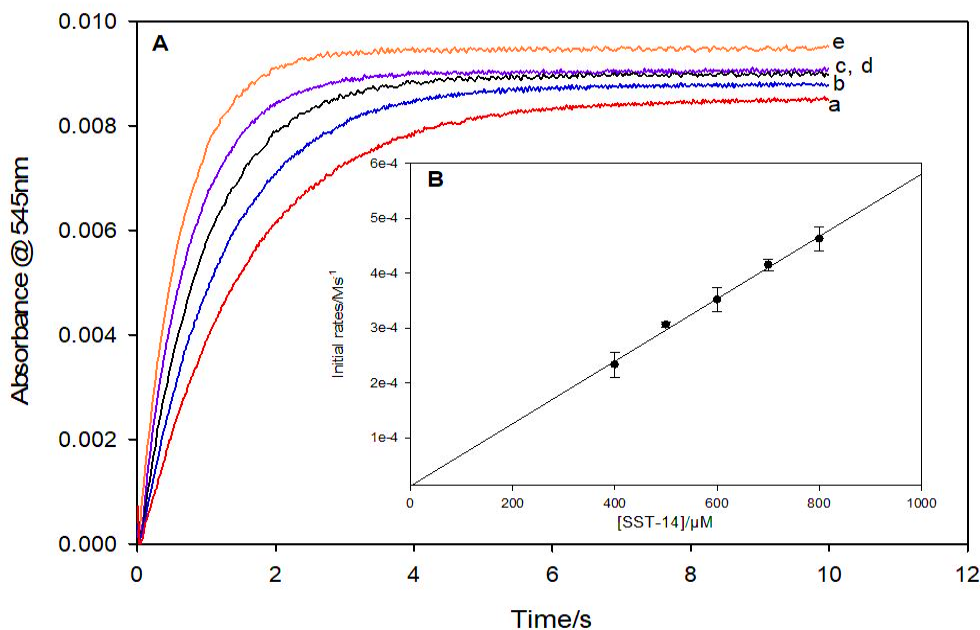


Figure 4.15: Effect of [SST-14(SH)] variation on reaction with SNAP in PBS at pH 7.4. Fixed [EDTA] = 100 μ M, [SNAP] = 1 mM. (A) Varied [SST-14(SH)] = (a) 400 μ M, (b) 500 μ M, (c) 600 μ M, (d) 700 μ M, (e) 800 μ M. (B) Shows linear relationship between initial rates of SST-14(SNO) formation and SST-14(SH) concentrations for traces in (A).

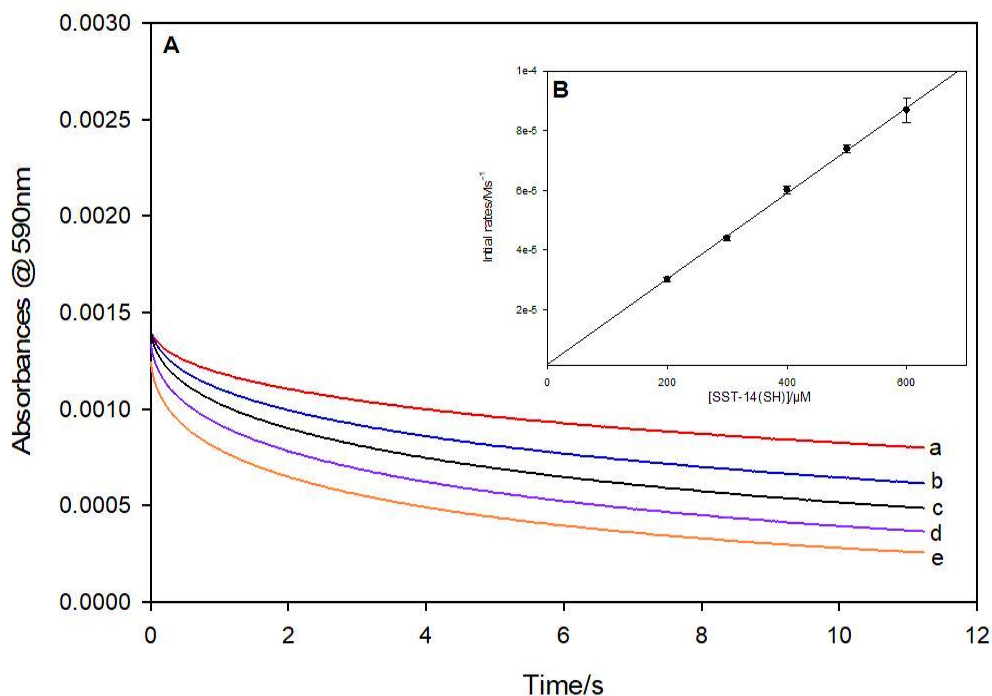


Figure 4.16: (A) Effect of [SST-14(SH)] variation on SNAP depletion at 590 nm in PBS at pH 7.4. Fixed [EDTA] = 100 μM , [SNAP] = 1 mM. (A) Varied [SST-14(SH)] = (a) 200 μM , (c) 300 μM , (d) 400 μM , (e) 500 μM , (f) 600 μM . (B) Shows linear relationship between initial rates of SNAP depletion and SST-14(SH) concentrations for traces in (A).

The effect of varying SNAP on SNAP depletion and SST-14(SNO) formation is shown in Figures 4.17 and 4.18 respectively. From kinetic data in Figures 4.16- 4.19 and Eq 3.12, we determined the bimolecular rate constant for the direct S-nitrosylation of SST-14(SH) by SNAP to be $261 \pm 5.4 \text{ M}^{-1}\text{s}^{-1}$.

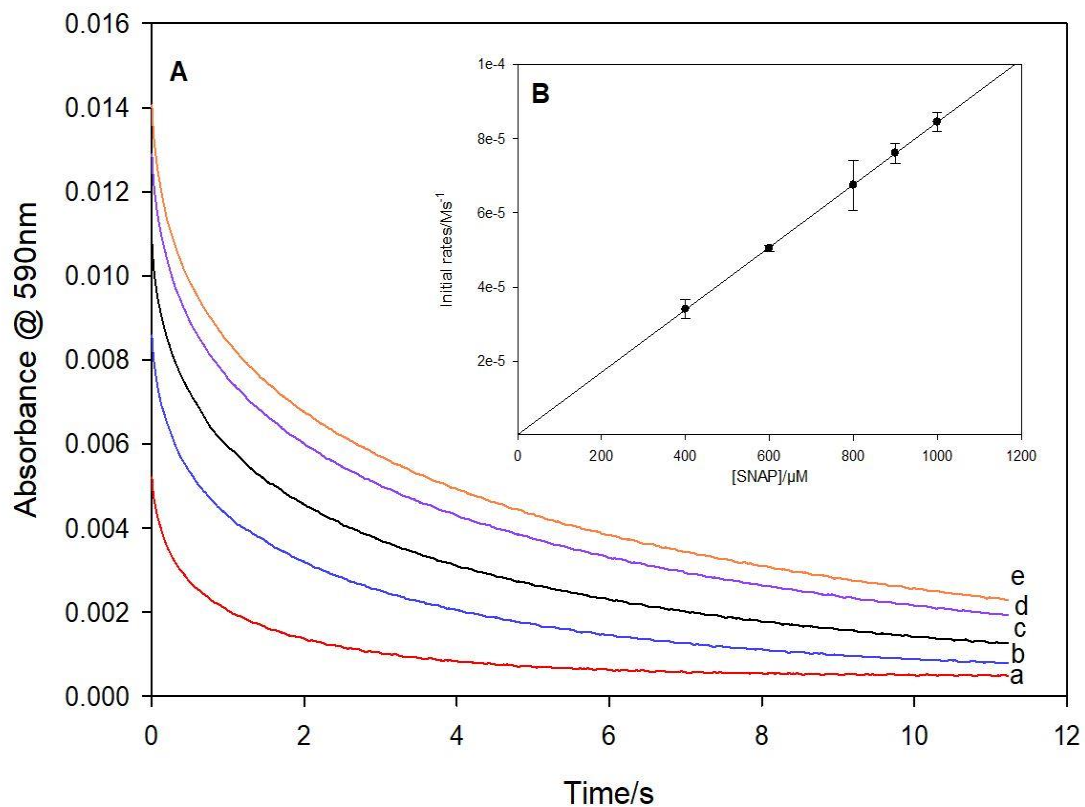


Figure 4.17: Depletion of varied SNAP concentrations at 590 nm in PBS at pH 7.4. Fixed [EDTA] = 100 μM , [SST-14(SH)] = 250 μM . **(A)** Varied [SNAP] = (a) 400 μM , (b) 600 μM , (c) 800 μM , (d) 900 μM , (e) 1 mM **(B)** Shows linear relationship between initial rates of SNAP depletion and SST-14(SH) concentrations for traces in (A).

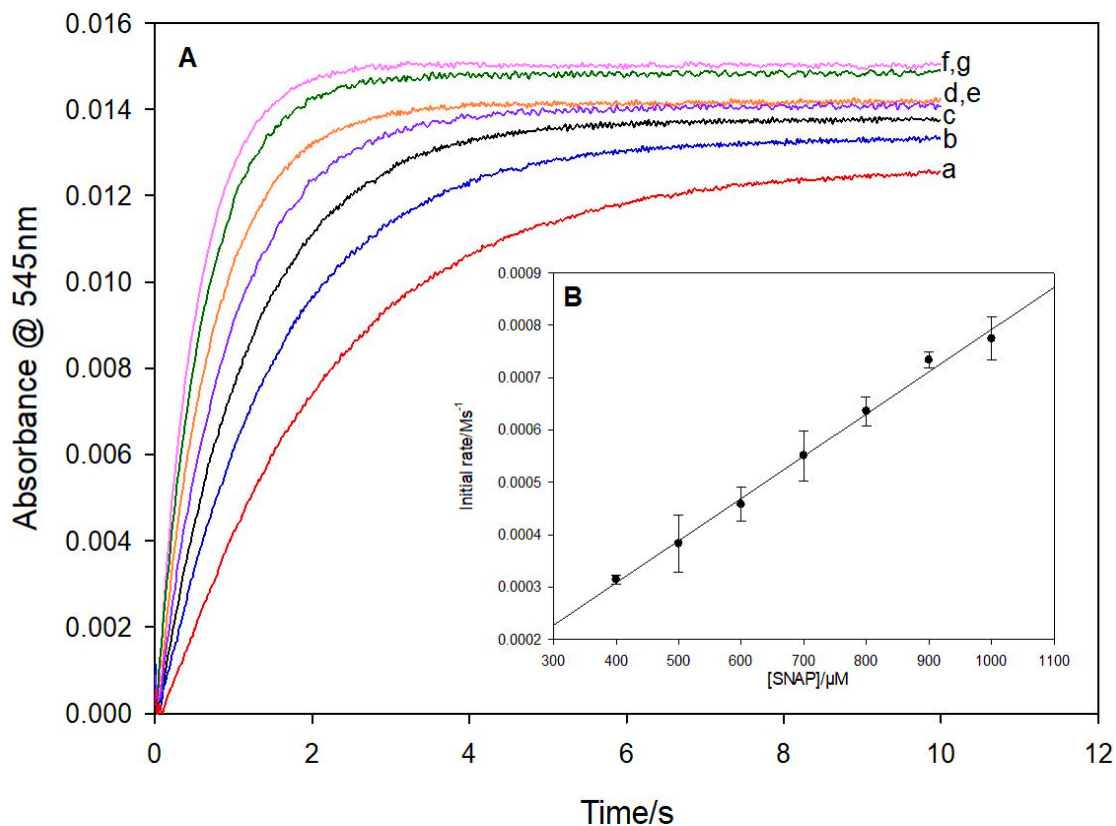


Figure 4.18: Effect of [SNAP] variation on SST-14(SNO) formation in PBS at pH 7.4. Fixed [EDTA] = 100 μM , [SST-14(SH)] = 1 mM. (A) Varied [SNAP] = (a) 400 μM , (b) 500 μM , (c) 600 μM , (d) 700 μM , (e) 800 μM , (f) 900 μM , (g) 1 mM. (B) Shows linear relationship between initial rates of SST-14(SNO) formation and [SNAP] concentrations for traces in (A).

4.2.4.2 SST-14(SH) transnitrosylation thermodynamic parameters.

Using methods described in section 3.2.2.5, we ran traces in Fig 4.18 in 10-fold excess of SNAP (10-55 mM). The k_{obs} rates for SNAP mediated SST-14(SNO) formation were plotted against [SNAP] at each temperature (Fig 4.19A) and the derived k_{on} and k_{off} values stated in Table 4.8. Observed k_{obs} rates are less but within range of SNAP mediated AVP(SNO) formation k_{obs} values (Table 3.8). Derived thermodynamic parameters were; for k_{on} as $E_a = 37.2 \text{ kJ mol}^{-1}$; $\Delta H^\ddagger_{\text{on}} = 34.8 \text{ kJ mol}^{-1}$ and $\Delta S^\ddagger_{\text{on}} = -111.1 \text{ J mol}^{-1} \text{ K}^{-1}$; for k_{off} these are $E_a = 15.1 \text{ kJ mol}^{-1}$; $\Delta H^\ddagger_{\text{off}} = 58.9 \text{ kJ mol}^{-1}$ and $\Delta S^\ddagger_{\text{off}} = -149.3 \text{ J mol}^{-1} \text{ K}^{-1}$ (Table

4.9). Both $\Delta S_{\text{on}}^{\ddagger}$ and $\Delta S_{\text{off}}^{\ddagger}$ entropic parameters are negative, which correlates with comparable entropic parameters in SNAP mediated AVP(SH) trans-nitrosylating reactions. The largest difference is the considerably smaller k_{off} activation (15.1 kJmol^{-1}) for SST-14(SNO) decomposition than that obtained for AVP(SNO) decomposition. One can reasonably conclude that SNAP mediated SST-14(SNO) formation is both kinetic and thermodynamically less favorable than AVP(SNO) formation.

Table 4.8: SST-14(SH) SNAP mediated S-nitrosylation observed k_{on} and k_{off} rate constants.

Temp (°C)	k_{on} ($\text{M}^{-1}\text{s}^{-1}$)	k_{off} (s^{-1})
15	5.2 ± 0.1	494 ± 3.2
20	6.5 ± 0.6	525 ± 21
25	8.9 ± 1.1	595 ± 28
30	11.8 ± 0.5	633 ± 17
35	13.6 ± 1.4	751 ± 45

Table 4.9: SST-14(SH) SNAP mediated S-nitrosylation thermodynamic parameters.

	E_{a}^{a}	$\Delta G^{\ddagger\text{b}}$	$\Delta H^{\ddagger\text{c}}$	$\Delta S^{\ddagger\text{d}}$
k_{on}	37.2	69.0	34.8	-111.1
k_{off}	15.1	58.9	13.0	-149.3

^{a, b and c} Values are in kJ/mol, whilst ^d values are in $\text{J}\cdot\text{mol}^{-1}\text{K}^{-1}$. Temperature = 37°C ^b

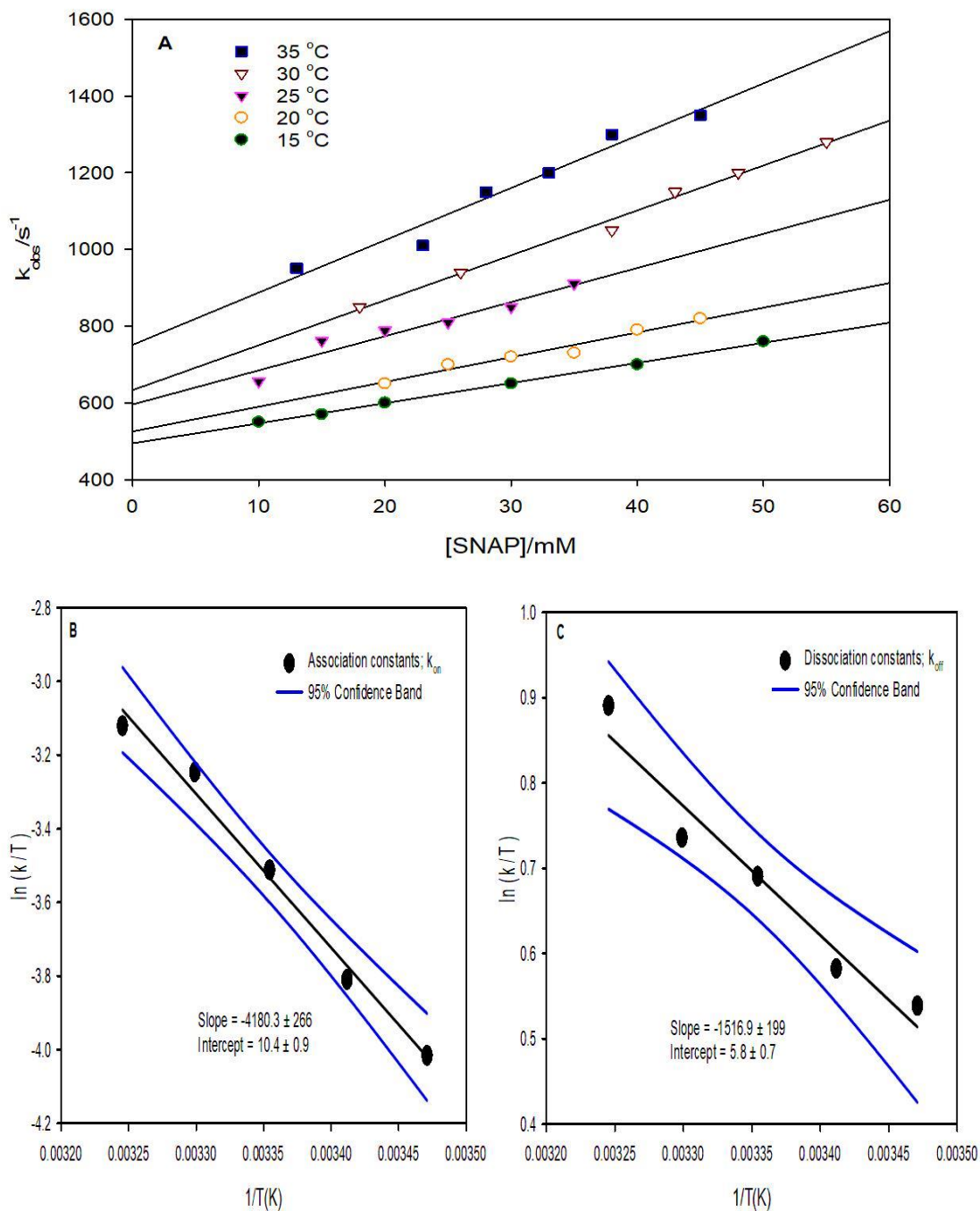


Figure 4.19: (A) Temperature dependence plot of k_{obs} vs [SNAP] for the reaction with SST-14(SH) in PBS at pH 7.4. Fixed [EDTA] = 100 μ M, [SST-14(SH)] = 1 mM. Varied [SNAP] in the range 10-55 mM. (B) and (C) depicts linear Eyring plots from k_{on} and k_{off} values in Table 4.8.

4.3 Conclusion. Autoxidation of SST-14(SH) at physiological temperature and pH took ~ 44 mins for 95% SST-14(S-S) reformation, which is sufficient time for thiol S-nitrosylation reactions to occur. This study has outlined rudimentary steps involved in the S-nitrosylation of SS-14(SH) by HNO₂, ONOO⁻ and SNAP. Acidic conditions that are found protein membrane microdomains would promote SST-14(SNO) formation through HNO₂/NO⁺ mediated S-nitrosylation. Bimolecular rate constants of $390 \pm 56 \text{ M}^{-1}\text{s}^{-1}$ and $8.7 \times 10^4 \text{ M}^{-1}\text{s}^{-1}$ are reported here for HNO₂ and NO⁺ mediated SST-14(SNO) formation respectively. Our experiments reveal how peroxynitrite could alter SST-14 function specifically through cysteine modification after reduction of the peptide thiol. Bimolecular rate constants of $308 \pm 24 \text{ M}^{-1}\text{s}^{-1}$ and $1.5 \times 10^3 \text{ M}^{-1}\text{s}^{-1}$ are reported here for ONOO⁻ and ONOOH mediated SST-14(SNO) formation respectively. Further studies could focus on deciphering which cysteine residue is selectively S-nitrosylated first (if any), as has been reported for the reaction of peroxynitrite with various amino acids²⁴². Reactions between SST-14 with H₂O₂ or hydroxyl radicals (R4.3) could lead to SST-14 inactivation through other cysteine residue modification. Besides modifying Cys, peroxy radicals are also known to target tyrosine residues, yielding bityrosine²⁴³, a modification not observed for the peroxynitrite reactions with SST-14(SH). EPR studies confirmed NO radical release from SST-14(SNO) within timescales that suggest that SST-14(SNO) could be an NO carrier and donor. Kinetic and thermodynamical data suggests that SNAP mediated SST-14(SNO) formation is less favorable than AVP(SNO) formation. We also propose that SST-14(SH) is a good candidate for further studies as a peroxynitrite detoxifying compound. Our findings agree with growing evidence that implicates small molecular weight thiols as essential effectors of NO signaling mechanisms.

CHAPTER 5: KINETICS AND THERMODYNAMICS OF THE REVERSIBLE BINDING OF NITRIC OXIDE TO UROTENSIN-II

5.1 INTRODUCTION.

Urotensin II (U-II) has the highest vasoconstrictive potency of any mammalian vasoconstrictor known to man and it's been implicated in cardiovascular regulation²⁴⁴⁻²⁴⁵. U-II isopeptides have a sequence motif; [Cys-Phe-Trp-Lys-Tyr-Cys] that is conserved in every isoform (Fig 5.1). Human urotensin II (hU-II) has eleven amino acid residues, and it is expressed in the CNS and various other organs that makeup the endocrine system²⁴⁶⁻²⁴⁷. Plasma levels of hU-II are elevated in patients with congestive heart failure, liver damage and hypertension²⁴⁸⁻²⁴⁹. The development of UT receptor antagonists is a hot area of research, with the hope that they may provide a novel treatment for cardiorenal diseases²⁵⁰. Sensitive and specific homologous radioimmunoassay used to measure tissue and circulating levels of U-II, have provided clear evidence that U-II does enter the circulation and is present in the 10^{-12} - 10^{-11} M range²⁵¹. U-II stimulates NO production by upregulating eNOS expression, which then diffuses into vascular smooth muscle cells thus stimulating smooth muscle relaxation²⁵². U-II induced vasodilatation has been linked to improved prognosis in perfused rat hearts after a myocardial ischemic episode²⁵³. Studies on the role of U-II in females with a pregnancy related complication called intrauterine growth restriction (IUGR), link elevated U-II thiol-disulfide levels, U-II levels, and oxidative stress index measurements between the control groups and the cohorts with pregnancies to the pathophysiology of IUGR²⁵⁴⁻²⁵⁶.

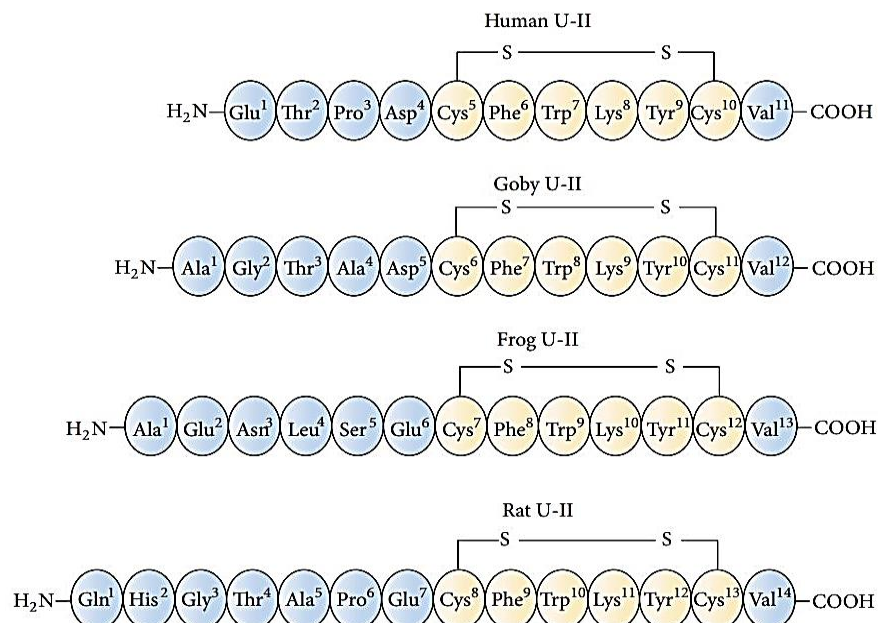


Figure 5.1: U-II isopeptides sequences conserved in vertebrates. [Adapted from Francesco Merlino, Salvatore Di Maro, Ali Munaim Yousif, Michele Caraglia, Paolo Grieco, "Urotensin-II Ligands: An Overview from Peptide to Nonpeptide Structures", Journal of Amino Acids, vol. 2013, Article ID 979016, 15 pages, 2013.]²⁵⁷.

Despite documented co-localization of U-II and NO, there has been no research into NO-mediated S-nitrosylation reactions that have the potential to alter U-II thiol-disulfide levels and U-II/UT receptor interactions that may be linked to various pathologies. This chapter will explore kinetic and thermodynamic parameters of U-II S-nitrosothiol (U-II(SNO)) formation through reactions involving NO moieties.

5.2 RESULTS AND DISCUSSION

5.2.1 U-II thiol formation and stability. We extrapolated methods described in section 3.2.1 to investigate U-II thiol (U-II(SH)) half-lives using HPLC (Fig 5.2). ϵ_{280} of U-II disulfide (U-II(S-S)) and U-II(SH) were determined to be $7115 \text{ M}^{-1}\text{cm}^{-1}$ and $6990 \text{ M}^{-1}\text{cm}^{-1}$, respectively (Eq 5.1). Chromatogram (A, Figure 5.2) was derived from a standard sample of $20\mu\text{M}$ U-II(S-S) eluting at 1.87 min. Chromatogram (B) shows product elution at 1.51 min after incubation of $15\mu\text{M}$ U-II(S-S) with $400 \mu\text{M}$ TCEP for 30 min. Mass spectrometric analysis of the standard ((chromatogram (A)), identifies eluant as U-II(S-S) with singly protonated $(\text{M}+\text{H})^+$ ions at m/z 1388.56 and the doubly protonated $(\text{M}+2\text{H})^{2+}$ ions at m/z 694.78 (Fig 5.3A). The product (chromatogram (B)) was identified as the singly protonated $[(\text{M}+\text{H})^+]$ thiol at m/z 1390.58 and the doubly protonated $[(\text{M}+2\text{H})^{2+}]$ thiol at m/z 695.79 (Fig 5.3B).

$$\epsilon_{280} = (\# \textit{Tryptophan} \times 5500) + (\# \textit{Cysteine} \times 125) + (\# \textit{Tyrosine} \times 1490) \quad \text{Eq 5.1}$$

Variation of temperature, pH, and the effect of metal chelators on U-II(S-S) reformation through disulfide reduction was evaluated using HPLC-UV according to equation 3.1. The time course for U-II(S-S) reformation is summarized in Table 5.1. The half-life of U-II(SH) at physiological pH and temperature was determined to be 33.2 mins. As previously described for AVP(SH) and SST-14(SH), we also found U-II(S-S) autoxidation to be slow in acidic media in the absence of a catalyst.

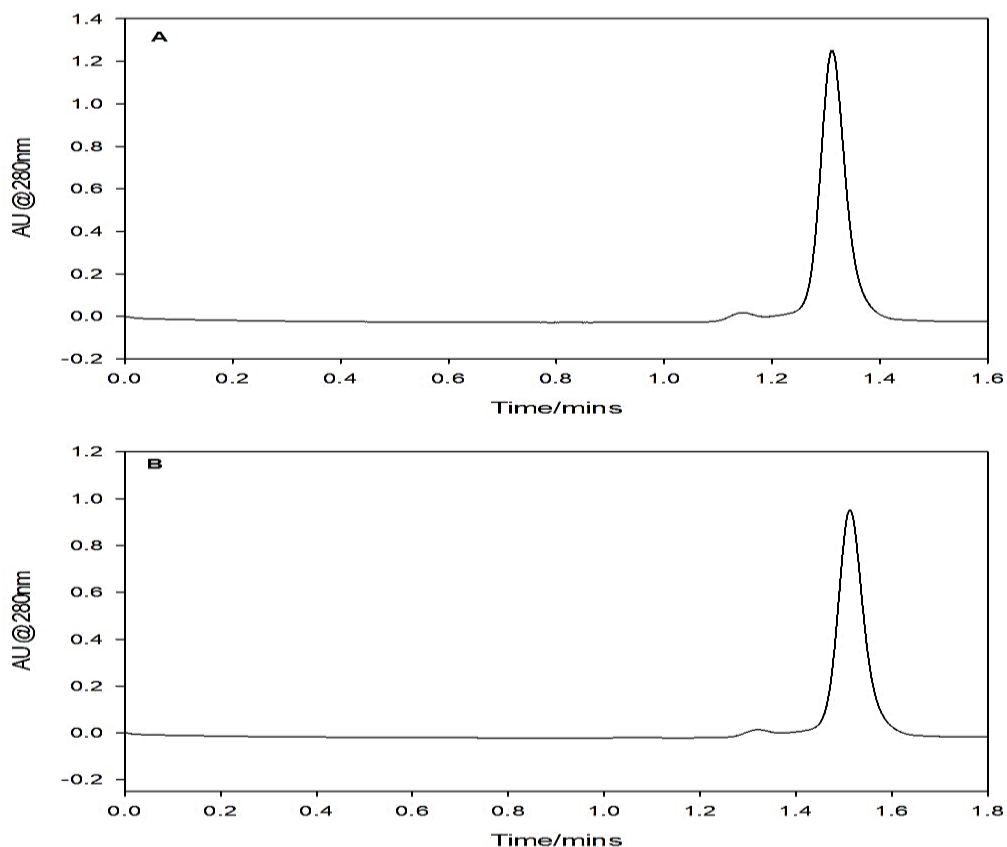


Figure 5.2: HPLC-UV analysis of U-II(S-S) reduction. (A) A chromatogram of 20 μ M U-II(S-S) was run as a standard and eluted at 1.32 mins. (B) 15 μ M U-II(S-H) in pH 3 water was incubated for 30 minutes in 600 μ M TCEP (40-fold excess), the product was eluted at 1.51 mins.

An increase in temperature from 25 - 50 $^{\circ}$ C resulted in a 5-fold enhancement in the rate of U-II autoxidation in acid media. Experiments at physiological pH gave U-II(SH) half-lives of 81 mins and 33.2 mins at 25 $^{\circ}$ C and 37 $^{\circ}$ C respectively. Metal chelators had an inhibitory effect on U-II(S-S) reformation.

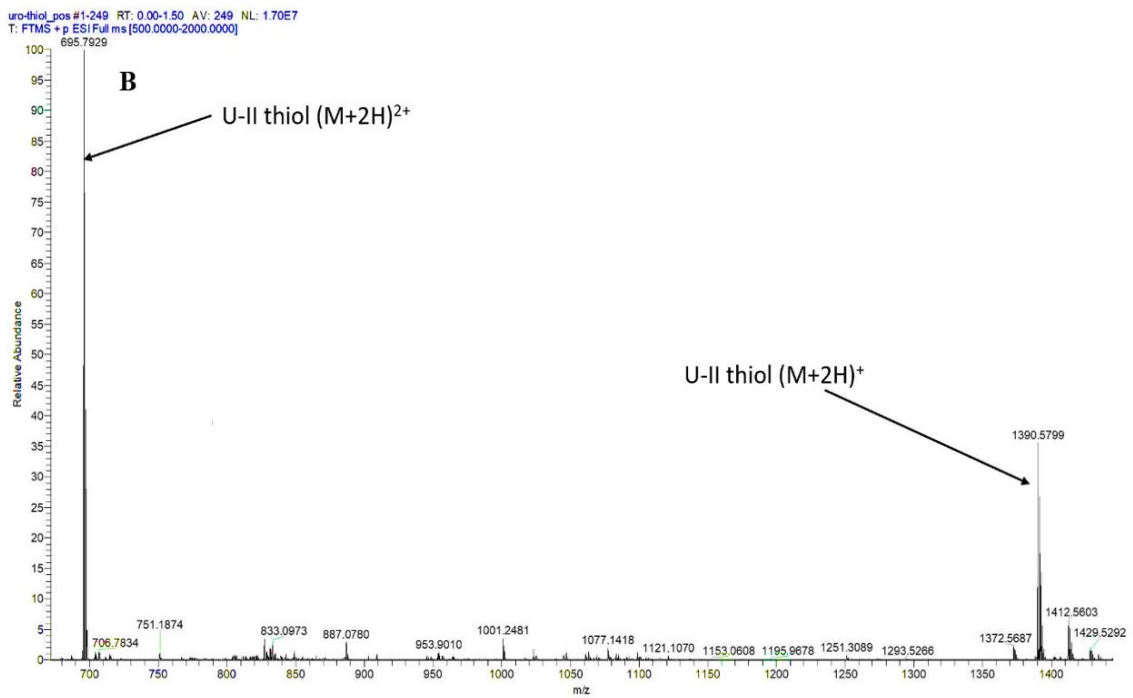
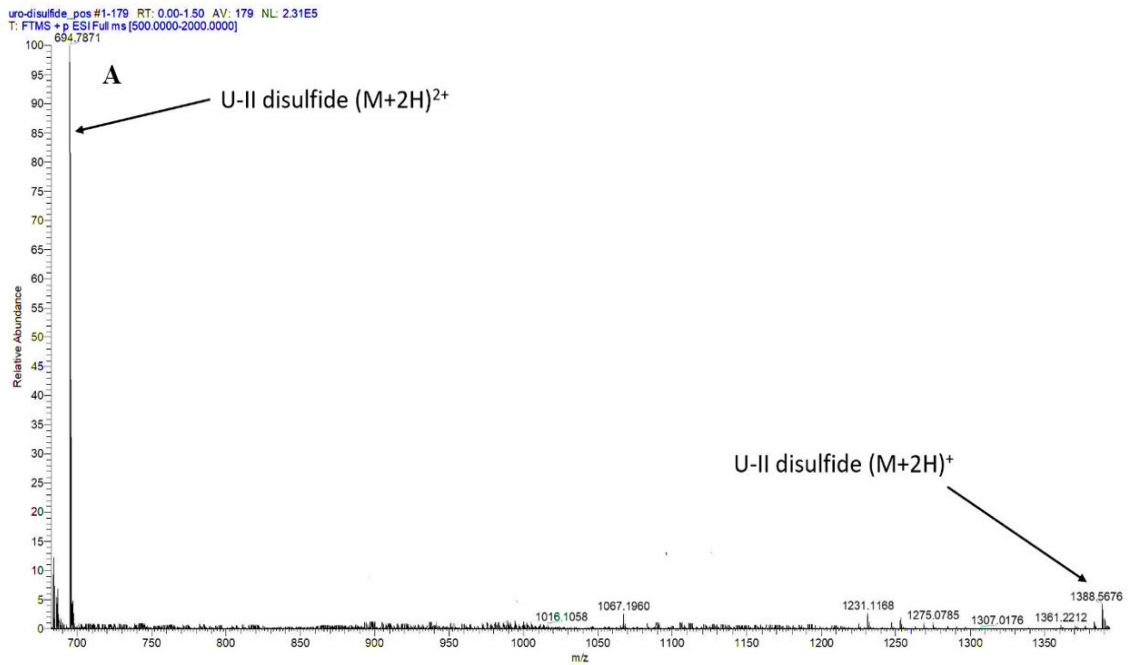


Figure 5.3: ESI-MS analysis of HPLC chromatograms in Fig 5.2. (A) ESI mass spectra confirmed chromatogram A as U-II disulfide. (B) ESI mass spectra confirms chromatogram B as U-II thiol.

Table 5.1. The effects of temperature, pH, and copper chelators on required for U-II(S-S) reformation.

Temperature	Time for disulfide reformation (>95%)		
	Water pH 3.0	30mM PBS, pH 7.4	30mM PBS, pH 7.4 + chelators
25°C	174hrs	81mins	20.3hrs
37°C	66hrs	33.2mins	9hrs
50°C	33.8hrs		

Data presented in Table 5.1 is applicable for chemical optimization strategies aimed at discovering therapeutic tools for disorders linked to U-II derivatives, peptides or nonpeptide analogues. Studies into structure-activity relationship pertaining to U-II(S-S)/(SH) exchange reactions would provide useful insights with regards to pharmacodynamic and pharmacokinetic properties that can be used to mitigate the accumulation of undesirable metabolites in tissues. It is still unclear how the stability of U-II(SH) affects U-II's affinity for the UT receptor. Advances in the optimization of oligopeptides as UT receptor antagonists are poised to lead to powerful pharmacological tools streamlining the role of autogenous U-II species in a plethora of pathophysiological processes. Based on the reported half-lives of U-II(SH) in Table 5.1 and the potential for co-localization with NO, we proceeded to investigate the possible subsequent S-nitrosylation reactions.

5.2.2 Reaction kinetics and thermodynamics

5.2.2.1 Nitrous acid mediated U-II(SH) S-nitrosylation. A multiscan UV spectrum of reactants and products depicts HNO_2 (Fig 5.4a) and NO_2^- (Fig 5.4b) with an absorptivity coefficient of $22.9 \text{ M}^{-1}\text{cm}^{-1}$ at 355 nm. The product of a reaction between U-II(SH) and HNO_2 , shows distinct absorbance peaks at 335 nm and 545 nm (Fig 5.4c) which are attributed to the S-nitrosothiol; U-II(SNO). The peaks for U-II(S-S) (Fig 5.4d) and U-II(SH) (Fig 5.4e) are depicted at 280 nm with absorptivity coefficients $7115 \text{ M}^{-1}\text{cm}^{-1}$ and $6990 \text{ M}^{-1}\text{cm}^{-1}$ respectively.

5.2.2.2 Effect of nitrite variation. The effect of NO_2^- variation on U-II(SNO) formation followed simple first order kinetics with regards to $[\text{NO}_2^-]_0$ (Fig 5.5).

5.2.2.3 Effect of acid on U-II(SNO) formation. The effect of acid variation adhered to similar trends as those reported for AVP(SH) and SST-14(SH) reactions with HNO_2 as seen in Figure 5.6. When $[\text{NO}_2^-]_0 > [\text{H}^+]_0$, the concentration of HNO_2 is the limiting reagent, and we observed a gradual increase in U-II(SNO) formation upon an increase in $[\text{H}^+]_0$ (Fig 5.6A, traces (a)-(c)). Traces (d)-(f) depict reaction conditions where $[\text{H}^+]_0 \geq [\text{NO}_2^-]_0$, with a continued increase in U-II(SNO) formation even with excess $[\text{H}^+]_0$, which implicates NO^+ mediated U-II(SNO) formation according to reaction R3.4.

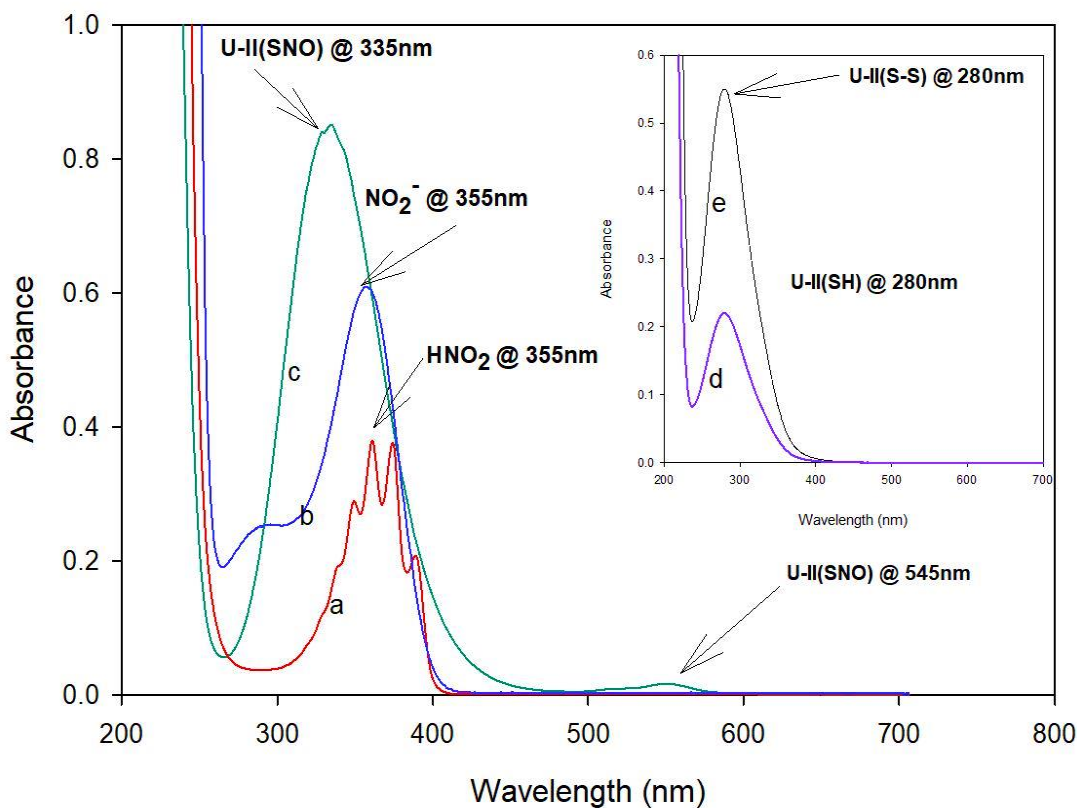


Figure 5.4: Spectra scan of; (a) $[\text{HNO}_2] = 16 \text{ mM}$, (b) $[\text{NO}_2^-] = 27 \text{ mM}$, (c) $[\text{U-II}] = 1 \text{ mM}$, $[\text{NO}_2^-] = 5 \text{ mM}$ and $[\text{H}^+] = 5 \text{ mM}$, (d) $[\text{U-II(S-S)}] = 77 \text{ }\mu\text{M}$ and (e) $\text{U-II(SH)} = 32 \text{ }\mu\text{M}$.

Initial rate plots gave a sigmoidal curve (Fig 5.6B) with a steep increase in U-II (SNO) formation corresponding to increase in $[\text{H}^+]_0$ when $[\text{NO}_2^-]_0 > [\text{H}^+]_0$, followed by an inflection point at $[\text{H}^+]_0 \geq [\text{NO}_2^-]_0$ (Fig 5.6B trace (d)), after which U-II (SNO) formation rates plateau due to U-II(S-H) depletion. Using Eq 3.7 (section 3.2.2.4) and Fig 5.6, we determined the bimolecular rate constants for U-II(SH) S-nitrosylation by HNO_2 and NO^+ to be $722 \pm 43 \text{ M}^{-1}\text{s}^{-1}$ and $1.3 \times 10^4 \text{ M}^{-1}\text{s}^{-1}$.

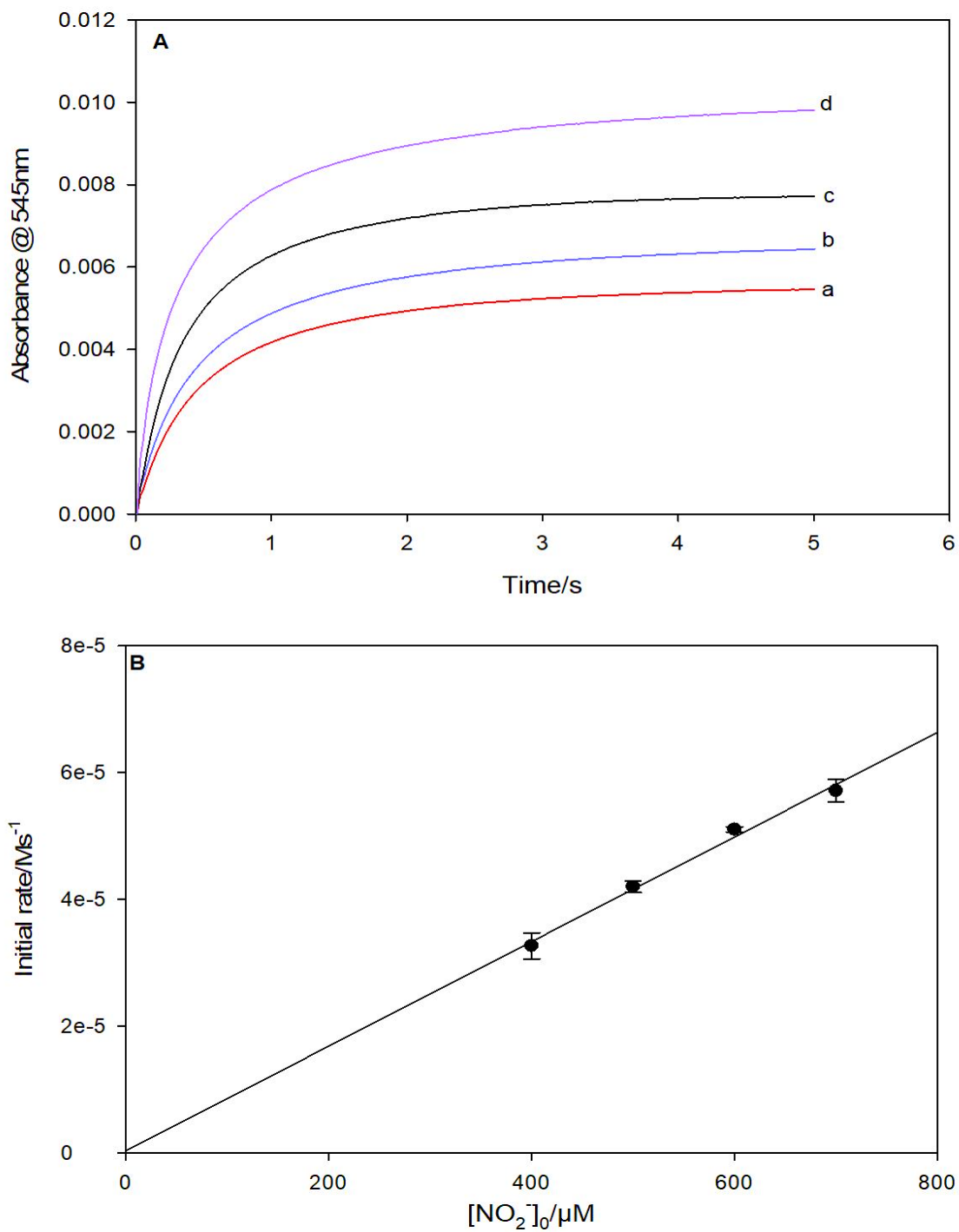


Figure 5.5: (A) Effect of $[\text{NO}_2^-]$ variation on U-II(SNO) formation. Fixed $[\text{H}^+] = 1 \text{ mM}$, $[\text{EDTA}] = 100 \mu\text{M}$, $[\text{U-II(S-S)}] = 1 \text{ mM}$. Varied $[\text{NO}_2^-] =$ (a) $400 \mu\text{M}$, (b) $500 \mu\text{M}$, (c) $600 \mu\text{M}$, (d) $700 \mu\text{M}$. (B) Initial rate plot shows strong dependence of U-II(SNO) formation on NO_2^- concentration.

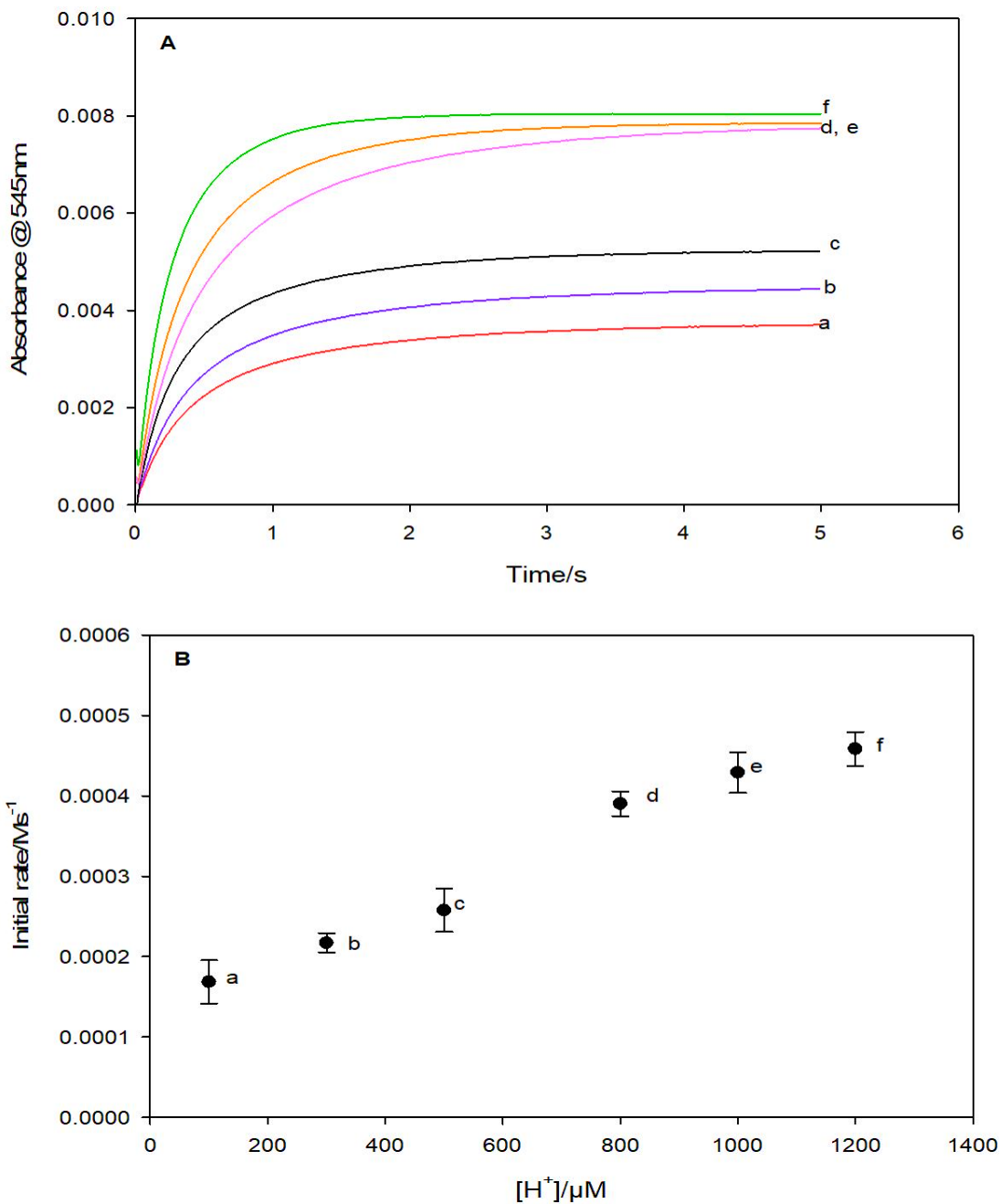


Figure 5.6: Effect of $[H^+]$ variation on U-II(SNO) formation. (A) Fixed $[U-II(SH)] = 800 \mu M$, $[EDTA] = 100 \mu M$, $[NO_2^-] = 800 \mu M$. Varied $[H^+] =$ (a) $100 \mu M$, (b) $300 \mu M$, (c) $500 \mu M$, (d) $800 \mu M$, (e) 1 mM , (f) 1.2 mM . (B) Initial rate plot shows 1^{st} -order dependence of U-II(SNO) formation initial rates on acid, with continued increase at high acid concentrations leading to saturation.

5.2.2.4 Effect of U-II(SH) variation. Increments in U-II(SH) concentrations resulted in increased rates of U-II(SNO) formation where $[\text{NO}_2^-]_0$ and $[\text{H}^+]_0 > [\text{U-II(SH)}]_0$ (Fig 5.7). Rate plots were linear with a first order dependence on $[\text{U-II(SH)}]$ with an intercept kinetically indistinguishable from zero (Fig 5.7B).

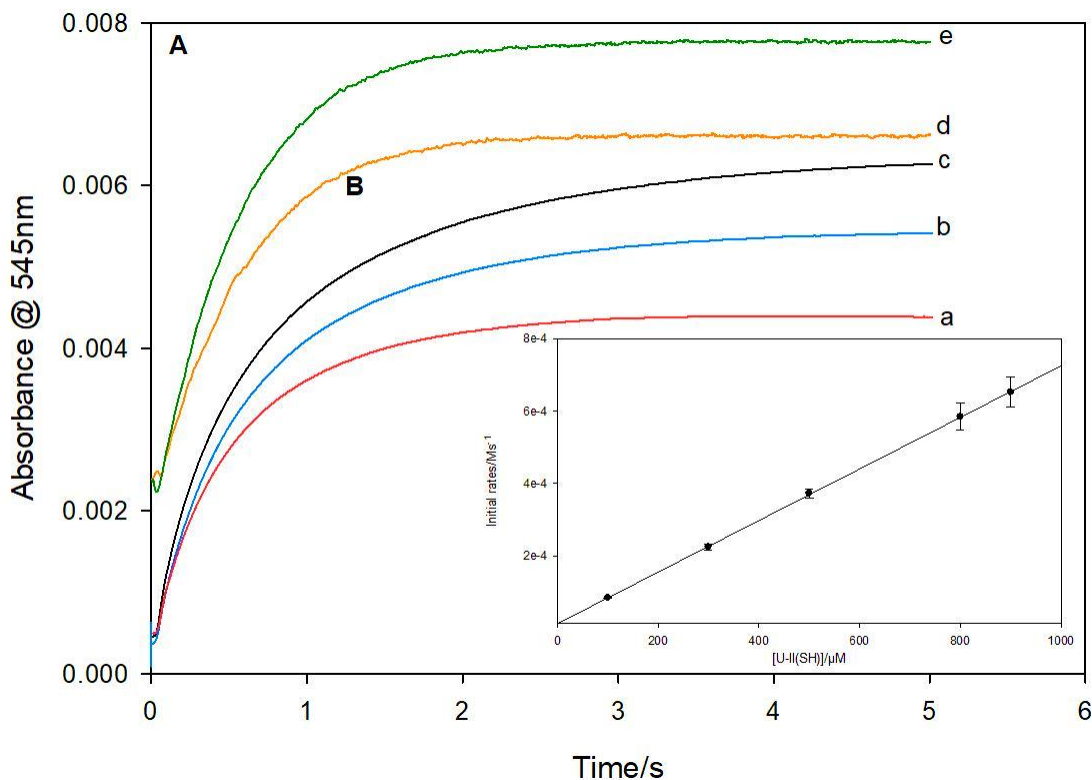


Figure 5.7: The reaction between U-II(SH) and HNO_2 exhibits 1st-order kinetics in U-II(SH). (A) Effect of varying U-II(SH) concentrations on U-II(SNO) formation. Fixed $[\text{NO}_2^-] = 1 \text{ mM}$, $[\text{EDTA}] = 100 \text{ } \mu\text{M}$, $[\text{H}^+] = 1 \text{ mM}$. Varied $[\text{U-II(SH)}] =$ (a) $100 \text{ } \mu\text{M}$, (b) $300 \text{ } \mu\text{M}$, (c) $500 \text{ } \mu\text{M}$, (d) $800 \text{ } \mu\text{M}$, (e) $900 \text{ } \mu\text{M}$. (B) Initial rate plots a linear dependence of U-II(SNO) formation rates on $[\text{U-II(SH)}]$.

5.2.2.5 Thermodynamic parameters for NO^+ mediated U-II(SNO) formation. Using methods described in section (section 3.2.2.5) and traces in Figure 5.6, we obtained Figure 5.8A which depicts a plot of varied $[\text{HNO}_2]$ against k_{obs} rates at each temperature, and derived k_{on} and k_{off} values (Table 5.2). Rates of k_{obs} for NO^+ mediated U-II(SNO) formation

were lower than those for SST-14(SNO) formation but within the same order of magnitude. The slope and intercept values from Arrhenius plots for k_{on} and k_{off} (Fig 5.8B and Fig 5.8C) respectively were used to calculate thermodynamic parameters; for k_{on} and k_{off} (Table 5.3).

Table 5.2. NO^+ mediated U-II S-nitrosylation observed rate constants: k_{on} and k_{off} .

Temp (°C)	k_{on} ($\text{M}^{-1}\text{s}^{-1}$)	k_{off} (s^{-1})
15	5.4 ± 0.1	89 ± 2.9
20	8 ± 0.2	107 ± 7.4
25	12.6 ± 0.4	161 ± 9
30	14 ± 1	196 ± 40
35	17.3 ± 0.5	288 ± 16

Table 5.3: NO^+ mediated U-II(SH) S-nitrosylation thermodynamic parameters.

	E_{a}^{a}	$\Delta G^{\ddagger\text{b}}$	$\Delta H^{\ddagger\text{c}}$	$\Delta S^{\ddagger\text{d}}$
k_{on}	42.8	67.9	40.3	-90
k_{off}	43.6	60.8	40.9	65

a, b and c Values are in kJ/mol, whilst **d** values are in $\text{J}\cdot\text{mol}^{-1}\text{K}^{-1}$. Temperature = 37°C **b**

A relatively poorer agreement was found with regards to the magnitude of ΔS^{\ddagger} values, as a result of experimental temperature fluctuations that led to some extrapolated values of ΔS^{\ddagger} being outside of standard deviations limits. Despite these shortcomings, our data gave constantly negative k_{on} entropy values for NO^+ mediated AVP(SNO), SST-14(SNO) and U-II(SNO) formation reactions, which further supports our evaluation of an associative mechanism with an unstable transition state. A strong agreement is shown with regards to positive k_{off} entropy values which describes a dissociative mechanism for target peptide SNO decompositions.

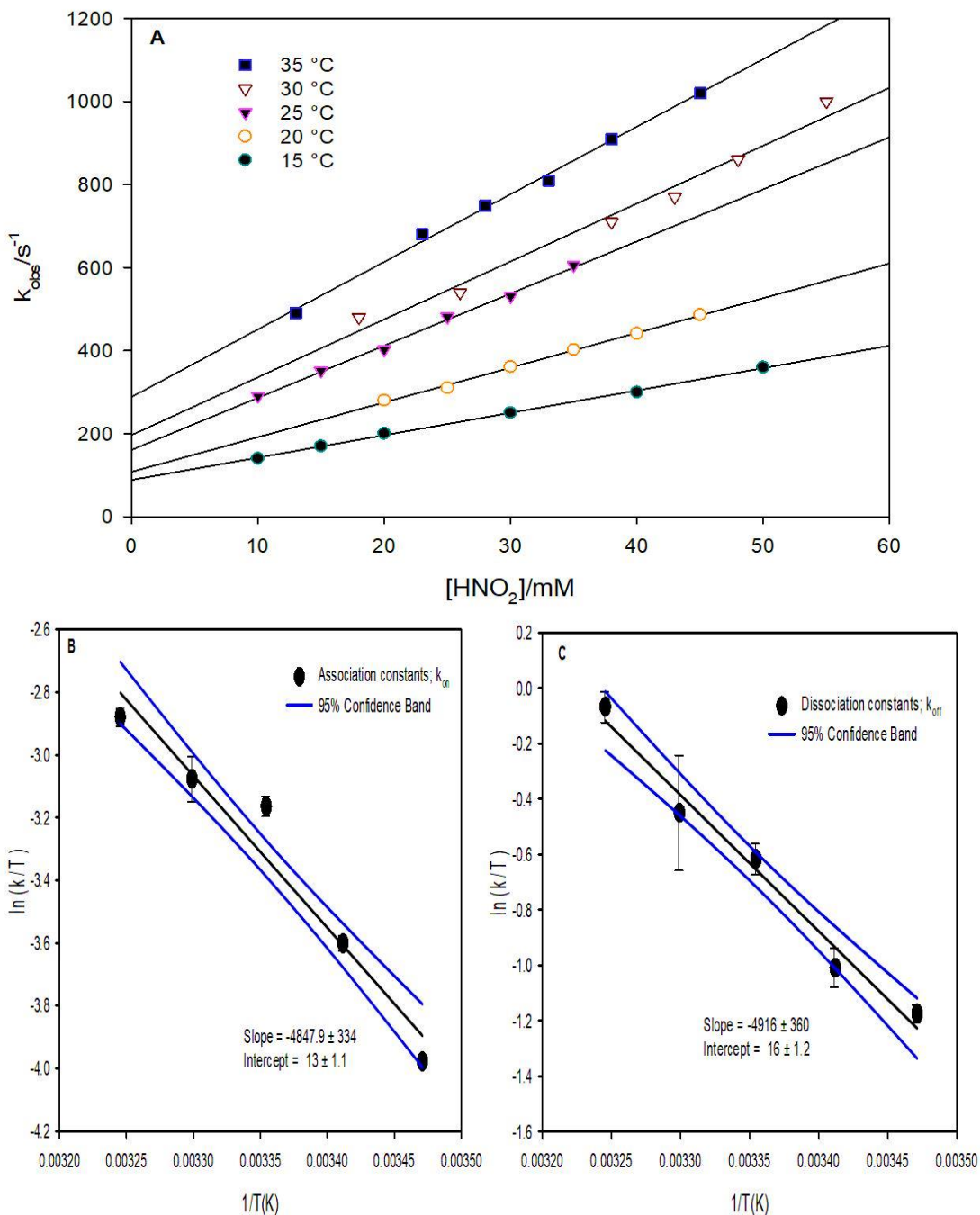


Figure 5.8: (A) Observed rate constants for the S-nitrosylation of U-II(SH) by varied HNO_2 concentrations. Fixed $[EDTA] = 100 \mu M$, $[U-II] = 1 mM$. Varied $[HNO_2]$ in the range 10-55 mM. (B) and (C) depicts linear Eyring plots from k_{on} and k_{off} values stated in Table 5.2 respectively.

5.2.3 Peroxynitrite-mediated U-II(SH) S-nitrosylation.

5.2.3.1 Effect of U-II(SH) variation. All ONOO⁻ mediated U-II(SH) S-nitrosylation kinetic experiments were conducted in mildly acidic media and at pH 7.4 in phosphate buffer according to reactions R3.10- R3.12. Depletion of ONOO⁻ was monitored as described in section 3.2.3. Rates of U-II(SNO) formation showed a linear first order dependence on [U-II(SH)] (Fig 5.10). We evaluated the bimolecular rate constant for the S-nitrosylation of U-II(SH) by ONOO⁻ to be $460 \pm 15 \text{ M}^{-1}\text{s}^{-1}$. Rates of ONOO⁻ depletion by U-II(SH) shows rapid autocatalytic decay kinetics with residual absorbance due to [ONOO⁻] in excess of that of [U-II(SH)] (Fig 5.11A). Rate plots gave a non-zero y-intercept corresponding to the rate of ONOO⁻ decomposition in the absence of U-II(SH) (Fig 5.11B).

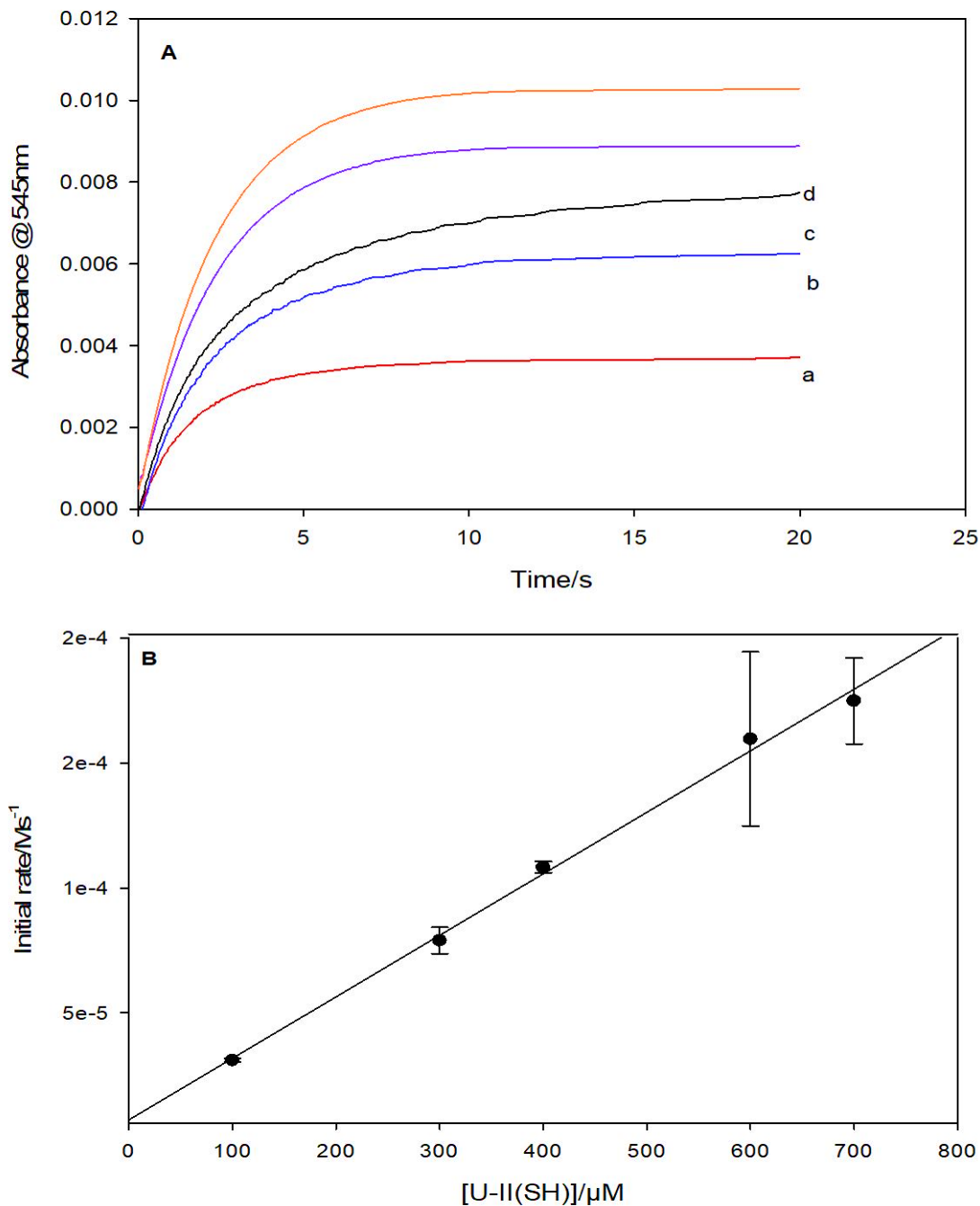


Figure 5.10: Effect of varying U-II(SH) concentration on U-II(SNO) formation in pH 7.4 PBS. Fixed [EDTA] = 100 μM , [ONOO⁻] = 1 mM. **(A)** Varied [U-II(SH)] = (a) 100 μM , (b) 300 μM , (c) 400 μM , (d) 600 μM , (e) 700 μM . **(B)** Shows linear relationship between initial rates of U-II(SNO) formation and U-II(SH) concentrations for traces in (A).

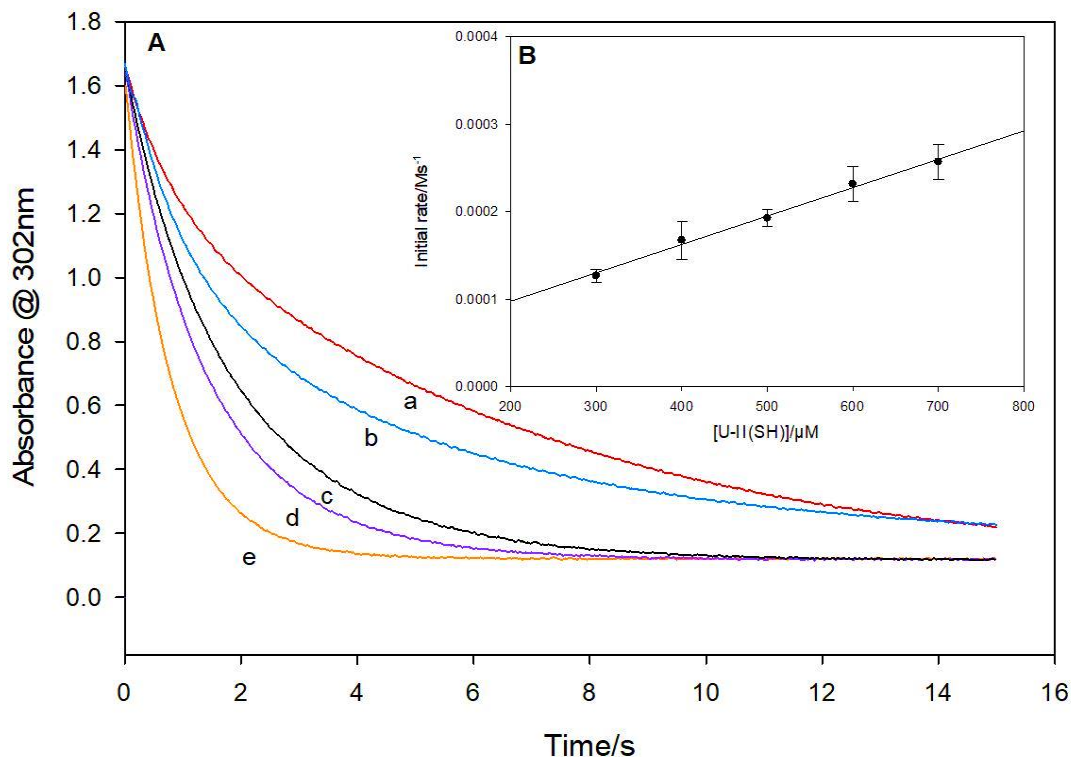


Figure 5.11: Effect of varying U-II(SH) concentration on ONOO⁻ depletion in pH 7.4 PBS. Fixed [EDTA] = 100 μM, [ONOO⁻] = 1 mM. **(A)** Varied [AVP(SH)] = (a) 300 μM, (b) 400 μM, (c) 500 μM, (d) 600 μM, (e) 700 μM. **(B)** Shows linear relationship between initial rates of ONOO⁻ depletion and U-II(SH) concentrations for traces in (A).

5.2.3.2 Effect of acid variation on ONOOH depletion and U-II(SNO) formation.

The rates of ONOO⁻ depletion by U-II(SH) increased with added acid concentrations as formation of the conjugate acid, ONOOH, catalyzed the reaction (Fig 5.12A). A nonlinear curve is obtained from initial rate plots (Fig 5.12B) for the reaction of U-II(SH) and ONOOH at 25°C. Kinetics of ONOOH mediated U-II(SNO) formation showed similar dependence on acid as previously described for AVP(SH) and SST-14(SH) reactions with ONOOH. Increasing acid where $[H^+] < [ONOO^-]$ (Fig 5.13) showed linearity characteristic of a direct function of increase in H^+ (Fig 5.13).

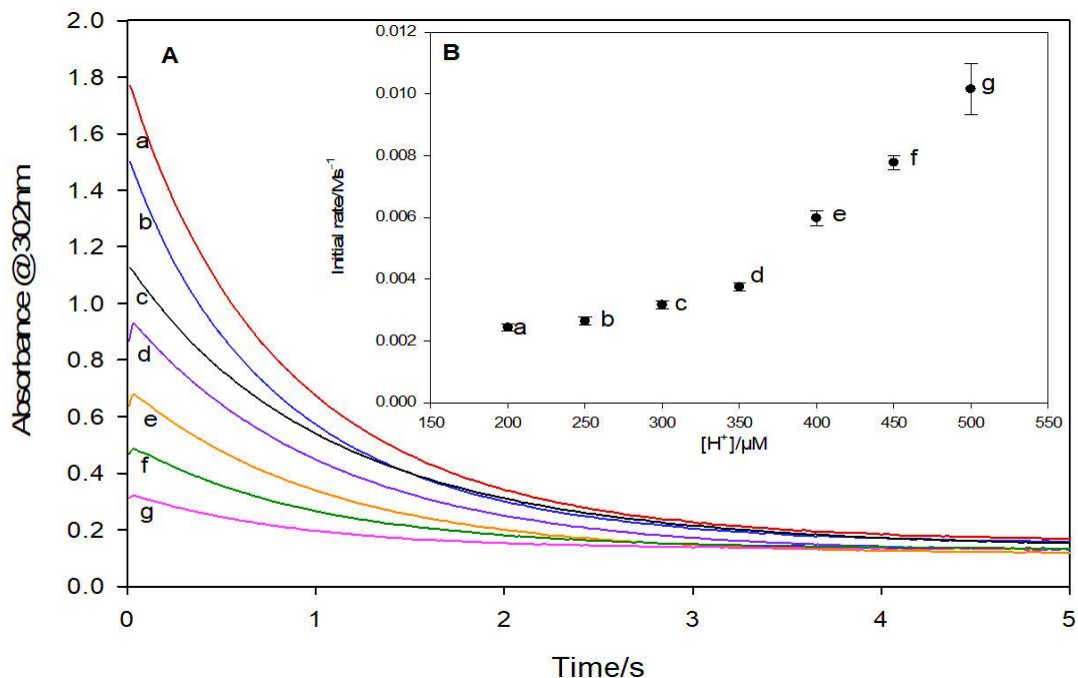


Figure 5.12: (A) Effect of varying H^+ concentration on $ONOO^-$ depletion. Fixed $[U-II(SH)] = 800 \mu M$, $[EDTA] = 100 \mu M$, $[ONOO^-] = 1 \text{ mM}$. Varied $[H^+] =$ (a) $200 \mu M$, (b) $250 \mu M$, (c) $300 \mu M$, (d) $350 \mu M$, (e) $400 \mu M$, (f) $450 \mu M$ and (g) $500 \mu M$ (B) Initial rates plot shows an exponential increase in $ONOO^-$ depletion with increased acid concentrations.

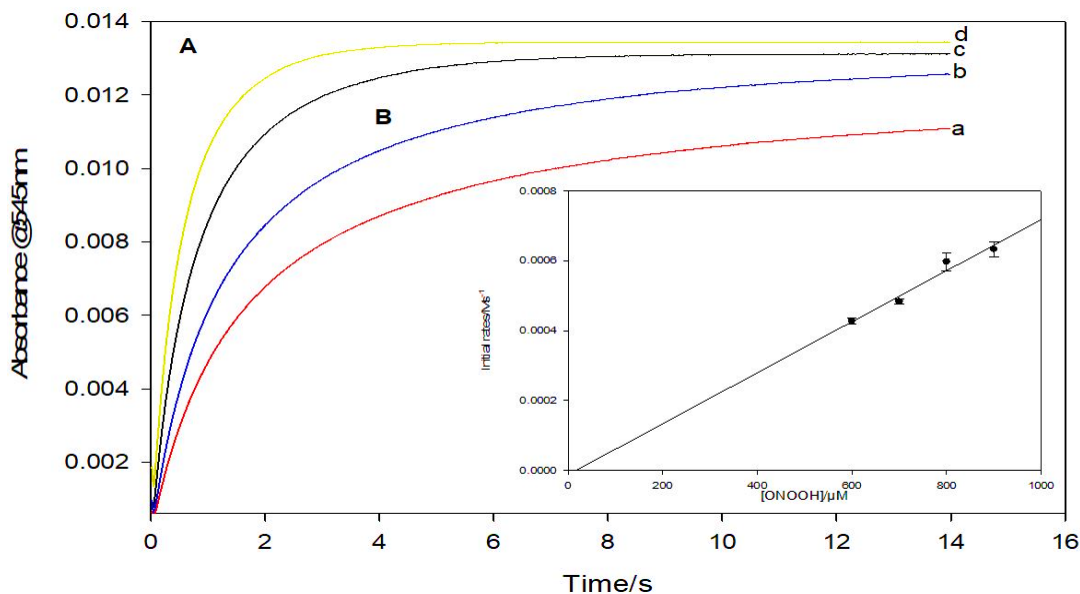


Figure 5.13: (A) Effect of varying H^+ concentration on $ONOO^-$ mediated $U-II(SNO)$ formation. Fixed $[U-II(SH)] = 1 \text{ mM}$, $[EDTA] = 100 \mu M$, $[ONOO^-] = 1 \text{ mM}$. Varied $[H^+] =$ (a) $600 \mu M$, (b) $700 \mu M$, (c) $800 \mu M$, (d) $900 \mu M$. (B) Initial rate plot shows a linear relationship between acid concentration and $U-II(SNO)$ formation

5.2.3.4 Peroxynitrite variation and EPR analysis. A familiar simple linear dependence on ONOO⁻ concentrations at pH 7.4 was also observed for the reaction with U-II(SH) in pH 7.4 phosphate buffer (Fig 5.14). Our data shows commonality in the manner ONOO⁻ reacts with target peptide thiols. These apparent second-order rate constants of ONOO⁻ with thiols are well described in literature, with numerous studies agreeing with our data that ONOO⁻ mediated thiol oxidation reaction mechanisms are first order in ONOO⁻ and the target²⁵⁸⁻²⁵⁹. EPR spectra with DMPO shows typical hydroxyl radical production from the Fenton's reaction as a control (Fig 5.15A). Figure 5.15; traces B-C, shows spectra similar to trace (A), with an increase in signal intensity that corresponds to added U-II(SH). Whilst Figure 5.15D, shows the quenching effect of adding the hydroxyl radical scavenger mannitol.

5.2.3.5 Thermodynamic parameters for ONOO⁻/ONOOH mediated U-II(SNO) formation. We ran traces in Figures 5.13 and 5.14 under pseudo-first-order conditions with 10-fold (10-55 mM) excess of ONOOH and ONOO⁻ respectively. Figure 5.16A, shows k_{obs} plots of ONOOH mediated U-II(SNO) formation. Surprisingly, we observed k_{obs} values for ONOOH (Table 5.4) that closely resembled those recorded for NO⁺ S-nitrosylations (Table 5.2). Derived thermodynamic parameters were; for k_{on} as $E_a = 37.2 \text{ kJmol}^{-1}$; $\Delta H^{\ddagger}_{on} = 42.7 \text{ kJ mol}^{-1}$ and $\Delta S^{\ddagger}_{on} = -80.3 \text{ J mol}^{-1} \text{ K}^{-1}$; for k_{off} these are $E_a = 45.1 \text{ kJmol}^{-1}$; $\Delta H^{\ddagger}_{off} = 38 \text{ kJ mol}^{-1}$ and $\Delta S^{\ddagger}_{off} = 155 \text{ J mol}^{-1} \text{ K}^{-1}$) (Table 5.5). Figure 5.17A, shows k_{obs} plots of ONOO⁻ mediated U-II(SNO) formation. As expected, observed k_{obs} values for ONOO⁻ (Table 5.6) are an order of magnitude smaller than ONOOH mediated S-nitrosylations (Table 5.4). Derived thermodynamic parameters were; for k_{on} as $E_a = 61.4 \text{ kJmol}^{-1}$; $\Delta H^{\ddagger}_{on} = 58.9 \text{ kJ mol}^{-1}$ and $\Delta S^{\ddagger}_{on} = -10 \text{ J mol}^{-1} \text{ K}^{-1}$; for k_{off} these are $E_a = 43 \text{ kJmol}^{-1}$; $\Delta H^{\ddagger}_{off} = 55 \text{ kJ mol}^{-1}$

and $\Delta S_{\text{off}}^{\ddagger} = 17 \text{ J mol}^{-1} \text{ K}^{-1}$) (Table 5.7).

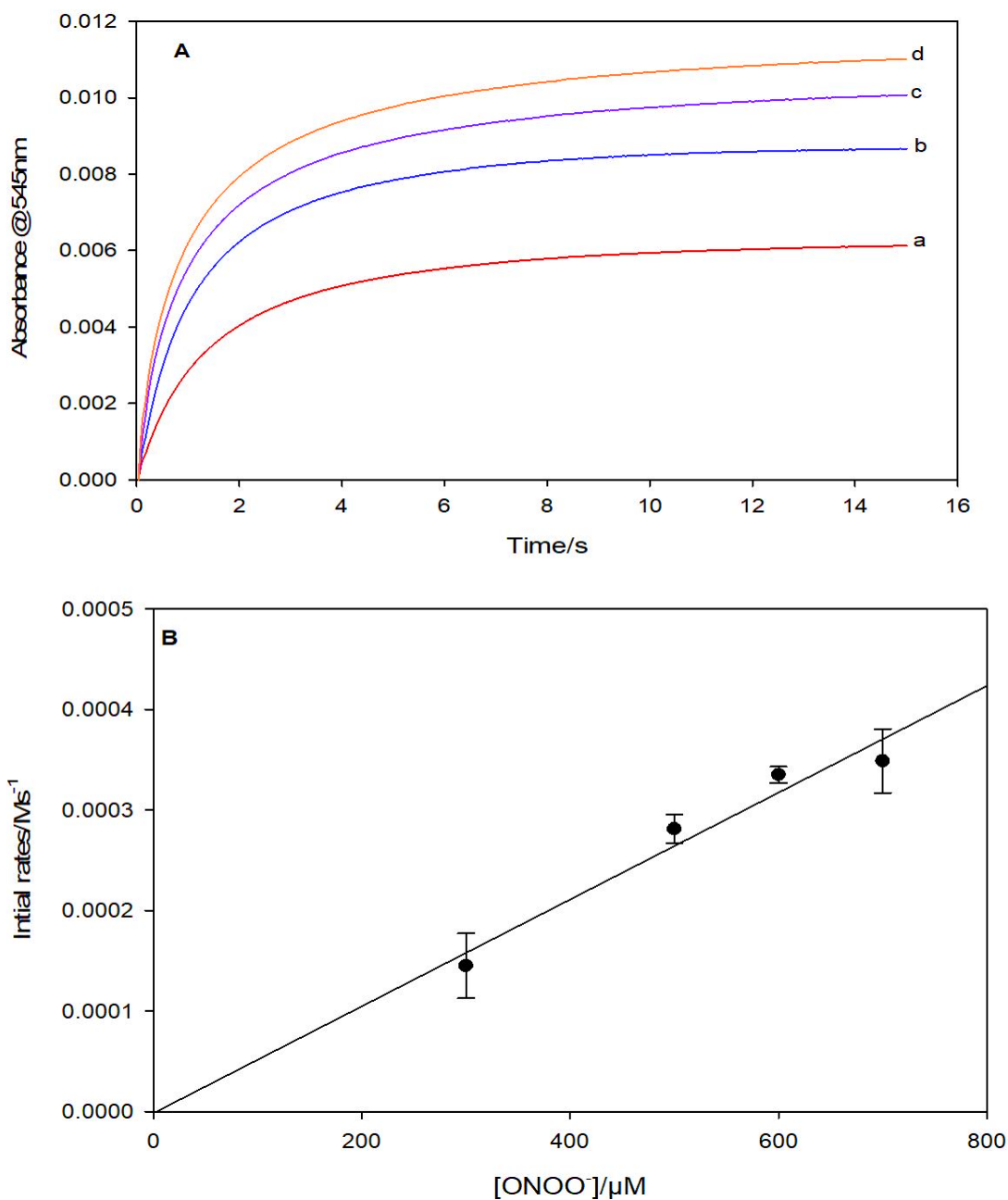


Figure 5.14: Effect of $[\text{ONOO}^-]$ variation on U-II(SNO) formation in phosphate buffer pH 7.4. Fixed $[\text{EDTA}] = 100 \mu\text{M}$, $[\text{U-II(SH)}] = 1 \text{ mM}$. (A) Varied $[\text{ONOO}^-] =$ (a) 300 μM , (b) 500 μM , (c) 600 μM , (d) 700 μM . (B) Shows linear relationship between initial rates of U-II(SNO) formation and ONOO^- concentrations for traces in (A).

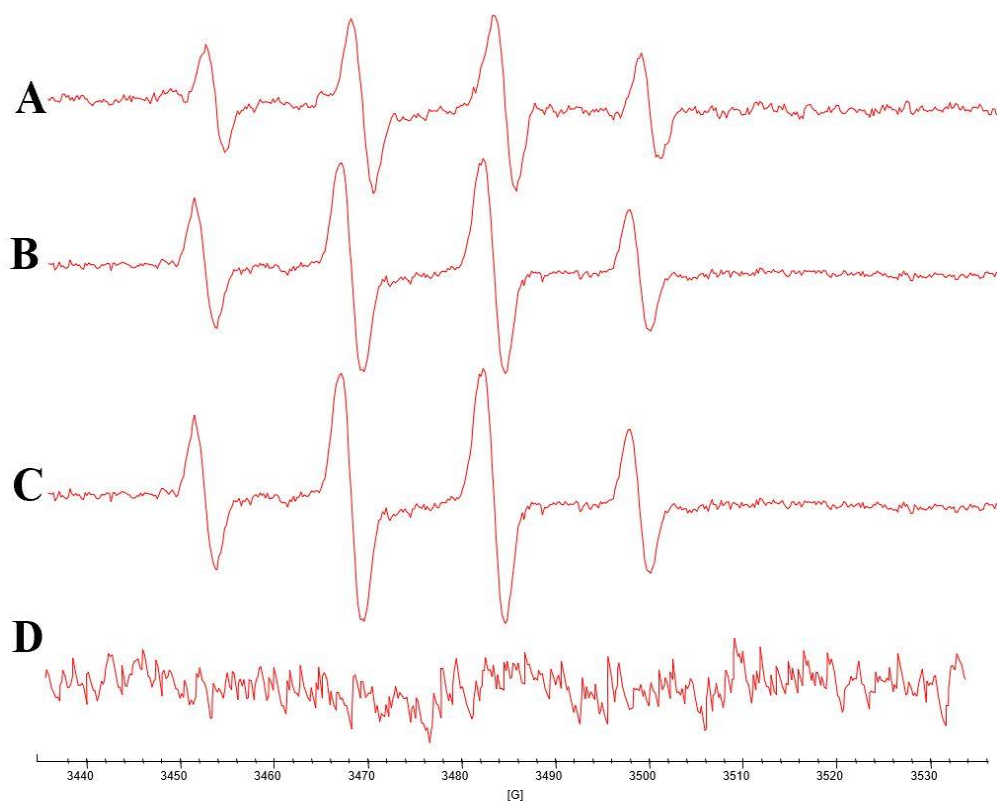


Figure 5.15: EPR spectra of OH radical adducts produced during ONOO⁻ mediated U-II(SNO) formation at pH 7.4. Spectra was collected immediately upon mixing reactants at room temperature. (A) Fenton's reaction; [H₂O₂] = 0.1M, [FeSO₄] = 0.025M, [DMPO]= 50 mM. Spectra (B-D) had fixed [ONOO⁻] = 1 mM, and [DMPO]= 50 mM. (B) [U-II(SH)] = 500 μM, (C) [U-II(SH)] = 700 μM. (D) [U-II(SH)] = 900 μM and [Mannitol]= 1.5 mM

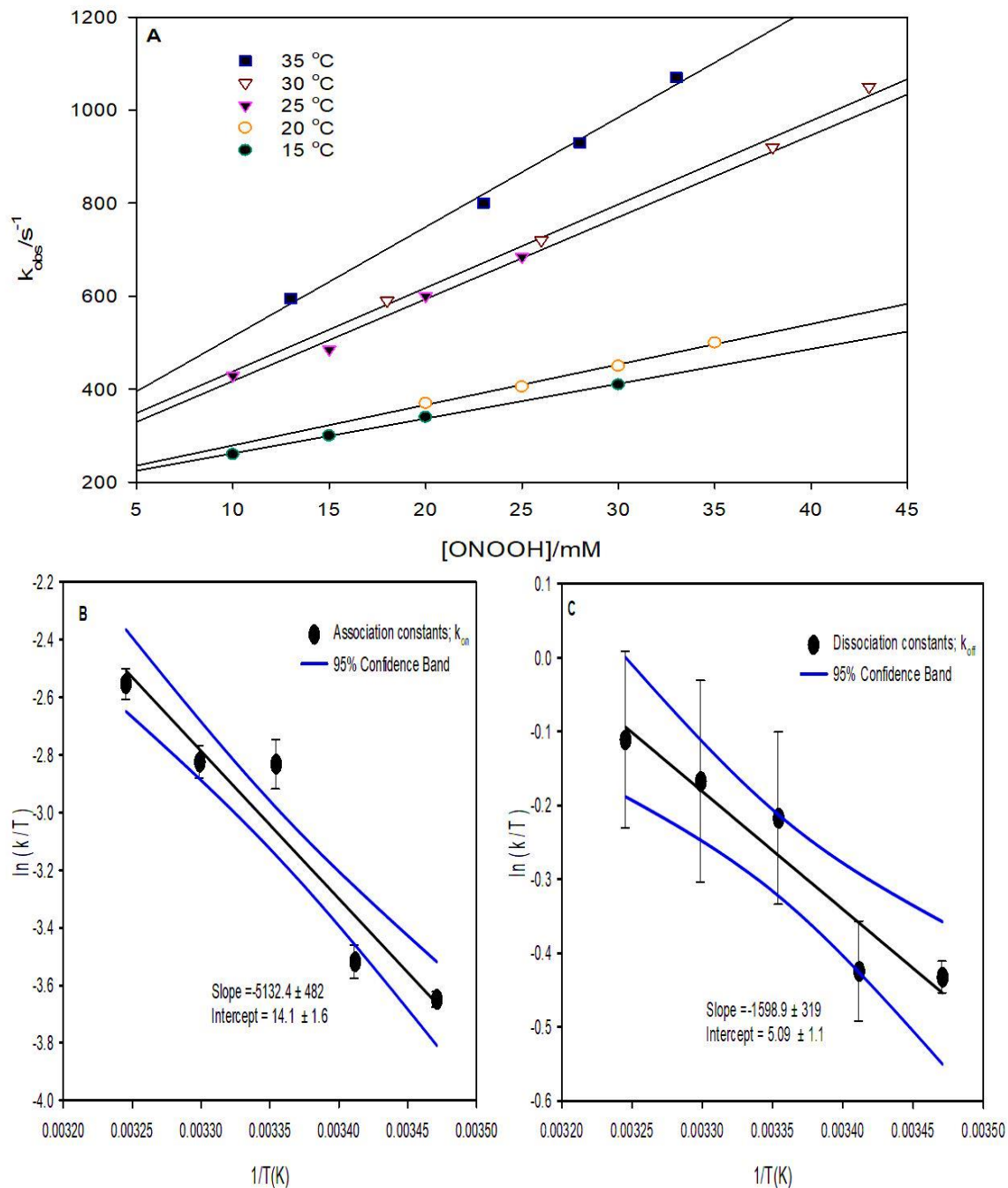


Figure 5.16: (A) Observed rate constants for the S-nitrosylation of U-II(SH) by varied ONOOH concentrations. Fixed [EDTA] = 100 μ M, [U-II(SH)] = 1 mM. Varied [ONOO⁻]: [H⁺] on a 1:1 ratio in the range 10-55 mM (B) and (C) depicts linear Eyring plots from k_{on} and k_{off} values that are stated Table 5.4 respectively.

Table 5.4: Observed rate constants for ONOOH mediated U-II(SH) thiol S-nitrosylation reactions.

Temp (°C)	k_{on} (M ⁻¹ s ⁻¹)	k_{off} (s ⁻¹)
15	7.5 ± 0.2	187 ± 4
20	8.7 ± 0.5	192 ± 13
25	17.6 ± 1.5	241 ± 28
30	18 ± 1	258 ± 35
35	24 ± 1.3	277 ± 33

Table 5.5: Thermodynamic parameters for ONOOH mediated U-II(SH) thiol S-nitrosylation reactions.

	E_a^a	ΔG^\ddagger^b	ΔH^\ddagger^c	ΔS^\ddagger^d
k_{on}	37.2	67.4	42.7	-80.3
k_{off}	45	61.1	38	155

^a, ^b and ^c Values are in kJ/mol, whilst ^d values are in J.mol⁻¹K⁻¹. Temperature = 37°C ^b

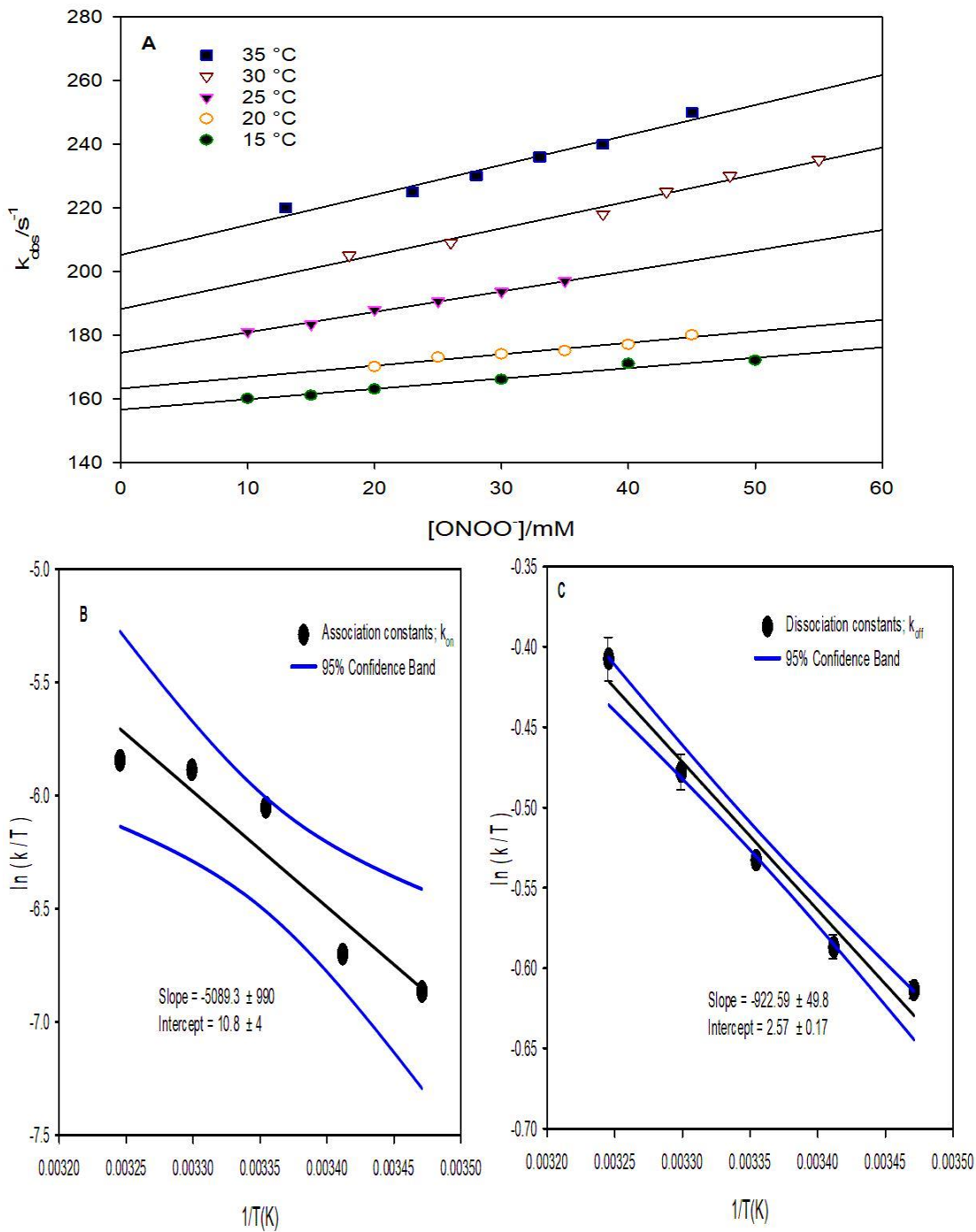


Figure 5.17: (A) Observed rate constants for the S-nitrosylation of U-II(SH) by varied ONOO⁻ concentrations over a broad temperature range of 15-35 °C in PBS at pH7.4. Fixed [EDTA] = 100 μM, [U-II(SH)] = 1 mM. Varied [ONOO⁻] in the range 10-55 mM (B) and (C) depicts linear Eyring plots from k_{on} and k_{off} values that are stated Table 5.6 respectively.

Table 5.6: Observed rate constants for ONOO⁻ mediated U-II(SH) thiol S-nitrosylation reactions.

Temp (°C)	k_{on} (M ⁻¹ s ⁻¹)	k_{off} (s ⁻¹)
15	0.3 ± 0.02	156 ± 0.8
20	0.36 ± 0.3	163 ± 1.2
25	0.7	175 ± 0.5
30	0.84 ± 0.05	188 ± 2.1
35	0.89 ± 0.07	205. ± 2.8

Table 5.7: Thermodynamic parameters for ONOO⁻ mediated U-II(SH) thiol S-nitrosylation reactions.

	Ea^a	ΔG^{‡b}	ΔH^{‡c}	ΔS^{‡d}
k_{on}	61.4	62.0	58.9	-10
k_{off}	43.0	49.8	55.0	17

^{a, b and c} Values are in kJ/mol, whilst ^d values are in J.mol⁻¹K⁻¹. Temperature = 37°C ^b

5.3 Conclusion. The reaction dynamics and mechanisms involved in U-II(SNO) formation through oxidation by HNO_2 and ONOO^- are similar to those reported in this study for AVP(SNO) and SST-14(SNO) formation reaction. In acidic media, the major nitrosants are HNO_2 and NO^+ , our kinetic data does not provide and evidence for the role of N_2O_3 as a nitrosating agent as reported in S-nitrosoglutathione (GSNO) formation from NO and excess glutathione²³¹. U-II(SNO) also seems to have sufficient half-life (~ 5s) under physiologically relevant conditions to be an efficient NO carrier. Copper catalyzed U-II(SNO) formation and decomposition suggesting a complex dynamic that is largely dependent on the presence of transition metal ions and cofactors in the physiological milieu. Even though our bimolecular rate constants for U-II(SNO) formation pale in comparison to those reported for GSNO, we propose that co-localization of U-II(SH) and NO would be the key to U-II(SNO) production *in vivo*. At pH 7.4, our data shows ONOO^- and SNAP as kinetically and thermodynamically favorable nitrosating agents with the potential reformation of disulfides in the case of ONOO^- . Oxidative mechanisms implicated in the etiology of heart failure and liver disease are curiously accompanied by upregulation in U-II expression²⁶⁰, it would be interesting to probe the possibility of a correlation between U-II thiol and U-II(SNO) formation with disease etiology.

CHAPTER 6: SUMMARY, CONCLUSIONS AND FUTURE PERSPECTIVES

6.1. SUMMARY

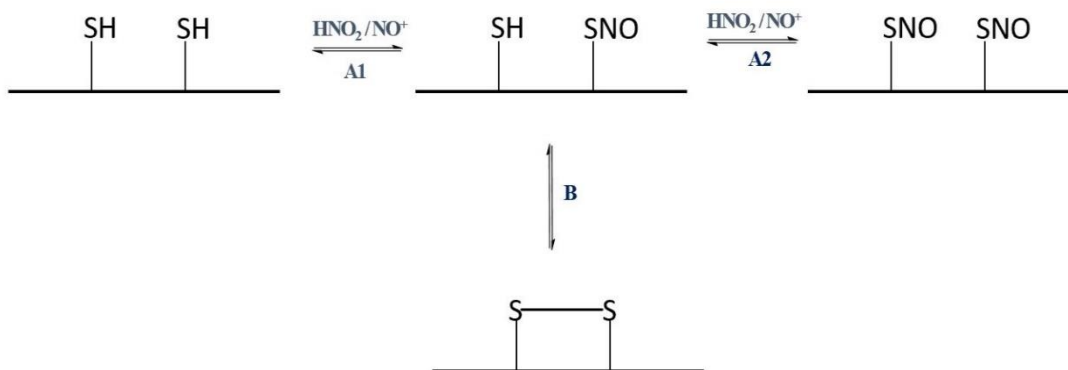
Peptide thiol stability and the formation of SNOs from neuropeptides; arginine vasopressin (AVP), somatostatin-14 (SST-14) and urotensin II (U-II) were studied. Investigations into the effects of temperature, copper chelators and pH on peptide disulfide reformation show that AVP, SST-14 and U-II thiols have half-lives of 30, 44 and 28.2 mins respectively at physiologically relevant temperature and pH in the absence of metal chelators. Target peptide thiols were shown to have half-lives sufficient for subsequent S-nitrosylation reactions.

This study also reports that S-nitrosothiols: AVP(SNO), SST-14(SNO) and U-II(SNO) are produced by HNO_2 and NO^+ mediated S-nitrosylations. The reaction dynamics suggest only four reactions (R3.3- R3.6) as being relevant in the production of SNOs by HNO_2 . Nitrite is initially protonated to produce HNO_2 followed by the production of NO^+ and the reaction of HNO_2/NO^+ with peptide thiols. Reported bimolecular rate constants suggests that HNO_2 and NO^+ would be efficient and the predominant nitrosating agents at low pH (Table 6.1). However, our data does not show a good correlation between primary peptide structure with increased susceptibility to S-nitrosylation.

Table 6.1: HNO_2/NO^+ mediated S-nitrosylations bimolecular rate constants ($\text{M}^{-1}\text{s}^{-1}$)

S-nitrosothiol	Nitrosating agent	
	HNO_2	NO^+
AVP(SNO)	278 ± 10	2.24×10^3
SST-14(SNO)	390 ± 56	8.7×10^4
U-II(SNO)	722 ± 43	1.3×10^4

Using Reactions R3.3- R3.6, together with HPLC-MS data we propose Scheme 6.1 for reactions occurring in solutions with peptide thiol and HNO_2/NO^+ ²⁶¹. At high HNO_2/NO^+ concentrations, pathway (A1-A2) would be favored, giving doubly S-nitrosylated SNO.



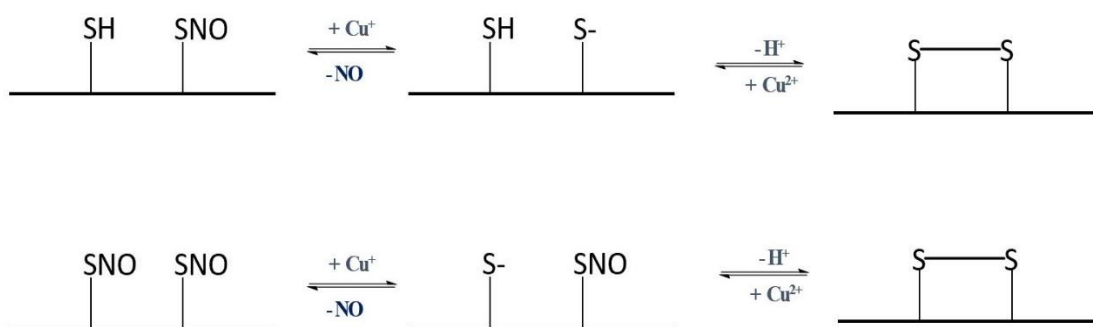
Scheme 6.1: Proposed reactions of peptide thiols with HNO_2

Pathway (B) resulting in disulfide reformation would be favored low HNO_2 and high thiol concentrations. Therefore, the intramolecular nucleophilic attack on the SNO sulfur occurs below the pKa of HNO_2 , even though thiols are usually much less reactive under acidic conditions. We have established that S-nitrosation of peptide thiols by HNO_2 at low pH

would be the most likely physiologically relevant S-nitrosylation/de-nitrosylation pathway.

Results from this study show the effectiveness of copper chelators; neocuproine (Cu^+) and DTPA (Cu^{2+}) in decelerating copper-catalyzed peptide thiol autoxidation. We also elucidated the competitive kinetics involved in both SNO formation and decomposition as discussed in terms of redox cycling that occurs between Cu^{2+} and Cu^+ (R3.1 and R3.2). We propose Scheme 6.2 for reactions involving copper catalyzed SNO decomposition^{109, 147,}

261.



Scheme 6.2: Proposed scheme for Cu^+ catalyzed SNO decomposition

Peroxynitrite mediated peptide SNO formation reactions are complex with two distinct nitrosating agents; (i) ONOO^- (at pH 7.4) and (ii) ONOOH with possibly HNO_2 in acidic media. The kinetics and mechanism of peroxynitrite S-nitrosylation reactions were characterized by rapid SNO formation, with acid as a catalyst for both SNO formation and decomposition. The reaction dynamics observed in this study implicates eight reactions (R4.1 – R4.8) as being the most relevant in ONOO^- mediated S-nitrosylation reactions.

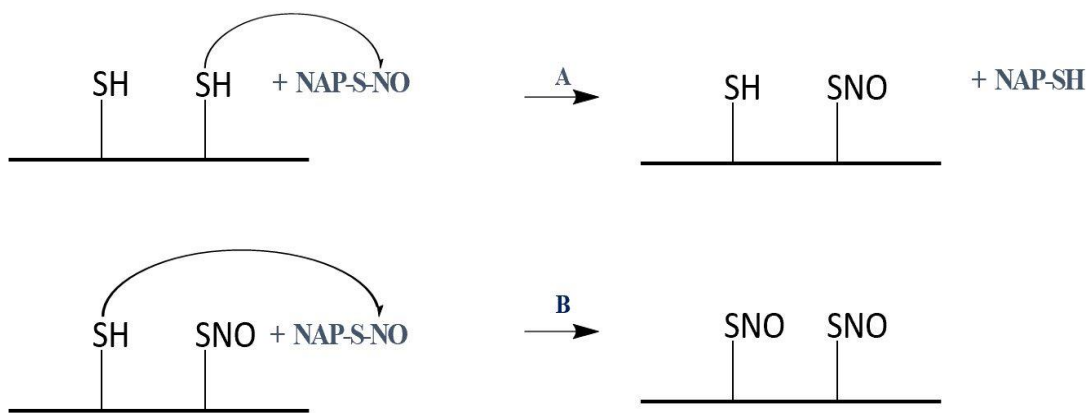
Bimolecular rate constants for ONOO⁻/ONOOH mediated S-nitrosylations (Table 6.2), depict ONOOH as a more robust nitrosating agent than its conjugate base, largely due to formation of HNO₂ which leads to increased SNO production (R 4.7 and R 4.8). Our data suggests novel roles for peptide thiols as antioxidant species that counteract damaging effects of RNOS. The neuropeptides in this study may serve as efficient scavengers which would effectively mop up excess peroxynitrite and mitigate peroxynitrite-induced oxidative injury. The reported half-lives of peptide SNOs, suggests that these neuropeptides may also have crucial roles as carriers and reservoirs for NO bioactivity in the physiological environments. Studies report that endogenous S-nitrosohaemoglobin has an essential role in regulating blood homeostasis, whilst SNAP inhibits platelet aggregation and facilitates vasodilation²⁶²⁻²⁶³.

Table 6.2: Bimolecular rate constants (M⁻¹s⁻¹) for ONOO⁻/ONOOH mediated S-nitrosylations

S-nitrosothiols	Nitrosating agents	
	ONOO ⁻	ONOOH
AVP(SNO)	884 ± 31	1.72 x 10 ⁴
SST-14(SNO)	308 ± 24	1.55 x 10 ³
U-II(SNO)	572 ± 45	2.4 x 10 ³

Our results suggest that transfer of NO from RSNO to thiols is a direct process without the formation of free NO as an intermediate. We propose that nucleophilic attack by peptide sulfhydryl's on RSNO is fast (as evidence by kinetic data) and facile under physiological

conditions and insensitive to transition metal ions (R3.21). We therefore propose Scheme 6.3 for elementary two consecutive steps (A-B) involved peptide thiol transnitrosation by SNAP leading to the production either singly and/or doubly S-nitrosylated SNOs^{182, 206, 261}. The main factors that govern whether singly/doubly S-nitrosylated SNOs are formed is largely dependent on reactant concentrations, peptide sequence, hydrophobicity and electronic environment. The highly negative activation entropy for transnitrosation reaction suggests that these rate-limiting elementary steps of the transnitrosylation process are characterized by a relatively ordered associative transition state. These activation parameters suggest low energy barriers for transnitrosylation under physiological conditions and support growing evidence that transnitrosylation may be a viable posttranslational mechanism for NO transport *in vivo*.



Scheme 6.3: Proposed mechanism for reactions involving peptide thiol transnitrosation by SNAP.

6.2. CONCLUSIONS AND FUTURE PERSPECTIVES

This dissertation presents neuropeptide RSNOs as good candidates deserving of more attention as efficient NO carrier and donor compounds for numerous diagnostic and therapeutic applications. The rapid decomposition rates of these SNOs at physiological pH 7.4, may limit applicability as biomedical tools but slight modifications in structure could prolong their durability. This could be accomplished by covalently bonding RSNOs to the polymer backbone of hydrophobic macromolecules. Kinetic and thermodynamic parameters outlined in this work can serve as the basis for developing these polymers. The observed catalytic effect of Cu^{2+} and Cu^+ in stimulating SNO formation and decomposition respectively can be used to designing biomedical devices with the capacity for gradual and continuous release of NO. Further work could include *in vivo* detection of these neuropeptide SNOs. Since AVP, SST-14 and U-II are hormones that can be detected and isolated from biological fluids, it would be immensely informative to conduct a comparison of cross-reactivities between neuropeptide immunoglobulins and neuropeptide thiol and S-nitrosothiol species. Antibodies could be designed specifically against the thiol and SNO species to detect these species *in vivo*. Additional, *in vitro* studies could be performed using recombinant peptide receptors, where the affinity and specificity of disulfide, thiol and SNO species could be evaluated.

This dissertation provides essential insights regarding kinetic, thermodynamic and mechanistic parameters of novel neuropeptide S-nitrosylation reactions as well as an analysis of SNO stabilities of that can aid in the design of SNOs with better pharmacokinetic properties. The protocols, kinetic models and thermodynamic parameters

from this study are expected to elucidate key steps toward understanding mechanistic processes by which S-nitrosylation may alter neuropeptide protein function. Researchers can use these insights in the development of potential therapeutics that target endogenous SNOs, and/or utilize synthetic SNOs to stimulate or inhibit NO-signaling in pathologies in where NO-signaling is clearly implicated. Kinetic models presented in this work can be used to infer the NO release profile of potential NO-donor based drugs by enhancing our understanding of the underlying pharmacokinetics.

REFERENCES

1. Bredt, D. S.; Snyder, S. H., Nitric oxide: a physiologic messenger molecule. *Annu Rev Biochem* **1994**, *63*, 175-95.
2. Furchgott, R. F.; Zawadzki, J. V., The obligatory role of endothelial cells in the relaxation of arterial smooth muscle by acetylcholine. *Nature* **1980**, *288* (5789), 373-6.
3. Stuehr, D. J.; Tejero, J.; Haque, M. M., Structural and mechanistic aspects of flavoproteins: electron transfer through the nitric oxide synthase flavoprotein domain. *FEBS J* **2009**, *276* (15), 3959-74.
4. Aoyagi, M.; Arvai, A. S.; Tainer, J. A.; Getzoff, E. D., Structural basis for endothelial nitric oxide synthase binding to calmodulin. *EMBO J* **2003**, *22* (4), 766-75.
5. Panda, K.; Ghosh, S.; Stuehr, D. J., Calmodulin activates intersubunit electron transfer in the neuronal nitric-oxide synthase dimer. *J Biol Chem* **2001**, *276* (26), 23349-56.
6. Stuehr, D. J.; Kwon, N. S.; Nathan, C. F.; Griffith, O. W.; Feldman, P. L.; Wiseman, J., N omega-hydroxy-L-arginine is an intermediate in the biosynthesis of nitric oxide from L-arginine. *J Biol Chem* **1991**, *266* (10), 6259-63.
7. Klatt, P.; Schmidt, K.; Uray, G.; Mayer, B., Multiple catalytic functions of brain nitric oxide synthase. Biochemical characterization, cofactor-requirement, and the role of N omega-hydroxy-L-arginine as an intermediate. *J Biol Chem* **1993**, *268* (20), 14781-7.
8. Keshet, R.; Erez, A., Arginine and the metabolic regulation of nitric oxide synthesis in cancer. *Dis Model Mech* **2018**, *11* (8).
9. Boucher, J. L.; Moali, C.; Tenu, J. P., Nitric oxide biosynthesis, nitric oxide synthase inhibitors and arginase competition for L-arginine utilization. *Cell Mol Life Sci* **1999**, *55* (8-9), 1015-28.
10. Kuboniwa, H.; Tjandra, N.; Grzesiek, S.; Ren, H.; Klee, C. B.; Bax, A., Solution structure of calcium-free calmodulin. *Nat Struct Biol* **1995**, *2* (9), 768-76.
11. Habib, S.; Ali, A., Biochemistry of nitric oxide. *Indian J Clin Biochem* **2011**, *26* (1), 3-17.
12. Forstermann, U.; Sessa, W. C., Nitric oxide synthases: regulation and function. *Eur Heart J* **2012**, *33* (7), 829-37, 837a-837d.
13. White, K. A.; Marletta, M. A., Nitric oxide synthase is a cytochrome P-450 type hemoprotein. *Biochemistry* **1992**, *31* (29), 6627-31.
14. Knott, A. B.; Bossy-Wetzel, E., Nitric oxide in health and disease of the nervous system. *Antioxid Redox Signal* **2009**, *11* (3), 541-54.
15. Boulton, C. L.; Southam, E.; Garthwaite, J., Nitric oxide-dependent long-term potentiation is blocked by a specific inhibitor of soluble guanylyl cyclase. *Neuroscience* **1995**, *69* (3), 699-703.
16. Schuman, E. M.; Madison, D. V., A requirement for the intercellular messenger nitric oxide in long-term potentiation. *Science* **1991**, *254* (5037), 1503-6.
17. Shibuki, K.; Okada, D., Endogenous nitric oxide release required for long-term synaptic depression in the cerebellum. *Nature* **1991**, *349* (6307), 326-8.
18. Hardingham, N.; Fox, K., The role of nitric oxide and GluR1 in presynaptic and postsynaptic components of neocortical potentiation. *J Neurosci* **2006**, *26* (28), 7395-404.
19. East, S. J.; Garthwaite, J., NMDA receptor activation in rat hippocampus induces cyclic GMP formation through the L-arginine-nitric oxide pathway. *Neurosci Lett* **1991**, *123* (1), 17-9.
20. Southam, E.; East, S. J.; Garthwaite, J., Excitatory amino acid receptors coupled to the nitric oxide/cyclic GMP pathway in rat cerebellum during development. *J Neurochem* **1991**, *56* (6), 2072-81.
21. Bruning, G., NADPH-diaphorase histochemistry in the postnatal mouse cerebellum suggests specific developmental functions for nitric oxide. *J Neurosci Res* **1993**, *36* (5), 580-7.
22. Gouge, R. C.; Marshburn, P.; Gordon, B. E.; Nunley, W.; Huet-Hudson, Y. M., Nitric oxide

as a regulator of embryonic development. *Biol Reprod* **1998**, *58* (4), 875-9.

23. Kalb, R. G.; Agostini, J., Molecular evidence for nitric oxide-mediated motor neuron development. *Neuroscience* **1993**, *57* (1), 1-8.
24. Hillier, B. J.; Christopherson, K. S.; Prehoda, K. E.; Bredt, D. S.; Lim, W. A., Unexpected modes of PDZ domain scaffolding revealed by structure of nNOS-syntrophin complex. *Science* **1999**, *284* (5415), 812-5.
25. Brown, T. H.; Chapman, P. F.; Kairiss, E. W.; Keenan, C. L., Long-term synaptic potentiation. *Science* **1988**, *242* (4879), 724-8.
26. Garthwaite, J.; Charles, S. L.; Chess-Williams, R., Endothelium-derived relaxing factor release on activation of NMDA receptors suggests role as intercellular messenger in the brain. *Nature* **1988**, *336* (6197), 385-8.
27. Arnold, W. P.; Mittal, C. K.; Katsuki, S.; Murad, F., Nitric oxide activates guanylate cyclase and increases guanosine 3':5'-cyclic monophosphate levels in various tissue preparations. *Proc Natl Acad Sci U S A* **1977**, *74* (8), 3203-7.
28. Brenman, J. E.; Chao, D. S.; Gee, S. H.; McGee, A. W.; Craven, S. E.; Santillano, D. R.; Wu, Z.; Huang, F.; Xia, H.; Peters, M. F.; Froehner, S. C.; Bredt, D. S., Interaction of nitric oxide synthase with the postsynaptic density protein PSD-95 and alpha1-syntrophin mediated by PDZ domains. *Cell* **1996**, *84* (5), 757-67.
29. Valtschanoff, J. G.; Weinberg, R. J., Laminar organization of the NMDA receptor complex within the postsynaptic density. *J Neurosci* **2001**, *21* (4), 1211-7.
30. Burette, A.; Zabel, U.; Weinberg, R. J.; Schmidt, H. H.; Valtschanoff, J. G., Synaptic localization of nitric oxide synthase and soluble guanylyl cyclase in the hippocampus. *J Neurosci* **2002**, *22* (20), 8961-70.
31. Russwurm, M.; Wittau, N.; Koesling, D., Guanylyl cyclase/PSD-95 interaction: targeting of the nitric oxide-sensitive alpha2beta1 guanylyl cyclase to synaptic membranes. *J Biol Chem* **2001**, *276* (48), 44647-52.
32. Olthof, B. M. J.; Gartside, S. E.; Rees, A., Puncta of Neuronal Nitric Oxide Synthase (nNOS) Mediate NMDA Receptor Signaling in the Auditory Midbrain. *J Neurosci* **2019**, *39* (5), 876-887.
33. Endoh, M.; Maiese, K.; Wagner, J. A., Expression of the neural form of nitric oxide synthase by CA1 hippocampal neurons and other central nervous system neurons. *Neuroscience* **1994**, *63* (3), 679-89.
34. Ono, M.; Bishop, D. C.; Oliver, D. L., Long-Lasting Sound-Evoked Afterdischarge in the Auditory Midbrain. *Sci Rep* **2016**, *6*, 20757.
35. Ito, T.; Bishop, D. C.; Oliver, D. L., Functional organization of the local circuit in the inferior colliculus. *Anat Sci Int* **2016**, *91* (1), 22-34.
36. Calabrese, V.; Mancuso, C.; Calvani, M.; Rizzarelli, E.; Butterfield, D. A.; Stella, A. M., Nitric oxide in the central nervous system: neuroprotection versus neurotoxicity. *Nat Rev Neurosci* **2007**, *8* (10), 766-75.
37. Aquilano, K.; Baldelli, S.; Rotilio, G.; Ciriolo, M. R., Role of nitric oxide synthases in Parkinson's disease: a review on the antioxidant and anti-inflammatory activity of polyphenols. *Neurochem Res* **2008**, *33* (12), 2416-26.
38. Choi, S.; Won, J. S.; Carroll, S. L.; Annamalai, B.; Singh, I.; Singh, A. K., Pathology of nNOS-Expressing GABAergic Neurons in Mouse Model of Alzheimer's Disease. *Neuroscience* **2018**, *384*, 41-53.
39. Sharma, N. M.; Patel, K. P., Post-translational regulation of neuronal nitric oxide synthase: implications for sympathoexcitatory states. *Expert Opin Ther Targets* **2017**, *21* (1), 11-22.
40. Mattila, J. T.; Thomas, A. C., Nitric oxide synthase: non-canonical expression patterns. *Front Immunol* **2014**, *5*, 478.

41. Nathan, C. F.; Hibbs, J. B., Jr., Role of nitric oxide synthesis in macrophage antimicrobial activity. *Curr Opin Immunol* **1991**, *3* (1), 65-70.
42. Wink, D. A.; Kasprzak, K. S.; Maragos, C. M.; Elespuru, R. K.; Misra, M.; Dunams, T. M.; Cebula, T. A.; Koch, W. H.; Andrews, A. W.; Allen, J. S.; et al., DNA deaminating ability and genotoxicity of nitric oxide and its progenitors. *Science* **1991**, *254* (5034), 1001-3.
43. Hosseinimehr, S. J.; Mahmoudzadeh, A.; Rafiei, A., Arginine increases genotoxicity induced by methyl methanesulfonate in human lymphocytes. *Cytotechnology* **2013**, *65* (3), 379-84.
44. Mohr, S.; McCormick, T. S.; Lapetina, E. G., Macrophages resistant to endogenously generated nitric oxide-mediated apoptosis are hypersensitive to exogenously added nitric oxide donors: dichotomous apoptotic response independent of caspase 3 and reversal by the mitogen-activated protein kinase kinase (MEK) inhibitor PD 098059. *Proc Natl Acad Sci U S A* **1998**, *95* (9), 5045-50.
45. Bogdan, C., Nitric oxide synthase in innate and adaptive immunity: an update. *Trends Immunol* **2015**, *36* (3), 161-78.
46. Liu, Y.; Trnka, M. J.; Guan, S.; Kwon, D.; Kim, D. H.; Chen, J. J.; Greer, P. A.; Burlingame, A. L.; Correia, M. A., A Novel Mechanism for NF-kappaB-activation via IkappaB-aggregation: Implications for Hepatic Mallory-Denk-Body Induced Inflammation. *Mol Cell Proteomics* **2020**, *19* (12), 1968-1986.
47. Mao, K.; Chen, S.; Chen, M.; Ma, Y.; Wang, Y.; Huang, B.; He, Z.; Zeng, Y.; Hu, Y.; Sun, S.; Li, J.; Wu, X.; Wang, X.; Strober, W.; Chen, C.; Meng, G.; Sun, B., Nitric oxide suppresses NLRP3 inflammasome activation and protects against LPS-induced septic shock. *Cell Res* **2013**, *23* (2), 201-12.
48. Mishra, B. B.; Rathinam, V. A.; Martens, G. W.; Martinot, A. J.; Kornfeld, H.; Fitzgerald, K. A.; Sasseti, C. M., Nitric oxide controls the immunopathology of tuberculosis by inhibiting NLRP3 inflammasome-dependent processing of IL-1beta. *Nat Immunol* **2013**, *14* (1), 52-60.
49. Niedbala, W.; Alves-Filho, J. C.; Fukada, S. Y.; Vieira, S. M.; Mitani, A.; Sonogo, F.; Mirchandani, A.; Nascimento, D. C.; Cunha, F. Q.; Liew, F. Y., Regulation of type 17 helper T-cell function by nitric oxide during inflammation. *Proc Natl Acad Sci U S A* **2011**, *108* (22), 9220-5.
50. Nath, N.; Morinaga, O.; Singh, I., S-nitrosoglutathione a physiologic nitric oxide carrier attenuates experimental autoimmune encephalomyelitis. *J Neuroimmune Pharmacol* **2010**, *5* (2), 240-51.
51. Ischiropoulos, H.; Gow, A., Pathophysiological functions of nitric oxide-mediated protein modifications. *Toxicology* **2005**, *208* (2), 299-303.
52. Lu, G.; Zhang, R.; Geng, S.; Peng, L.; Jayaraman, P.; Chen, C.; Xu, F.; Yang, J.; Li, Q.; Zheng, H.; Shen, K.; Wang, J.; Liu, X.; Wang, W.; Zheng, Z.; Qi, C. F.; Si, C.; He, J. C.; Liu, K.; Lira, S. A.; Sikora, A. G.; Li, L.; Xiong, H., Myeloid cell-derived inducible nitric oxide synthase suppresses M1 macrophage polarization. *Nat Commun* **2015**, *6*, 6676.
53. Krausgruber, T.; Blazek, K.; Smallie, T.; Alzabin, S.; Lockstone, H.; Sahgal, N.; Hussell, T.; Feldmann, M.; Udalova, I. A., IRF5 promotes inflammatory macrophage polarization and TH1-TH17 responses. *Nat Immunol* **2011**, *12* (3), 231-8.
54. Jensen, S. S.; Gad, M., Differential induction of inflammatory cytokines by dendritic cells treated with novel TLR-agonist and cytokine based cocktails: targeting dendritic cells in autoimmunity. *J Inflamm (Lond)* **2010**, *7*, 37.
55. Jayaraman, P.; Alfarano, M. G.; Svider, P. F.; Parikh, F.; Lu, G.; Kidwai, S.; Xiong, H.; Sikora, A. G., iNOS expression in CD4+ T cells limits Treg induction by repressing TGFbeta1: combined iNOS inhibition and Treg depletion unmask endogenous antitumor immunity. *Clin Cancer Res* **2014**, *20* (24), 6439-51.
56. Stiff, A.; Trikha, P.; Wesolowski, R.; Kendra, K.; Hsu, V.; Uppati, S.; McMichael, E.;

- Duggan, M.; Campbell, A.; Keller, K.; Landi, I.; Zhong, Y.; Dubovsky, J.; Howard, J. H.; Yu, L.; Harrington, B.; Old, M.; Reiff, S.; Mace, T.; Tridandapani, S.; Muthusamy, N.; Caligiuri, M. A.; Byrd, J. C.; Carson, W. E., 3rd, Myeloid-Derived Suppressor Cells Express Bruton's Tyrosine Kinase and Can Be Depleted in Tumor-Bearing Hosts by Ibrutinib Treatment. *Cancer Res* **2016**, *76* (8), 2125-36.
57. Douguet, L.; Bod, L.; Lengagne, R.; Labarthe, L.; Kato, M.; Avril, M. F.; Prevost-Blondel, A., Nitric oxide synthase 2 is involved in the pro-tumorigenic potential of gamma delta 17 T cells in melanoma. *Oncoimmunology* **2016**, *5* (8), e1208878.
58. Xue, Q.; Yan, Y.; Zhang, R.; Xiong, H., Regulation of iNOS on Immune Cells and Its Role in Diseases. *Int J Mol Sci* **2018**, *19* (12).
59. Forstermann, U.; Closs, E. I.; Pollock, J. S.; Nakane, M.; Schwarz, P.; Gath, I.; Kleinert, H., Nitric oxide synthase isozymes. Characterization, purification, molecular cloning, and functions. *Hypertension* **1994**, *23* (6 Pt 2), 1121-31.
60. Wu, K. K., Regulation of endothelial nitric oxide synthase activity and gene expression. *Ann N Y Acad Sci* **2002**, *962*, 122-30.
61. Bauer, V.; Sotnikova, R., Nitric oxide--the endothelium-derived relaxing factor and its role in endothelial functions. *Gen Physiol Biophys* **2010**, *29* (4), 319-40.
62. Vanhoutte, P. M.; Shimokawa, H.; Feletou, M.; Tang, E. H., Endothelial dysfunction and vascular disease - a 30th anniversary update. *Acta Physiol (Oxf)* **2017**, *219* (1), 22-96.
63. Tang, E. H.; Leung, F. P.; Huang, Y.; Feletou, M.; So, K. F.; Man, R. Y.; Vanhoutte, P. M., Calcium and reactive oxygen species increase in endothelial cells in response to releasers of endothelium-derived contracting factor. *Br J Pharmacol* **2007**, *151* (1), 15-23.
64. Tang, E. H.; Vanhoutte, P. M., Gene expression changes of prostanoid synthases in endothelial cells and prostanoid receptors in vascular smooth muscle cells caused by aging and hypertension. *Physiol Genomics* **2008**, *32* (3), 409-18.
65. Li, Z.; Wang, Y.; Vanhoutte, P. M., Upregulation of heme oxygenase 1 by hemin impairs endothelium-dependent contractions in the aorta of the spontaneously hypertensive rat. *Hypertension* **2011**, *58* (5), 926-34.
66. Li, Z.; Wang, Y.; Man, R. Y.; Vanhoutte, P. M., Upregulation of heme oxygenase-1 potentiates EDH-type relaxations in the mesenteric artery of the spontaneously hypertensive rat. *Am J Physiol Heart Circ Physiol* **2013**, *305* (10), H1471-83.
67. Fleming, I.; Bauersachs, J.; Fisslthaler, B.; Busse, R., Ca²⁺-independent activation of the endothelial nitric oxide synthase in response to tyrosine phosphatase inhibitors and fluid shear stress. *Circ Res* **1998**, *82* (6), 686-95.
68. Li, Y.; Zheng, J.; Bird, I. M.; Magness, R. R., Effects of pulsatile shear stress on signaling mechanisms controlling nitric oxide production, endothelial nitric oxide synthase phosphorylation, and expression in ovine fetoplacental artery endothelial cells. *Endothelium* **2005**, *12* (1-2), 21-39.
69. Devika, N. T.; Jaffar Ali, B. M., Analysing calcium dependent and independent regulation of eNOS in endothelium triggered by extracellular signalling events. *Mol Biosyst* **2013**, *9* (11), 2653-64.
70. Chen, Z.; Peng, I. C.; Sun, W.; Su, M. I.; Hsu, P. H.; Fu, Y.; Zhu, Y.; DeFea, K.; Pan, S.; Tsai, M. D.; Shyy, J. Y., AMP-activated protein kinase functionally phosphorylates endothelial nitric oxide synthase Ser633. *Circ Res* **2009**, *104* (4), 496-505.
71. Motley, E. D.; Eguchi, K.; Patterson, M. M.; Palmer, P. D.; Suzuki, H.; Eguchi, S., Mechanism of endothelial nitric oxide synthase phosphorylation and activation by thrombin. *Hypertension* **2007**, *49* (3), 577-83.
72. Harris, M. B.; Ju, H.; Venema, V. J.; Liang, H.; Zou, R.; Michell, B. J.; Chen, Z. P.; Kemp, B. E.; Venema, R. C., Reciprocal phosphorylation and regulation of endothelial nitric-oxide synthase in response to bradykinin stimulation. *J Biol Chem* **2001**, *276* (19), 16587-91.

73. Kong, X.; Qu, X.; Li, B.; Wang, Z.; Chao, Y.; Jiang, X.; Wu, W.; Chen, S. L., Modulation of low shear stress-induced eNOS multisite phosphorylation and nitric oxide production via protein kinase and ERK1/2 signaling. *Mol Med Rep* **2017**, *15* (2), 908-914.
74. Balligand, J. L.; Feron, O.; Dessy, C., eNOS activation by physical forces: from short-term regulation of contraction to chronic remodeling of cardiovascular tissues. *Physiol Rev* **2009**, *89* (2), 481-534.
75. Li, H.; Liu, X.; Cui, H.; Chen, Y. R.; Cardounel, A. J.; Zweier, J. L., Characterization of the mechanism of cytochrome P450 reductase-cytochrome P450-mediated nitric oxide and nitrosothiol generation from organic nitrates. *J Biol Chem* **2006**, *281* (18), 12546-54.
76. Klinger, J. R.; Abman, S. H.; Gladwin, M. T., Nitric oxide deficiency and endothelial dysfunction in pulmonary arterial hypertension. *Am J Respir Crit Care Med* **2013**, *188* (6), 639-46.
77. Pacher, P.; Beckman, J. S.; Liaudet, L., Nitric oxide and peroxynitrite in health and disease. *Physiol Rev* **2007**, *87* (1), 315-424.
78. Leiper, J.; Nandi, M.; Torondel, B.; Murray-Rust, J.; Malaki, M.; O'Hara, B.; Rossiter, S.; Anthony, S.; Madhani, M.; Selwood, D.; Smith, C.; Wojciak-Stothard, B.; Rudiger, A.; Stidwill, R.; McDonald, N. Q.; Vallance, P., Disruption of methylarginine metabolism impairs vascular homeostasis. *Nat Med* **2007**, *13* (2), 198-203.
79. Roberts, A. C.; Porter, K. E., Cellular and molecular mechanisms of endothelial dysfunction in diabetes. *Diab Vasc Dis Res* **2013**, *10* (6), 472-82.
80. Sasaki, N.; Yamashita, T.; Takaya, T.; Shinohara, M.; Shiraki, R.; Takeda, M.; Emoto, N.; Fukatsu, A.; Hayashi, T.; Ikemoto, K.; Nomura, T.; Yokoyama, M.; Hirata, K.; Kawashima, S., Augmentation of vascular remodeling by uncoupled endothelial nitric oxide synthase in a mouse model of diabetes mellitus. *Arterioscler Thromb Vasc Biol* **2008**, *28* (6), 1068-76.
81. Chen, C. A.; Wang, T. Y.; Varadharaj, S.; Reyes, L. A.; Hemann, C.; Talukder, M. A.; Chen, Y. R.; Druhan, L. J.; Zweier, J. L., S-glutathionylation uncouples eNOS and regulates its cellular and vascular function. *Nature* **2010**, *468* (7327), 1115-8.
82. Brecht, D. S.; Hwang, P. M.; Glatt, C. E.; Lowenstein, C.; Reed, R. R.; Snyder, S. H., Cloned and expressed nitric oxide synthase structurally resembles cytochrome P-450 reductase. *Nature* **1991**, *351* (6329), 714-8.
83. Schmidt, H. H.; Pollock, J. S.; Nakane, M.; Forstermann, U.; Murad, F., Ca²⁺/calmodulin-regulated nitric oxide synthases. *Cell Calcium* **1992**, *13* (6-7), 427-34.
84. Stuehr, D. J.; Abu-Soud, H. M.; Rousseau, D. L.; Feldman, P. L.; Wang, J., Control of electron transfer in neuronal nitric oxide synthase by calmodulin, substrate, substrate analogs, and nitric oxide. *Adv Pharmacol* **1995**, *34*, 207-13.
85. Zoche, M.; Bienert, M.; Beyermann, M.; Koch, K. W., Distinct molecular recognition of calmodulin-binding sites in the neuronal and macrophage nitric oxide synthases: a surface plasmon resonance study. *Biochemistry* **1996**, *35* (26), 8742-7.
86. Roman, L. J.; Martasek, P.; Masters, B. S., Intrinsic and extrinsic modulation of nitric oxide synthase activity. *Chem Rev* **2002**, *102* (4), 1179-90.
87. Schuck, P.; Minton, A. P., Analysis of mass transport-limited binding kinetics in evanescent wave biosensors. *Anal Biochem* **1996**, *240* (2), 262-72.
88. Wu, G.; Berka, V.; Tsai, A. L., Binding kinetics of calmodulin with target peptides of three nitric oxide synthase isozymes. *J Inorg Biochem* **2011**, *105* (9), 1226-37.
89. Abu-Soud, H. M.; Wang, J.; Rousseau, D. L.; Fukuto, J. M.; Ignarro, L. J.; Stuehr, D. J., Neuronal nitric oxide synthase self-inactivates by forming a ferrous-nitrosyl complex during aerobic catalysis. *J Biol Chem* **1995**, *270* (39), 22997-3006.
90. Zhao, Y.; Vanhoutte, P. M.; Leung, S. W., Vascular nitric oxide: Beyond eNOS. *J Pharmacol Sci* **2015**, *129* (2), 83-94.
91. Ray, S. S.; Tejero, J.; Wang, Z. Q.; Dutta, T.; Bhattacharjee, A.; Regulski, M.; Tully, T.;

- Ghosh, S.; Stuehr, D. J., Oxygenase domain of *Drosophila melanogaster* nitric oxide synthase: unique kinetic parameters enable a more efficient NO release. *Biochemistry* **2007**, *46* (42), 11857-64.
92. Palmer, R. M.; Ferrige, A. G.; Moncada, S., Nitric oxide release accounts for the biological activity of endothelium-derived relaxing factor. *Nature* **1987**, *327* (6122), 524-6.
93. Mason, M. G.; Nicholls, P.; Wilson, M. T.; Cooper, C. E., Nitric oxide inhibition of respiration involves both competitive (heme) and noncompetitive (copper) binding to cytochrome c oxidase. *Proc Natl Acad Sci U S A* **2006**, *103* (3), 708-13.
94. Tuteja, N.; Chandra, M.; Tuteja, R.; Misra, M. K., Nitric Oxide as a Unique Bioactive Signaling Messenger in Physiology and Pathophysiology. *J Biomed Biotechnol* **2004**, *2004* (4), 227-237.
95. Vallance, P.; Collier, J.; Moncada, S., Effects of endothelium-derived nitric oxide on peripheral arteriolar tone in man. *Lancet* **1989**, *2* (8670), 997-1000.
96. Beckman, J. S.; Koppenol, W. H., Nitric oxide, superoxide, and peroxynitrite: the good, the bad, and ugly. *Am J Physiol* **1996**, *271* (5 Pt 1), C1424-37.
97. Sharma, V. S.; Traylor, T. G.; Gardiner, R.; Mizukami, H., Reaction of nitric oxide with heme proteins and model compounds of hemoglobin. *Biochemistry* **1987**, *26* (13), 3837-43.
98. Traylor, T. G.; Sharma, V. S., Why NO? *Biochemistry* **1992**, *31* (11), 2847-9.
99. Butler, A. R.; Megson, I. L.; Wright, P. G., Diffusion of nitric oxide and scavenging by blood in the vasculature. *Biochim Biophys Acta* **1998**, *1425* (1), 168-76.
100. Tsoukias, N. M.; Popel, A. S., Erythrocyte consumption of nitric oxide in presence and absence of plasma-based hemoglobin. *Am J Physiol Heart Circ Physiol* **2002**, *282* (6), H2265-77.
101. Wood, J.; Garthwaite, J., Models of the diffusional spread of nitric oxide: implications for neural nitric oxide signalling and its pharmacological properties. *Neuropharmacology* **1994**, *33* (11), 1235-44.
102. Tsoukias, N. M.; Kavdia, M.; Popel, A. S., A theoretical model of nitric oxide transport in arterioles: frequency- vs. amplitude-dependent control of cGMP formation. *Am J Physiol Heart Circ Physiol* **2004**, *286* (3), H1043-56.
103. Newsholme, P.; Homem De Bittencourt, P. I.; C, O. H.; De Vito, G.; Murphy, C.; Krause, M. S., Exercise and possible molecular mechanisms of protection from vascular disease and diabetes: the central role of ROS and nitric oxide. *Clin Sci (Lond)* **2009**, *118* (5), 341-9.
104. Czapski, G.; Goldstein, S., The role of the reactions of .NO with superoxide and oxygen in biological systems: a kinetic approach. *Free Radic Biol Med* **1995**, *19* (6), 785-94.
105. Radi, R., Peroxynitrite, a stealthy biological oxidant. *J Biol Chem* **2013**, *288* (37), 26464-72.
106. Radi, R., Oxygen radicals, nitric oxide, and peroxynitrite: Redox pathways in molecular medicine. *Proc Natl Acad Sci U S A* **2018**, *115* (23), 5839-5848.
107. Beckman, J. S.; Beckman, T. W.; Chen, J.; Marshall, P. A.; Freeman, B. A., Apparent hydroxyl radical production by peroxynitrite: implications for endothelial injury from nitric oxide and superoxide. *Proc Natl Acad Sci U S A* **1990**, *87* (4), 1620-4.
108. Ferrer-Sueta, G.; Campolo, N.; Trujillo, M.; Bartesaghi, S.; Carballal, S.; Romero, N.; Alvarez, B.; Radi, R., Biochemistry of Peroxynitrite and Protein Tyrosine Nitration. *Chem Rev* **2018**, *118* (3), 1338-1408.
109. Szabo, C.; Ischiropoulos, H.; Radi, R., Peroxynitrite: biochemistry, pathophysiology and development of therapeutics. *Nat Rev Drug Discov* **2007**, *6* (8), 662-80.
110. Radi, R.; Beckman, J. S.; Bush, K. M.; Freeman, B. A., Peroxynitrite oxidation of sulfhydryls. The cytotoxic potential of superoxide and nitric oxide. *J Biol Chem* **1991**, *266* (7), 4244-50.
111. Bartesaghi, S.; Radi, R., Fundamentals on the biochemistry of peroxynitrite and protein

tyrosine nitration. *Redox Biol* **2018**, *14*, 618-625.

112. Winterbourn, C. C., Reconciling the chemistry and biology of reactive oxygen species. *Nat Chem Biol* **2008**, *4* (5), 278-86.

113. Quijano, C.; Castro, L.; Peluffo, G.; Valez, V.; Radi, R., Enhanced mitochondrial superoxide in hyperglycemic endothelial cells: direct measurements and formation of hydrogen peroxide and peroxynitrite. *Am J Physiol Heart Circ Physiol* **2007**, *293* (6), H3404-14.

114. Imlay, J. A., Cellular defenses against superoxide and hydrogen peroxide. *Annu Rev Biochem* **2008**, *77*, 755-76.

115. Kuwahara, H.; Miyamoto, Y.; Akaike, T.; Kubota, T.; Sawa, T.; Okamoto, S.; Maeda, H., Helicobacter pylori urease suppresses bactericidal activity of peroxynitrite via carbon dioxide production. *Infect Immun* **2000**, *68* (8), 4378-83.

116. Zhu, L.; Gunn, C.; Beckman, J. S., Bactericidal activity of peroxynitrite. *Arch Biochem Biophys* **1992**, *298* (2), 452-7.

117. Alvarez, M. N.; Peluffo, G.; Piacenza, L.; Radi, R., Intraphagosomal peroxynitrite as a macrophage-derived cytotoxin against internalized Trypanosoma cruzi: consequences for oxidative killing and role of microbial peroxiredoxins in infectivity. *J Biol Chem* **2011**, *286* (8), 6627-40.

118. Zielonka, J.; Sikora, A.; Hardy, M.; Joseph, J.; Dranka, B. P.; Kalyanaraman, B., Boronate probes as diagnostic tools for real time monitoring of peroxynitrite and hydroperoxides. *Chem Res Toxicol* **2012**, *25* (9), 1793-9.

119. Rios, N.; Piacenza, L.; Trujillo, M.; Martinez, A.; Demicheli, V.; Prolo, C.; Alvarez, M. N.; Lopez, G. V.; Radi, R., Sensitive detection and estimation of cell-derived peroxynitrite fluxes using fluorescein-boronate. *Free Radic Biol Med* **2016**, *101*, 284-295.

120. Ferrer-Sueta, G.; Radi, R., Chemical biology of peroxynitrite: kinetics, diffusion, and radicals. *ACS Chem Biol* **2009**, *4* (3), 161-77.

121. Denicola, A.; Freeman, B. A.; Trujillo, M.; Radi, R., Peroxynitrite reaction with carbon dioxide/bicarbonate: kinetics and influence on peroxynitrite-mediated oxidations. *Arch Biochem Biophys* **1996**, *333* (1), 49-58.

122. Radi, R.; Denicola, A.; Freeman, B. A., Peroxynitrite reactions with carbon dioxide-bicarbonate. *Methods Enzymol* **1999**, *301*, 353-67.

123. Radi, R., Peroxynitrite reactions and diffusion in biology. *Chem Res Toxicol* **1998**, *11* (7), 720-1.

124. Lyman, S. V.; Hurst, J. K., Radical nature of peroxynitrite reactivity. *Chem Res Toxicol* **1998**, *11* (7), 714-5.

125. Mirzahosseini, A.; Noszal, B., Species-Specific Standard Redox Potential of Thiol-Disulfide Systems: A Key Parameter to Develop Agents against Oxidative Stress. *Sci Rep* **2016**, *6*, 37596.

126. Becker, D.; Summerfield, S.; Gillich, S.; Sevilla, M. D., Influence of oxygen on the repair of direct radiation damage to DNA by thiols in model systems. *Int J Radiat Biol* **1994**, *65* (5), 537-48.

127. Kalinina, E. V.; Gavriluk, L. A., Glutathione Synthesis in Cancer Cells. *Biochemistry (Mosc)* **2020**, *85* (8), 895-907.

128. Pijning, A. E.; Hogg, P., Classification of Protein Disulphide Bonds. *Methods Mol Biol* **2019**, *1967*, 1-8.

129. Grimsrud, P. A.; Xie, H.; Griffin, T. J.; Bernlohr, D. A., Oxidative stress and covalent modification of protein with bioactive aldehydes. *J Biol Chem* **2008**, *283* (32), 21837-41.

130. Biteau, B.; Labarre, J.; Toledano, M. B., ATP-dependent reduction of cysteine-sulphinic acid by *S. cerevisiae* sulphiredoxin. *Nature* **2003**, *425* (6961), 980-4.

131. Fukata, Y.; Fukata, M., Protein palmitoylation in neuronal development and synaptic plasticity. *Nat Rev Neurosci* **2010**, *11* (3), 161-75.

132. McBean, G. J.; Aslan, M.; Griffiths, H. R.; Torrao, R. C., Thiol redox homeostasis in neurodegenerative disease. *Redox Biol* **2015**, *5*, 186-194.
133. Hickok, J. R.; Vasudevan, D.; Thatcher, G. R.; Thomas, D. D., Is S-nitrosocysteine a true surrogate for nitric oxide? *Antioxid Redox Signal* **2012**, *17* (7), 962-8.
134. Broniowska, K. A.; Diers, A. R.; Hogg, N., S-nitrosoglutathione. *Biochim Biophys Acta* **2013**, *1830* (5), 3173-81.
135. Koppenol, W. H., Nitrosation, thiols, and hemoglobin: energetics and kinetics. *Inorg Chem* **2012**, *51* (10), 5637-41.
136. Sun, J.; Murphy, E., Protein S-nitrosylation and cardioprotection. *Circ Res* **2010**, *106* (2), 285-96.
137. Stamler, J. S.; Lamas, S.; Fang, F. C., Nitrosylation. the prototypic redox-based signaling mechanism. *Cell* **2001**, *106* (6), 675-83.
138. Fra, A.; Yoboue, E. D.; Sitia, R., Cysteines as Redox Molecular Switches and Targets of Disease. *Front Mol Neurosci* **2017**, *10*, 167.
139. Klatt, P.; Pineda Molina, E.; Perez-Sala, D.; Lamas, S., Novel application of S-nitrosoglutathione-Sepharose to identify proteins that are potential targets for S-nitrosoglutathione-induced mixed-disulphide formation. *Biochem J* **2000**, *349* (Pt 2), 567-78.
140. Klatt, P.; Lamas, S., Regulation of protein function by S-glutathiolation in response to oxidative and nitrosative stress. *Eur J Biochem* **2000**, *267* (16), 4928-44.
141. Perez-Mato, I.; Castro, C.; Ruiz, F. A.; Corrales, F. J.; Mato, J. M., Methionine adenosyltransferase S-nitrosylation is regulated by the basic and acidic amino acids surrounding the target thiol. *J Biol Chem* **1999**, *274* (24), 17075-9.
142. Sun, J.; Xin, C.; Eu, J. P.; Stamler, J. S.; Meissner, G., Cysteine-3635 is responsible for skeletal muscle ryanodine receptor modulation by NO. *Proc Natl Acad Sci U S A* **2001**, *98* (20), 11158-62.
143. Stamler, J. S.; Toone, E. J.; Lipton, S. A.; Sucher, N. J., (S)NO signals: translocation, regulation, and a consensus motif. *Neuron* **1997**, *18* (5), 691-6.
144. Williams, J. G.; Pappu, K.; Campbell, S. L., Structural and biochemical studies of p21Ras S-nitrosylation and nitric oxide-mediated guanine nucleotide exchange. *Proc Natl Acad Sci U S A* **2003**, *100* (11), 6376-81.
145. Stamler, J. S.; Simon, D. I.; Osborne, J. A.; Mullins, M. E.; Jaraki, O.; Michel, T.; Singel, D. J.; Loscalzo, J., S-nitrosylation of proteins with nitric oxide: synthesis and characterization of biologically active compounds. *Proc Natl Acad Sci U S A* **1992**, *89* (1), 444-8.
146. Montesanti, G.; Parisella, M. L.; Garofalo, G.; Pellegrino, D., Nitrite as Direct S-Nitrosylating Agent of Kir2.1 Channels. *Int Sch Res Notices* **2014**, *2014*, 517126.
147. Romero-Puertas, M. C.; Laxa, M.; Matte, A.; Zaninotto, F.; Finkemeier, I.; Jones, A. M.; Perazzolli, M.; Vandelle, E.; Dietz, K. J.; Delledonne, M., S-nitrosylation of peroxiredoxin II E promotes peroxynitrite-mediated tyrosine nitration. *Plant Cell* **2007**, *19* (12), 4120-30.
148. Gaston, B., Nitric oxide and thiol groups. *Biochim Biophys Acta* **1999**, *1411* (2-3), 323-33.
149. Bredt, D. S., Nitric oxide signaling specificity--the heart of the problem. *J Cell Sci* **2003**, *116* (Pt 1), 9-15.
150. Ziolo, M. T.; Bers, D. M., The real estate of NOS signaling: location, location, location. *Circ Res* **2003**, *92* (12), 1279-81.
151. Nathan, C.; Shiloh, M. U., Reactive oxygen and nitrogen intermediates in the relationship between mammalian hosts and microbial pathogens. *Proc Natl Acad Sci U S A* **2000**, *97* (16), 8841-8.
152. Singh, R. J.; Hogg, N.; Joseph, J.; Kalyanaraman, B., Mechanism of nitric oxide release from S-nitrosothiols. *J Biol Chem* **1996**, *271* (31), 18596-603.
153. Arnelo, D. R.; Stamler, J. S., NO⁺, NO, and NO⁻ donation by S-nitrosothiols: implications

for regulation of physiological functions by S-nitrosylation and acceleration of disulfide formation. *Arch Biochem Biophys* **1995**, *318* (2), 279-85.

154. Kim, W. K.; Choi, Y. B.; Rayudu, P. V.; Das, P.; Asaad, W.; Arnelle, D. R.; Stamler, J. S.; Lipton, S. A., Attenuation of NMDA receptor activity and neurotoxicity by nitroxyl anion, NO. *Neuron* **1999**, *24* (2), 461-9.

155. Kim, J. E.; Tannenbaum, S. R., S-Nitrosation regulates the activation of endogenous procaspase-9 in HT-29 human colon carcinoma cells. *J Biol Chem* **2004**, *279* (11), 9758-64.

156. Morakinyo, M. K.; Strongin, R. M.; Simoyi, R. H., Modulation of homocysteine toxicity by S-nitrosothiol formation: a mechanistic approach. *J Phys Chem B* **2010**, *114* (30), 9894-904.

157. Barlow, M., Vasopressin. *Emerg Med (Fremantle)* **2002**, *14* (3), 304-14.

158. Treschan, T. A.; Peters, J., The vasopressin system: physiology and clinical strategies. *Anesthesiology* **2006**, *105* (3), 599-612; quiz 639-40.

159. Grazzini, E.; Lodboerer, A. M.; Perez-Martin, A.; Joubert, D.; Guillon, G., Molecular and functional characterization of V1b vasopressin receptor in rat adrenal medulla. *Endocrinology* **1996**, *137* (9), 3906-14.

160. Ma, S.; Shipston, M. J.; Morilak, D.; Russell, J. A., Reduced hypothalamic vasopressin secretion underlies attenuated adrenocorticotropin stress responses in pregnant rats. *Endocrinology* **2005**, *146* (3), 1626-37.

161. Serradeil-Le Gal, C.; Wagnon, J.; Valette, G.; Garcia, G.; Pascal, M.; Maffrand, J. P.; Le Fur, G., Nonpeptide vasopressin receptor antagonists: development of selective and orally active V1a, V2 and V1b receptor ligands. *Prog Brain Res* **2002**, *139*, 197-210.

162. Jard, S., Vasopressin receptors. A historical survey. *Adv Exp Med Biol* **1998**, *449*, 1-13.

163. Cossu, A. P.; Mura, P.; De Giudici, L. M.; Puddu, D.; Pasin, L.; Evangelista, M.; Xanthos, T.; Musu, M.; Finco, G., Vasopressin in hemorrhagic shock: a systematic review and meta-analysis of randomized animal trials. *Biomed Res Int* **2014**, *2014*, 421291.

164. Gonzalez-Hernandez, T.; Perez de la Cruz, M. A.; Mantolan-Sarmiento, B., Histochemical and immunohistochemical detection of neurons that produce nitric oxide: effect of different fixative parameters and immunoreactivity against non-neuronal NOS antisera. *J Histochem Cytochem* **1996**, *44* (12), 1399-413.

165. Sagar, S. M.; Ferriero, D. M., NADPH diaphorase activity in the posterior pituitary: relation to neuronal function. *Brain Res* **1987**, *400* (2), 348-52.

166. Reid, I. A., Role of nitric oxide in the regulation of renin and vasopressin secretion. *Front Neuroendocrinol* **1994**, *15* (4), 351-83.

167. Kovacs, I.; Lindermayr, C., Nitric oxide-based protein modification: formation and site-specificity of protein S-nitrosylation. *Front Plant Sci* **2013**, *4*, 137.

168. Hess, D. T.; Matsumoto, A.; Kim, S. O.; Marshall, H. E.; Stamler, J. S., Protein S-nitrosylation: purview and parameters. *Nat Rev Mol Cell Biol* **2005**, *6* (2), 150-66.

169. Lundberg, J. O.; Weitzberg, E.; Gladwin, M. T., The nitrate-nitrite-nitric oxide pathway in physiology and therapeutics. *Nat Rev Drug Discov* **2008**, *7* (2), 156-67.

170. Wink, D. A.; Nims, R. W.; Darbyshire, J. F.; Christodoulou, D.; Hanbauer, I.; Cox, G. W.; Laval, F.; Laval, J.; Cook, J. A.; Krishna, M. C.; et al., Reaction kinetics for nitrosation of cysteine and glutathione in aerobic nitric oxide solutions at neutral pH. Insights into the fate and physiological effects of intermediates generated in the NO/O₂ reaction. *Chem Res Toxicol* **1994**, *7* (4), 519-25.

171. Lane, P.; Hao, G.; Gross, S. S., S-nitrosylation is emerging as a specific and fundamental posttranslational protein modification: head-to-head comparison with O-phosphorylation. *Sci STKE* **2001**, *2001* (86), re1.

172. Foster, M. W.; McMahon, T. J.; Stamler, J. S., S-nitrosylation in health and disease. *Trends Mol Med* **2003**, *9* (4), 160-8.

173. Massy, Z. A.; Fumeron, C.; Borderie, D.; Tuppin, P.; Nguyen-Khoa, T.; Benoit, M. O.; Jacquot, C.; Buisson, C.; Druke, T. B.; Ekindjian, O. G.; Lacour, B.; Iliou, M. C., Increased plasma S-nitrosothiol concentrations predict cardiovascular outcomes among patients with end-stage renal disease: a prospective study. *J Am Soc Nephrol* **2004**, *15* (2), 470-6.
174. Heiss, C.; Lauer, T.; Dejam, A.; Kleinbongard, P.; Hamada, S.; Rassaf, T.; Matern, S.; Feelisch, M.; Kelm, M., Plasma nitroso compounds are decreased in patients with endothelial dysfunction. *J Am Coll Cardiol* **2006**, *47* (3), 573-9.
175. Anand, P.; Stamler, J. S., Enzymatic mechanisms regulating protein S-nitrosylation: implications in health and disease. *J Mol Med (Berl)* **2012**, *90* (3), 233-44.
176. Kopacz, A.; Kloska, D.; Proniewski, B.; Cysewski, D.; Personnic, N.; Piechota-Polanczyk, A.; Kaczara, P.; Zakrzewska, A.; Forman, H. J.; Dulak, J.; Jozkowicz, A.; Grochot-Przeczek, A., Keap1 controls protein S-nitrosation and apoptosis-senescence switch in endothelial cells. *Redox Biology* **2020**, *28*.
177. Nakamura, T.; Lipton, S. A., Emerging role of protein-protein transnitrosylation in cell signaling pathways. *Antioxid Redox Signal* **2013**, *18* (3), 239-49.
178. Levison, M. E.; Josephson, A. S.; Kirschenbaum, D. M., Reduction of biological substances by water-soluble phosphines: gamma-globulin (IgG). *Experientia* **1969**, *25* (2), 126-7.
179. Han, J. C.; Han, G. Y., A procedure for quantitative determination of tris(2-carboxyethyl)phosphine, an odorless reducing agent more stable and effective than dithiothreitol. *Anal Biochem* **1994**, *220* (1), 5-10.
180. Cline, D. J.; Redding, S. E.; Brohawn, S. G.; Psathas, J. N.; Schneider, J. P.; Thorpe, C., New water-soluble phosphines as reductants of peptide and protein disulfide bonds: reactivity and membrane permeability. *Biochemistry* **2004**, *43* (48), 15195-203.
181. Pawelec, M.; Stochel, G.; van Eldik, R., Mechanistic information on the copper-catalysed autoxidation of mercaptosuccinic acid in aqueous solution. *Dalton Trans* **2004**, (2), 292-8.
182. Cline, D. J.; Thorpe, C.; Schneider, J. P., General method for facile intramolecular disulfide formation in synthetic peptides. *Anal Biochem* **2004**, *335* (1), 168-70.
183. Paige, J. S.; Xu, G.; Stancevic, B.; Jaffrey, S. R., Nitrosothiol reactivity profiling identifies S-nitrosylated proteins with unexpected stability. *Chem Biol* **2008**, *15* (12), 1307-16.
184. Foster, M. W.; Hess, D. T.; Stamler, J. S., Protein S-nitrosylation in health and disease: a current perspective. *Trends Mol Med* **2009**, *15* (9), 391-404.
185. Iwakiri, Y.; Satoh, A.; Chatterjee, S.; Toomre, D. K.; Chalouni, C. M.; Fulton, D.; Groszmann, R. J.; Shah, V. H.; Sessa, W. C., Nitric oxide synthase generates nitric oxide locally to regulate compartmentalized protein S-nitrosylation and protein trafficking. *Proc Natl Acad Sci U S A* **2006**, *103* (52), 19777-82.
186. Marino, S. M.; Gladyshev, V. N., Structural analysis of cysteine S-nitrosylation: a modified acid-based motif and the emerging role of trans-nitrosylation. *J Mol Biol* **2010**, *395* (4), 844-59.
187. Marozkina, N. V.; Gaston, B., S-Nitrosylation signaling regulates cellular protein interactions. *Biochim Biophys Acta* **2012**, *1820* (6), 722-9.
188. Stubauer, G.; Giuffre, A.; Sarti, P., Mechanism of S-nitrosothiol formation and degradation mediated by copper ions. *J Biol Chem* **1999**, *274* (40), 28128-33.
189. Diers, A. R.; Keszler, A.; Hogg, N., Detection of S-nitrosothiols. *Biochim Biophys Acta* **2014**, *1840* (2), 892-900.
190. Seckler, J. M.; Meyer, N. M.; Burton, S. T.; Bates, J. N.; Gaston, B.; Lewis, S. J., Detection of trace concentrations of S-nitrosothiols by means of a capacitive sensor. *PLoS One* **2017**, *12* (10), e0187149.
191. Pace, C. N.; Vajdos, F.; Fee, L.; Grimsley, G.; Gray, T., How to measure and predict the molar absorption coefficient of a protein. *Protein Sci* **1995**, *4* (11), 2411-23.
192. Gill, S. C.; von Hippel, P. H., Calculation of protein extinction coefficients from amino

- acid sequence data. *Anal Biochem* **1989**, *182* (2), 319-26.
193. Abbruzzetti, S.; Bruno, S.; Faggiano, S.; Grandi, E.; Mozzarelli, A.; Viappiani, C., Time-resolved methods in Biophysics. 2. Monitoring haem proteins at work with nanosecond laser flash photolysis. *Photochem Photobiol Sci* **2006**, *5* (12), 1109-20.
194. Laverman, L. E.; Wanat, A.; Oszajca, J.; Stochel, G.; Ford, P. C.; van Eldik, R., Mechanistic studies on the reversible binding of nitric oxide to metmyoglobin. *J Am Chem Soc* **2001**, *123* (2), 285-93.
195. Reszka, K. J.; Bilski, P.; Chignell, C. F., Spin trapping of nitric oxide by aci anions of nitroalkanes. *Nitric Oxide* **2004**, *10* (2), 53-9.
196. Pryor, W. A.; Squadrito, G. L., The chemistry of peroxyxynitrite: a product from the reaction of nitric oxide with superoxide. *Am J Physiol* **1995**, *268* (5 Pt 1), L699-722.
197. Khan, A. U.; Kovacic, D.; Kolbanovskiy, A.; Desai, M.; Frenkel, K.; Geacintov, N. E., The decomposition of peroxyxynitrite to nitroxyl anion (NO⁻) and singlet oxygen in aqueous solution. *Proc Natl Acad Sci U S A* **2000**, *97* (7), 2984-9.
198. Goldstein, S.; Czapski, G.; Lind, J.; Merenyi, G., Mechanism of Decomposition of Peroxyxynitric Ion (O(2)NOO(-)): Evidence for the Formation of O(2)(*-) and (*)NO(2) Radicals. *Inorg Chem* **1998**, *37* (16), 3943-3947.
199. Goldstein, S.; Czapski, G.; Lind, J.; Merenyi, G., Carbonate radical ion is the only observable intermediate in the reaction of peroxyxynitrite with CO(2). *Chem Res Toxicol* **2001**, *14* (9), 1273-6.
200. Goldstein, S.; Czapski, G.; Lind, J.; Merenyi, G., Gibbs energy of formation of peroxyxynitrite--order restored. *Chem Res Toxicol* **2001**, *14* (6), 657-60.
201. Luo, Y.; Wang, X. R.; Ji, L. L.; Su, Y., EPR detection of hydroxyl radical generation and its interaction with antioxidant system in *Carassius auratus* exposed to pentachlorophenol. *J Hazard Mater* **2009**, *171* (1-3), 1096-102.
202. Moro, M. A.; Darley-USmar, V. M.; Goodwin, D. A.; Read, N. G.; Zamora-Pino, R.; Feelisch, M.; Radomski, M. W.; Moncada, S., Paradoxical fate and biological action of peroxyxynitrite on human platelets. *Proc Natl Acad Sci U S A* **1994**, *91* (14), 6702-6.
203. Mayer, B.; Schrammel, A.; Klatt, P.; Koesling, D.; Schmidt, K., Peroxyxynitrite-induced accumulation of cyclic GMP in endothelial cells and stimulation of purified soluble guanylyl cyclase. Dependence on glutathione and possible role of S-nitrosation. *J Biol Chem* **1995**, *270* (29), 17355-60.
204. Roy, B.; Lepoivre, M.; Henry, Y.; Fontecave, M., Inhibition of ribonucleotide reductase by nitric oxide derived from thionitrites: reversible modifications of both subunits. *Biochemistry* **1995**, *34* (16), 5411-8.
205. Hogg, N., Biological chemistry and clinical potential of S-nitrosothiols. *Free Radic Biol Med* **2000**, *28* (10), 1478-86.
206. Chipinda, I.; Simoyi, R. H., Formation and stability of a nitric oxide donor: S-nitroso-N-acetylpenicillamine. *J Phys Chem B* **2006**, *110* (10), 5052-61.
207. Romeo, A. A.; Capobianco, J. A.; English, A. M., Heme nitrosylation of deoxyhemoglobin by s-nitrosoglutathione requires copper. *J Biol Chem* **2002**, *277* (27), 24135-41.
208. Tao, L.; English, A. M., Mechanism of S-nitrosation of recombinant human brain calbindin D28K. *Biochemistry* **2003**, *42* (11), 3326-34.
209. Meyer, D. J.; Kramer, H.; Ozer, N.; Coles, B.; Ketterer, B., Kinetics and equilibria of S-nitrosothiol-thiol exchange between glutathione, cysteine, penicillamines and serum albumin. *FEBS Lett* **1994**, *345* (2-3), 177-80.
210. Kronenfeld, G.; Engelman, R.; Weisman-Shomer, P.; Atlas, D.; Benhar, M., Thioredoxin-mimetic peptides as catalysts of S-denitrosylation and anti-nitrosative stress agents. *Free Radic Biol Med* **2015**, *79*, 138-46.

211. Jeong, W.; Yoon, H. W.; Lee, S. R.; Rhee, S. G., Identification and characterization of TRP14, a thioredoxin-related protein of 14 kDa. New insights into the specificity of thioredoxin function. *J Biol Chem* **2004**, *279* (5), 3142-50.
212. Szeto, A.; Nation, D. A.; Mendez, A. J.; Dominguez-Bendala, J.; Brooks, L. G.; Schneiderman, N.; McCabe, P. M., Oxytocin attenuates NADPH-dependent superoxide activity and IL-6 secretion in macrophages and vascular cells. *Am J Physiol Endocrinol Metab* **2008**, *295* (6), E1495-501.
213. Albano, E., Alcohol, oxidative stress and free radical damage. *Proc Nutr Soc* **2006**, *65* (3), 278-90.
214. Kokkola, T.; Savinainen, J. R.; Monkkonen, K. S.; Retamal, M. D.; Laitinen, J. T., S-nitrosothiols modulate G protein-coupled receptor signaling in a reversible and highly receptor-specific manner. *BMC Cell Biol* **2005**, *6* (1), 21.
215. Fanelli, F.; Barbier, P.; Zanchetta, D.; de Benedetti, P. G.; Chini, B., Activation mechanism of human oxytocin receptor: a combined study of experimental and computer-simulated mutagenesis. *Mol Pharmacol* **1999**, *56* (1), 214-25.
216. Kawaguchi, Y.; Kubota, Y., GABAergic cell subtypes and their synaptic connections in rat frontal cortex. *Cereb Cortex* **1997**, *7* (6), 476-86.
217. Patel, Y. C., Somatostatin and its receptor family. *Front Neuroendocrinol* **1999**, *20* (3), 157-98.
218. Tostivint, H.; Lihrmann, I.; Vaudry, H., New insight into the molecular evolution of the somatostatin family. *Mol Cell Endocrinol* **2008**, *286* (1-2), 5-17.
219. Dun, N. J.; Dun, S. L.; Wong, R. K.; Forstermann, U., Colocalization of nitric oxide synthase and somatostatin immunoreactivity in rat dentate hilar neurons. *Proc Natl Acad Sci U S A* **1994**, *91* (8), 2955-9.
220. Jaglin, X. H.; Hjerling-Leffler, J.; Fishell, G.; Batista-Brito, R., The origin of neocortical nitric oxide synthase-expressing inhibitory neurons. *Front Neural Circuits* **2012**, *6*, 44.
221. Vasilaki, A.; Papadaki, T.; Notas, G.; Kolios, G.; Mastrodimou, N.; Hoyer, D.; Tsilimbaris, M.; Kouroumalis, E.; Pallikaris, I.; Thermos, K., Effect of somatostatin on nitric oxide production in human retinal pigment epithelium cell cultures. *Invest Ophthalmol Vis Sci* **2004**, *45* (5), 1499-506.
222. Holtkamp, G. M.; Kijlstra, A.; Peek, R.; de Vos, A. F., Retinal pigment epithelium-immune system interactions: cytokine production and cytokine-induced changes. *Prog Retin Eye Res* **2001**, *20* (1), 29-48.
223. Rabenstein, D. L.; Weaver, K. H., Kinetics and Equilibria of the Thiol/Disulfide Exchange Reactions of Somatostatin with Glutathione. *J Org Chem* **1996**, *61* (21), 7391-7397.
224. Friedman, M.; Noma, A. T.; Masri, M. S., New internal standards for basic amino acid analyses. *Anal Biochem* **1973**, *51* (1), 280-7.
225. Halliwell, B.; Gutteridge, J. M., Oxygen toxicity, oxygen radicals, transition metals and disease. *Biochem J* **1984**, *219* (1), 1-14.
226. Aruoma, O. I.; Halliwell, B., Superoxide-dependent and ascorbate-dependent formation of hydroxyl radicals from hydrogen peroxide in the presence of iron. Are lactoferrin and transferrin promoters of hydroxyl-radical generation? *Biochem J* **1987**, *241* (1), 273-8.
227. Schoneich, C., Thiyl radicals and induction of protein degradation. *Free Radic Res* **2016**, *50* (2), 143-9.
228. Bonifacic, M.; Asmus, K. D., Radical reactions in aqueous disulphide-thiol systems. *Int J Radiat Biol Relat Stud Phys Chem Med* **1984**, *46* (1), 35-45.
229. Nauser, T.; Koppenol, W. H.; Schoneich, C., Protein thiyl radical reactions and product formation: a kinetic simulation. *Free Radic Biol Med* **2015**, *80*, 158-63.
230. Pietraforte, D.; Minetti, M., Direct ESR detection of peroxynitrite-induced tyrosine-centred

- protein radicals in human blood plasma. *Biochem J* **1997**, *325* (Pt 3), 675-84.
231. Jourdeheuil, D.; Jourdeheuil, F. L.; Feelisch, M., Oxidation and nitrosation of thiols at low micromolar exposure to nitric oxide. Evidence for a free radical mechanism. *J Biol Chem* **2003**, *278* (18), 15720-6.
232. Bosworth, C. A.; Toledo, J. C., Jr.; Zmijewski, J. W.; Li, Q.; Lancaster, J. R., Jr., Dinitrosyliron complexes and the mechanism(s) of cellular protein nitrosothiol formation from nitric oxide. *Proc Natl Acad Sci U S A* **2009**, *106* (12), 4671-6.
233. Raines, K. W.; Bonini, M. G.; Campbell, S. L., Nitric oxide cell signaling: S-nitrosation of Ras superfamily GTPases. *Cardiovasc Res* **2007**, *75* (2), 229-39.
234. Butler, A. R.; Rhodes, P., Chemistry, analysis, and biological roles of S-nitrosothiols. *Anal Biochem* **1997**, *249* (1), 1-9.
235. Anoop, A.; Ranganathan, S.; Das Dhaked, B.; Jha, N. N.; Pratihari, S.; Ghosh, S.; Sahay, S.; Kumar, S.; Das, S.; Kombrabail, M.; Agarwal, K.; Jacob, R. S.; Singru, P.; Bhaumik, P.; Padinhateeri, R.; Kumar, A.; Maji, S. K., Elucidating the role of disulfide bond on amyloid formation and fibril reversibility of somatostatin-14: relevance to its storage and secretion. *J Biol Chem* **2014**, *289* (24), 16884-903.
236. Augusto, O.; Goldstein, S.; Hurst, J. K.; Lind, J.; Lymar, S. V.; Merenyi, G.; Radi, R., Carbon dioxide-catalyzed peroxynitrite reactivity - The resilience of the radical mechanism after two decades of research. *Free Radic Biol Med* **2019**, *135*, 210-215.
237. van der Vliet, A.; Hoen, P. A.; Wong, P. S.; Bast, A.; Cross, C. E., Formation of S-nitrosothiols via direct nucleophilic nitrosation of thiols by peroxynitrite with elimination of hydrogen peroxide. *J Biol Chem* **1998**, *273* (46), 30255-62.
238. Radi, R.; Cosgrove, T. P.; Beckman, J. S.; Freeman, B. A., Peroxynitrite-induced luminol chemiluminescence. *Biochem J* **1993**, *290* (Pt 1), 51-7.
239. Lymar, S. V.; Hurst, J. K., Carbon dioxide: physiological catalyst for peroxynitrite-mediated cellular damage or cellular protectant? *Chem Res Toxicol* **1996**, *9* (5), 845-50.
240. Uppu, R. M.; Squadrito, G. L.; Pryor, W. A., Acceleration of peroxynitrite oxidations by carbon dioxide. *Arch Biochem Biophys* **1996**, *327* (2), 335-43.
241. Molina, C.; Kissner, R.; Koppenol, W. H., Decomposition kinetics of peroxynitrite: influence of pH and buffer. *Dalton Trans* **2013**, *42* (27), 9898-905.
242. Viner, R. I.; Huhmer, A. F.; Bigelow, D. J.; Schoneich, C., The oxidative inactivation of sarcoplasmic reticulum Ca(2+)-ATPase by peroxynitrite. *Free Radic Res* **1996**, *24* (4), 243-59.
243. Viner, R. I.; Krainev, A. G.; Williams, T. D.; Schoneich, C.; Bigelow, D. J., Identification of oxidation-sensitive peptides within the cytoplasmic domain of the sarcoplasmic reticulum Ca²⁺-ATPase. *Biochemistry* **1997**, *36* (25), 7706-16.
244. Bern, H. A.; Pearson, D.; Larson, B. A.; Nishioka, R. S., Neurohormones from fish tails: the caudal neurosecretory system. I. "Urophysiology" and the caudal neurosecretory system of fishes. *Recent Prog Horm Res* **1985**, *41*, 533-52.
245. Ames, R. S.; Sarau, H. M.; Chambers, J. K.; Willette, R. N.; Aiyar, N. V.; Romanic, A. M.; Loudon, C. S.; Foley, J. J.; Sauermelch, C. F.; Coatney, R. W.; Ao, Z.; Disa, J.; Holmes, S. D.; Stadel, J. M.; Martin, J. D.; Liu, W. S.; Glover, G. I.; Wilson, S.; McNulty, D. E.; Ellis, C. E.; Elshourbagy, N. A.; Shabon, U.; Trill, J. J.; Hay, D. W.; Ohlstein, E. H.; Bergsma, D. J.; Douglas, S. A., Human urotensin-II is a potent vasoconstrictor and agonist for the orphan receptor GPR14. *Nature* **1999**, *401* (6750), 282-6.
246. Totsune, K.; Takahashi, K.; Arihara, Z.; Sone, M.; Satoh, F.; Ito, S.; Kimura, Y.; Sasano, H.; Murakami, O., Role of urotensin II in patients on dialysis. *Lancet* **2001**, *358* (9284), 810-1.
247. Totsune, K.; Takahashi, K.; Arihara, Z.; Sone, M.; Ito, S.; Murakami, O., Increased plasma urotensin II levels in patients with diabetes mellitus. *Clin Sci (Lond)* **2003**, *104* (1), 1-5.
248. Russell, F. D.; Meyers, D.; Galbraith, A. J.; Bett, N.; Toth, I.; Kearns, P.; Molenaar, P.,

- Elevated plasma levels of human urotensin-II immunoreactivity in congestive heart failure. *Am J Physiol Heart Circ Physiol* **2003**, 285 (4), H1576-81.
249. Ng, L. L.; Loke, I.; O'Brien, R. J.; Squire, I. B.; Davies, J. E., Plasma urotensin in human systolic heart failure. *Circulation* **2002**, 106 (23), 2877-80.
250. Carotenuto, A.; Grieco, P.; Rovero, P.; Novellino, E., Urotensin-II receptor antagonists. *Curr Med Chem* **2006**, 13 (3), 267-75.
251. Winter, M. J.; Hubbard, P. C.; McCrohan, C. R.; Balment, R. J., A homologous radioimmunoassay for the measurement of urotensin II in the euryhaline flounder, *Platichthys flesus*. *Gen Comp Endocrinol* **1999**, 114 (2), 249-56.
252. Kelly, R. A.; Balligand, J. L.; Smith, T. W., Nitric oxide and cardiac function. *Circ Res* **1996**, 79 (3), 363-80.
253. Katano, Y.; Ishihata, A.; Aita, T.; Ogaki, T.; Horie, T., Vasodilator effect of urotensin II, one of the most potent vasoconstricting factors, on rat coronary arteries. *Eur J Pharmacol* **2000**, 402 (1-2), R5-7.
254. Cakar, E.; Ayvaci, H.; Karcaaltincaba, D.; Aydin, G.; Cilli, A.; Bicer, C.; Erel, O.; Kayatas Eser, S., Thiol-disulfide homeostasis in pregnancies with fetal growth restriction. *J Matern Fetal Neonatal Med* **2019**, 32 (23), 3974-3979.
255. Celik, E.; Taysi, S.; Sucu, S.; Ulusal, H.; Sevincler, E.; Celik, A., Urotensin 2 and Oxidative Stress Levels in Maternal Serum in Pregnancies Complicated by Intrauterine Growth Restriction. *Medicina (Kaunas)* **2019**, 55 (7).
256. Erel, O.; Neselioglu, S., A novel and automated assay for thiol/disulphide homeostasis. *Clin Biochem* **2014**, 47 (18), 326-32.
257. Merlino, F.; Di Maro, S.; Munaim Yousif, A.; Caraglia, M.; Grieco, P., Urotensin-II Ligands: An Overview from Peptide to Nonpeptide Structures. *J Amino Acids* **2013**, 2013, 979016.
258. Carballal, S.; Bartesaghi, S.; Radi, R., Kinetic and mechanistic considerations to assess the biological fate of peroxynitrite. *Biochim Biophys Acta* **2014**, 1840 (2), 768-80.
259. Quijano, C.; Alvarez, B.; Gatti, R. M.; Augusto, O.; Radi, R., Pathways of peroxynitrite oxidation of thiol groups. *Biochem J* **1997**, 322 (Pt 1), 167-73.
260. Ong, K. L.; Lam, K. S.; Cheung, B. M., Urotensin II: its function in health and its role in disease. *Cardiovasc Drugs Ther* **2005**, 19 (1), 65-75.
261. Roy, J. F.; Chretien, M. N.; Woodside, B.; English, A. M., Reduction and S-nitrosation of the neuropeptide oxytocin: implications for its biological function. *Nitric Oxide* **2007**, 17 (2), 82-90.
262. Salas, E.; Moro, M. A.; Askew, S.; Hodson, H. F.; Butler, A. R.; Radomski, M. W.; Moncada, S., Comparative pharmacology of analogues of S-nitroso-N-acetyl-DL-penicillamine on human platelets. *Br J Pharmacol* **1994**, 112 (4), 1071-6.
263. Jia, L.; Bonaventura, C.; Bonaventura, J.; Stamler, J. S., S-nitrosohaemoglobin: a dynamic activity of blood involved in vascular control. *Nature* **1996**, 380 (6571), 221-6.